UNIVERSITY OF SOUTHAMPTON
Faculty of Engineering, Science and Mathematics
Optoelectronics Research Centre

# QPM GRATING DESIGN FOR NOVEL PPLN STRUCTURES

**by**

**Huw E. Major**

A thesis submitted for the degree of
Doctor of Philosophy

August 2009

UNIVERSITY OF SOUTHAMPTON

ABSTRACT

FACULTY OF SCIENCE, ENGINEERING AND MATHEMATICS
OPTOELECTRONICS RESEARCH CENTRE

Doctor of Philosophy

# QPM GRATING DESIGN FOR NOVEL PPLN STRUCTURES

by Huw E. Major

This thesis describes a series of theoretical and experimental studies into modifying the phase-matching characteristics of nonlinear parametric interactions, specifically second harmonic generation, using quasi-phase-matched structures. The use of quasi-phase-matching by periodic poling affords a flexibility in designing tailored phase-matching characteristics not offered by alternative techniques. In this work phase matching characteristics are modified to provide enhanced acceptance bandwidths, compensation for focusing effects and high power operation.

The first result of this work describes the design and manufacture of 20 mm long $LiNbO_3$ aperiodic quasi-phase-matched devices for the generation of stable second harmonic power across wide temperature ranges. Theoretical simulations have demonstrated constant power output over a range of 9 °C. Providing over 35 times the bandwidth of equivalent length periodic structures, whilst offering almost an order of magnitude efficiency enhancement over periodic devices with the same bandwidth. Experimental verification of these devices has shown that stable power can be obtained across wide temperature ranges with only slight deviation from theory.

Additionally, an investigation into the effects of focusing on second harmonic generation is undertaken. In this work the Gouy phase of a focused beam has been analytically identified as the source of dephasing in bulk nonlinear interactions, causing such effects as back conversion, reduced efficiency and errors in the phase matching condition. A method to negate these effects, using a modified QPM structure has been proposed and experimentally demonstrated.

Finally, simultaneous compensation of both the Gouy phase and focused intensity variation has been applied to aperiodic, wide temperature bandwidth devices. Removal of these deleterious effects has been shown theoretically to correct the experimentally observed bandwidth errors, resulting in the focused interactions performing identically to plane-wave simulations.

# Acknowledgements

I have greatly enjoyed my time at the ORC and would therefore like to thank firstly my supervisor Prof. Peter Smith for allowing me this opportunity. It is through his encouragement during my final year of undergraduate study that I undertook this endeavour. Since then I have been offered a greatly varied area of research under his guidance, through fabrication, theoretical modeling and optical testing, all of which I have enjoyed thoroughly.

I cannot of course forget the great help I have received from other members of the ORC. Be it from Dr. Corin Gawith and his ability to make even the cleanroom feel like a fun place to be, although I'll never forget my first nerve racking day trying not to smash the wafers. Or Dr. James Gates for his great help in all things optical (just don't ask him to explain how he obtains all those vital bits of kit). To Dr. Anna Peacock for her help with many of the more complex simulations. My thanks also to Stratophase for so generously sponsoring me through much of my PhD

To my friends who tried to ensure I had some form of a life. Alex, Geoff, Froody, Corin, Gates, Dave, Nick, Greg, Chris, Tim, Mark and Ed and all the others, cheers.

To my family I'd like to say thank you for all the support. Especially to my sister, Sarah, for having been there and done it all before and being great to chat to when things went wrong. Euan, thank you for understanding what I have been working on and helping me to explain to everyone else what I have been doing for the last 4 years. Although hopefully even you won't be able to understand it all.

To Emma, thank you so much.

# Declaration of Authorship

I, Huw Major, declare that this thesis titled, "QPM Grating Design for Novel PPLN Structures," and the work presented in it are my own. I confirm that:

- This work was done wholly or mainly while in candidature for a research degree at this University
- Where any part of this thesis has previously been submitted for a degree or any other qualification at this University or any other institution, this has been clearly stated
- Where I have consulted the published work of others, this is always clearly attributed
- Where I have quoted from the work of others, the source is always given. With the exception of such quotations, this thesis is entirely my own work
- I have acknowledged all main sources of help
- Where the thesis is based on work done by myself jointly with others, I have made clear exactly what was done by others and what I have contributed myself
- Parts of this work have been published as:
  - H. E. Major et al. , Opt. Commun. 281(19), pp 5036-5040, 2008
  - C. B. E. Gawith et al. , Patent No. WO2008/152377 A1
  - H. E. Major et al. , Patent Application No. GB0801322.9
  - C. B. E. Gawith et al. , Patent Application No. GB0802852.4

Signed:

Date: 29th August 2009

# Contents

# Nomenclature

## Acronyms

BLIIRA Blue light Induced Infra-Red Absorption

DFG Difference Frequency Generation

GQPM Gouy phase compensated QPM

GRIIRA Green light Induced Infra-Red Absorption

GVM Group Velocity Mismatch

KDP Potassium Dihydrogen Phosphate

MLM multi-longitudinal mode

OPO Optical Parametric Oscillation

PPLN Periodically-Poled Lithium Niobate

QPM Quasi-Phase Matching

SFG Sum Frequency Generation

SHG Second Harmonic Generation

SLM Single Longitudinal Mode

# Symbols

| | |
|---|---|
| $B$ | Magnetic Flux Density |
| $b$ | $2z_R$ |
| $\beta$ | Poynting Vector Walk-Off |
| $\chi^{(1)}$ | Linear Susceptibility |
| $\chi^{(2)}$ | 2nd Order Nonlinearity |
| $L_c$ | Coherence Length |
| $D$ | Electric Displacement Field |
| $\mathrm{d_{eff}}$ | Effective Nonlinearity |
| $\Delta S$ | Scaled Phase Mismatch |
| $E$ | Electric Field |
| $\epsilon_0$ | Permittivity of free space |
| $H$ | Magnetic Field |
| $h()$ | Boyd and Klienman Focusing Factor |
| $J$ | Conduction Current |
| $\Lambda$ | QPM Period |
| $L$ | Nonlinear Device Length |
| $\mu_0$ | Permeability of free space |
| $\omega_0$ | Focused Spot Size |
| $P\left(t\right)$ | Material Polarisation |
| $\Phi$ | Gaussian Mode Gouy Phase |
| $P_\omega$ | Fundamental Optical Power |
| $P_{2\omega}$ | Second Harmonic Optical Power |
| $\Psi$ | Gaussian Mode Phase Curvature |

| | |
|---|---|
| $\rho$ | Double Refraction Angle |
| $u^2$ | Scaled Fundamental Power |
| $v^2$ | Scaled Harmonic Power |
| $\xi$ | Focusing Ratio, $L/b$ |
| $\zeta$ | $z/z_R$ |
| $z_R$ | Rayleigh Range |

# Chapter 1

# Introduction

## 1.1 Motivations and Aims

The concept of harmonic frequency generation using nonlinear materials is now well established. One of the earliest reported examples of electromagnetic harmonic generation was observed in electrical coil modulators at Bell Telephone Labs in 1916 [1], with such structures being studied for possible use in long distance telephony communication systems. With a new found understanding gained from these early observations a classical interpretation of the recently encountered nonlinear Raman effect [2] was proposed by Hartley in 1929 [3]. Although further developments were made in the field of nonlinear harmonic generation in electrical systems it was not until the advent of the ruby laser in 1960 [4, 5], however, that significant harmonic generation was encountered at optical frequencies [6]. Here, the intense optical fields generated by the ruby laser were sufficient to cause a small nonlinear polarisation response within a sample of nonlinear crystaline quartz, generating an optical second harmonic at a wavelength of 347 nm.

Since this initial foray into optical harmonic generation significant enhancements have been made, with large gains in optical efficiencies being achieved. These increased efficiencies have been brought about through advances in laser technology, the discovery of high quality, highly nonlinear optical materials and efficient methods of phase matching. Arguably the most important of these factors is the availability of high nonlearity optical materials, such as $LiNbO_3$ and $LiTaO_3$ which provide up to a 60 fold increase in nonlinearity compared with the crystaline quartz used for the earliest optical experiments [7, 8]. However, even with the availability of improved nonlinear optical materials it was demonstrated by Maker [9] that in order to obtain useful amounts of harmonic power careful phase-matching of the traveling fundamental and harmonic waves was essential. Using the material potassium dihydrogen phosphate (KDP), which

has a nonlinearity 30 times that of quartz, it was shown that through angle tuning of the crystal optic axis relative to the polarised input it is possible to balance out the negative effects of dispersion using the material birefringence. This first demonstration of optical birefringent phase-matching resulted in a 300 fold increase in harmonic power compared with the on axis power, and clearly demonstrated the huge benefits phase-matching can provide.

Following on from the initial experimental verification of the importance of phase-matching considerable effort was made to fully understand its effects. This lead to the publication of the seminal paper by Armstrong et. al. [10] which details, in depth, the importance of phase-matching in achieving high optical efficiencies and perhaps more importantly introduces the concept of quasi-phase-matching. Combined with the important material types of $LiNbO_3$ and $LiTaO_3$ it is this concept of quasi-phase-matching that helped harmonic generation to gain widespread adoption as an efficient, versatile method of laser light production.

Concurrently with his investigation into the effects of phase-matching Maker also highlighted the relationship between tight focusing and high conversion efficiency, showing a 3000 fold increase in efficiency with a tightly focused beam in KDP compared with a confocal beam in quartz [9]. Again numerous groups proceeded to generate theoretical papers detailing the effects of focusing on optical efficiency [11, 12, 13] but it was not until 1968 that the definitive paper on the subject was published [14]. This important paper provided the universal optimum focusing conditions for maximal conversion efficiency for many second order nonlinear parametric interactions. Although originally calculated for birefringently phase-matched interactions these results were found to equally apply to quasi-phase-matched interactions and are still being utilised 40 years later.

The research described in this thesis is based on improving the efficiency of nonlinear interactions, specifically second harmonic generation, with the expressed aim of investigating devices suitable for commercial visible light generation. Nonlinear generation of high intensity visible light is especially interesting in the commercial fields of display and projection as there are currently no alternative means of generating a high brightness, pure green source, as is required to fully saturate the colour gamut.

Despite the many advantages modern nonlinear sources can offer there are still several limitations which must be overcome before rugged and cheap solutions can be offered. Of particular importance is the reduction of the sensitivity of quasi-phase matched devices to fluctuations in operating temperature and fundamental input wavelength. Current devices struggle in real world applications, with extremely precise control of these two parameters essential for continuous, efficient operation. Existing solutions to this problem have thus far been unsatisfactory,

with enhanced stability gained at considerable cost to the optical conversion efficiency. As such a large portion of this work is devoted to improving on these existing techniques, aiming to provide high efficiency solutions suitable for a mass production market.

In addition to producing devices stable to environmental fluctuations in order to achieve widespread adoption of harmonic generation light sources advances must be made in the conversion efficiencies of such devices. To this end the remainder of the work in this thesis concentrates on methods for providing the highest levels of conversion efficiency from nonlinear interactions, in particular bulk focused interactions. With these being the most suited to high power, high efficiency operation. As a result of this investigation a new optimum focusing condition has been identified, for a suitably modified quasi-phase-matched structure, that improves upon the conditions proposed by Boyd and Kleinman 40 years previously, providing amongst other attributes improved conversion efficiencies.

## 1.2 Thesis Synopsis

Beginning with a brief introduction to optical nonlinearity, in particular second order nonlinearity, Chapter 2 introduces many of the theoretical principles required to understand the nature of parametric interactions in nonlinear optical materials. Particular attention is paid to the techniques required for efficient phase matching of second harmonic process, with this being a central theme for the work in the thesis. Following on from this the nonlinear optical material Lithium Niobate is introduced, with methods for achieving quasi-phase-matching in this material discussed. Chapter 3 describes techniques for improving the acceptance bandwidth of QPM devices through engineering of the periodic grating structure. A new analytic simulation technique is developed for analysing complex grating structures, with the resulting structures fabricated in Lithium Niobate and optically tested. In Chapter 4 a thorough investigation into the effects of focused Gaussian beams on the conversion efficiency of second harmonic generation is undertaken, with the initial aim of this work being to explain an unexpected focus induced feature in the wide bandwidth QPM devices of Chapter 3. In performing this analysis a new optimum QPM grating structure has been developed that improves on the previous maximum theoretical conversion efficiency obtainable in focused nonlinear interactions. Building on the work in Chapters 3 and 4, further examples of increased acceptance banwidth QPM devices have been given in Chapter 5, with these new designs theoretically able to compensate fully for the deleterious effects of focused Gaussian beams. Chapter 6 returns to the earlier work on increased efficiency focused SHG interactions. This Chapter adds to the work by considering the case of high power, high efficiency focused operation and examines the advantages offered

by the modified grating structures of Chapter 4. Finally, conclusions and a brief description of further future experiments on high power focused interactions are given. Additional device types for high power, high efficiency SHG are also briefly introduced, making use of the simulation techniques of Chapter 6.

# References


[1] J. M. Manley and H. E. Rowe. Some general properties of non-linear elements. *Proc. Inst. Radio Engrs.*, 44(7):904–913, July 1956.

[2] C. V. Raman. *Molecular diffraction of light.* University of Calcutta, 1922.

[3] R. V. L. Hartley. A wave mechanism of quantum phenomena. *Phys. Rev.*, 33:289, Feb 1929.

[4] T. H. Maiman. Stimulated optical radiation in ruby. *Nature*, 187(493), 1960.

[5] R. J. Collins. Coherence, narrowing, directionality, and relaxation oscillations in the light emission from ruby. *Phys. Rev. Lett.*, 5:303, 1960.

[6] P. A. Franken, A. E. Hill, C. W. Peters, and G. Weinreich. Generation of optical harmonics. *Phys. Rev. Lett.*, 7(4):118–119, 1961.

[7] M. Houe and P. Townsend. An introduction to methods of periodic poling for second harmonic generation. *J. Phys. D Appl. Phys.*, 28:1747–1763, 1995.

[8] M. Ohama, T. Fujiwara, and A. J. Ikushima. Induced defects and increase of second-order nonlinearity in ultraviolet-poled $GeO_2$-$SiO_2$ glass. *Jpn. J. Appl. Phys.*, 38(11):6359–6361, 1999.

[9] P. D. Maker, R. W. Terhune, M. Nisenoff, and C. M. Savage. Effects of dispersion and focusing on the production of optical harmonics. *Phys. Rev. Lett.*, 8(1):21–23, 1962.

[10] J. A. Armstrong, N. Bloembergen, J. Ducuing, and P. S. Pershan. Interactions between light waves in a nonlinear dielectric. *Phys. Rev.*, 127(6):1918–1939, 1962.

[11] G. D. Boyd, A. Ashkin, J. M. Dziedzic, and D. A. Kleinman. Second-harmonic generation of light with double refraction. *Phys. Rev.*, 137(4A):A1305–A1320, Feb 1965.

[12] D. A. Kleinman and R. C. Miller. Dependence of second-harmonic generation on the position of the focus. *Phys. Rev.*, 148(1):302–312, Aug 1966.

[13] D. A. Kleinman, A. Ashkin, and G. D. Boyd. Second-harmonic generation of light by focused laser beams. *Phys. Rev.*, 145(1):338–379, May 1966.

[14] G. D. Boyd and D. A. Kleinman. Parametric interaction of focused Gaussian light beams. *J. Appl. Phys.*, 39(8):3597–3639, 1968.

# Chapter 2

# Harmonic generation in nonlinear media

## 2.1 Introduction

Since the demonstration of the first laser systems in 1960 [1, 2] the introduction of coherent, high intensity light has paved the way for novel physical phenomena previously impossible to observe. One such phenomena is the field of nonlinear optics, the primary use being to generate sources of tuneable light at wavelengths previously unattainable by standard lasers.

Nonlinear optics was first realised in 1961 by Franken et al [3] shortly after the production of the first laser. The high light intensities provided by the laser were essential for the observation of this subtle effect. Their initial work concentrated on the generation of the second harmonic of a ruby laser with the use of the nonlinearity occurring in quartz crystals. However, this work was rapidly extended to include other nonlinear effects such as difference frequency generation (DFG) [4] and optical parametric oscillation (OPO) [5]. It was shown later in 1962 [6] that the efficiency of the initial experiments was limited by the effects of dispersion, but that this effect could be much reduced with the use of birefringent phase-matching. An number of alternative schemes for phase-matching were proposed in 1962 by Armstrong et al. [7]. Arguably the most important of which was the scheme of quasi-phase matching (QPM) which, unlike alternative techniques that prevent the phase slippage of the fundamental and harmonic waves, allows a phase offset to occur. But, with a suitable modification to the properties of the material, QPM can counteract the effects.

In this chapter an analysis of the fundamental equations governing electromagnetic wave

propagation in a nonlinear media is undertaken. This standard analysis starts from Maxwell's equations and derives coupled first-order equations by using the slowly varying envelope plane wave approximation for the parametric process of harmonic generation. From these coupled equations expressions for the harmonic field growth are obtained for both the simplistic case assuming no depletion of the pump wave and then further extended to derive exact solutions for the case of pump depletion. A brief overview of the standard treatment of utilising focussed Gaussian beams on the conversion efficiency is discussed, with more detailed analysis occurring in Chapter 4.

Additionally, the concepts of phase matching, essential for efficient harmonic growth, are introduced; including some of the physical techniques employed to ensure efficient phase matching. Finally, a technique for fabrication of periodically-poled lithium niobate (PPLN) structures using high voltage electric field poling is presented.

## 2.2 Induced polarisation

When an electro-magnetic field passes through a medium the electric field, and to a much lesser extent the magnetic field, interacts with the charged particles within the medium, which for optical materials constitute mostly the ion cores and their bound electrons. This interaction results in a movement of the positively charged particles in the direction of the field whilst the negative electrons move in opposition. The resulting separation of charges induces an electric dipole moment or an induced polarisation. As a result of the high frequencies of optical fields the more massive ion cores are less able to respond to rapidly varying electric fields and as such the dipoles created are almost entirely due to a distortion of electron clouds about their mostly stationary ion cores.

With optical electric fields being oscillatory in nature the induced dipoles are forced to oscillate at the frequency of the driving field, which in turn creates a radiated electric field at the same frequency. The motion of the dipoles can be likened with the simple model of a mass on a spring, where the electron is bound to the parent ion core by the spring, the motion of which is governed by the rules of harmonic oscillation. For mechanical oscillations when a small force acts on the system the response is almost entirely linear to the applied force, the same is also true for the response of the induced dipoles to a small optical field giving rise to the following definition of small signal polarisation

$$P(t) = \epsilon_0 \chi^{(1)} E(t), \tag{2.1}$$

where $\chi^{(1)} = n^2 - 1$ is the linear susceptibility of the material, with $n$ being the refractive index.

However, analogously to that of the mechanical spring model an increase in the applied oscillatory force can, if sufficiently large, alter the linear response becoming nonlinear in nature. It is evident that Equation 2.1 is insufficient to account for any anharmonic terms in the equation of oscillatory motion and must therefore be extended to account for this. Providing that the nonlinearities are small compared with the linear polarisation an approximate solution to the oscillator response can be achieved by replacing the linear polarisation with a power series expansion, where increasing accuracy can be obtained with the inclusion of higher order coefficients. Thus, for an intense optical field the induced polarisation can be approximated by

$$P(t) = \epsilon_0 \left( \chi^{(1)} E(t) + \chi^{(2)} E^2(t) + \chi^{(3)} E^3(t) + \cdots + \chi^{(n)} E^n(t) \right), \tag{2.2}$$

where for simplicity the vectorial aspects of $E(t)$ and $P(t)$ as well as the tensorial nature and frequency dependence of $\chi$ have been neglected.

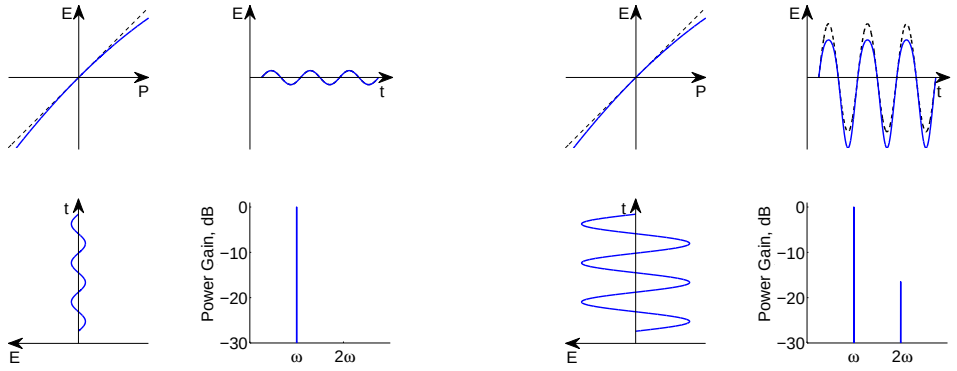


(a) (b)

Figure 2.1: A numerical simulation of the effects of a non zero second-order nonlinear component in the polarisability of an optical medium and the effect this has on the radiated field of an incident optical plane-wave at both low (a) and high (b) field intensities.

The effects of the medium nonlinearity on an applied field are demonstrated in Figures 2.1(a) and 2.1(b) which show the variation in induced polarisation of a hypothetical optical material for both low and high intensity optical fields respectively. Here, these results have been generated by defining $E(t)$ in Equation 2.2 as a sinusoidally varying function and setting $\chi^{(2)}$ to be non-zero. In Figure 2.1(a) the input field is small and thus the induced polarisation responds in an almost perfectly linear way, as shown by the top right plot. This linearity is further emphasised by the results of the lower right plot, which is a plot of the Fourier transform of the induced polarisation, showing negligible harmonic components. However, in Figure 2.1(b) a much larger optical field

is applied resulting in significant distortions to the sinusoidally varying induced polarisation. Comparing the frequency components of 2.1(a) and 2.1(b) a marked increase in the magnitude of the frequency $2\omega$ is observed for the higher intensity plot.

This frequency component at $2\omega$ arises through the process of second harmonic generation (SHG) [8] which is just one of the many processes that can occur due to the influence of 2nd order nonlinearity $\chi^{(2)}$. Other second order processes include three wave mixing (which can be further expanded to include difference frequency generation (DFG) [9], sum frequency generation (SFG) [10], optical parametric amplification (OPA) [11] and optical parametric oscillation (OPO) [12]), optical d.c. rectification [13] and the linear electro-optic effects [14]. Additionally, other familiar nonlinear effects such as third harmonic generation [15], the optical Kerr effect [16], Raman [17], Rayleigh [18] and Brillouin scattering [19] and two photon absorption [20] are a result of the 3rd order nonlinearity $\chi^{(3)}$.

In order to fully understand the physical mechanisms for these numerous nonlinear effects it can be necessary to consider the quantum mechanical effects of applied fields on the induced dipoles. However, a good understanding of the macroscopic interactions can be obtained from the solutions of Maxwell's equations assuming a nonlinear material polarisation.

## 2.3 Electro-magnetic wave theory

Before formulating expressions for the nonlinear interactions of an electromagnetic wave it is first necessary to obtain the general expression for a wave in a transparent material, (note that here the material need only be transparent for the frequencies of interest). Starting with Maxwell's equations governing electric and magnetic fields $\mathbf{E}(t)$ and $\mathbf{B}(t)$:

$$\nabla \times \mathbf{E}(t) = -\frac{\partial}{\partial t}\mathbf{B}(t) \tag{2.3}$$

$$\nabla \times \mathbf{H}(t) = \frac{\partial}{\partial t}\mathbf{D}(t) + \mathbf{J}(t) \tag{2.4}$$

Here $\mathbf{D}(t) = \epsilon_0 \mathbf{E}(t) + \mathbf{P}(t)$, and $\mathbf{J}(t)$ is the current density or the conduction current. By assuming that the media of interest has no free charges, as is common for optical materials which constitute mostly bound charges, $\mathbf{J}(t)$ can be ignored. Furthermore, optical materials are generally non-magnetic media simplifying $\mathbf{H}(t)$ to:

$$\mathbf{H}(t) = \frac{1}{\mu_0}\mathbf{B}(t) \tag{2.5}$$

This simplifies the subset of Maxwell's equations to,

$$\nabla \times \mathbf{E}(t) = -\frac{\partial}{\partial t}\mathbf{B}(t) \tag{2.6}$$

$$\nabla \times \mathbf{B}(t) = \mu_0\epsilon_0\frac{\partial}{\partial t}\mathbf{E}(t) + \mu_0\frac{\partial}{\partial t}\mathbf{P}(t). \tag{2.7}$$

These two equations can be further combined to give an expression for the electric field in the media in terms of the material polarisation. By taking the curl of Equation 2.6 and differentiating Equation 2.7 with respect to $t$ the following is obtained.

$$\nabla \times \nabla \times \mathbf{E}(t) = -\nabla \times \frac{\partial}{\partial \mathbf{t}}\mathbf{B}(t) = -\frac{\partial}{\partial t}\left[\nabla \times \mathbf{B}(t)\right] \tag{2.8}$$

$$\frac{\partial}{\partial t}\left[\nabla \times \mathbf{B}(t)\right] = \nabla \times \frac{\partial}{\partial t}\mathbf{B}(t) = \mu_0\epsilon_0\frac{\partial^2}{\partial t^2}\mathbf{E}(t) + \mu_0\frac{\partial^2}{\partial t^2}\mathbf{P}(t) \tag{2.9}$$

with a further substitution resulting in the following expression for the electric field,

$$\nabla \times \nabla \times \mathbf{E}(t) = -\mu_0\epsilon_0\frac{\partial^2}{\partial t^2}\mathbf{E}(t) - \mu_0\frac{\partial^2}{\partial t^2}\mathbf{P}(t). \tag{2.10}$$

At this point it is convenient to convert from the time domain into the frequency domain via the Fourier transform. By continuing the calculations in the frequency domain many of the requisite steps become quite intuitive, with results such as sum-frequency generation (SFG) and difference frequency generation (DFG) becoming a simple addition or subtraction of the input fields. Using the following definition of the Fourier transform,

$$f(t) = \int_{-\infty}^{\infty} f(\omega)\, e^{-i\omega t}\delta\omega \tag{2.11}$$

$$\hat{f}(\omega) = \frac{1}{2\pi}\int_{-\infty}^{\infty} f(t)\, e^{i\omega t}\delta t \tag{2.12}$$

$\mathbf{E}(t)$ and $\mathbf{P}(t)$ can be expressed in terms of the frequency components $\mathbf{E}(\omega)$ and $\mathbf{P}(\omega)$, resulting in the following definition for the electric field:

$$\nabla \times \nabla \times \mathbf{E}(\omega) = -\epsilon\mu_0\omega^2\mathbf{E}(w) - \mu_0\omega^2\mathbf{P}(w) \tag{2.13}$$

The above solution of the wave equation is a general solution for use within most common optical media (with the above assumptions of no free charge and no magnetism), this result is now further extend for use in nonlinear media. Initially, the polarisation term $\mathbf{P}(\omega)$ is separated out into its linear and nonlinear parts

$$\mathbf{P}(\omega) = \epsilon_0\boldsymbol{\chi}^{(1)}(-\omega;\omega)\cdot\mathbf{E}(\omega) + \mathbf{P}^{NL}(\omega) \tag{2.14}$$

where $\chi^{(1)}(-\omega;\omega)$ is the linear optic susceptibility second rank tensor, which is function of the frequencies $-\omega$ and $\omega$, and $\mathbf{P}^{NL}(\omega) = \sum_{n=2}^{\infty}\mathbf{P}^{(n)}(\omega)$, with $\mathbf{P}^{(n)}(\omega)$ being the $n$th order polarisation. Substituting this into 2.13 gives

$$\nabla \times \nabla \times \mathbf{E}(\omega) = -\frac{\omega^2}{c^2}\boldsymbol{\epsilon}(\omega)\,\mathbf{E}(\omega) - \mu_o\omega^2\mathbf{P}^{NL}(\omega) \tag{2.15}$$

where here $\boldsymbol{\epsilon}(\omega)$ is the linear dielectric tensor defined as

$$\boldsymbol{\epsilon}(\omega) = 1 + \boldsymbol{\chi}^{(1)}(-\omega;\omega) \tag{2.16}$$

### 2.3.1 Superposition of plane-waves

Now, investigating the solutions of the wave equation for travelling waves it is assumed these travelling waves can be expressed as a superposition, which may be written as

$$\mathbf{E}(\omega) = \hat{\mathbf{E}}(\omega)\, e^{i\mathbf{k}\cdot\mathbf{r}}. \tag{2.17}$$

Substituting this into 2.15 results in

$$\nabla \times \nabla \times \left[\hat{\mathbf{E}}(\omega)\, e^{i\mathbf{k}\cdot\mathbf{r}}\right] = \frac{\omega^2}{c^2}\boldsymbol{\epsilon}(\omega)\,\hat{\mathbf{E}}(\omega)\, e^{i\mathbf{k}\cdot\mathbf{r}} + \mu_o\omega^2\mathbf{P}^{NL}(\omega) \tag{2.18}$$

This analysis is simplified by the assumption that the wave envelope $\hat{\mathbf{E}}(\omega)$ is comprised of a superposition of infinite plane waves. Defining that these waves are propagating along an arbitrary axis denoted by $\mathbf{z}$ it is possible to stipulate that $\hat{\mathbf{E}}(\omega)$ is now solely a function of $\mathbf{z}$, additionally making the substitution $\mathbf{k}\cdot\mathbf{r} = \pm kz$, here $+$ references the forward travelling wave along the $\mathbf{z}$ direction and vice versa for $-$. Using these two assumptions the left hand side of Eq. 2.18 can be simplified to $-\partial^2\hat{\mathbf{E}}(\omega)/\partial z^2$ resulting in the new reduced form

$$\frac{\partial^2}{\partial z^2}\left[\hat{\mathbf{E}}(\omega)\, e^{\pm ikz}\right] = \frac{\omega^2}{c^2}\boldsymbol{\epsilon}(\omega)\cdot\hat{\mathbf{E}}(\omega)\, e^{\pm ikz} + \mu_o\omega^2\mathbf{P}^{NL}(\omega) \tag{2.19}$$

Now, by performing the differentiation of the LHS of the above the following result is obtained

$$\frac{\partial^2}{\partial z^2}\hat{\mathbf{E}}(\omega) + 2ike^{ikz}\frac{\partial}{\partial z}\hat{\mathbf{E}}(\omega) = \mu_0\omega^2\mathbf{P}^{NL}(\omega) \tag{2.20}$$

In obtaining this result significant simplifications have been made by noting that the wave vector $(k)$ and the field vector are orthogonal to one another, thus equating their product to zero.

### 2.3.2 Slowly-varying envelope approximation

Previously the wave-envelope has been defined as a superposition of waves containing information on both the amplitude and phase of the field $\mathbf{E}(\omega)$, by further defining the envelope to be slowly varying in the z direction additional simplifications to Equation 2.20 can be made. This proposition of a slowly varying envelope is valid for many nonlinear interactions as significant power transfer between interacting waves is usually only achieved over lengths much longer than their wavelengths. With this assumption it is now possible to assume

$$\left|\frac{\partial^2}{\partial z^2}\hat{\mathbf{E}}(\omega)\right| \ll \left|k\frac{\partial}{\partial z}\hat{\mathbf{E}}(\omega)\right|. \tag{2.21}$$

Utilising this statement in Eq. 2.20 a first order differential equation relating electric field and induced polarisation is obtained,

$$\frac{\partial}{\partial z}\hat{\mathbf{E}}(\omega) \simeq -i\frac{\mu_0\omega^2}{2k}\mathbf{P}^{NL}(\omega)\, e^{\pm kz} \tag{2.22}$$

This simplification is known as the slowly-varying envelope approximation. It should be noted that the justification given above for ignoring the second-order derivative term is common in literature. However, it has been shown via Green's function analysis [21] that the physical interpretation of this simplification is in fact equivalent to neglecting the backward propagating wave in the analysis.

### 2.3.3 Monochromatic wave propagation

Leading on from the general solution given by Equation 2.22 the analysis of monochromatic plane-waves is now considered. This is achieved by assuming that $\mathbf{E}(\omega)$ is a superposition of monochromatic plane waves, each with identical polarisation.

$$\mathbf{E}(\omega) = \frac{1}{2}\sum_{\omega_j \geq 0}\left[\hat{\mathbf{E}}_{\omega_j} e^{ik_j z}\delta(\omega-\omega_j) + \hat{\mathbf{E}}^{*}_{\omega_j} e^{-ik_j z}\delta(\omega+\omega_j)\right] \tag{2.23}$$

Here, the wave-vector $k_j = \omega_j n(\omega_j)/c$ and $\delta(\omega-\omega_j)$ is the Dirac-delta function centred at frequency $\omega_j$. On choosing a frequency of interest, $\omega_\rho$, an expression for the variation in its associated electric field is readily obtained,

$$\frac{\partial}{\partial z}\hat{\mathbf{E}}_{\omega_\rho} = i\,\frac{\mu_0\omega_\rho^2}{2k_\rho}\,\mathbf{P}^{NL}_{\omega_\rho} e^{ik_\rho z}, \tag{2.24}$$

where $\mathbf{P}^{NL}_{\omega_\rho} = \sum_{n=2}^{\infty}\mathbf{P}^{(n)}_{\omega_\rho}$, with $\mathbf{P}^{(n)}_{\omega_\rho}$ being the $n$th order susceptibility at frequency $\omega_\rho$ given as

$$\mathbf{P}^{(n)}_{\omega_\rho} = \epsilon_0\sum_{\omega} K(-\omega_\rho;\omega_1,\cdots,\omega_n)\,\chi^{(n)}(-\omega_\rho;\omega_1,\cdots,\omega_n)\,\mathbf{E}_{\omega_1}\cdots\mathbf{E}_{\omega_n}e^{ik_\rho z}. \tag{2.25}$$

Here, the summation over $\omega$ accounts for all the possible distinct sets of $\omega_1,\cdots,\omega_n$ that can mix to give rise to $\omega_\rho$, with $k_\rho = k_1+\cdots+k_n$. Finally, $K$ is simply a numerical factor that is used to track the $1/2$ factors introduced by the substitutions of Equation 2.23 and is defined as

$$K(-\omega_\rho;\omega_1,\cdots,\omega_n) = 2^{l+m-n}p \tag{2.26}$$

where $p$ is the number of distinct permutations of the frequencies $\omega_1,\cdots,\omega_n$, $m$ is the set of frequencies containing zero frequency or d.c. fields, $n$ is the nonlinearity order, and $l=1$ if the frequency of interest, $\omega_\rho \neq 0$. As an example considering the simple case of second harmonic generation (SHG) $n=2$, $p=1$, $m=0$ and $l=1$ giving a $K$ factor of $1/2$. For the slightly more complex cases of sum frequency generation (SFG) or difference frequency generation (DFG) by

invoking Kleinman symmetry [6] it is noted that $(-\omega_\rho\,;\omega_1,\pm\omega_2) = (-\omega_\rho\,;\pm\omega_2,\omega_1)$, however the two are still strictly distinguishable and therefore both sets must be included producing a $K$ factor of 1.

Finally, substituting 2.25 into 2.24 the following general solution for the variation in electric field due to an induced polarisation of order $n$ is obtained,

$$\frac{\partial}{\partial z}\hat{E}_\rho = i\frac{\omega_\rho^2}{2k_\rho c^2}K\left(-\omega_\rho\,;\omega_1,\cdots,\omega_n\right)\chi^{(n)}\left(-\omega_\rho\,;\omega_1,\cdots,\omega_n\right)\hat{E}_1\cdots\hat{E}_n e^{i\Delta kz}. \tag{2.27}$$

Here, $\Delta k = k_\rho$ is the phase mismatch describing the propagating phase error between the interacting waves.

## 2.4 Harmonic generation

Having reviewed the general case the above analysis is now be clarified for the specific example of second harmonic generation, which is the main focus of this work.

Using Equation 2.27 the two coupled equations linking the fundamental ($\omega$) and harmonic fields ($2\omega$) have been determined,

$$\frac{\partial}{\partial z}\hat{E}_{2\omega} = i\frac{(2\omega)^2}{2k_{2\omega}c^2}\left[\frac{1}{2}\chi^{(2)}\left(-2\omega\,;\omega,\omega\right)\hat{E}_\omega^2\right]e^{i\Delta kz} \tag{2.28}$$

$$\frac{\partial}{\partial z}\hat{E}_{\omega} = i\frac{\omega^2}{2k_{\omega}c^2}\left[\chi^{(2)}\left(-2\omega\,;\omega,\omega\right)\hat{E}_{2\omega}\hat{E}_\omega^*\right]e^{i\Delta kz} \tag{2.29}$$

where, $\Delta k = 2k_\omega - k_{2\omega}$ and the K values have been evaluated according to Equation 2.26. Here, it is noted that the electric fields are necessarily real and thus $E_{-\omega} = E_\omega^*$. Note also that the coefficients in the $\chi^{(2)}$ tensor of the fundamental field have been altered in accordance with Kleinman symmetry.

At this point it is prudent to introduce the Manley-Rowe relation [22] governing power transfer between the two waves. Assuming zero absorption at either frequency this relation can be written as $(1/2\omega)\,\delta I_{2\omega}/\delta z = -1/2\,(1/\omega)\,\delta I_\omega/\delta z$. In the case of SHG this relation simply implies photon conservation, with two pump photons joining to form one harmonic with twice the energy.

### 2.4.1 Low-conversion efficiency

In the low conversion limit it is assumed that the fundamental field is undepleted and thus $\mathrm{d}E_\omega/\mathrm{d}z = 0$, $E_\omega(z) = E_\omega(0)$. Using this assumption it is possible to integrate directly Equation 2.28, pulling $E_\omega$ outside the integral, obtaining an expression for the growth of the harmonic

electric field through a nonlinear medium of length L:

$$E_{2\omega}(L) = \frac{i(2\omega)}{4n_{2\omega}c}\chi^{(2)}(-2\omega;\omega,\omega)\hat{E}_{\omega}^{2}\int_{-L/2}^{L/2}e^{i\Delta kz}\mathrm{d}z \tag{2.30}$$

$$= \frac{(2\omega)}{4n_{2\omega}c}\chi^{(2)}(-2\omega;\omega,\omega)\hat{E}_{\omega}^{2}L\frac{\sin(\Delta kL/2)}{\Delta kL/2}. \tag{2.31}$$

Expressing this in terms of intensity,

$$I_{2\omega}(L) = \frac{(2\omega)^2}{8n_{\omega}^{2}n_{2\omega}c^{3}\epsilon_0}\left|\chi^{(2)}(-2\omega;\omega,\omega)\right|^{2}I_{\omega}^{2}L^{2}\,\mathrm{sinc}^{2}(\Delta kL/2). \tag{2.32}$$

From this it is noted that the final harmonic efficiency is proportional to the fundamental intensity, leading to ever higher conversion efficiencies with increasing fundamental input. Additionally, it is clear that the output power is highly dependent on the length of the nonlinear interaction, displaying a quadratic proportionality. It should be noted at this point that the length squared dependence of the conversion efficiency only applies to infinite plane-wave interactions, as is discussed shortly for the more common focussed interactions this dependency falls back to a linear proportionality for optimally focused SHG.

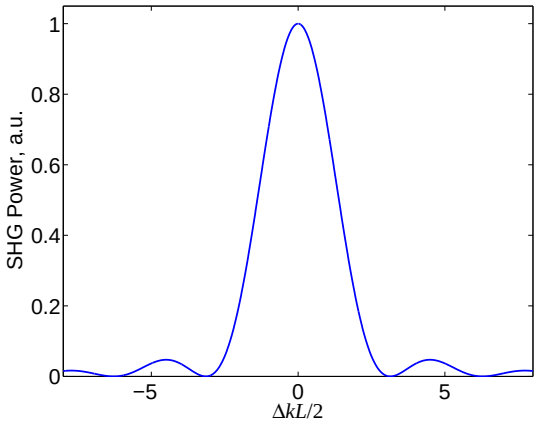


Figure 2.2: A plot of the $\mathrm{sinc}^2$ harmonic conversion efficiency for variations in the phase-matching parameter $\Delta kL/2$. Note here the phase-matching parameter has been scaled to be device length independent

One final observation regards $\mathrm{sinc}^2(\Delta kL/2)$, from this term it is evident that the harmonic conversion efficiency has a single maximum when $\Delta kL/2 = 0$ and has minima at $\Delta kL = \pm 2n\pi$, where n is any integer value. This is shown explicitly in Figure. 2.2. To achieve efficient power transfer from the fundamental to the harmonic $\Delta k$ must be close to zero. This implies that the harmonic and the fundamental fields are propagating in phase-lock with one another allowing continuous positive power transfer, giving rise to the term phase-matching. However, due to material dispersion $\Delta k \neq 0$ in general. It can thus be inferred from Equation 2.32 that the

harmonic growth is oscillatory in nature, initially increasing with interaction length before depleting back to the fundamental. The length over which this oscillation occurs is known as the coherence length and is defined as $L_c = |\pi/\Delta k|$ which is simply the length over which the two fields become 180° out of phase.

With $\Delta k$ being highly dependent on material dispersion it is often found that it is physically impossible to achieve efficient conversion for many harmonic interactions. However, by utilising phase-matching techniques, which are discussed shortly, it is possible to mitigate the effects allowing for substantial conversion efficiencies.

### 2.4.2 High-conversion efficiency

If it is assumed that the harmonic process is well phase matched, i.e. $\Delta k \to 0$, it follows that $L_c \to \infty$ and that large harmonic fields can be generated given sufficiently high fundamental intensity and long interaction lengths.

With appreciable conversion efficiency it is no longer possible to neglect the effects of pump depletion, thus the coupled equations of 2.28 and 2.29 must now be solved explicitly to obtain a true representation of the harmonic process. The analysis required to solve these equations with phase mismatch is complex [7] but, with perfect phase-matching results in a simple definition for the coupled intensities given as[1]

$$I_{2\omega}(L) = I_{\omega}(0)\tanh^2(\Gamma L) \tag{2.33}$$

$$I_{\omega}(L) = I_{\omega}(0)\operatorname{sech}^2(\Gamma L), \tag{2.34}$$

with

$$\Gamma^2 = \frac{(2\omega)^2}{n_{\omega}^2 n_{2\omega} c^3 \epsilon_0}\left|\chi^{(2)}(-2\omega;\omega,\omega)\right|^2 I_{\omega}(0) \tag{2.35}$$

From the above expression it is clear that with a large fundamental intensity or long interaction length, L, the produced second harmonic can obtain intensities approaching that of the fundamental. However, this equation clearly demonstrates that as the harmonic intensity increases it is at the expense of the fundamental intensity resulting in the harmonic conversion efficiency asymptotically approaching 100% as shown in Fig. 2.3.

Although in theory it is possible to achieve nominally 100% efficiency there are many factors that reduce this value in practice. These can include non-perfect phase-matching, where a small amount of phase error can allow significant back-conversion of the second harmonic to the fundamental. Aligned to this effect is power dependent de-phasing [23], here the $\Delta k$ tuning

[1] A complete derivation of this result is given in Appendix A, with this analysis being an integral part of the work in Chapter 3

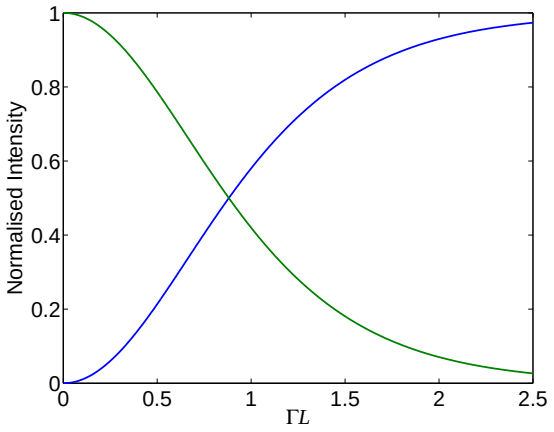


Figure 2.3: A numerical simulation of the growth of the second harmonic intensity (blue), and subsequent reduction in the fundamental intensity (green), with increasing $\Gamma L$, with this factor relating fundamental frequency, material nonlinearity, fundamental plane-wave field intensity and material length.

response of the harmonic process becomes more sensitive to phase errors at high power leading to a narrowing of the $\text{sinc}^2$ profile, see Fig. 2.4. The cause of this narrowing is explained analytical in Chapter 3.

Additionally, in practice the output of a laser source is not an infinite plane-wave but instead usually a Gaussian mode. With a non-uniform spatial power distribution across the beam profile complex depletion mechanisms occur which result in the high intensity at the centre of the beam converting to the harmonic frequency before the low intensity wings. With a small phase-matching error, to which the high intensity centre of the harmonic beam is more sensitive, back conversion of the harmonic beam centre can commence before complete conversion of the wings is achieved. This, in practice, has placed a limit of ∼85% on the experimental SHG conversion efficiency in bulk interactions [24]. However, this limitation is not present in waveguide interactions, where the mode can be thought of as converting as a whole thus satisfying the boundary conditions of the wave equation; as such efficiencies close to 100% can be achieved [25]. These limitations in the bulk interactions are reviewed in Chapter 6 and possible routes to overcome the deleterious effects are offered.

## 2.5 Focussed beams

In many bulk interactions the fundamental input light intensity is insufficient to create such extreme depletion mechanisms as mentioned above. In fact, to achieve even moderate levels of conversion efficiency it is often necessary to focus tightly the interacting waves providing

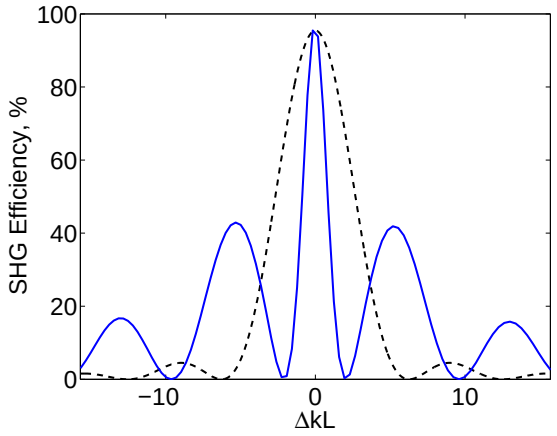


Figure 2.4: A numerical simulation of generated harmonic intensity for a range of length normalised phase-matching values at high peak conversion efficiency, highlighting the narrowing of the phase matching response at high efficiencies. Here the simulations are performed by numerical integration of the coupled equations given in Equation 2.28 and 2.29. Also shown overlayed (dotted curve) is the low efficiency $\text{sinc}^2\ \Delta k$ dependency.

strong spatial confinement, which in turn increases the magnitude of the electric fields and the induced polarisation. For focussed interactions effects such as diffraction invalidate the equations for plane-wave conversion efficiency. Thus, most turn to the analysis undertaken by Boyd and Kleinman [26] to obtain an expression for the conversion efficiency assuming no pump depletion. This analysis took into account such effects as diffraction and transverse variations in electric field culminating in the following definition,

$$P_{2\omega} = \frac{(2\omega)^2}{\pi n_\omega^2 n_{2\omega} \epsilon_0 c^3} \left|\chi^{(2)}\left(-2\omega\,;\omega,\omega\right)\right|^2 P_\omega^2 k_\omega L\, h\left(\beta,\xi\right). \tag{2.36}$$

Here, $h\left(\beta,\xi\right)$ is commonly referred to as the Boyd and Kleinman focussing factor where $\beta = \rho b/\left(2w_0\right)$ is a measure of Poynting vector walk-off, [$\rho$ is the double refraction direction, $b = 2z_R$ with $z_R$ being the Rayleigh range and $w_0$ the focussed spot size] and $\xi = L/b$ is a definition for the degree of focussing relating device length and focussed Rayleigh range. Subsequently, unlike ideal plane-wave interactions the focussed conversion efficiency is proportional to the length of the nonlinear material (not the length squared). But, as in plane wave interactions the conversion efficiency is proportional to the power or intensity resulting in high efficiencies with intense pump inputs.

Boyd and Kleinman further analysed the optimal conditions for focussed conversion efficiency and discovered that assuming no Poynting vector walk-off, i.e. $\beta = 0$, a maximum efficiency[2]

[2]It is shown in Chapter 4 that this result is in fact not the optimum, with higher efficiencies achievable at

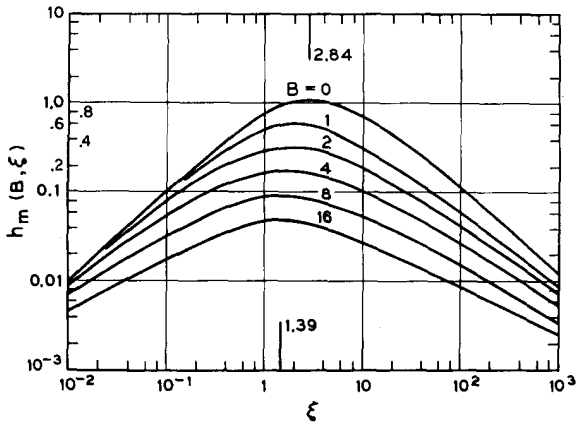


Figure 2.5: The theoretical variation in the Boyd and Kleinman focusing factor $h(B,\xi)$ for a range of focused spot sizes, characterised by the scaled dimensionless parameter $\xi$. Peak conversion efficiency is achieved at the maximum of $h(B,\xi)$, obtained at $\xi = 2.84$. Figure taken from [26]

could be obtained when $\xi = 2.84$. What is perhaps surprising about this result is that this condition holds true for all lengths of nonlinear material. This may not at first be obvious, as with increasing length this ratio implies that the spot size is progressively enlarged resulting in a reduction in the peak electric fields at the focussed waist which, in turn, would result in reduced conversion efficiency. However, at this particular ratio the reduction in focussed intensity is exactly balanced by the increase in interaction length of the beam and the nonlinear material.

For the more complex case of non-zero spatial walk-off the interaction length of significant power overlap, or aperture length, between fundamental and harmonic waves can for some interactions be considerably shorter than the phase-matching coherence length. As such the focussing parameter $\xi$ must be varied to attempt to maximise the field intensities whilst overlap occurs. By choosing a small focussed spot the high intensities occur over short lengths which would seem to help minimise the effects of Poynting vector walk-off. However, tighter focus creates larger diffraction angles which in turn accelerate this effect, as such Boyd and Kleinman proved that to obtain efficient harmonic generation in birefringent materials the focussing parameter $\xi$ has to be reduced becoming progressively lower with increasing walk-off, as shown in Figure 2.5.

## 2.6 Phase matching techniques

Aside from tight spatial confinement, to obtain efficient harmonic generation the deleterious effects of wavelength dispersion must be negated. Wavelength dispersion generally causes the

tighter focusing using carefully structured nonlinear devices.

phase velocity of the fundamental and harmonic waves to be unequal. The result of this is a dephasing of the two waves over the length of the material. If this mismatch is significant it can result in the two waves becoming $\pi$ radians out of phase with one-another leading to complete back-conversion of any generated harmonic field, as shown in Figure 2.6. This behaviour is oscillatory with the period of the oscillation being known as the coherence length given as:

$$L_c = \frac{\pi}{\Delta k} = \frac{\lambda_\omega}{4\left(n_{2\omega} - n_\omega\right)}. \tag{2.37}$$

For some materials such as $LiNbO_3$ or $LiTaO_3$ this length can be as short as a few microns, depending on the frequencies of interest. In such circumstances the maximum conversion efficiency is obtained in just a few microns before reducing. However, if the device length is an odd multiple of the coherence lengths limited quantities of second harmonic can still be generated.

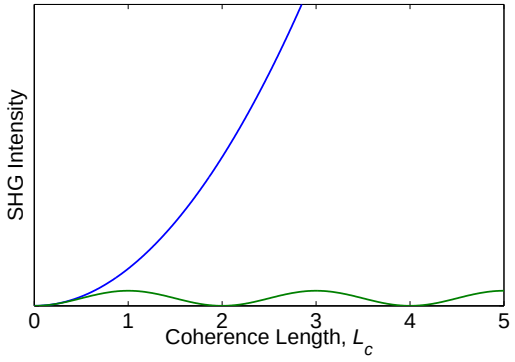


Figure 2.6: A simulation of the effects of phase-matching parameter, $\Delta k$, on the growth of the second harmonic signal along a nonlinear material of length $5L_c$. Here perfect phase matching (blue) is contrasted with an imperfect phase-matching of $\Delta kL/2 = 5\pi/4$, (green)

To overcome the effects of wavelength dispersion there are three main techniques that can be employed, with each technique offering distinct advantages and disadvantages over the others. These techniques include, birefringent phase matching, waveguide dispersion compensation and quasi-phase-matching. Using any one of these techniques may lead to large increases in conversion efficiency, for example, extending the coherence length to 1cm from a few microns results in approximately a $10^6$ increase in efficiency for plane wave interactions.

### 2.6.1 Birefringent phase-maching

The technique of birefringent phase-matching makes use of the differing values of refractive index for orthogonally polarised light in birefringent materials. For the case of SHG the condition for perfect phase matching is simply $n_\omega = n_{2\omega}$, in a material with suitably large birefringence

this may be accomplished if one wave is ordinarily polarised and the other frequency is extra-ordinarily polarised. For a negatively birefringent material such as $LiNbO_3$ [27] this is achieved with an ordinarily polarised fundamental wave, $n^o_\omega$, and an extra-ordinarily polarised generated harmonic wave, $n^e_{2\omega}$, with the polarisation states reversed for positively birefringent materials. Such an interaction is known as type-I phase-matching; an alternative technique known as type-II phase matching requires a fundamental wave comprising of both ordinary and extra-ordinary waves which in turn generate an extra-ordinary second harmonic wave. The technique of type-II phase-matching can be thought of as birefringence averaging, with the indices for phase matching given as $n^e_{2\omega} = 1/2\,(n^e_\omega + n^o_\omega)$.

At this point it is prudent to note that it is rarely the case that phase-matching can be achieved when propagating directly along the optical axis of the nonlinear material as is implied by the notation $n^e_\omega$. Instead it is usually the case that phase-matching can only occur when propagating at an angle, $\theta$, to the optic axis which allows for a variation in the extra-ordinary refractive index given as

$$n^e\,(\theta) = \frac{1}{\left[\frac{\sin^2\theta}{n^2_e} + \frac{\cos^2\theta}{n^2_o}\right]^{1/2}} \tag{2.38}$$

In this way it is possible to adjust the refractive indices by careful alignment of the material with the input waves such that $n^o_\omega = n^e_{2\omega}\,(\theta)$. An example of the variation of index with propagation angle is given in Fig. 2.7 . For the special case of $\theta = \pi/2$ the above expression reduces to the refractive index along the optic axis, with this scenario known as non-critical phase-matching.

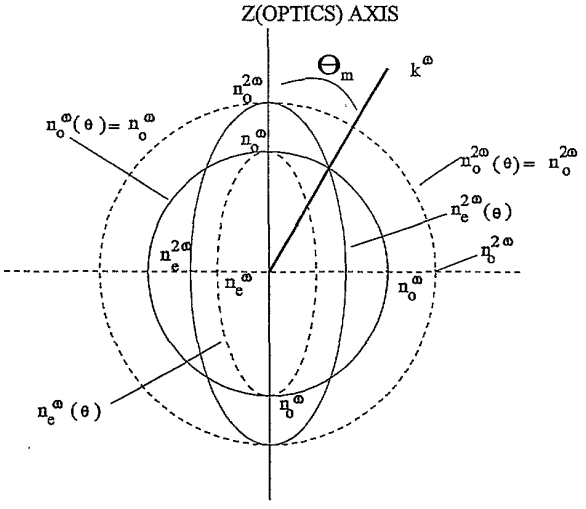


Figure 2.7: A graphical representation of the variation in refractive index for e and o polarised light for both the fundamental and second harmonic fields in the negative birefringent material $LiNbO_3$, highlighting a possible birefringent phase matching angle. Taken from [27]

Propagation at an angle to the optic axis allows for continuous phase-matching of the nonlinear process; however, this propagation may also be at an angle to the nonlinear coefficients resulting in a reduction in the effective nonlinearity. The amount of reduction is material dependent but for $LiNbO_3$, for example, the effective nonlinearity, $d_{eff}$, is given as

$$d_{eff} = d_{15} \sin\theta - d_{22} \cos\theta \sin 3\psi, \tag{2.39}$$

where $d_{15}$ and $d_{22}$ are contracted notations for the components of the nonlinear coefficient tensor where Kleinman symmetry has been applied [6] and $\psi$ is the propagation angle relative to the optical axis. A significant problem with the technique of angle tuning the phase-matching condition can be the complete reduction of nonlinearity at certain angles, in such circumstances the optimal angle for phase-matching may not equate to the angle for optimum efficiency.

Additionally, birefringent phase-matching suffers from an effect known as Poynting vector walk-off. As the extra-ordinary wave propagates through the nonlinear medium the direction of power flow, or Poynting vector, differs from the k-vector direction by the double refraction angle, $\rho$. This results in the walk-off of the high power centres of the interacting beams which in turn leads to significant reduction in conversion efficiency. The double refraction angle is given by

$$\rho \approx \tan\rho = \frac{n_\omega^o}{2}\left[\frac{1}{\left(n_{2\omega}^e\right)^2} - \frac{1}{\left(n_{2\omega}^o\right)^2}\right]\sin 2\theta \tag{2.40}$$

For theoretical infinite plane-waves this is not a problem but for the real world case of focussed beams the problem leads to a separation of the extra-ordinary and ordinary beams after a distance

$$L_a = \frac{\sqrt{\pi} w_o}{\rho} \tag{2.41}$$

known as the aperture length. Here $w_o$ is the focussed spot size. It is quite often a problem that the aperture length of the nonlinear interaction is significantly less than that of the coherence length for efficient power transfer, leading to large reductions in attainable power. For example, with a walk-off angle of only $2^\circ$ and a spot size of $30\,\mu$m the aperture length is only 1.5mm which may well be less than the phase-matched coherence length. However, if $\theta = \pi/2$ i.e. non-critical phase-matching $\rho = 0$ resulting in an infinite aperture length.

### 2.6.2 Waveguide dispersion compensation

With confinement of the nonlinear interaction in a waveguide structure it is possible to tailor the phase-matching conditions by mode dispersion. By careful adjustment of the waveguide dimensions it is possible to control the mode index, which lies between that of the core and the cladding, for both the fundamental and harmonic waves. An example of the variation in

mode index for varying core size is shown in Fig. 2.8. As is shown in this figure by adjusting the physical size of the core it is possible to match the indices of the harmonic and fundamental modes, in this case the first order fundamental mode has equal index to that of a higher order harmonic mode. Using this technique can additionally allow use of any waveguide birefringence such that phase-matching can occur between different polarisation states.

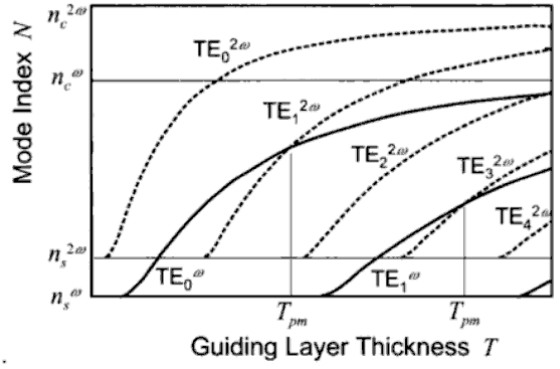


Figure 2.8: A plot of the refractive index variations of numerous spatial modes of both fundamental and harmonic fields for changes in waveguide core dimensions. In this instance phase-matching can be achieved through using the zeroth order fundamental mode mixing with the first higher order SHG mode. Taken from [28]

However, this technique does have the significant disadvantage of poor modal coupling. The spatial power variations between a zeroth order mode with a single Gaussian peak and the oscillatory behaviour of higher order modes reduces the coupling coefficient and so the conversion efficiency.

### 2.6.3 Quasi-phase-matching

Quasi-phase-matching (QPM) was first proposed in 1962 [7] as an alternative to the already established birefringence phase-matching technique. The premise of QPM is to remove the difficulties in overcoming dispersion to obtain matched phase velocities of the interacting waves. This is accomplished by intentionally allowing phase slippage between the waves along one coherence length but correcting for this phase before back conversion can occur. The required phase correction can be achieved by a sign change in the value of the nonlinearity. Inverting the nonlinearity counteracts the $\pi$ phase shift accumulated over the coherence length due to dispersion resulting in continued growth of the harmonic field.

This effect is clearly demonstrated in Figure 2.9, which shows a representation of the phase addition for un-matched and QPM processes. The period of this inverted nonlinearity for second

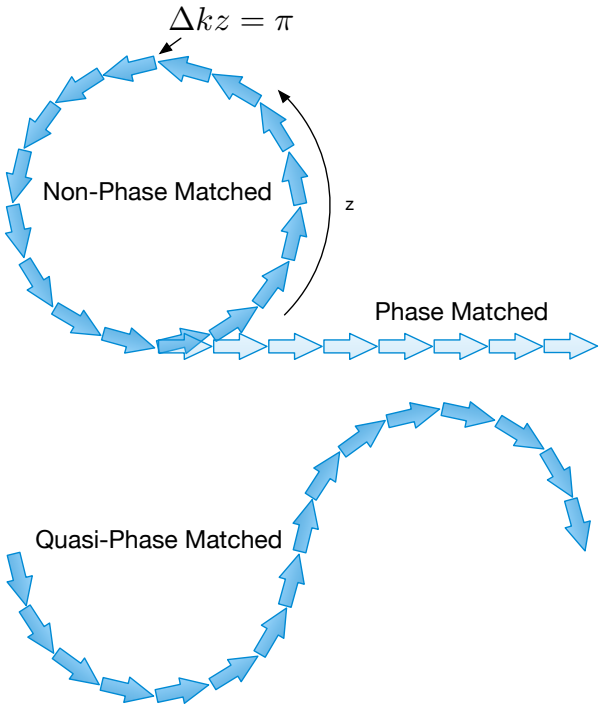


Figure 2.9: A phasor representation of the k-vector variation in un-phase-matched, perfectly phase-matched and quasi-phase-matched interactions. Here it is clear for un-phase matched interactions zero net harmonic contribution is obtained. For quasi-phase matched interactions an inversion in the device nonlinearity leads to continued growth of the harmonic signal.

harmonic generation is defined as

$$\Lambda = 2L_c = \frac{\lambda}{2\left(n_{2\omega} - n_{\omega}\right)}. \tag{2.42}$$

Although perfect phase matching is not achieved the distance of efficient energy transfer can be extended from the order of a few microns, depending on the material, to an infinitely long interaction only limited by the maximum physical sample sizes attainable. An example of the increase in efficiency that can be obtained from only a few coherence lengths of quasi-phase-matched material is show in Figure 2.10.

There are numerous techniques to achieving an inversion in nonlinearity, the first such technique proposed [7] made use of many identical samples of nonlinear material cut to exactly the coherence length of the desired interaction. By stacking these samples end to end whilst alternately rotating the crystals 180° about the nonlinear axis a periodic structure of inverted nonlinearity can be obtained. However, this technique is for many processes impracticable as the lengths of each sample is generally between 10 $\mu$m to 100 $\mu$m long resulting in significant fabrication issues.

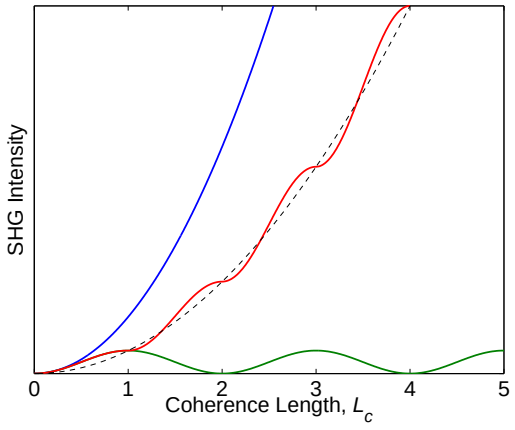


Figure 2.10: A theoretical plot of the variation in harmonic intensity with propagation distance for phase-matched (blue), un-phase-matched (green) and quasi-phase-matched interactions (red). Also shown is the effective average conversion efficiency of a QPM interaction (black), this is equivalent to a phase-matched interaction with a nonlinearity value reduced by a factor of $2/\pi$.

An alternative technique of nonlinearity inversion, which is the basis of all the results presented in this work, is that of domain inversion. This process alters the domain structure of ferroelectric nonlinear materials, such as $LiNbO_3$, to produce a periodic reversal in the in-built spontaneous polarisation. As the sign of nonlinearity is related to the orientation of the spontaneous polarisation, it is clear that such a technique allows for correction of the dispersion induced phase slippage. Although this technique is not dissimilar from that previously mentioned it does have the significant advantage of being a single sample of material thus reducing many of the fabrication issues.

There are certainly other techniques to achieve inversion, such as controlled periodic growth of non-ferroelectric nonlinear semiconductors [29], however these are not discussed here as they do not directly pertain to this work.

As can be seen in Figure 2.10 the growth of the second harmonic wave in a QPM device is not a smoothly increasing function, containing sections at the start and end of each inverted region where growth is nearly flat. As a result the conversion efficiency per unit length is smaller than that of birefringence phase matching, assuming a birefringent material with the same nonlinearity. In fact in QPM the nonlinear coupling coefficient is effectively reduced to a factor of $2/\pi$ [30] of the bulk nonlinearity.

However, despite this reduction in effective nonlinear coefficient the process of QPM can still be substantially more efficient than birefringence techniques. As previously detailed under birefringence phase-matching it is common to have to propagate at an angle to the optical axis,

which as stated results in a reduction in the effective nonlinear coefficient. Additionally, in birefringent devices the choice of the component of the tensoral nonlinear coefficient is restricted by the phase matching characteristics. In contrast, QPM devices have greater flexibility in choice of nonlinear coefficients, limited only by the fabrication techniques for nonlinearity inversion. As an example, in the ferroelectric material $LiNbO_3$ QPM can access the largest nonlinear coefficient, $d_{33}$ with a nonlinearity of $\sim 30 pmV^{-1}$, but by using non-critical birefringence techniques in the same material the largest coefficient is $d_{31}$ at $\sim 5 pmV^{-1}$ [27]. Clearly, even with a factor of $2/\pi$ reduction the effective nonlinearity in the QPM interaction is higher.

Further advantages to QPM include no Poynting vector walk-off and a much larger phase-matching range. By not requiring independent polarisations to achieve phase matching QPM is inherently free from the effects of walk-off. It is however still possible to achieve phase-matching of orthogonal polarisations, but as propagation is generally chosen to be along the material optic axis walk-off is not present. Finally, QPM is able to phase-match a much wider range of frequencies than other techniques, being able to phase-match interactions across the entire transparency band of the material. In comparison, even with angle and temperature tuning birefringence phase-matching is generally only able to efficiently convert a small subset of the wavelengths to which the material is transparent. Again using $LiNbO_3$ as an example, for QPM the nonlinear process can operate for any wavelengths in the transparency range of 350nm - 4800nm [27]. In contrast, birefringent phase-matching in $LiNbO_3$ is limited to harmonic processes with fundamental frequencies above $1\,\mu$m [31].

## 2.7 Periodically-poled lithium niobate

Lithium niobate ($LiNbO_3$) has long been popular as a nonlinear material, being used in early harmonic experiments [5] which utilised its birefringence to achieve phase matching. This material has many properties that facilitate its widespread use as a nonlinear material, but perhaps the most important of the properties is the large nonlinear coefficients, with the $d_{33}$ coefficient being $\sim 30\,pmV^{-1}$ and $d_{31} \sim 5\,pmV^{-1}$ [27]. Although other nonlinear materials in the same family, such as lithium tantalate ($LiTaO_3$) and to a lesser extent lithium iodate ($LiIO_3$) have nonlinear coefficients [32] approaching that of $LiNbO_3$ these materials have historically been scarce at the qualities required for optical use. With one reason for the widespread availability of high quality $LiNbO_3$ being it's use as surface acoustic wave (SAW) filters, which themselves are essential parts of all mobile telecommunications devices.

Aside from high nonlinearity, $LiNbO_3$ has the advantage of a large transparency range, spanning the complete visible spectrum (from $\sim 350nm$) all the way to the near-mid infra-red

($\sim 4800nm$ [27]), allowing its use as a material for SFG and DFG of visible light as well as an optical parametric amplifier/oscillator for tuneable laser light in the infra-red.

Finally, perhaps the property that has ensured this materials commercial dominance is its ability to be domain reversed, providing it as an ideal candidate for quasi-phase-matching. Lithium niobate is a ferroelectric material with 3m crystal class composed of distorted octahedrons of oxygen ions, the arrangement of the oxygen ions is triangular in the plane perpendicular to the z-axis of the material. Between the oxygen planes, at the interstitial sites, lie the lithium and niobium ions, with the sequence of ions arranged as lithium, niobium followed by a vacancy before repeating. It is the positions of these ions that determine the magnitude and sign of the nonlinearity.

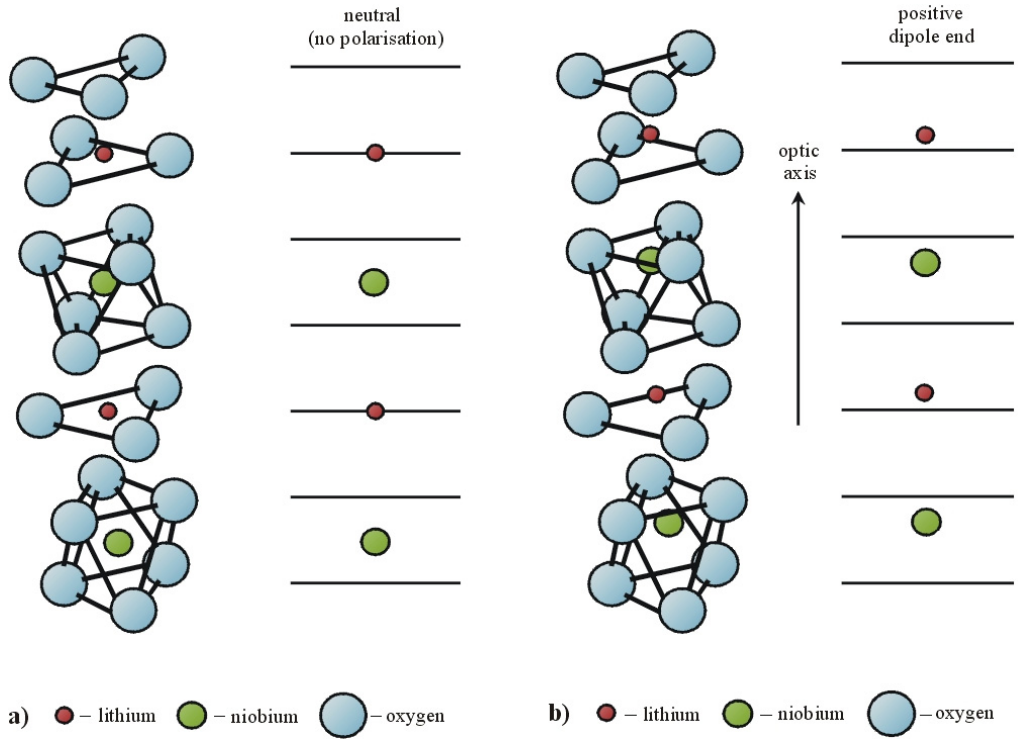


(a) (b)

Figure 2.11: (a) A diagram of the paraelectric phase of lithium niobate as obtained at the Curie temperature. (b) The ferroelectric crystal structure of $LiNbO_3$.

As shown in Figure 2.11(a) at the Curie temperature, $\sim 1120°$ [33], the lithium ions are situated in the plane of the oxygen lattice, with the niobium ions centred in the oxygen octahedra. At this temperature there is a centre of symmetry in the material, resulting in zero net polarisation,

preventing the formation of a $\chi^{(2)}$ nonlinearity. At the Curie point the crystal is said to be in its para-electric phase, below the Curie point the metallic ions are displaced from the oxygen planes creating a material polarisation and resultant nonlinearity. The relative position of the displaced ions defines the direction of the spontaneous polarisation and thus the sign of the nonlinearity. It is readily seen from Figure 2.11(b) that if a lithium ion is forced through the oxygen plane, in turn repelling a niobium core, the effect is to rotate the spontaneous polarisation about the optic axis. It is this poling of the crystal structure that allows for the required change in the sign of the material nonlinearity.

### 2.7.1 Methods of periodic poling

Poling of the lithium niobate structure can be performed via many techniques, with perhaps the simplest technique being the application of a static electric field as the material is cooled through its Curie temperature. However, for efficient harmonic generation via QPM it is necessary for the nonlinearity to be sign inverted on the order of every few microns, thus making this high temperature technique impracticable for all but the initial bulk poling of the crystal. Further techniques have used an out-diffusion process to distort chemically the polarisation of the material, however such methods usually result in a reduction of the material nonlinearity and produce only very shallow regions of domain inversion [34], and as such are not widely used in bulk interactions. Additional procedures include direct e-beam writing of the grating structure [35], although this technique is not suitable for mass production due to the slow write times and poor domain wall quality, and light assisted poling [36]. Where light is used in situ with an applied electric field allowing localised poling with reduced electric fields [36, 37] or alternatively uses higher intensity light that enables a lowering of the coercive field even after removal of the applied light [38], although neither mechanism is yet fully understood.

At room temperature $LiNbO_3$ is in its ferroelectric phase with the material having an in-built polarisation, to achieve QPM this polarisation must be reversed. Inversion of the domain structure can be achieved with the application of an electric field across the optic axis, with this field exceeding the strength of the coercive field ($E_c =\sim 21\,\mathrm{kV\,mm^{-1}}$ at 25°C [27]). Application of a field approaching this magnitude squeezes the position of the lithium ions towards the oxygen plane, temporarily reducing the material polarisation towards that of the paraelectric phase. Additional field strength, ($> E_c$), is sufficient to force the lithium ions through the oxygen plane resulting in a permanent re-orientation of the polarisation. Using a structured electrode it is possible to create localised domain inversions on the order of a few microns in width and many 100's of microns in length.

The poling technique utilised in this work was pioneered at the Optoelectronics Research Centre circa 1998 and is markedly different from alternative techniques more commonly used. Using this proprietary technique the structured electrode is defined on the -z face of the crystal using standard photolithography techniques (in contrast the more widespread technique applies the structured electrode to the +z face), with the patterned photoresist material acting as a dielectric barrier to the applied field and the subsequent un-patterned regions allowing electrical contact to the crystal surface, as shown in Figure 2.12. Contact to the crystal is made using a conductive gel, which allows for electrode application without further cleanroom steps as required for deposited metal electrodes [39] or the potentially hazardous use of liquid electrodes [40] used in alternative techniques.

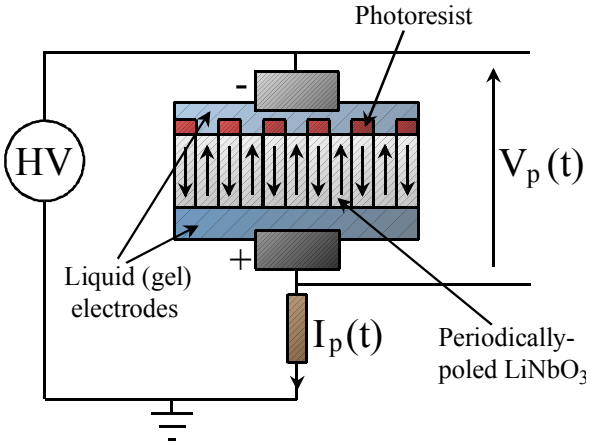


Figure 2.12: Experimental arrangement for room temperature electric field poling of $LiNbO_3$.

Surprisingly the small layer of photoresist, nominally 1 $\mu$m thick, is sufficient to inhibit unwanted domain inversion, however application of the poling field must be carefully controlled to prevent poling under the masked regions or even the catastrophic failure of the crystal structure. During the poling procedure the applied electric field is controlled via current feedback, which in-turn allows precise control of the applied voltage. Current control is chosen over voltage control due to the close link between the poling current and the amount of domain inverted material. Due to the inbuilt spontaneous polarisation a single crystal sample of $LiNbO_3$ has a surface charge on both the positive and negative z faces of the material, with a value of $0.72\,\mathrm{Cm}^{-2}$ [41].

Thus, it can be seen that by constraining both the magnitude and duration of the supplied poling current exacting control of the quantity of domain inverted material is achieved. This is in contrast to the more simplistic approach of voltage control, which to an extent requires an amount of guess work to obtain the optimum poling voltage to achieve the same quality domain

structures, having no in-situ feedback of the progress of domain growth. For the case of current control this ambiguity of poling voltage is removed by the self regulating nature of the poling current, too much current flow leads to a reduction in applied voltage preventing overgrowth of the domains. By careful optimisation of the magnitude of the supplied poling current and its temporal profile it is possible to achieve excellent domain nucleation and subsequent growth in a controlled and highly repeatable manner.

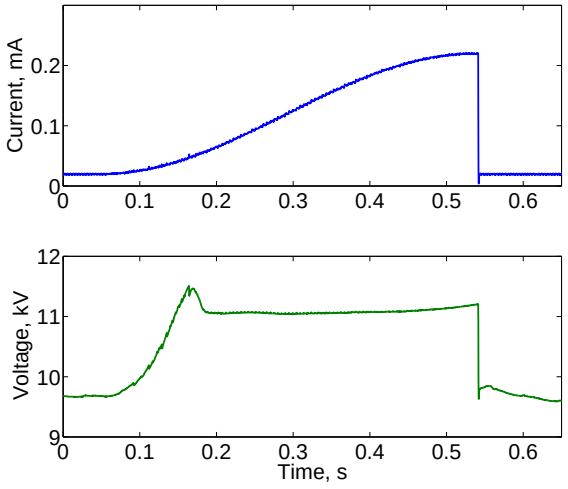


Figure 2.13: A characteristic poling curve showing the demanded poling current and resulting high voltage required to achieve high quality poling of a 6.5 $\mu$m period, 0.5 mm thick PPLN device, for frequency doubling 1064 nm infra-red light to green at 532 nm, using current controlled feedback.

An example of a typical poling curve is shown in Figure 2.13, here a large jump in supplied voltage, to a value matching that of the coercive field, is clearly evident before any current can flow. Additionally, it is apparent from the initial overshoot in voltage that this process automatically optimises the applied voltage to achieve good domain nucleation before reducing to maintain steady domain growth. Finally, towards the end of the poling curve a rise in applied voltage can be attributed to the final lateral expansion of the domains under the insulating photoresist to achieve the desired 50:50 mark to space ratio.

Using this versatile technique, PPLN samples have been created that are capable of phase matching numerous nonlinear interactions including infra-red OPOs with a period of $\sim 30\,\mu$m, all the way down to blue generation from doubled 920 nm sources using a 4.1 $\mu$m grating pitch. An example of the domain quality that is routinely achievable is shown in Figure 2.14, which is a microscope image of an HF acid etched, 6.5 $\mu$m period device for green light generation. Here, the HF etching allows clear differentiation of the poled domains due to the differing etch rates

of the +z and -z faces of the crystal [42].

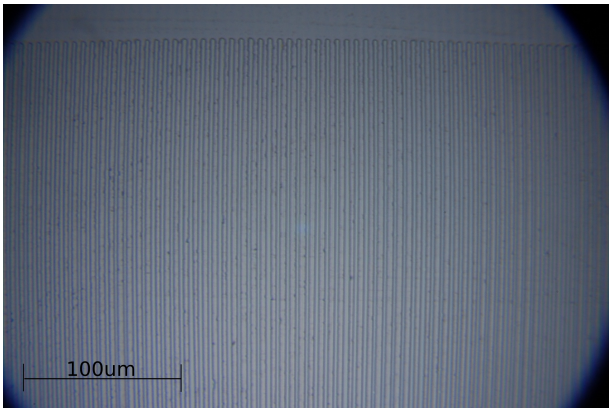


Figure 2.14: A microscope image of anE-Field poled PPLN structure with 6.5 $\mu$m period for frequency doubling 1064 nm infra-red light to green at 532 nm. Here, the darker structures are the inverted domains whilst the lighter colour is that of the bulk un-poled material, (the visibility of the domains has been enhanced through acid etching).

Despite its many advantages PPLN does suffer from effects that limit its usefulness in practical situations. One such problem is the photorefractive effect, an optical phenomenon whereby the interaction of light and a material creates a refractive index change along the gradients of the light intensity [43]. To exhibit the photorefractive effect a material must be either photoconductive or photovoltaic in nature in addition to having electro-optic properties. Here, the photoconduction creates an optically induced electric field within the material and the electro-optic effect creates a resulting index change in proportion to this field. Such a phenomenon can prove detrimental to nonlinear interactions causing such effects as de-focussing of the incident fundamental beam and variation in phase-matching conditions resulting in a reduction in harmonic conversion efficiency.

In the material $LiNbO_3$ photoconduction is attributed to iron impurities present in the crystal melt prior to fabrication, which under illumination are able to release charges into the conduction band. With the effect usually described by the relation

$$Fe^{2+} + hv \rightarrow Fe^{3+} + e^{-}$$

where $h$ is Planck's constant and $v$ is the frequency of incident light. Thus with constant illumination it has been proposed [44, 45] that $Fe^{2+}$ ions release electrons into the conduction band, which are unable to recombine with the $Fe^{3+}$ traps due to the laser excitation. However, by diffusion processes or built in fields these electrons can migrate away from the intense laser focus towards the extremities of beam where they are able to recombine with available $Fe^{3+}$ traps,

resulting in a charge distribution and thus an electric field leading to a change in refractive index through the electro-optic or Pockels effect. It is however possible to negate these charge effects by operating PPLN devices at temperatures close to 180 °C. With the elevated temperature creating charge diffusion processes, considerably stronger than the optical field induced diffusion, preventing regions of localised charge building up. However, this comes at the expense of flexibility in deployment with many temperature sensitive applications unable to accommodate such extreme temperatures.

As an alternative to high temperature operation it has been shown that by artificially increasing the electrical conductivity of $LiNbO_3$, with the inclusion of certain metallic impurities [46], charge build up can be prevented thus ameliorating the effects of photorefraction. Of particular interest is the inclusion of $Mg^{2+}$ ions in the crystal lattice, with a value of $5\%\,\mathrm{mol}^{-1}$ showing the best results for limiting the photorefractive effect whilst maintaining high optical nonlinearities [47]. Further advantages to the use of magnesium doped PPLN (MgO:PPLN) include a reduction in the coercive field, to approximately $3\mathrm{kVmm}^{-1}$, allowing larger thicknesses of material to be poled at relatively low temperatures [48], a moderately expanded transparency range towards the UV [49] and higher power handling capabilities [50].

However, due to the changes in the material conductivity and coercive field the standard technique employed for poling PPLN is not suitable for high yield production of MgO:PPLN, and as such a new technique has been developed. The fabrication difficulties stem from a reduction in the nucleation sites on the application of electric field when compared with standard $LiNbO_3$, resulting in the formation of small numbers of large over-poled domains. To counter this a new patent applied two step poling process has been developed as part of the work described in this thesis [51] which initially forces numerous nucleation sites using short duration high voltage pulses considerably larger than the coercive field followed by a much longer duration voltage just above the coercive field value to spread the domains from the nucleation points. The importance of encouraging additional nucleation prior to steady domain growth was identified by the author during poling trials. The use of sets of high voltage pulses of approximately 10ms duration is an important step which encourages complete domain nucleation across the device without allowing significant spreading, only once every period in the device is nucleated is a sustained voltage applied. Doing this two step process helps ensure that all domains have the ability to grow at the same rate preventing the formation of a single runaway domain reversal.

Finally, an additional limitation of $LiNbO_3$, which MgO doping can partly rectify, is the inability to generate UV light due to its low end transparency cut-off at 350nm. As an alternative $LiTaO_3$ may be used, this material is very similar to $LiNbO_3$ being a ferroelectric material in

the same family with a large nonlinearity value of $d_{33} = 26\,\mathrm{pmV}^{-1}$ [52] and high resistance to photorefractive damage (approximately 30 times that of $LiNbO_3$ [53, 52]). However, importantly where these two materials differ is in their transparency bandwidths, with $LiTaO_3$ having a lower bound of 280nm [54] and an upper bound of 4.5 $\mu$m, and their birefringence, with $LiTaO_3$ having insufficient birefringence for standard phase matching leaving QPM as the only viable option for harmonic generation.

In spite of the advantages that $LiTaO_3$ offers it is only now becoming an important material for commercial applications with one of the likely causes of the slow uptake being the issues of high quality periodic poling of this material (PPLT). Poling techniques have proven to be similar to $LiNbO_3$, with room temperature electric field poling being the primary choice. However, due to subtle differences in the formation of poled domains the resulting device quality is often inferior to PPLN. In $LiNbO_3$ domains form as hexagons aligned with the crystal axis, but for $LiTaO_3$, despite the almost identical crystal structure, poled domains grow preferentially as triangles. This triangular growth prevents the formation of high quality straight domain walls on both faces of the crystal, thus reducing the finesse of the poled device. Additionally, it was reported that LT has a much lower domain nucleation density than LN [55] and as a result was believed to only pole with the use of metal electrodes.

Notwithstanding, it has since been shown [56, 57] that by careful optimisation of the poling technique it is indeed possible to achieve good quality PPLT devices using current-controlled room temperature poling techniques with the use of gel electrodes, culminating in a patent to this effect [57]. The basis of this technique is the application of a sustained high voltage bias, a few tens of volts below the coercive field, to the crystal surface prior to the application of the current-controlled voltage pulse. The application of this high bias has been seen to dramatically increase the overall uniformity of the poled domain structures, overcoming the nucleation issues observed by others when using non-metallic electrodes. Using this technique it has so far been possible to fabricate PPLT with a period of 4.5 $\mu$m, as shown in Figure 2.15, which is suitable for the frequency doubling of a 920nm laser source for blue generation.

## 2.8 Conclusions

In this chapter a thorough analysis of nonlinear optical interactions has been undertaken, with particular attention paid to the process of second harmonic generation. With this being the main focus of the work detailed in this thesis. Starting from Maxwells equations a theoretical background is given for the formation of higher order optical frequencies through the second order nonlinearity coefficient. From these fundamental equations expressions for both the low

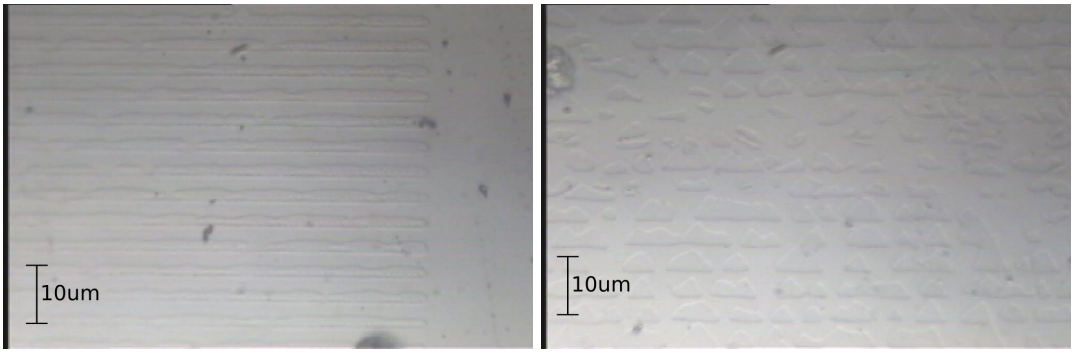


(a) (b)

Figure 2.15: Microscope images of E-Field poled PPLT device with 4.5 $\mu$m period for frequency doubling 920 nm near infra-red source to blue at 460 nm. (a) -z crystal surface with mostly straight domain growth, (b) the unpatterned +z surface showing triangular poled domains.

efficiency and more complex high efficiency interactions are given with the slowly varying envelope approximation applied. In later chapters, Chapter 3 and Appendix A, these often quoted results are fully derived and the complex analysis utilised as the basis for a novel simulation tool.

Further, the effects of phase-matching on the efficiency of SHG processes is discussed along with methods for achieving phase-matching, such as birefringent or quasi-phase-matching and waveguide dispersion compensation. Additionally, a brief introduction into the effects of focused Gaussian beams on the efficiency of second harmonic generation is given. Here, the results presented are those of Boyd and Klienman [26], which are generally considered to be the definitive results for any focused interaction. However, in Chapter 4 improvements on these results, arising through the work detailed in this thesis, are given.

Finally, the materials lithium niobate and to a lesser extent lithium tantalate and magnesium doped lithium niobate are introduced, with their benefits and limitations briefly discussed. Methods for achieving phase-matching in these materials are additionally covered, with particular attention paid to quasi-phase-matching through periodic poling. Periodically poled materials are extensively utilised throughout this work, with their high degree of flexibility allowing new and novel phase-matching processes which are discussed in the proceeding chapters. As a result of this work patents co-authored by this author, detailing methods for the formation of poled, periodic domains in lithium niobate and lithium tantalate [57] and magnesium oxide doped lithium niobate [51], have been generated. The techniques described in these patents have been extensively utilised by this author in the fabrication of all the physical devices investigated.

# References


[1] T. H. Maiman. Stimulated optical radiation in ruby. *Nature*, 187(493), 1960.

[2] R. J. Collins. Coherence, narrowing, directionality, and relaxation oscillations in the light emission from ruby. *Phys. Rev. Lett.*, 5:303, 1960.

[3] P. A. Franken, A. E. Hill, C. W. Peters, and G. Weinreich. Generation of optical harmonics. *Phys. Rev. Lett.*, 7(4):118–119, 1961.

[4] C. C. Wang and G. W. Racette. Measurement of parametric gain accompanying optical difference frequency generation. *Applied Physics Letters*, 6(8):169–171, 1965.

[5] J. A. Giordmaine and R. C. Miller. Tunable coherent parametric oscillation in $LiNbO_3$ at optical frequencies. *Phys. Rev. Lett.*, 14(24):973–976, June 1965.

[6] D. A. Kleinman. Nonlinear dielectric polarization in optical media. *Phys. Rev.*, 126(6):1977–1979, 1962.

[7] J. A. Armstrong, N. Bloembergen, J. Ducuing, and P. S. Pershan. Interactions between light waves in a nonlinear dielectric. *Phys. Rev.*, 127(6):1918–1939, 1962.

[8] D. A. Kleinman. Theory of second harmonic generation of light. *Phys. Rev.*, 128(4):1761–1775, Nov 1962.

[9] T. Umeki, M. Asobe, Y. Nishida, O. Tadanaga, K. Magari, T. Yanagawa, and H. Suzuki. Widely tunable $3.4\,\mu$m band difference frequency generation using apodized $\chi^{(2)}$ grating. *Opt. Lett.*, 32(9):1129–1131, 2007.

[10] D. Taverner, P. Britton, P. G. R. Smith, D. J. Richardson, G. W. Ross, and D. P. Hanna. Highly efficient second-harmonic and sum-frequency generation of nanosecond pulses in a cascaded erbium-doped fiber:periodically poled lithium niobate source. *Opt. Lett.*, 23(3):162–164, 1998.

[11] I. Jovanovic, B. J. Comaskey, and D. M. Pennington. Angular effects and beam quality in optical parametric amplification. *J. Appl. Phys.*, 90(9):4328–4337, 2001.

[12] R. L. Byer. Parametric oscillators and nonlinear materials. In P. G. Harper and B. S. Wherrett, editors, *Nonlinear Optics*, pages 47–160. Academic Press, 1977.

[13] M. Bass, P. A. Franken, J. F. Ward, and G. Weinreich. Optical rectification. *Phys. Rev. Lett.*, 9(11):446–449, 1962.

[14] D. Erasme and M. G. F. Wilson. Analysis and optimization of integrated-optic travelling-wave modulators using periodic and non-periodic phase reversals. *Opt. & Quantum Electron.*, 18:203–211, 1986.

[15] J. F. Ward and G. H. C. New. Optical third harmonic generation in gases by a focused laser beam. *Phys. Rev.*, 185(1):57–72, Sep 1969.

[16] R. W. Mink, R. W. Terhune, and C. C. Wang. Nonlinear optics. *Appl. Opt.*, 5, 1966.

[17] G. Eckhart, R. W. Hellwarth, F. J. McClung, S. E. Schwarz, and D. Weiner. Stimulated raman scattering from organic liquids. *Phys. Rev. Lett.*, 9(11):445–457, 1962.

[18] D. I. Mash, V. V. Morozov, V. S. Starunov, and I. L. Fabelinskii. Forced scattering of light at the edge of a rayleigh line. *JETP Lett*, 2(22), 1965.

[19] R. Y. Chiao, C. H. Townes, and B. P. Stoicheff. Stimulated brillouin scattering and coherent generation of intense hypersonic waves. *Phys. Rev. Lett.*, 12(592), 1964.

[20] W. Kaiser and C. G. B. Garret. Two-photon excitation in $CaF_2$:$Eu^{2+}$. *Phys. Rev. Lett.*, 7(229), 1961.

[21] Y. R. Shen. *The Principles of Nonlinear Optics*. John Wiley and Sons, 1984.

[22] J. M. Manley and H. E. Rowe. Some general properties of non-linear elements. *Proc. Inst. Radio Engrs.*, 44(7):904–913, July 1956.

[23] D. Eimerl. High average power harmonic generation. *IEEE J. Quantum Electron.*, QE-23(5):575–592, 1987.

[24] R. Paschotta, P. Kürz, R. Henking, S. Schiller, and J. Mlynek. 82% efficient continuous-wave frequency doubling of 1.06$\mu$m with a monolithic MgO:$LiNbO_3$ resonator. *Opt. Lett.*, 19(17):1325–1327, 1994.

[25] K. R. Parameswaran, J. R. Kurz, R. V. Roussev, and M. M. Fejer. Observation of 99% pump depletion in single-pass second-harmonic generation in a periodically poled lithium niobate waveguide. *Opt. Lett.*, 27(1):43–45, 2002.

[26] G. D. Boyd and D. A. Kleinman. Parametric interaction of focused Gaussian light beams. *J. Appl. Phys.*, 39(8):3597–3639, 1968.

[27] M. Houe and P. Townsend. An introduction to methods of periodic poling for second harmonic generation. *J. Phys. D Appl. Phys.*, 28:1747–1763, 1995.

[28] T. Suhara and M. Fujimura. *Waveguide Nonlinear-Optic Devices*. Springer, 2003.

[29] M. J. Angell, R. M. Emerson, J. L. Hoyt, J. F. Gibbons, L. A. Eyres, M. L. Bortz, and M. M. Fejer. Growth of alternating (100)/(111) oriented II-VI regions for quasi phase matched nonlinear optical devices on GaAs substrates. *Appl. Phys. Lett.*, 64:3107–3109, 1994.

[30] K. Rustagi, S. Mehendale, and S. Meenakshi. Optical frequency conversion in quasi-phase-matched stacks of nonlinear crystal. *IEEE J. Quantum Electron.*, QE-18(6):1029–1041, 1982.

[31] R. L. Byer. Quasi-phase-matched nonlinear interactions and devices. *J. Nonlinear Opt. Phys. Mater.*, 6(4):549–592, 1997.

[32] J. Jerphagnon. Optical nonlinear susceptibilities of lithium iodate. *Appl. Phys. Lett.*, 16(8):298–299, 1970.

[33] A. M. Prokhorov and Y. S. Kuz'Minov. *Physics and chemistry of crystalline lithium niobate*. Adam Hilger, 1990.

[34] K. Yamamoto, K. Mizuuchi, K. Takeshige, Y. Sasai, and T. Taniuchi. Characteristics of periodically domain-inverted $LiNbO_3$ and $LiTaO_3$ waveguides for second harmonic generation. *J. Appl. Phys.*, 70(4):1947–1951, 1991.

[35] C. Restoin, C. Darraud-Taupiac, J. L. Decossas, J. C. Vareille, J. Hauden, and A. Martinez. Ferroelectric domain inversion by electron beam on $LiNbO_3$ and Ti:$LiNbO_3$. *J. Appl. Phys.*, 88(11):6665–6668, 2000.

[36] M. Fujimura, T. Sohmura, and T. Suhara. Fabrication of domain-inverted gratings in mgo:$LiNbO_3$ by applying voltage under ultraviolet irradiation through photomask at room temperature. *Electron. Lett.*, 39:719–721, 2003.

[37] H. Steigerwald, F. Luedtke, and K. Buse. Ultraviolet light assisted periodic poling of near-stoichiometric, magnesium-doped lithium niobate crystals. *Appl. Phys. Lett.*, 94(3):032906, 2009.

[38] S. Mailis, C. E. Valdivia, C. L. Sones, A. C. Muir, and R. W. Eason. Latent ultrafast laser-assisted domain inversion in congruent lithium niobate. In *Lasers and Electro-Optics, 2007 and the International Quantum Electronics Conference. CLEOE-IQEC 2007. European Conference on*, June 2007.

[39] S. Nagano, M. Konishi, T. Shiomi, and M. Minakata. Study on formation of small polarization domain inversion for high-efficiency quasi-phase-matched second-harmonic generation device. *Jpn. J. Appl. Phys.*, 42(7A):4334–4339, 2003.

[40] L. E. Myers, R. C. Eckardt, M. M. Fejer, R. L. Byer, W. R. Bosenberg, and J. W. Pierce. Quasi-phase-matched optical parametric oscillators in bulk periodically poled $LiNbO_3$. *J. Opt. Soc. Am. B*, 12(11):2102–2116, 1995.

[41] V. Pruneri, J. Webjörn, P. S. J. Russell, J. R. M. Barr, and D. C. Hanna. Intracavity second harmonic generation of 0.532 $\mu$m in bulk periodically poled lithium niobate. *Optics Communications*, 116:159–162, 1995.

[42] I. E. Barry, G. W. Ross, P. G. R. Smith, R. W. Eason, and G. Cook. Microstructuring of lithium niobate using differential etch-rate between inverted and non-inverted ferroelectric domains. *Mater. Lett.*, 37:246–254, 1998.

[43] A. Ashkin, G. D. Boyd, J. M. Dziedzic, R. G. Smith, A. A. Ballman, J. J. Levinstein, and K. Nassau. Optically-induced refractive index inhomogeneities in $LiNbO_3$ and $LiTaO_3$. *Appl. Phys. Lett.*, 9(1):72–74, 1966.

[44] N. V. Kukhtarev, V. B. Markov, S. G. Odulov, M. S. Soskin, and V. L. Vinetskii. Holographic storage in elecectrooptic crystals. I steady state. *Ferroelectrics*, 22:949–960, 1979.

[45] N. V. Kukhtarev, V. B. Markov, S. G. Odulov, M. S. Soskin, and V. L. Vinetskii. Holographic storage in elecectrooptic crystals. II beam coupling-light amplification. *Ferroelectrics*, 22:961–964, 1979.

[46] X. He and D. Xue. Doping mechanism of optical-damage-resistant ions in lithium niobate crystals. *Opt. Commun.*, 265(2):537–541, 2006.

[47] Y. Furukawa, K. Kitamura, S. Takekawa, A. Miyamoto, M. Terao, and N. Suda. Photorefraction in $LiNbO_3$ as a function of [Li]/[Nb] and MgO concentrations. *Appl. Phys. Lett.*, 77(16):2494–2496, 2000.

[48] H. Ishizuki, T. Taira, S. Kurimura, J. H. Ro, and M. Cha. Periodic poling in 3mm thick MgO:$LiNbO_3$ crystals. *Jpn. J. Appl. Phys.*, 42(2A):L108–L110, 2003.

[49] R. Choubey, P. Sen, P. Sen, R. Bhatt, S. Kar, V. Shukla, and K. Bartwal. Optical properties of MgO doped $LiNbO_3$ single crystals. *Opt. Mater.*, 28:467–472, 2006.

[50] Y. Furukawa, K. Kitamura, A. Alexandrovski, R. Route, M. M. Fejer, and G. Foulon. Green-induced infrared absorption in MgO doped $LiNbO_3$. *Appl. Phys. Lett.*, 78(14):1970–1972, 2001.

[51] C. B. E. Gawith, H. E. Major, and P. G. R. Smith. A process for poling a ferroelectric material doped with a metal, 2008.

[52] S. Matsumoto, E. J. Lim, H. M. Hertz, and M. M. Fejer. Quasiphase-matched second harmonic generation of blue light in electrically periodically-poled lithium tantalate waveguides. *Electron. Lett.*, 27(22):2040–2042, 1991.

[53] G. L. Tangonan, M. K. Barnoski, J. F. Lotspeich, and A. Lee. High optical power capabilities of Ti-diffused $LiTaO_3$ waveguide modulator structures. *Appl. Phys. Lett.*, 30(5):238–239, 1977.

[54] S.-n. Zhu, Y.-y. Zhu, Z.-j. Yang, H.-f. Wang, Z.-y. Zhang, J.-f. Hong, C.-z. Ge, and N.-b. Ming. Second-harmonic generation of blue light in bulk periodically poled $litao_3$. *Appl. Phys. Lett.*, 67(3):320–322, 1995.

[55] J. Meyn, C. Laue, R. Knappe, R. Wallenstein, and M. M. Fejer. Fabrication of periodically poled lithium tantalate for uv generation with diode lasers. *Appl. Phys. B*, 73:111–114, 2001.

[56] A. A. Lagatsky, E. U. Rafailov, A. R. Sarmani, C. T. A. Brown, W. Sibbet, L. Ming, and P. G. R. Smith. Efficient femtosecond green-light source with a diode-pumped mode locked $Yb^{3+}$:$KY(WO_4)_2$ laser. *Opt. Lett.*, 30(10):1144–1146, 2005.

[57] C. B. E. Gawith, H. E. Major, L. Ming, and P. G. R. Smith. Improved electric field poling of ferroelectric materials, Dec 2008.

# Chapter 3

# Increasing the phase-matching tolerances of QPM devices

## 3.1 Introduction

Miniaturised high power visible laser components are becoming increasingly interesting for commercial display applications, such as laser projectors and televisions. Laser based sources have the potential to replace traditional lamp-based white-light sources with improved colour gamut Red-Green-Blue (RGB), packaged, frequency converted, laser diode modules. Such devices promise to overcome the short working lifetimes and non-optimal wavelengths currently offered by the alternative visible diode technology. Here, the nonlinear process of Second Harmonic Generation (SHG) [1] offers an ideal route towards generating high quality visible light from existing infrared laser diodes. However, the route of packaging nonlinear materials with semiconductor lasers requires investigation of several important operational effects, the most important of which are conversion efficiency and stability.

Of the nonlinear materials currently available, the family of periodically-poled lithium niobate (PPLN) (and its various compositions and dopants) remains among the most popular due to its high nonlinear coefficient, ready availability, and widely tunable phase-matching range. However, in order to promote wider acceptance of this material platform several inherent operational issues that arise while generating visible wavelengths must be resolved. These include photorefractive damage, long term degradation, and, of relevance to this thesis, a narrow temperature acceptance bandwidth that requires stringent thermal packaging for use in mass-market applications. Generally, the SHG conversion efficiency temperature tuning response of a PPLN crystal grating

shows a sinc squared dependency, resulting in a relatively narrow range of temperatures over which efficient harmonic conversion can occur. Typically this means that to maintain maximum conversion efficiency the crystal temperature must be stabilised to within 0.1 °C, a range that becomes progressively narrower as longer devices are used to obtain higher efficiencies.

To overcome these practical limitations a method for converting the narrow sinc squared harmonic temperature tuning response of a standard PPLN grating into a broad, flat-top temperature tuning response by mathematical design and selective reallocation of poled grating domains is proposed. Based on this process the output power of poled nonlinear devices has been shown to be substantially more robust to fluctuations in crystal temperature and simultaneously more stable to pump laser wavelength drift.

## 3.2 An overview of techniques for modifying the bandwidth of QPM devices

It had long been known from the fields of linear optical gratings that it is possible to modify significantly the response of a grating structure to tailor it to one's needs. For example in the field of linear electro-optic modulators it was shown that with the use of a pseudo-random binary pattern in the structure of an applied electric field, as opposed to the more common periodic structures, it was possible to alter the velocity matching of the devices to significantly expand their working bandwidth [2]. Still earlier work on broad band grating filters sputtered onto thin film waveguides showed that a linear chirp could be used to provide a wide range of working wavelengths with high efficiencies [3].

However, it was not until the technique of QPM had been sufficiently advanced in practice that applications of modified bandwidth nonlinear devices started to appear in any number. Where before this technique changes to the phase-matching characteristics of a material were generally limited to refractive index variations via impurity diffusion, the creation of periodic cladding structures on nonlinear waveguides [4], or by ion implantation to reduce the local nonlinearity [5]. With the advent of high quality periodic QPM structures in nonlinear materials such as lithium tantalate and lithium niobate many theoretical and experimental papers began to be published providing routes to significantly alter the phase-matching bandwidths for a range of applications.

The scope of the applications of modified nonlinear grating structures is vast including applications such as pulse shaping in short pulse harmonic generation [6, 7], the generation of multiple harmonics simultaneously [8, 9, 10], the reduction of side lobes in the phase-matching

response [11] and, of interest to this work, the enhancement of the standard sinc like bandwidth to a more broad bandwidth constant power output. Within these areas the device types can be further separated into three main modification techniques, these are: chirped grating structures, aperiodic grating structures and phase shifted gratings, however recent advancements have seen the merging of some of these techniques in the hope of producing more desirable responses. The merits of these device types and some of the applications and results are now be presented.

### 3.2.1 Chirped gratings

Chirped grating designs, where the period of the grating is varied either linearly or otherwise along the length of the device, have long been proposed as methods for increasing the bandwidth of nonlinear interactions. By utilising a spatially varying quasi-phase matching period it is possible to approximately phase-match numerous optical frequencies simultaneously providing a relatively constant power output for a range of parametric interactions. A detailed theoretical analysis of the effects of chirping the grating period was undertaken by Suhara et. al [12], where parameters such as grating length, fundamental input power and chirp rate were analytically analysed for both low and high power regimes. Despite this detailed analysis little experimental research has been performed on chirped grating structures designed specifically for the purpose of expanding their bandwidth, perhaps due to the non-ideal frequency response obtained. It was shown in the original analysis by Suhara that although chirping can lead to significantly broadened bandwidths the power stability obtained is far from optimal, where depending on the degree of chirp applied and the length of the grating it is common to produce unwanted oscillations along the otherwise flat-top bandwidth with magnitudes approaching 25% of the peak power output.

A further complication with chirped grating structures is the small variation in domain placement required to achieve the desired bandwidth. For example for a linearly chirped grating structure designed with a nominal 28.4 $\mu$m period, suitable for generating the difference frequency between a 1064 nm pump and a 1550 nm signal in a $LiNbO_3$ waveguide, and a device length of 38mm it was found that to provide seven times the standard bandwidth a chirp in the period from 28.489 $\mu$m to 28.311 $\mu$m is required [13]. If this chirp is considered in terms of the relative shift in domain positions it is found to be approximately 0.06 nm per period, this resolution is of course considerably below that which can be achieved with mask technologies and photolithography. Although the exact placement of each domain is not essential, as long as the overall average period is correct, with mask manufacturers usually working with a minimum of a  nm grid it is clear that the manufactured chirp can quickly become highly nonlinear, resulting in significant

changes in theorised performance.

To overcome the fabrication difficulties of linearly chirped devices recent work has attempted to limit the minimum domain position variation in the chirped devices by using a step chirp grating (SCG) [14, 15]. Here instead of constantly varying the chirp along the length of the grating the device is now made up of discrete segments of continuous period gratings, the period of which is chirped from section to section. If the grating is considered as a whole the average period variation can reasonably well represent a continuously varying period structure, this approximation can, of course, be improved by increasing the number of sections in a given length with a corresponding decrease in the period change. This technique again has its limitations in that it can only realistically be applied when large bandwidths are required. By limiting the change in period between sections to a 1 nm accuracy it is clear that the overall level of chirp for say a 10 section device is at a minimum of 0.01 $\mu$m, but with so few sections the average period does not accurately represent a continuously varying structure producing artefacts in the phase-matching response. As a result of this the work in [15] utilised over 300 sections of constant period changing by 1 nm, resulting in an equivalent linear chirp of 0.3 $\mu$m which for generating the second harmonic of 1064 nm in $LiNbO_3$ for example results in approximately a 20 nm bandwidth.

Finally, there has been a recent further advancement in chirped QPM grating devices that eliminates the unwanted oscillation in their flat-top response. As shown by Suhara and further demonstrated in [13] and [15] the oscillation of the harmonic power along the otherwise flat-top $\Delta k$ response can be significant, preventing the use of either linearly chirped gratings (LCG) or SCG in many applications, especially the proposed temperature stable generation of the second harmonic. The cause of the oscillation is relatively simple in nature and can be explained through basic Fourier analysis, where the discontinuous nonlinearity of the grating and the truncated periods of the quasi-phase matched structure give rise to unwanted frequency components that increase the efficiency for some frequencies along the flat-top. Thankfully, Fourier analysis is able to provide a mechanism to minimise these effects. By applying an apodisation to the grating structure, so as to reduce the strength of the nonlinearity at the device extremities, it is possible to eliminate its discontinuous nature and reduce any unwanted frequency components in the Fourier transform. Unfortunately it is not readily feasible to reduce the nonlinearity of a QPM device without causing unwanted damage to the material which can prevent the formation of polarisation reversed domains [16] or introduce index changes which alter the phase matching characteristics. Despite this limitation it is, however, possible to reduce the effective nonlinearity of the device such that at the extremities the relative conversion efficiency from

the pump wavelength to the harmonic is reduced compared with the unaltered central region. There are numerous techniques for reducing the effective nonlinearity of a QPM device [11] however one of the simplest in concept, taken from the work on linear gratings, is the technique of duty cycle variation. Here the duty cycle is the ratio of the size of the poled domain to the remaining material in the phase-matching period. By deliberately reducing the duty cycle from the ideal 50:50 ratio continuous harmonic growth along the phase-matching period is prevented, with larger variations in the duty cycle ratio leading to greater reductions in the local conversion efficiency and thus effective nonlinearity.

The technique of duty cycle variation has recently been theoretically applied to both LCG [13] and SCG [14] structures and experimentally verified in the LCG devices, where the measured ripple is reduced from 1.5 dB in the un-apodised device to ±0.5 dB (or approximately ±12%), this compares with ±0.2 dB for the theoretical analysis. However, this technique itself has limitations in that to achieve small non-zero effective nonlinearities the size of the poled domains must be significantly reduced from the normal dimensions leading to difficulties in fabrication. To further overcome this difficulty work has been undertaken to model the effects of setting a minimum domain size in the duty-cycle apodised SCG devices [15], here the domain size was limited to a minimum of 1 $\mu$m, increased from the optimal 100 nm, to help with fabrication issues. It was theoretically shown that even with this non-optimal domain sizes the flat-top ripple could be reduced to ±0.15 dB, up from an ideal value of ±0.05 dB with 100 nm sized domains. However, even with this increased minimum domain size the fabrication of such a device is non-trivial, with only a handful of examples of such small domains being fabricated [17, 18, 19].

### 3.2.2 Aperiodic gratings

As for chirped grating structures the first examples of aperiodic gratings appeared in linear optical systems with many such examples appearing in electro-optic modulator designs [2, 20, 21], where the aperiodic structures allowed much greater velocity matching bandwidths. The first examples of aperiodic QPM grating structures in nonlinear systems occurred shortly after the first experimental demonstration of aperiodically poled electro-optic modulators [20], where not only the fabrication techniques but also the aperiodic designs themselves had great similarity. For both the electro-optic modulator and the aperiodic QPM grating the aperiodicity of the structure was defined by a Barker sequence [22] of constant domain size polarisation reversals, such a sequence is used for its excellent spread spectrum properties which ensures a wide range of phase-matching conditions. With the maximum length of a Barker sequence being limited to 13 bits [23] it proved necessary to utilise multiple sets of such polarisation blocks within the QPM

grating to achieve long nonlinear interaction lengths thus increasing conversion efficiency [24]. To further increase the acceptance bandwidth of the final structure block level phase reversals were periodically introduced, where the polarisations in of the sequence were reversed. Using such a phase reversed Barker sequence structure it proved possible to create devices with bandwidths 10 times that of an equivalent length periodic device. This work was further extended and improved upon by Bortz et. al [25] where they expanded the length of the Barker sequence, from the 11 bits of the previous work to the maximum 13, and introduced variably placed phase shifted blocks of the code. It was found that using a 13 bit code with periodically placed blocks an unacceptable level of ripple occurred along the flat-top, in this case almost 7 dB of variation. By utilising variably placed phase shifted sections it proved possible to reduce this oscillation level to less than 3 dB.

A further technique proposed is that of using numerous sections of constant length 'building blocks', with the length chosen to be an even integer multiple of the coherence length of the chosen parametric interaction. Within each block there is both a positive and negative polarity domain, with the length of the inverted domain chosen so as to alter the effective nonlinearity [26]. Here an inverted domain length exactly half the length of the building block would produce the highest effective nonlinearity, with this value decreasing towards zero as the inverted domain length is reduced. With this technique it is possible to build a digitised representation of an arbitrary spatially varying effective nonlinearity, which in the paper was chosen to be that of a sinc function the Fourier transform of which is an ideal flat-top structure. To obtain the negative effective nonlinearity as is required to accurately represent the sinc function it was suggested that the order of the negative and positive domains within the building blocks be reversed. This technique proved somewhat successful in theory, producing flat-top tuning responses approximately 3 times the bandwidth of an equivalent length device, however along this bandwidth the theoretical ripple is of the order of 13%. Further, this technique also suffers from the issues of difficult manufacturing, where the small poled domain sizes required to achieve the lower effective nonlinearities could prove difficult to reliably fabricate. This of course can be minimised by using a 'building block' that is a higher multiple of the coherence length, but this leads to more pronounced discretisation of the desired effective nonlinearity which introduces further oscillations on the $\Delta k$ tuning response.

The final example of an aperiodic grating discussed here is relatively similar to that of the last design, in that it is formed of discrete blocks of nonlinearity. However, in contrast the blocks within this particular example are now an integer fractions of the coherence length, in this case the block length is $L_c/3$ with $L_c$ being the coherence length, and each block is only a single domain

of nonlinearity [27]. Using a simulated annealing algorithm the orientation of each nonlinearity block was optimised to achieve the desired response. With this technique excellent theoretical results have been achieved with almost ripple free flat-top bandwidths of 2, 3 and 5 nm being theorised in an 11.22 mm long sample of $LiNbO_3$ phase matching SHG from a 1550 nm source. For comparison the lower of these bandwidths is 6.5 times that of the full-width 95% maximum bandwidth of a standard QPM grating phase-matching the same interaction. Further at the lower bandwidth of 2 nm the reduction in the effective nonlinearity is only 25%, or alternatively a 50% reduction in conversion efficiency. From this it is clear that this technique combines a high degree of flexibility, being able to produce almost perfectly flat-top response devices, and very high efficiencies. Despite the excellent advantages this design technique can provide it does have a considerable limitation for the proposed use of flat-top devices in this chapter, where it is requirement for flat-top temperature stable devices providing visible wavelengths. In particular green generation at 532 nm and blue generation at approximately 460 nm, with corresponding 6.52 $\mu$m and 4.05 $\mu$m phase-matching periods in $LiNbO_3$ respectively. In the paper the minimum domain size was a third of the coherence length, which for the 1550 nm doubler interaction is a relatively large 3.4 $\mu$m domain. However, for blue and green generation the equivalent domain sizes would be 0.68 $\mu$m and 1.08 $\mu$m respectively, both of which are at the limits of electric field poling-technology. As such this technique is not currently viable for the mass production of temperature stable visible wavelength sources.

### 3.2.3 Phase-shifted gratings

To conclude this brief overview of bandwidth broadening techniques the merits of devices with phase shifted grating structures are now discussed. In these device types the use of a phase shift can cause the back conversion of generated harmonic signals within a particular range of frequencies whilst allowing further growth of other harmonic frequencies that may have been starting to back convert to the harmonic frequency. With the appropriate positioning and magnitude these phase shifts can be applied to alter dramatically the phase-matching response. To some extent these device types can be considered as purely aperiodic structures, where if the position of a phase shift is in suitably close proximity to the preceding phase shift it can lead to the formation of domains smaller than those determined by the the standard phase matching condition, further with a high density of phase shifts all long range periodicity may be removed. However, the device types considered here are limited to structures containing large regions of periodic or near periodically poled nonlinearity, where devices with more numerous phase shifts have effectively been covered above.

One of the earliest works on phase shifted gratings was by Mizuuchi et. al [28], where the explicit aim was to create a high efficiency second harmonic device that could be made robust to changes in phase-matching conditions, caused by laser drift or poorly stabilised nonlinear crystal temperature, maintaining a constant power output. In this work two distinct examples of phase shifted gratings were proposed as suitable structures to achieve the above aims, the first of these structures was a simple device with two segments of equal lengths of periodic poling and a single phase shift. In this structure the segments had differing grating periods, with the difference in the k-vector values of the two gratings being one of the free parameters for optimisation. It was unsurprisingly found that the greater the difference in grating k-vectors the broader the bandwidth, further the broader the bandwidth the greater the oscillation along the flat-top response. In an attempt to correct this high degree of oscillation the secondary parameter of the phase-difference between the sections was adjusted. However, for this simple structure it was found that constant phase provided the least oscillations. As the alternative, it was proposed that the phase-shifted structure be made of up 4 segments of equal length linearly chirped nonlinear gratings [28], where the difference in the average k-vectors between sections was a fixed parameter. Again the difference in grating k-vectors was optimised with constant phase, before allowing the phase to become an optimisable parameter. However, even by moving to a higher segmentation number and chirped gratings it was found impossible to reduce the flat-top ripple below the 3 dB level.

The final structure that is discussed is by far the most promising, achieving excellent efficiency, having a moderate bandwidth suitable for stabilising to a few °C and importantly it is based on a physically realisable grating layout [29]. The concept of this structure is not markedly different from the previous two segment single phase shift device above, where now there are 3 segments with two independent phase shifts that can be optimised. The important differences between these structures are the relative lengths and periods of the segmented regions, with the lengths being variable and the periods of all sections being equal. Despite these relatively minor adjustments, which would at first appear to offer no greater control of the device response, the obtained grating structures provide high efficiency flat-top bandwidth with no ringing along the flat-top. Remarkably such designs are independent of the grating period or grating length, where if the ratio of segment lengths and phase-shift are kept constant an efficiency of 30% can be obtained producing a bandwidth almost 6 times broader than an equivalent length of standard QPM. However, in obtaining the flat-top response it is clear from the high efficiency in the side lobes, $> 30\%$ of the peak efficiency, that some compromises have been made. Where having high powers in the side lobes indicates that the available nonlinearity of the device has not been

effectively distributed to the phase-matching values of interest and as such higher efficiencies should be possible using a more flexible design technique.

In summary it is evident that there are numerous techniques for modifying the phase-matching responses of QPM gratings, with some more practical than others. Yet despite the huge variety of techniques there is no one clear winner that provides all the favourable characteristics required for complete control of the phase-matching conditions whilst producing designs feasible for fabrication. Where simple easily fabricated phase-shifted gratings, although able to provide good efficiencies with flat-top responses of the correct bandwidth, are ultimately unable to match the overall efficiency and fine control afforded by truly aperiodic gratings. But here the best aperiodic designs are generally unsuitable for use in visible SHG devices due to the extreme tolerances on the poled domain size, with domains widths for wide-bandwidth blue generation reducing to almost 600 nm. Finally, chirped devices, which lie between aperiodic and phase-shifted in terms of the flexibility and design constraints have thus far proven unsuitable for the relatively narrow-band flat-top response required for temperature stability. Where in order to obtain flat-top devices that have realistic minimum domain sizes and period chirps a compromise has been made resulting in overly wide bandwidth responses.

As a result of these limitations a new approach has been taken to achieve flat-top designs that borrows concepts from many of the previously mentioned device types, with the resulting structures consisting of phase-shifted regions of constant period yet with a domain flexibility approaching that of aperiodic devices all whilst maintaining a minimum domain size that is readily fabricated for all visible wavelengths. Having a large degree of freedom in the nonlinear polarity of the many thousands of domains in a such a structure does however produce considerable difficulties in verifying the performance of a design. Traditionally the phase-matching responses of complex gratings have been approximated via the spatial Fourier transform of the structures, however this technique although rapid is not suitable for modelling high power high efficiency interactions. Of course for the intended application of temperature stable generation of visible laser light high efficiency is of utmost importance if such devices are to become widely useful. Alternatively, simple numerical integration techniques can be used to approximately solve the coupled equations of the interacting fields, such methods can lead to accurate simulations of grating performance under all power conditions. But, to achieve these high levels of accuracy such calculations can prove time consuming and computationally inefficient. Thus before introducing the new design type an alternative simulation technique, based on the analytic solutions of the coupled wave equations, is discussed. This technique offers the advantages of high accuracy at all harmonic power levels coupled with high computational efficiency.

## 3.3 High speed modelling of second harmonic generation with pump depletion

With existing simulation techniques being incapable of the high speed, accurate analysis of coupled nonlinear parametric systems an alternative technique has been developed. In 1962 the seminal paper on the interactions of plane-waves in a nonlinear media was published by Armstrong and Bloembergen [30], providing an analytical analysis of the complex parametric processes. Importantly this work included the analysis of power transfer between generated waves within the nonlinear medium, allowing for the first time a full understanding of the processes involved. By analytically solving the coupled equations of the generated harmonic and fundamental beams a simulation technique based on this analysis can offer the benefits of speed and high precision.

The key advantage of this technique over the more familiar Rung-Kutta [31] split-step numerical integration approach to solving the coupled equations is that the generated harmonic power can be explicitly calculated after the interacting waves have travelled arbitrary distances through a medium of constant nonlinearity. In comparison split-step techniques approximately solve the coupled parametric equations by simple numerical integration, requiring calculations of the nonlinear coupling many times every coherence length to obtain an accurate representation of the interacting electric fields. Obviously for near phase-matched interactions, such as for birefringently matched systems, the penalty for solving the coupled equations many times along the coherence length is negligible. With the coherence length being considerably longer than the physical device length for some interactions. However, for the QPM structures that are the focus of this work the coherence length can be orders of magnitude shorter than the total device length, resulting in many tens of thousands of calculations for a typical length device. For example in a 20 mm long QPM device of periodically-poled lithium niobate (PPLN) approximately 6000 regions of polarisation inversion (or 3000 coherence lengths) are required to efficiently phase-match the generation of the second harmonic from a 1064 nm infra-red laser source.

From this it can be seen that the Armstrong technique can provide significant computational efficiency enhancements over more standard simulation techniques in QPM materials, where now only a single calculation must be performed to provide the nonlinear contribution for each polarisation inverted region. The suitability of this analysis for QPM structures was later further emphasised by Rustagi et. al [32] who provided a subtle modification to the Armstrong-Bloembergen theory, which was more suited to analysing propagation through isolated singular

regions of nonlinearity, to account for the discontinuities of the nonlinear coefficient at polarisation inversion boundaries.

### 3.3.1 Armstrong-Bloembergen Analysis

A brief overview of the key steps in solving the coupled system via the Armstrong method is now given, with a further explanation of the application of this technique to solving the coupled equations for parametric interactions in complex QPM structures. A more detailed analysis of the Armstrong paper is given in Appendix A, which explicitly defines all the required steps to provide the complete analysis.

The analysis starts from the definition of the coupled equations of the second harmonic process, although this can equally be extended to account for more complex three wave mixing processes.

$$\frac{\mathrm{d}\hat{E}_\omega}{\mathrm{d}z} = i\frac{\omega^2}{2k_\omega c^2}\left[\frac{1}{2}\chi^{(2)}\left(-2\omega\,;\omega,\omega\right)\hat{E}_{2\omega}\hat{E}_\omega^*\right]e^{i\Delta kz} \tag{3.1}$$

$$\frac{\mathrm{d}\hat{E}_{2\omega}}{\mathrm{d}z} = i\frac{(2\omega)^2}{2k_{2\omega}c^2}\left[\frac{1}{2}\chi^{(2)}\left(-2\omega\,;\omega,\omega\right)\hat{E}_\omega^2\right]e^{i\Delta kz} \tag{3.2}$$

here $\omega$ is the fundamental frequency, $\Delta k = k_{2\omega} - 2k_\omega$ is the k-vector mismatch of the complex fundamental and harmonic fields, $E_\omega$ and $E_{2\omega}$ respectively. Writing the complex amplitudes of $E_\omega$ and $E_{2\omega}$ in terms of their real amplitudes and phase: $E_\omega = \rho_\omega e^{-i\phi_\omega}$ and $E_{2\omega} = \rho_{2\omega}e^{-i\phi_{2\omega}}$, Equations 3.1 & 3.2 can be written as three real coupled equations,

$$\frac{\mathrm{d}\rho_\omega}{\mathrm{d}z} = -i\frac{\omega^2 K}{2k_\omega}\rho_\omega\rho_{2\omega}\sin\theta \tag{3.3}$$

$$\frac{\mathrm{d}\rho_{2\omega}}{\mathrm{d}z} = i\frac{2\omega^2 K}{k_{2\omega}}\rho_\omega^2\sin\theta \tag{3.4}$$

$$\frac{\mathrm{d}\theta}{\mathrm{d}z} = \Delta k - \frac{\cos\theta}{\sin\theta}\frac{\mathrm{d}}{\mathrm{d}z}\ln\left(\rho_\omega^2\rho_{2\omega}\right) \tag{3.5}$$

where $\theta = 2\phi_\omega - \phi_{2\omega} + \Delta kz$ is the phase difference between the two propagating waves and $K = \chi^{(2)}\left(-2\omega\,;\omega,\omega\right)/\left(2c^2\right)$.

Further, from Equations 3.3 and 3.4 and the Manley-Rowe relationship [33], which states that the total energy in a parametric interaction must be maintained and thus the rate of change of energy of the fundamental and harmonic field must be exactly equal and opposite, a constant of integration may be obtained:

$$W = k_\omega\rho_\omega^2 + \frac{k_{2\omega}}{2}\rho_{2\omega}^2 \tag{3.6}$$

With this integration constant and the following substitutions

$$\rho_\omega = \left(\frac{W}{k_\omega}\right)^{1/2} u \tag{3.7}$$

$$\rho_{2\omega} = \left(\frac{2W}{k_{2\omega}}\right)^{1/2} v \tag{3.8}$$

$$z = \left(\frac{k_\omega}{2\omega^2 K}\right)\left(\frac{k_{2\omega}}{2W}\right)\zeta \tag{3.9}$$

$$\Delta k = \frac{\Delta S \zeta}{z} \tag{3.10}$$

Equations 3.3 - 3.5 can be simplified to:

$$\frac{\mathrm{d}u}{\mathrm{d}\zeta} = -uv\sin\theta \tag{3.11}$$

$$\frac{\mathrm{d}v}{\mathrm{d}\zeta} = u^2\sin\theta \tag{3.12}$$

$$\frac{\mathrm{d}\theta}{\mathrm{d}\zeta} = \Delta S + \frac{\cos\theta}{\sin\theta}\frac{\mathrm{d}}{\mathrm{d}\zeta}\ln\left(u^2 v\right). \tag{3.13}$$

From these simplifications the conservation of energy is now succinctly described as

$$1 = u^2 + v^2 \tag{3.14}$$

with $u^2$ and $v^2$ being the scaled fundamental and harmonic powers respectively.

Here it is worth noting that the units basis has been updated from the original Armstrong paper, resulting in a clearer progression to the above equations. However due to normalisation these final equations are identical regardless of the original unit system. By integrating Equation 3.13 for the case of $\Delta S = \Delta k = 0$ a further constant of integration can be obtained as:

$$\Gamma = u^2 v\cos\theta \tag{3.15}$$

which can be extended to the more general case of $\Delta S \neq 0$, as is encountered for QPM, using integration via variational methods to give

$$\Gamma_{\Delta S} = u^2 v\cos\theta + \frac{1}{2}\Delta S v^2 \tag{3.16}$$

which is itself related back to the original definition of $\Gamma$ as

$$\Gamma = \Gamma_{\Delta S} + \frac{1}{2}\Delta S v_0^2$$

where $v_0^2$ is the initial normalised harmonic power prior to propagation through the nonlinear medium.

Now from Equations 3.12 and 3.16 an expression for the variation of the scaled harmonic power, $v^2$, with propagation distance, $\zeta$, can be obtained in the form of an elliptic integral:

$$\zeta = \pm\frac{1}{2}\int_{v^2(0)}^{v^2(\zeta)} \frac{\mathrm{d}\left(v^2\right)}{\left[\left(1-v^2\right)^2 v^2 - \left\{\Gamma - \frac{1}{2}\Delta S\left[v^2 - v^2(0)\right]\right\}^2\right]^{1/2}} \tag{3.17}$$

Here, the above integral can be significantly simplified and made to match the form of an elliptic integral of the first kind by re-writing the denominator in terms of the roots, $v_c^2 \geq v_b^2 \geq v_a^2 \geq 0$, of the cubic equation:

$$\left(1-v^2\right)^2 v^2 - \left[\Gamma - \frac{1}{2}\Delta S\left[v^2 - v^2\left(0\right)\right]\right]^2 \tag{3.18}$$

Resulting in a new expression relating the harmonic power and normalised nonlinear path length, $\zeta$, that can be directly compared with the standard form of a Jacobi elliptic function of the first kind.

$$\zeta = \frac{\pm 1}{\left(v_c^2 - v_a^2\right)^{1/2}} \int_{y(0)}^{y(\zeta)} \frac{\mathrm{d}y}{\left[\left(1-y^2\right)\left(1-\gamma^2 y^2\right)\right]^{1/2}} \tag{3.19}$$

Where the following substitutions have been applied:

$$y^2 = \frac{v^2 - v_a^2}{v_b^2 - v_a^2}$$

$$\gamma^2 = \frac{v_b^2 - v_a^2}{v_c^2 - v_a^2}$$

Re-arranging Equation 3.19 in terms of the normalised power, $v^2$, gives:

$$v^2\left(\zeta\right) = v_a^2 + \left(v_b^2 - v_a^2\right)\mathrm{sn}^2\left[\left(\zeta + \zeta_0\right)\left(v_c^2 - v_a^2\right)^{1/2}, \gamma\right] \tag{3.20}$$

$$u^2\left(\zeta\right) = 1 - v^2 = 1 - v_a^2 + \left(v_b^2 - v_a^2\right)\mathrm{sn}^2\left[\left(\zeta + \zeta_0\right)\left(v_c^2 - v_a^2\right)^{1/2}, \gamma\right] \tag{3.21}$$

where $\mathrm{sn}\left(u, \gamma\right)$ is the Jacobi elliptic function with modulus $\gamma$, or alternatively, with parameter $\gamma^2$ and $\zeta_0$ is the initial normalised path length. From this it is clear that on solving the Jacobi function an analytic definition of the harmonic power generated over the normalised path length, $\zeta$, is readily obtained.

However, prior to solving the above Jacobian the parameter $\zeta_0$ must first be calculated from the initial conditions, satisfying the following:

$$v_0^2 = v_a^2 + \left(v_b^2 - v_a^2\right)\mathrm{sn}^2\left[\zeta_0\left(v_c^2 - v_a^2\right)^{1/2}, \gamma\right] \tag{3.22}$$

By considering the initial condition of $v_0^2 = 0$, the common condition for SHG, the integration constant $\Gamma = 0$. From this the lowest roots of the cubic Equation 3.18, between which the harmonic power is constrained to oscillate, are defined as $v_a^2 = 0$, $v_b^2 = 1$. Applying this set of conditions to the above formula it is readily found that with no input harmonic power the initial normalised path length $\zeta_0 = 0$.

Further, with the substitution of these initial values into Equation 3.17 it can be shown that the normalised harmonic amplitude, $v$, varies according to

$$v_{\Gamma=0} = \tanh\left(\zeta\right) \tag{3.23}$$

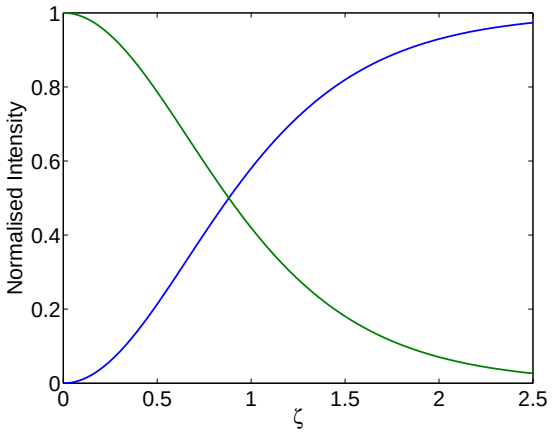


Figure 3.1: The $\tanh^2$ growth of harmonic field intensity (blue) along the scaled device length, $\zeta$, for $\Delta k = 0$ and zero initial harmonic field intensity. Also shown is the corresponding $\mathrm{sech}^2$ variation in the fundamental intensity (green).

with the corresponding normalised fundamental amplitude given as

$$u_{\Gamma=0} = \mathrm{sech}\,(\zeta) \tag{3.24}$$

These results are represented graphically in Figure 3.1 showing the growth of the harmonic amplitude, at the expense of the fundamental, towards 100% conversion as the scaled nonlinear interaction length $\zeta \to \infty$. Here an increasing value for $\zeta$ implies either the physical device length has been extended or the initial fundamental power is increasing.

### 3.3.2 Generalisation of the Armstrong analysis to QPM structures

In the previous section it was shown how for the most simplistic case of perfect phase-matching and zero initial harmonic power the Jacobian function of Equation 3.19 can readily be transformed into the familiar result of continuous growth of the harmonic power like $\tanh^2(\zeta)$. However, the application of this analysis is intended for QPM structures where apart from the very first section of material, it cannot be assumed that the initial harmonic power is zero. With the calculation of the Jacobi function being performed for each section of nonlinear polarisation reversal it is clear that the initial normalised harmonic path length $\zeta_0$ must be recalculated taking into account the new values of harmonic and fundamental powers.

This is achieved using the same method as for the simplistic case but here it is found that in calculating the initial path length information of the direction of $\zeta_0$ is lost, with only its magnitude being known. Here the direction of $\zeta_0$ is essential to determine whether the initial harmonic power is depleted by the fundamental or grows at its expense, of course for the first

domain with no initial harmonic this is irrelevant. Despite this loss of information the direction of power flow can be independently calculated from the initial phases of the two waves, with power flowing from the fundamental wave if $\sin\theta_0 > 0$

A further complication with the original Armstrong analysis is that all the units have been scaled by the value of the nonlinearity, taking into account its orientation. Of course for a bulk material with a constant nonlinearity orientation this is of no significane, but as Rustagi et. al highlighted [32] this significantly complicates the analysis for QPM structures where the nonlinearity periodically alternates direction. It is possible to overcome this limitation by completely redefining all the initial conditions for each new domain orientation, however, this adds unnecessary steps and can result in inaccuracy due to compounded rounding errors.

Alternatively, Rustagi redefined the analysis by scaling all the interactions by $|\zeta|$, instead of $\zeta$, thus making the scaled distance travelled in the nonlinear medium directly proportional to the physical dimensions irrespective of nonlinearity orientation. This leads to the following modified Jacobian function linking harmonic power and propagation length:

$$v^2\left(|\zeta|\right) = v_a^2 + \left(v_b^2 - v_a^2\right)\mathrm{sn}^2\left[\left(|\zeta| \pm |\zeta_0|\right)\left(v_c^2 - v_a^2\right)^{1/2}, \gamma\right] \tag{3.25}$$

Here the polarity of $\zeta_0$ is again chosen according the relative phase of the propagating waves, but now with the additional constraint that it be linked with the direction of the nonlinearity. Where a positive value is chosen if the harmonic power is to increase and a negative value for harmonic depletion. This power flow direction can be determined from Equation 3.25 as:

$$\begin{aligned}\frac{\mathrm{d}v^2}{\mathrm{d}|\zeta|} &= \left(v_b^2 - v_a^2\right)\left(v_c^2 - v_a^2\right)^{1/2}\mathrm{sn}\left[\left(v_c^2 - v_a^2\right)^{1/2}\left(|\zeta| \pm |\zeta_0|\right), \gamma\right] \\ &\quad \times \mathrm{cn}\left[\left(v_c^2 - v_a^2\right)^{1/2}\left(|\zeta| \pm |\zeta_0|\right), \gamma\right] \\ &\quad \times \mathrm{dn}\left[\left(v_c^2 - v_a^2\right)^{1/2}\left(|\zeta| \pm |\zeta_0|\right), \gamma\right]\end{aligned} \tag{3.26}$$

Here, $\mathrm{cn}\left(u, k\right)$ and $\mathrm{dn}\left(u, k\right)$ are simply the further two basic Jacobi elliptic functions with modulus $k$, which arise from the following definition:

$$\frac{\mathrm{dsn}\left(\mathrm{u}\right)}{\mathrm{d}u} = \mathrm{cn}\left(u\right)\mathrm{dn}\left(u\right) \tag{3.27}$$

### 3.3.3 Application of the Armstrong-Rustagi modelling technique

Having presented the theory for solving exactly the coupled nonlinear equations of SHG in a QPM structure a brief example application of this theory is given for a basic periodic structure. The results of this technique are compared to those obtained via both Fourier and Runge-Kutta analysis. For this example a PPLN based QPM device 1 mm in length is modelled for phase-matching SHG with a fundamental laser source at 1550 nm.

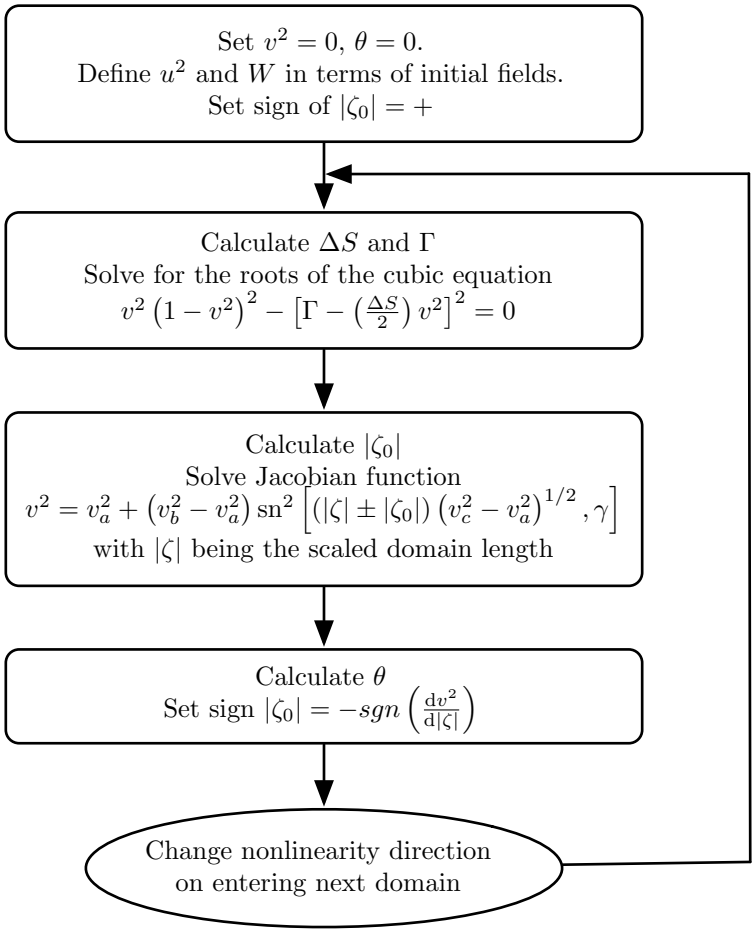


Figure 3.2: The programmatic steps required to analytically solve the nonlinear coupled equations arising through second harmonic generation using the analysis of Armstrong and Bloembergen [30], which has been further simplified using the later adaptation to QPM by Rustagi et. al [32].

With this being a parametric interaction to generate the second harmonic it is reasonable to assume that initially there is negligible harmonic power, other than random background fluctuations. With this assumption it is now trivial to define the fundamental laser amplitude in terms of the scaled units giving $u = 1, v = 0$ with $W = k_\omega \rho_\omega^2$. Further, with there being no initial harmonic field it is impossible to define the phase difference of the two propagating fields, so it is reasonable to set the initial phase to $\theta = 0$, although as can be seen for the first calculation the phase is irrelevant. Finally it is necessary to define the scaled k-vector mismatch $\Delta S$ and calculate the integration constant $\Gamma$, again for the first calculation with no harmonic field $\Gamma = 0$.

Now, from these initial values the roots of Equation 3.18 can be readily solved giving $v_a^2 = 0, v_b^2 = v_c^2 = 1$. With these roots it is now possible to solve the Jacobian function given in Equation 3.25 to obtain the harmonic power generated over the scaled length of the first polarisation inverted region $|\zeta|$. To achieve this it is important to note that for the first calculation significant simplifications are obtained with $|\zeta_0| = 0$ and as such there is no requirement to calculate the direction of power flow to determine the sign of $|\zeta_0|$.

Before propagating to the next region it is first necessary to calculate the phase between the two fields, using Equation 3.16, and determine the direction that power was flowing at the furthest extent of the current region. With this knowledge of the power flow it is now possible to define the sign of the variable $|\zeta_0|$ for the next region, which is, by virtue of the rotation in nonlinearity, the negative of the current direction of power flow, where a positive direction of power flow indicates an increasing harmonic signal.

On calculating the response of subsequent nonlinear regions the process remains the same, but now the fields from the previous region become the initial fields. However, with a non-zero harmonic signal the calculations are slightly more involved with the roots of the cubic now dependent on $\Delta S$ and $\Gamma$, where $\Gamma$ has been calculated using the new value for $\theta$ determined at the end of the last region. Additionally, $|\zeta_0|$ must now be explicitly determined by solving Equation 3.22. This process is further explained through the flow chart in Figure 3.2.

By repeating this process for all regions of nonlinearity within the QPM structure the response of the device to various input parameters can be rapidly determined to almost arbitrary precision, limited only by the machine resolution of the calculation. This is in contrast to the more familiar technique of solving the coupled equations by Runge-Kutta integration methods, where to achieve the same level of precision the integration step size must be reduced to small fractions of the coherence length resulting in significantly longer calculation times. Further, by reducing the step size of the Runge-Kutta calculation, in an effort to increase accuracy, the total error for the

harmonic power generated over a single domain can actually increase due to compounded errors. Some examples of the results obtained using the Armstrong (red), Runge-Kutta (green) and Fourier (blue) techniques are given in Figure 3.3, showing the variation in harmonic conversion efficiency with changing $\Delta k$ for a 1 mm long PPLN device phase-matching a SHG interaction from a 1550 nm laser source for increasing fundamental input powers.

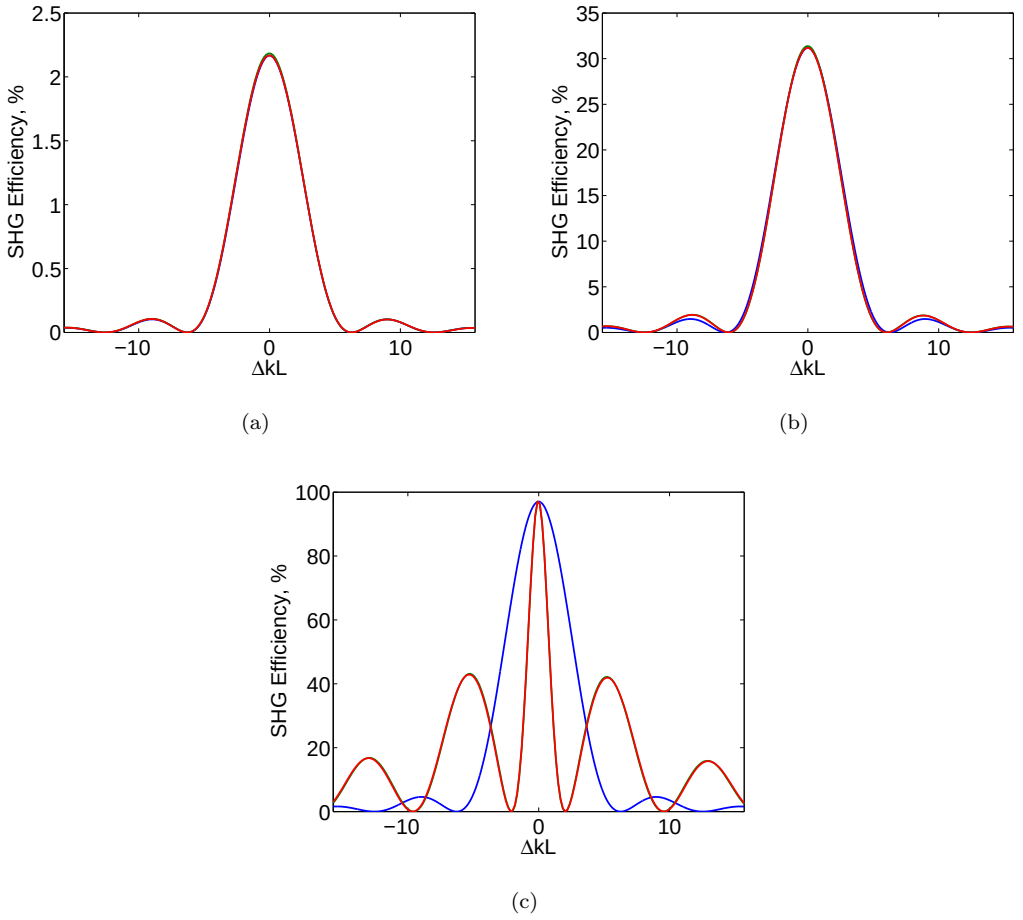


Figure 3.3: Length normalised $\Delta k$ tuning curves for a 1 mm long PPLN crystal generating the second harmonic of a theoretical 1064 nm laser with 10 W (a), 200 W (b) and 5 kW (c) of fundamental input power. For each plot the tuning curves have been calculated using Fourier analysis (blue), RK4(5) Runge-Kutta anlysis (green) and Armstrong-Bloemberg analysis (red). Note due to the excellent agreement between the high power modelling techniques it is difficult to discern the plot of the Runge-Kutta analysis.

Figure 3.3(a) is a plot of the harmonic conversion efficiency variation for a range of $\Delta k$ values when operating in the low power regime, where it has been specified that the fundamental input

field be $800\,\mathrm{kVm}^{-1}$ (approximately equivalent to a 10 W source with a $30\,\mu$m $1/e^2$ spot size), giving an efficiency of ∼2%. Here it can be seen that good agreement can be obtained between all techniques, although to ensure accuracy of the Runge-Kutta technique the calculation has been performed numerous times with increasing samples per domain length. For this simulation the standard Runge-Kutta 4(5) technique has been used, which from 4 calculations of the derivatives of the coupled equations provides a fifth order accuracy for the generated harmonic power. Here it should be noted that although the Fourier technique is perfectly capable of generating the correct $\Delta k$ tuning response it is however unable to give any information on the conversion efficiency of the interaction. As such the efficiency for the Fourier analysis has been scaled to match that of the analytic analysis to allow direct comparison of the phase-matching curves.

For higher input powers the simple Fourier analysis techniques becomes incapable of accurately determining the phase-matching characteristics. The cause of this inaccuracy is two fold. Looking at Figure 3.3(b) it can be seen that there is only a slight discrepancy in the response, where the efficiencies of the secondary phase-matching peaks are slightly lower in the Fourier analysis than either of the other two techniques. This difference can be attributed to reduced nonlinear drive, where at the optimal phase-matching conditions the fundamental has become depleted to such an extent by the nonlinear interaction that the rate of transfer to the harmonic becomes reduced. However, at some degree of de-tuning the depletion does not occur as rapidly which results in a higher nonlinear drive at this de-tuned $\Delta k$ value and thus a higher relative conversion efficiency. For higher peak powers the effects of reduced nonlinear drive of course become more severe, resulting in significantly higher conversion efficiency in the side lobes as can be seen in Figure 3.3(c). Further, at this higher power level a second more complex mechanism referred to as dephasing [34, 35] occurs. Here dephasing is the cause of the narrowing of the central peak and movement in the zero positions at higher power and is a result of the power dependence of the phases of the interacting waves, as seen in Equation 3.13. Where at higher powers small variations in the phase-matching condition are amplified resulting in a more rapidly varying response.

It is further clear from the plots of Figure 3.3 that the new Armstrong-Bloembergen simulation technique utilised throughout this chapter is fully capable of analysing both low and high power systems, with the obtained tuning responses matching that of the RK4(5) technique. Here the slight discrepancy between the two techniques is as a result of insufficient sampling along the domain lengths for the RK4(5) analysis. Where for each iteration of the Runge-kutta analysis the step size was decreased by a factor of two until the variation between the current and previous calculation became less that 1% on average. Thus it is clear that one of the main

advantages of analytically solving the coupled equations is the unambiguous answer obtained, where in contrast the results obtained with RK4(5) analysis can vary significantly if care is not taken over the choice of step size (although this problem can be somewhat alleviated through the use of adaptive step size algorithms [31]).

An additional advantage of the Armstrong-Bloembergen method not obvious from above analysis of standard QPM structures is that large computational efficiency gains can be obtained for aperiodic grating structures, where some nonlinearity regions may be much longer than the coherence length for normal phase-matching. Using a standard Runge-Kutta technique it is necessary to integrate the coupled equations at step size a fraction of the coherence length not the domain length, as such for large regions of constant nonlinearity relatively more calculations are required. Whereas, using the Armstrong technique it is possible to calculate directly the contribution of this extended region of constant nonlinearity in one step providing a significant computational efficiency increase.

Having verified the performance of the new Armstrong-Bloembergen simulation technique it is now possible to apply this high speed analysis procedure to predicting the temperature tuning responses of complex non-uniform grating structures designed for their enhanced flat-top bandwidth and stability.

## 3.4 Deleted reversal flat-top temperature tuning response QPM devices

It was earlier discussed that to design a QPM like grating device capable of efficiently generating harmonic power output over a wide range of operating temperatures or fundamental input wavelengths that the periodicity of the grating must be significantly altered. Examples were given of chirped grating devices [12, 15], phase-shifted devices [28, 29] and truly aperiodic devices [26, 27], all of which are to some extent capable of generating flat-top power stable responses, at least in theory. The problem common to the majority of these device types was found to be the excessively stringent tolerances on the fabrication process, where often the size of the polarisation inverted regions or their relative positions required for visible SHG are beyond the resolutions of even the most advanced poling techniques. Here an alternative technique, that maintains a minimum poled domain size well within the limits of standard high yield electric field poling methods, is theoretically and experimentally examined.

First it is necessary to define the final phase-matching characteristics that an ideal grating structure should possess. It was shown in Chapter 2 that for parametric second harmonic genera-

tion the variation in harmonic power output with changing phase-matching parameter, $\Delta k$, takes the form of a sinc squared function for low power interactions. For birefringent phase-matching materials this sinc squared function can be relatively broad, providing a corresponding large range of working temperatures or fundamental frequencies over which almost constant power output can be obtained. However, in the vast majority of materials used for QPM interactions this power stable bandwidth reduces rapidly with temperature or wavelength variations making stable operation of such devices difficult especially as longer lengths and higher input powers are used to improve the conversion efficiency.

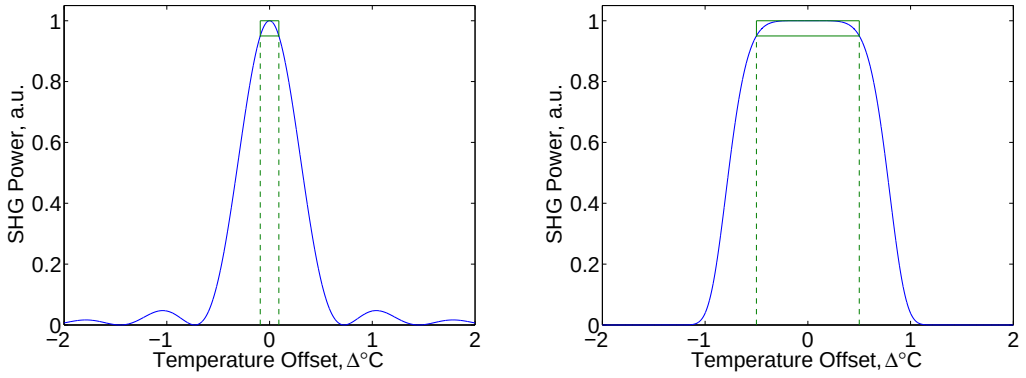


(a) (b)

Figure 3.4: (a) The standard sinc$^2$ temperature tuning response of a uniform 20mm long PPLN sample with 0.255 °C 95% stability bandwidth. (b) A plot of the idealised 1 °C flat-top bandwidth required for stable operation.

A typical power verses temperature tuning curve for the QPM material $LiNbO_3$ is shown in Figure 3.4(a). Also shown in this plot (green dashed line) is the temperature bandwidth across which the harmonic power output varies by less than 5% of its peak value at the optimum operating temperature. This particular plot is for a SHG interaction generating 532 nm light in a 20 mm long PPLN crystal and has a 95% stability bandwidth of only ±0.13 °C. For longer lengths, which provide higher efficiencies proportional to the length squared, the bandwidth reduces proportionally as the inverse of the length. So assuming negligible depletion it is found that the 95% stability bandwidth of a 40 mm long device falls to only ±0.06 °C, a range too small to reasonably control over a 40 mm sample.

For many applications such as stable laser sources for experimental work or visual display systems, which require a known output power for faithful colour representation, a variation of more than 5% in output power may be unacceptable. Further, it is often a requirement that

the final system, be it for research, display purposes etc., be miniaturised and as such the large insulating structures that would be required to achieve this stable operation may not be desirable. Thus for the broad-bandwidth devices proposed in this Chapter the dominant characteristics is for a wide flat-top temperature tuning response that varies by less than 5% of the peak value, where the bandwidth can be tailored to the final application but optimally of the order of 1-2 °C. An example of the temperature tuning response of such a structure is shown in Figure 3.4(b), here the flat-top bandwidth is four times that of the standard QPM device.

### 3.4.1 Altering the QPM grating structure for flat-top temperature tuning response

It is known that the sinc like nature of the $\Delta k$ tuning response of nonlinear devices at low power has a Fourier transform relationship with the nonlinear coefficient. Where the sudden discontinuity of the nonlinear coefficient at the ends of the device causes the Fourier space representation to be a sinc like distribution of frequency components. For QPM devices the added periodicity of the grating structure merely leads to an offset in the dominant frequency component of the sinc profile. It is thus reasonable to assume that the inverse relationship also holds, in that the Fourier transform of the desired spectral response produces the appropriate variation in the nonlinearity coefficient. In this case the desired spectral response is that of a top-hat function, the transform of which results in a sinc like variation in the nonlinearity coefficient.

Thus in principle to obtain a wide-bandwidth flat-top temperature stable harmonic output it is a simple matter of spatially altering the nonlinear coefficient of a material along its length to correspond with a sinc function. However, as discussed earlier, there is no practical method of altering the local nonlinearity of a material other than with implanted impurities [16], although such techniques alter the phase matching characteristics and can further lead to loss in the material. An alternative technique that has been utilised with some success is to reduce the effective nonlinear coefficient by reducing the nonlinear coupling in a parametric process through a deliberate phase mismatch. Previous work [26] achieved this phase mismatch by varying the duty-cycle of the poled grating structure, where the greater the variation from a 50:50 ratio the lower the nonlinear coupling. Although this technique can produce good results in theory it is impractical in real devices due to the small domain sizes required.

A further technique for modifying the nonlinear coefficient that has been experimentally demonstrated for reducing the side-lobes of the standard sinc squared tuning reponse, thus preventing cross talk between communications channels when used as an optical filter, is that

of deliberately disrupting the periodicity of a grating by selectively removing domains [11]. By deliberately removing poled domains from the otherwise periodic structure the local effective nonlinearity can be reduced by allowing a small amount of the harmonic signal to back convert to the fundamental. Such a technique, where now the local effective nonlinearity can only take the two values of $d_{eff} = 2\chi^{(2)}/\pi$ or 0, is not as flexible as varying the duty cycle which in theory allows a continuously varying effective nonlinearity. It is however possible to achieve an average effective nonlinearity of almost any value, where by utilising more periods and selectively removing or deleting a polarisation reversal the long range average can be made to approximate any value. The considerable advantage of this technique over all others comes in fabrication, where by having all poled domains fixed at a constant size and on a pre-defined spatial grid defined by the standard QPM phase-matching conditions the fabrication yield can equal that of standard periodic QPM structures.

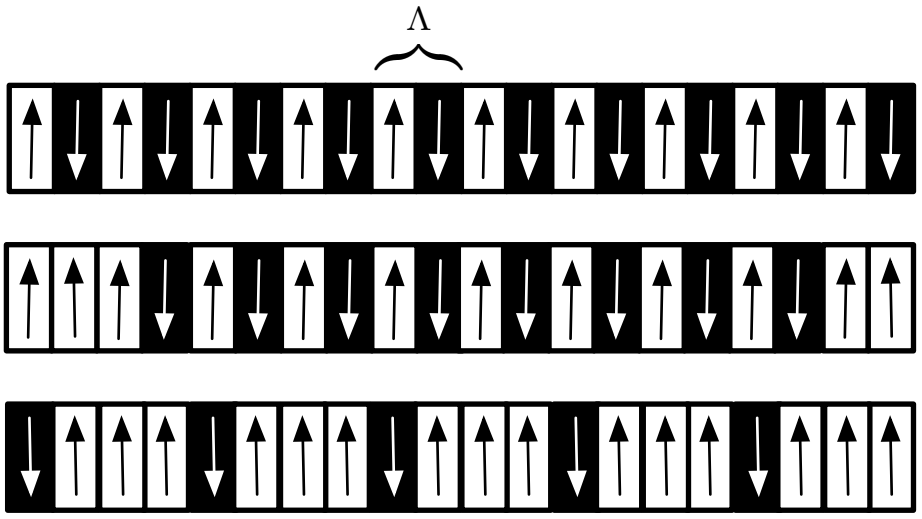


Figure 3.5: The grating patterns of a constant period, $\Lambda = 2\pi/(k_{2\omega} - 2k_{\omega})$, 10 level quantised deleted reversal QPM structure showing an average $d_{eff}$ of 100% (top), 80% (middle) and -50% (bottom). Note that the lower diagram has been $\pi$ phase shifted to provide a negative effective nonlinearity. Further it can be see there are no adjacent inverted domains (black), which maintains a constant inverted domains size.

Examples of the possible grating structures required to obtain a range of average $d_{eff}$ are shown in Figure 3.5. Here for all the grating sections shown the number of quantisation levels is set at 10, resulting in sections of grating 10 periods long defining the quantisation values. The uppermost diagram depicts a grating section with 100% $d_{eff}$, where all periods have received a domain inversion. In contrast, the central diagram has two poled domains deliberately deleted or

left un-poled, with the deletion such that the remaining poled domains are as uniformly spaced in the structure as possible, this results in an effective nonlinearity of only 80% on average. Finally, the lower of the three grating sections has an effective nonlinearity of only 50%. Here however, it can be seen that the positions of the poled domains have been shifted relative to the two previous structures resulting in a $\pi$ phase shift. As an individual element this phase-shifted grating would behave identically to an equivalent deleted reversal grating without a phase-shift, but when combined with sections of say the upper structure it can be seen that by being phase-shifted it provides a net reduction on the harmonic signal. As such this phase-shifted structure provides the equivalent of a negative $d_{eff}$, in this case $-50\%$.

Using this technique it is now possible to represent quantised versions of arbitrary real mathematical functions, in particular it is now possible to represent a sinc function to obtain the desired flat-top temperature tuning response. Although similar to the previous work on duty-cyle $d_{eff}$ control it is clear that this alternative technique is not restricted by the limits of fabrication processes, where as long as a process exist for fabricating the first-order standard QPM grating for phase-matching the same interaction devices designed with this technique can in principle be fabricated with no greater difficulty.

An example of the desired nonlinearity (green) and the achievable effective nonlinearity variation (blue) through deleted-reversals to obtain an approximate flat-top response are shown in Figure 3.6(a). Here the effective nonlinearity is shown normalised to the maximum effective nonlinearity which for a first order QPM structure is given as $2\chi^{(2)}/\pi$. As can be seen in the plot the desired nonlinearity has been chosen to be that of a sinc function ranging from $\pm 3\pi$, it is shown later that in general the greater the width of the sinc function the greater the flat-top bandwidth. Further, by careful choice of the number of quantisation levels, in this case 20 levels, a good compromise between the precision of the quantisation values and the number of domains required to represent each value can be reached. Where going to higher quantisation numbers leads to higher precision but also a longer length over which each value must be averaged, thus decreasing the spatial resolution of the desired function.

Shown in Figure 3.6(b) is the corresponding grating pattern that such a quantised $d_{eff}$ produces. In this diagram each black bar represents an individual poled domain, with regions of high $d_{eff}$ and thus fewer missing domains becoming much more densely packed, eventually leading to their representation as almost solid regions of poling. This is simply an artefact of representing domains on the order of a few microns as relatively large printed lines, and is not indicative of one large poled region. In this diagram it is clear to see the 5 regions of relatively dense poling which correspond to the peaks of the individual sinc oscillations, with the density of poled domains

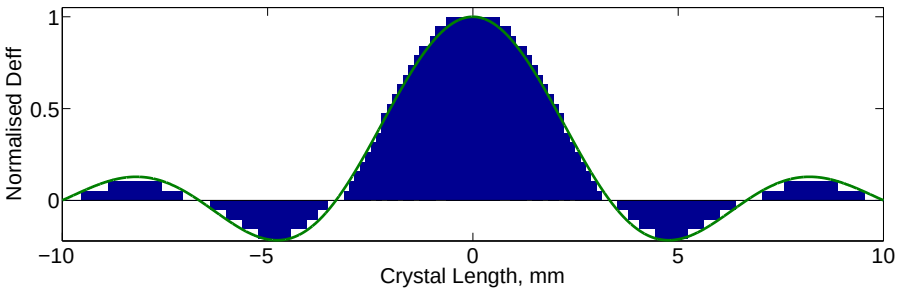


(a)

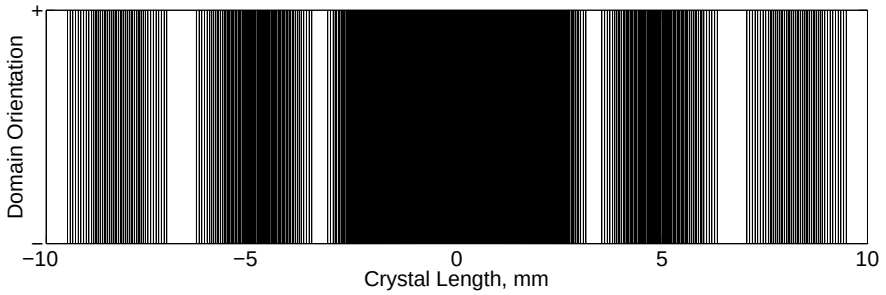


(b)

Figure 3.6: (a) the sinc like normalised effective nonlinearity variation required for achieving a flat top tuing response (green) and the approximated, quantised effective nonlinearity attainable through quasi-periodic domain reversals (blue). (b) A representation of the inverted domain pattern as required to match the effective nonlinearity. Here, each black band is a poled domain.

increasing towards the centre of each peak. Finally, by comparing the diagrams in Figure 3.5 it can be seen that upon a phase reversal it is theoretically possible for two adjacent poled domains to occur, with each domain residing in a separate quantised structure. However this only occurs if there is a relatively high concentration of poled domains in each section of quantised periods. By virtue of the sinc structure phase reversals are only required for low $d_{eff}$ values and as such no adjacent poled domains can occur, further easing fabrication issues.

It is now clear that the two main parameters to be optimised for optimal harmonic power temperature stability are the number of quantisations levels, with in general more quantisation levels providing a greater correlation between desired and attainable nonlinearity variations, and the width of the sinc function nonlinearity, where as is now demonstrated the greater the range of the sinc function the wider the flat-top bandwidth.

### 3.4.2 Theoretical performance of sinc like $d_{eff}$ QPM grating structures

Having established a robust, practical technique for modifying the local nonlinear coupling efficiency in a QPM grating and identified a suitable pattern with which to modify it to provide a flat-top temperature tuning response it is now possible to explore the effects of varying such parameters as the quantisation levels, the width of the sinc range and physical device length. This analysis has been performed using the analytic Armstrong-Bloembergen technique introduced earlier. The use of this technique affords considerable simplification in the analysis of complex grating structures, where exact solutions to the grating characteristics can be obtained with no concerns over calculation accuracy, even at high power. Further in the structures proposed above for regions of low nonlinear coupling, as required for large sections of a sinc like variation, as shown in Figure 3.5 that there can be relatively long regions of constant polarity nonlinearity. Here, the Armstrong-Bloembergen technique is able to provide the exact solution for these large unpoled regions in one step. In contrast, despite the lack of adequate phase-matching for these regions and thus limited power coupling, numerical integration methods must still calculate the solutions to the coupled equations at distances fractions of the coherence length. Thus use of the analytic technique can offer significant improvements in computational efficiency.

From Figure 3.6(a) it is clear that the greater the number of sinc oscillations the lower the proportion of the device with a high effective nonlinearity coefficient. From this it is reasonable to assume that with greater numbers of oscillations the bandwidth increases, due to a reduced effective device length, and further that this increased bandwidth leads to decreased efficiency. Prior to investigating the effects of altering the sinc oscillation number it is necessary to verify the predicted bandwidth increase and flat-top response such gratings provide. For this the device highlighted in Figure 3.6(b) is used as a test case.

The theoretical results of generating a stable 532 nm harmonic power output from a 20 mm PPLN device patterned as Figure 3.6(b) are shown in Figure 3.7(a) (blue). Here it was assumed that a low power laser of approximately 100 mW was input into the device. Using a plane-wave model it was further assumed that the input electric field amplitude is equivalent to that at the waist of an optimally focused laser with the same power, at this power level there is negligible fundamental depletion or bandwidth narrowing. Additionally, shown on the same plot is the theoretical plane-wave bandwidth of a standard 20 mm PPLN based QPM device (green), the bandwidth over which the power varies by less than 5% for such a device is approximately 0.255 °C. As can be seen a significant bandwidth increase has been achieved, with the new 95% flat-top bandwidth being approximately 4.5 °C or 18 times that of the standard device. However, along with this bandwidth increase is a significant reduction in efficiency, with the sinc structured

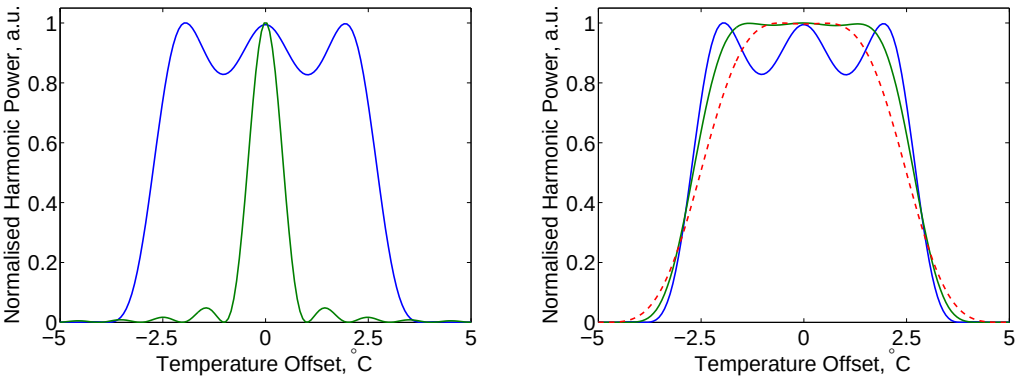


(a) (b)

Figure 3.7: (a) Harmonic power output of a standard 20 mm long, 6.5 $\mu$m period PPLN based QPM structure for varying operating temperature (green) and the output of the sinc structured 20 mm long PPLN device (blue) shown in Fig. 3.6(b). (b), The effect of raised cosine windowing on flat-top bandwidth, no windowing (blue), windowing with period equal to device length (red) and with period 1.6x the device length (green).

device being only 3% as efficient as the standard device.

Further, it is clear that using such a sinc structured device the obtained temperature tuning bandwidth is highly oscillatory, with the power variation along the 'flat-top' being greater than 15% and thus considerably outside the acceptable range of ±2.5%. This oscillation can be attributed to the poor representation of a sinc function by the grating structure, where a true sinc structure should be infinitely long. By truncating the sinc function to a finite length it is impossible to obtain a smoothly varying response due to the discontinuous nature of the nonlinearity. This same effect is prevalent in fields such as digital signal processing, where here continuous signals become truncated and discretised, and is commonly referred to as 'Gibbs' phenomenon. Thankfully, using standard signal processing techniques it is possible to significantly reduce the undesired oscillations. By applying a windowing or apodisation to the structure to remove the harsh discontinuity caused by truncating the sinc function it is possible to obtain a smoothly varying response.

Figure 3.7(b) shows the effect of applying a raised cosine windowing function to the effective nonlinearity variation of Figure 3.6(a). The use of a raised cosine window creates a smooth reduction in the effective nonlinearity at the extremes of the device and thus significantly reduces the flat-top oscillations. As can be seen the new response (green) maintains its wide bandwidth whilst having a power variation of less than 1%. To obtain this response a raised cosine window

with a period 1.6 times the length of the total device has been utilised. Initially a window with a period equal to the device length was modelled (red dashed), however, as can be seen although the response remained smooth a significant reduction in bandwidth was observed. Thus to obtain optimal results from such devices it is clear that a further optimisation of the applied windowing function is required.

### Bandwidth variation with increasing sinc width

The analysis now focuses on the effects of increasing the range of the sinc function that the gratings are based on, i.e. increasing $x$ in $\mathrm{sinc}(x)$. To simplify the analysis the problem is reduced from three to two free variables by maintaining a constant device length, leaving free the number of quantisation levels and the windowing width. Here a 20 mm long device has been selected for its compromise between a large number of periods, which provides flexibility in the design, and its compact size.

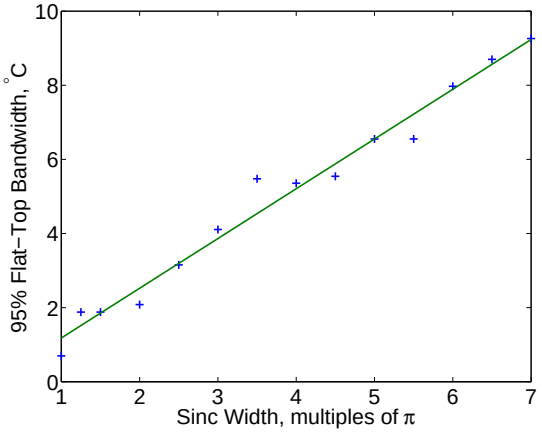


Figure 3.8: A plot of the theoretical flat-top bandwidths of 20 mm long sinc structured $d_{eff}$ PPLN devices for generating a 532 nm harmonic signal (blue) and best linear fit (green). Here the width of the sinc function has been increased to provide a wider bandwidth response, the windowing and quantisations of each device has been individually optimised to achieve maximum bandwidth.

Figure 3.8 shows the effect of increasing the range of the sinc function, where the width of the function has been increased in multiples of $\pi$. Here it can be seen that there is an approximate linear relationship between the flat-top bandwidth and the sinc width, with bandwidth increasing with the number of sinc oscillations. This increased bandwidth can of course be attributed to the reduction in the length of device with high density poling, where at greater sinc oscillations the central high density peak becomes narrowed. This reduction in the length of high

effective nonlinearity can be considered equivalent to a shorter length of standard QPM, with a correspondingly greater bandwidth. However, it must be stressed that for each sinc function width the flat-top bandwidth was maximised, through changes in the quantisation levels and windowing function, with no regard for overall efficiency. As such although the bandwidth has increased greatly it may be more beneficial in terms of conversion efficiency to utilise a shorter length of standard QPM material to achieve the same bandwidth broadening. The validity of this statement is now theoretically examined.

### Device efficiency verses flat-top bandwidth

Here, a comparison is made between the relative conversion efficiencies of sinc structured PPLN devices, again based on a 20 mm long sample, and lengths of standard PPLN QPM material with equivalent flat-top bandwidths. Here all device efficiencies are given as a percentage of the peak efficiency of a standard periodic 20 mm QPM device when operating at low fundamental power, i.e. negligible pump depletion.

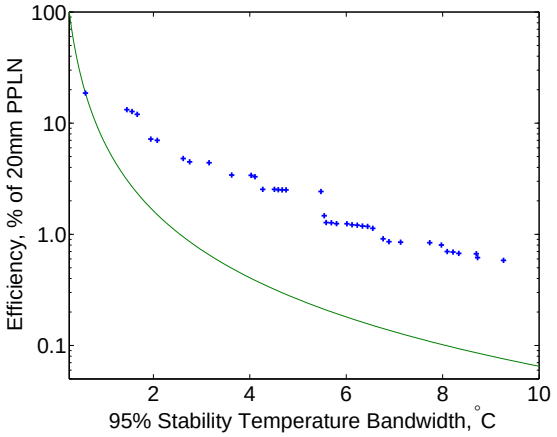


Figure 3.9: SHG efficiency (relative to a 20mm QPM device) vs 95% stability flat-top bandwidth for a range of Sinc like $d_{eff}$ devices (blue), where the range of the sinc function, the quantisation levels and the windowing function have been varied to provide greater bandwidth. Also shown is the relative efficiency for lengths of standard QPM material that provide the equivalent flat-top bandwidth (green).

Unlike the previous simulation on the effects of increasing the range of the sinc like $d_{eff}$, the flat-top bandwidths have now been optimised to provide wide bandwidth whilst maintaining a relatively high efficiency, with sinc range, quantisation and windowing all being free parameters. The results of this is shown in Figure 3.9. Here it can be seen that even for the narrowest bandwidth device designed, with a 95% stability bandwidth of $\sim$0.5 °C achieved using a 1.25$\pi$

sinc range, a large drop in efficiency to only 20% that of a standard uniform QPM device occurs. However, it is clear that when comparing this narrow bandwidth sinc structured device (blue) with a length of uniform QPM PPLN providing the same 95% stability bandwidth (green), approximately 9 mm long, that the reduction in efficiency is equivalent. As such although offering no benefit over a shorter length of uniform material, equally it is not detrimental to use such a structured device to obtain a wider bandwidth.

Now by increasing the range of the sinc like $d_{eff}$ it is expected from Figure 3.8 that significant bandwidth improvements can be obtained. Further, it is now evident from Figure 3.9 that at these greater bandwidths, despite the overall large efficiency reduction compared with standard 20 mm long narrow bandwidth QPM devices, the sinc structured devices begin to realise significant efficiency enhancements relative to equivalent bandwidth QPM samples. For the more wide bandwidth devices, 95% stability bandwidth $> 3.5\,^{\circ}$C, a relative efficiency of almost an order of magnitude greater than equivalent bandwidth uniform QPM devices is routinely achieved. For some special cases, for example a device with the sinc $d_{eff}$ ranging between $\pm 3.5\pi$ giving a bandwidth of 5.5 °C, this relative efficiency can be over an order of magnitude greater, although this appears to be an isolated case. For the less dramatic bandwidth increases the efficiency gains are more modest, with the efficiency breaking even with standard QPM for approximately twice the bandwidth of the reference 20 mm long uniform QPM device. Attempting to generate devices with even narrower bandwidths can be achieved by allowing the quantisation values to reduce to a two level system, resulting regions of 100% or 0% poling density. By using higher range sinc functions as the basis of such a structure the ratio of the lengths of poled and un-poled sections decreases, in effect becoming shorter lengths of uniform QPM.

#### Constant bandwidth with increasing length for higher efficiency

Having demonstrated theoretically that sinc like $d_{eff}$ devices can achieve large efficiency gains over uniform QPM devices providing the same wide bandwidth it is now necessary to investigate the performance of such sinc structured devices whilst providing a flat-top bandwidth of 1-2 °C. With this range being the initial design aim set out earlier. For this investigation three temperature stability ranges are considered, 1 °C, 1.5 °C and 2 °C, with these bandwidths being maintained whilst device length is increased in an attempt to provide high efficiency stable harmonic power.

Here as above the bandwidths are adjusted through variations in quantisation levels, windowing functions and the range of the sinc function. Due to the vast set of parameters to be investigated for each device length of interest the minimum step change in values for the free parameters has been significantly increased. This offers considerable reductions in computation

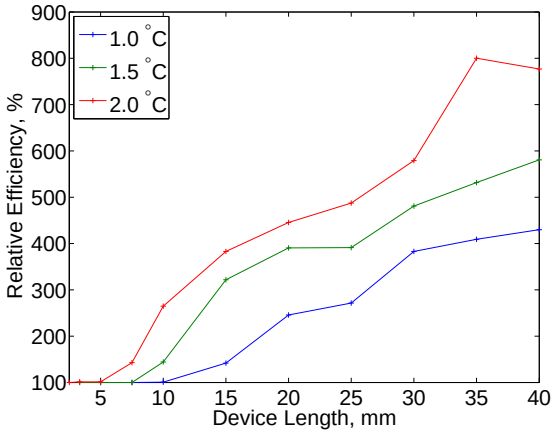


Figure 3.10: Plot of the relative harmonic efficiencies for a range of sinc structured devices of varying physical length designed to maintain 1 °C (blue), 1.5 °C (green) and 2.0 °C (red) flat-top bandwidth. Here the efficiencies have been scaled relative to those of 5 mm, 3.3 mm and 2.5 mm QPM devices respectively, with these material lengths offering equivalent bandwidths.

time but at the expense of the simulation being far from exhaustive. However, the results obtained are likely to be indicative of the general trend with a higher resolution investigation only improving on the obtained efficiencies. For this investigation the sample lengths have been limited to a maximum of 40 mm and a minimum set by the device length of uniform QPM providing equal bandwidth. In this case this is 2.5 mm, 3.33 mm and 5 mm for bandwidths of 2 °C, 1.5 °C and 1 °C respectively.

The results of these final set of simulations are shown in Figure 3.10. Here it is clear to see that for all three device bandwidths there is a threshold device length below which no efficiency advantages over short lengths of uniform QPM material are obtained. To provide comparable bandwidths to such uniform devices the sinc like structures have adopted a very simple quantised pattern, with the number of quantisation levels reduced to two and a single oscillation of the sinc function utilised. The result of this is simply a small section of uniform material, centrally located, equal in length to the standard uniform devices.

However, above a certain device length, which is dependent on the desired flat-top bandwidth, significant optical conversion efficiencies can be gained over the uniform devices. At these extended device lengths the number of available domains has increased to the point that relatively complex sinc like nonlinearity structures can be formed without overly compromising on device efficiency. It is clear from these results quite how significant an efficiency enhancement can be obtained using these complex structures, with efficiency gains of between 400 and 800% over uniform devices achievable with 40 mm long devices. As indicated earlier, in Figure 3.9,

the greater the desired bandwidth the more dramatic the efficiency enhancements that can be obtained.

## 3.5 Experimental Results

It has been theoretically demonstrated that deleted domain sinc like $d_{eff}$ based QPM devices can provide considerable bandwidth increases over standard QPM devices whilst maintaining greater efficiency, with bandwidths more than 35 times as wide as equivalent length uniform devices and associated efficiencies 8 times that of equivalent bandwidth uniform devices. In order to verify both the flat-top bandwidth grating design procedure of deleted domains and phase-shifts and the new analytical modelling technique devices have been fabricated and optically tested.

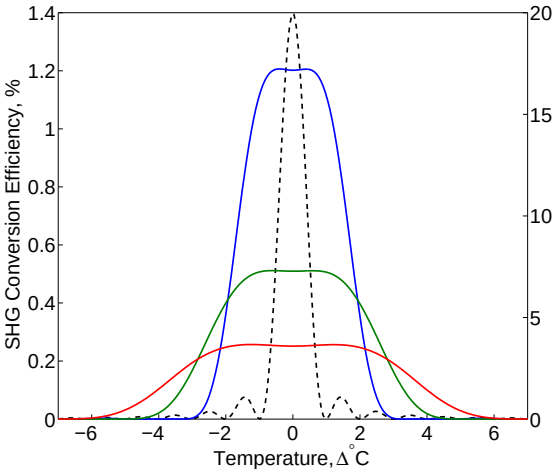


Figure 3.11: Theoretical harmonic conversion efficiency plots for the fabricated 20 mm long sinc structured PPLN based devices, for generating 532 nm harmonic radiation, with changing operating temperature. Flat-top bandwidths of 1.7 °C (blue), 2.8 °C (green) and 4.3 °C (red) are achieved, which compare with a 0.26 °C 95% stability bandwidth for a standard 20 mm uniform PPLN device.

The fabricated devices are based on a 20 mm long section of nonlinear material, in this case $LiNbO_3$, and have been designed to provide temperature stable visible harmonic power at a wavelength of 532 nm, with this wavelength being of considerable interest in display applications. In this material and at this wavelength the QPM period is 6.53 $\mu$m providing over 6000 polarisation inversion domains with which to design suitable sinc like grating structures. Three structures have been designed providing progressively wider flat-top bandwidths, the temperature tuning responses of which are shown in Figure 3.11. Also shown in this figure is the temperature tuning bandwidth of a standard 20 mm PPLN based structure, it must be noted that the sinc structured

and uniform devices are not plotted on the same vertical axis providing greater clarity of the bandwidth enhancement. For comparison the 95% stability bandwidth of a 20 mm section of uniform PPLN (black dotted) is 0.255 °C and for the sinc structured devices the flat-top bandwidths are 1.7 °C (blue), 2.8 °C (green) and 4.3 °C (red). These grating designs were fabricated early on in the course of this work and as such have considerably lower efficiencies for their given bandwidths compared to the results of Figure 3.9 which were obtained through a more exhaustive investigation of parameters. Despite the low efficiencies such designs are still useful for validating the simulation and design techniques.

### 3.5.1 Device Fabrication

As stated above the complex devices are manufactured in $LiNbO_3$ and have been fabricated using standard E-field poling techniques highlighted in Chapter 2. At the wavelengths specified the individual poled domain size is only 3.26 $\mu$m, a relatively small size for high yield, large scale devices. As such it becomes clear that the bandwidth broadening technique utilised for these devices is essential for maintaining high quality fabricated devices. Unlike alternative techniques which have varying poled domains which can be fractions of the ideal phase-matching domain size [26, 27], the technique utilised in this work sets the poled domain size as constant. This greatly simplifies photolithography mask design, the photolithography steps and the electric field fabrication process, where no special care must be taken to ensure a uniform growth rate of the poled domains.

An image of the narrowest bandwidth fabricated device is shown in Figure 3.12. Here the device was fabricated using standard electric field poling techniques where a high voltage, $\sim 21\,\mathrm{kVmm^{-1}}$, is applied to a photolithography defined electrode pattern to achieve domain inversion in 500 $\mu$m thick $LiNbO_3$. Prior to imaging the poled structure has been etched in 48% HF acid which highlights the poled domains due to a preferential etch rate between poled and un-poled regions. This image is a composite of 32 separate microscope images showing all the poled domains within the device (grey background), here the banding across the final image is due to uneven lighting in the microscope's field of view and is not a physical effect. Also shown in this image are the ideal domain positions as determined by the photolithographic mask (white background). As can be seen almost perfect poling is achieved, with only a few domains merging due to the application of an overly long duration high voltage pulse. Where the pulse duration determines the area of inverted crystal.

This particular grating is based on a 10 level quantised sinc function with a width of $\pm 2\pi$. For clarity the grating image has been truncated to include only the poled domains, where at the

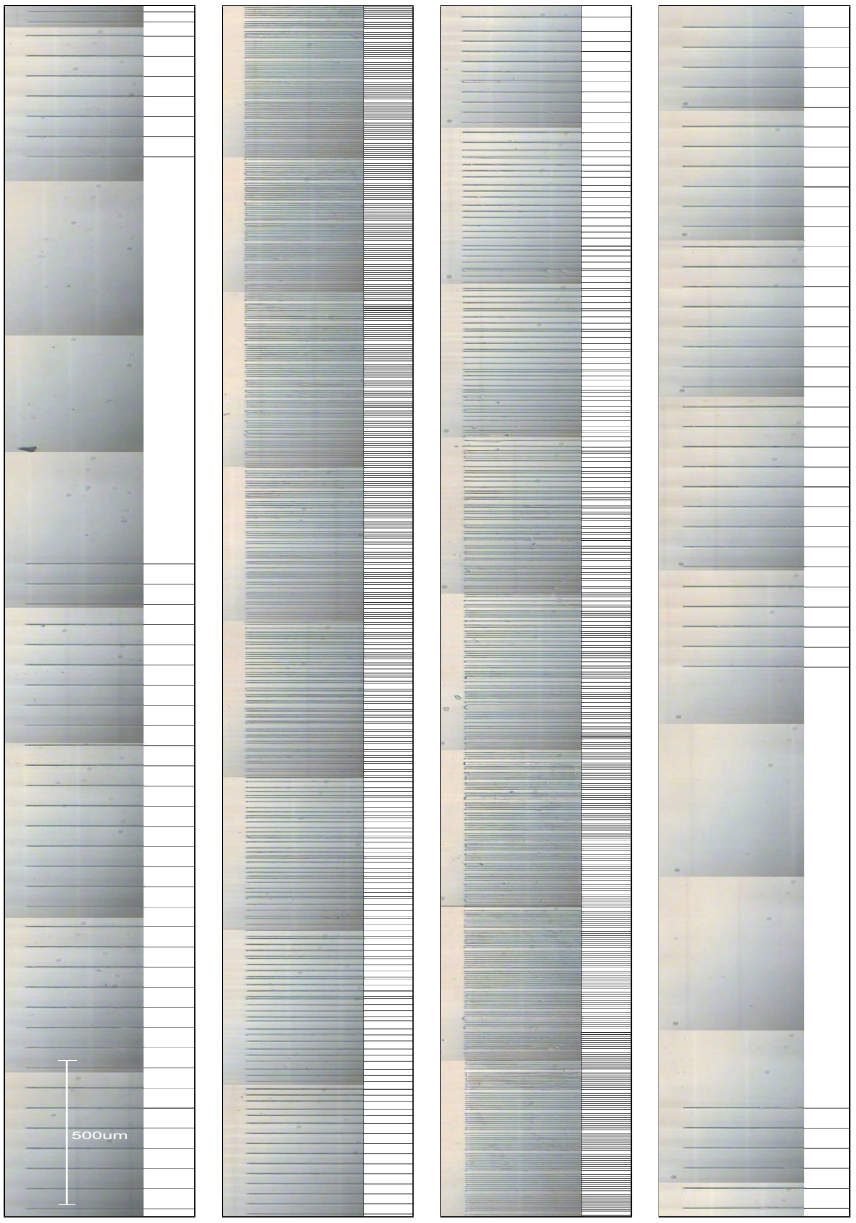


Figure 3.12: Composite microscope image (grey background) of a single electrically poled, acid etched PPLN grating designed for flat-top temperature tuning power output. Here the grating is structured such that the variation of $d_{eff}$ corresponds to a sinc function quantised into 10 levels. The nominal period is 6.51 $\mu$m suitable for the harmonic generation of green laser light at 532 nm. Also shown is the ideal theoretical position and size of the poled domains (white background). Note the four images are different sections of one physical grating, with the single grating reformed by stacking the images end to end from left to right.

extents of the device large regions of bulk un-poled material occur. By stacking the four images end on end, working from left to right, the domain density can be seen to represent the function $\mathrm{sinc}\,(x)$ for $x = -2\pi \ldots 2\pi$. Where a low domain density occurs at the two ends representing the low negative value of the first sinc side lobe, here there is of course a $\pi$ phase shift in the domain positions although this cannot readily be verified through visual inspection. Additionally, at the device centre it is clear that the poling density is greatly increased becoming like that of standard uniform QPM. It should be noted that in this early design a slight error was made converting the desired $d_{eff}$ into grating density, where due to a rounding error at the peak of the sinc function a domain density of only 90% not the optimal 100% is achieved. This error however was carried through to the device modelling and as such does not change the expected flat-top temperature tuning response.

### 3.5.2 Optical testing

With the flat-top bandwidth devices fabricated optical testing was undertaken to characterise the temperature tuning harmonic power variation. For this characterisation the fabricated devices were mounted in a temperature controlled oven capable of controlling the temperature to within 0.1 °C at an elevated temperature of approximately 180 °C. Here the high temperature ensures low loss operation of the devices, where at lower temperatures effects such as photorefractive damage can reduce harmonic output power over time [36, 37]. Further, a 1064 nm Nd:YAG laser was polarised and focused into the centre of the device with the resulting harmonic and residual fundamental beams collimated on exit. To separate the two beams and allow accurate readings of the harmonic power variation a dispersive prism was used providing physical separation, with this separation enhanced through a large propagation distance prior to measurement. The measurement is performed using a low-pass filtered amplified silicon photodetector in conjunction with a lock-in amplifier. Here the lock-in amplifier provides a large dynamic range of measurements which is essential for detecting both the large peak harmonic signal from a reference 20 mm PPLN grating and the much lower signal of the wide bandwidth device. Measurements of both harmonic power and device temperature are recorded using data acquisition software whilst the oven temperature was allowed to gradually reduce from a steady state at approximately 200 °C down to 160 °C, with the optimal phase-matching temperature at 180 °C.

#### Multi longitudinal mode laser results

For the initial characterisation a 100 mW Nd:YAG laser was used as the fundamental pump source. However, this particular laser had no active control of the laser cavity and as such

operated with multiple longitudinal modes spread across a relatively wide wavelength range. The effect of these multiple modes can be seen in Figure 3.13 which shows the temperature tuning response of both a uniform 20 mm PPLN device (blue) and that of sinc structured wide bandwidth device (green).

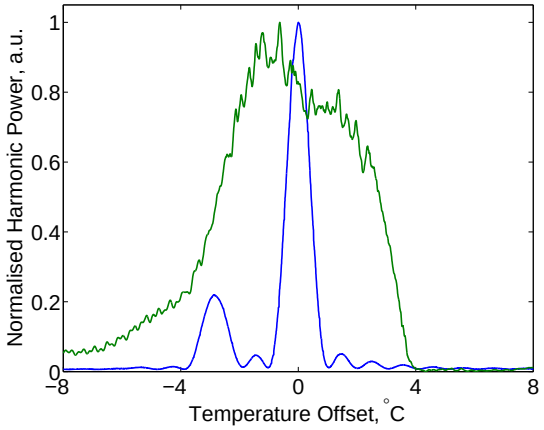


Figure 3.13: The measured harmonic output power for variations in operating temperature for both a uniform 20 mm long PPLN device (blue) and a sinc structured flat-top bandwidth device (green). Here the tuning curves exhibit significant asymmetry as the result of the pump laser having multiple longitudinal modes, where the modes undergo sum frequency generation and phase-match efficiently at temperatures offset from the central peak.

It is clear from the plot of the harmonic power of the uniform device that a significant additional mode at a lower wavelength exists, which phase-matches at a lower temperature than the dominant mode of the laser cavity. This additional wavelength has minimal effect on the central bandwidth of the sinc squared tuning response of the uniform device and as such is usually of little concern. However, if mode hopping occurs the harmonic power can fluctuate wildly as the fundamental power alternates between phase-matched and un-phase-matched wavelengths.

In addition to the harmonic power fluctuations a further effect caused by multiple longitudinal modes that is detrimental to the performance of the wide bandwidth devices, and evident in Figure 3.13, is sum frequency generation. Here, if the spectral modes of the pump laser fall within the bandwidth of the flat-top devices complex parametric processes can occur between the modes, where the resulting conversion efficiency at temperature offsets can be higher than that of the main spectral mode due to a more favourable phase-matching condition. This is clear in the above figure, where for temperatures below the central phase-matching temperature a large efficiency increase can be seen which in turn leads to a reduction in the 'flat-top' bandwidth. As such it is clear that multi-longitudinal mode lasers are unsuitable both for testing purposes and

of course real applications of flat-top bandwidth devices, although further analysis of multi-mode sources is undertaken in Chapter 6.

### Single longitudinal mode laser results

With simple multi-longitudinal mode lasers proving unsuitable for accurately testing the temperature tuning bandwidth of the flat-top devices an alternative single longitudinal mode (SLM) laser was utilised. The laser was a purpose built grating stabilised ytterbium fibre-laser, kindly provided by Dr. Carl Farrell. The laser had an output power of approximately 60 mW with a linewidth below the measurable limits of the available equipment, but no greater than 0.01 nm, at a wavelength of 1063.7nm. As above the fundamental beam was focused into the crystal, with a spot size of approximately 30 $\mu$m, with the harmonic output further collimated and separated from the fundamental using a dispersive prism prior to detection on a silicon photodiode and lock-in amplifier. The measurement technique is as for the multi-mode laser, aside from the additional collimation of the fibre output.

The results of the harmonic power measurements of all three wide bandwidth grating structures are shown in Figure 3.14. By directly comparing the results of the flat-top device in Figure 3.13 with that of Figure 3.14(c), which show the measurements for the same physical device but with differing fundamental sources, it is clear to see that a significant reduction in asymmetry has been achieved by using a SLM fundamental laser source. Further by comparing the measured results with those predicted by the plane wave model it is clear that good agreement has been achieved, with the measured bandwidth matching well. This result is especially noticeable for the widest bandwidth device which demonstrates a flat-top bandwidth agreeing almost exactly with theory.

However, it is very noticeable in the results for the lower bandwidth device that despite using a SLM laser considerable asymmetry and variation along the flat-top still occurs, with the measured bandwidth deviating markedly from the theoretical plot. What is further clear from the measurements of all the devices is that the variation from the modelling is consistent with an increase in efficiency at temperatures below the central phase-matching temperature (alternatively this could be interpreted as a reduction in efficiency at temperatures above the central temperature but this is later shown to be incorrect). By now examining the temperature tuning power output of the reference uniform PPLN device, which has been measured using the exact same optical setup, it is clear that an asymmetry in the response is also present. Here as for the flat-top devices this asymmetry and deviation from plane-wave theory occurs at temperatures below the central phase-matching temperature.

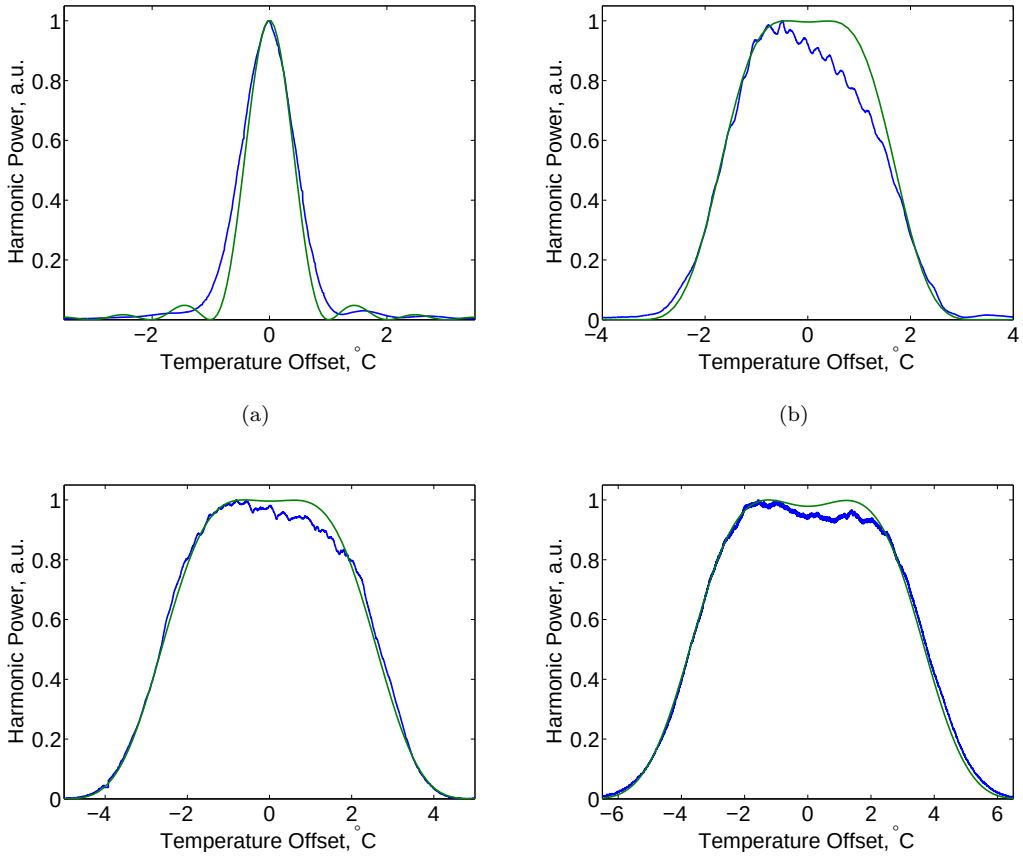


Figure 3.14: The measured harmonic power (blue), using a single longitudinal mode laser, for variations in device temperature for uniform 20 mm long PPLN (a) and deleted-domain flat-top bandwidth devices with 1.7 °C (b), 2.8 °C (c) and 4.3 °C (d) bandwidths. Also shown are the theoretical plane-wave tuning curves (green).

It has long been known that in focused parametric interactions the second harmonic power variation with changes of $\Delta$k does not exactly match the sinc squared tuning curve predicted by plane-wave theory, even assuming negligible pump depletion. It has been shown both theoretically [38] and experimentally [39] that with focusing an asymmetry occurs in the sinc squared $\Delta$k tuning curve, with the deviation from plane wave theory occurring for values below central phase-matching (where $\Delta k = k_{2\omega} - 2k_{\omega}$). This corresponds with the plot of Figure 3.14(a). This increased phase-matching efficiency at lower values of $\Delta k$ is commonly attributed to the angled k-vectors within the focused beam. Where the resultant sum of angled fundamental k-vectors is too short to efficiently phase-match with the grating at the peak operating temperature, with

these shortened resultant k-vectors only able to efficiently phase match with the grating as the temperature of the device is reduced.

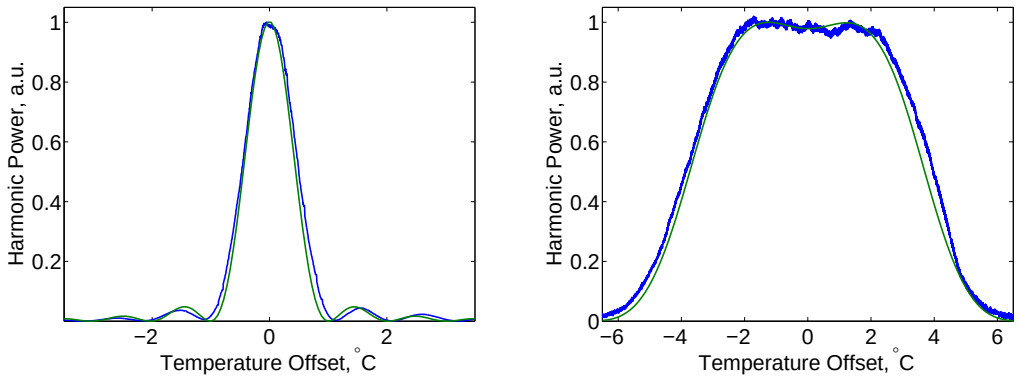


(a) (b)

Figure 3.15: Measured harmonic power (blue) for variations in operating temperature for both a 20 mm uniform PPLN device and a flat-top device with 4.3 °C bandwidth. Here the measurements are performed with a loosely focused fundamental beam, leading to symmetrical tuning responses, and have been compared with plane-wave theory (green).

By now applying this same reasoning to the flat-top bandwidth devices explanations for the measured asymmetry can be offered. Unlike for uniform PPLN devices, flat-top devices have sufficient bandwidth that the optimal phase-matching condition of the angled fundamental k-vectors falls within a region where high conversion efficiency can be obtained. Thus over a certain temperature range not only do the less angled k-vectors phase match efficiently, as they do for all temperatures across the flat-top, but now additional harmonic power is provided by the efficient phase matching of the angled beams. Of course this increased harmonic power provides a distortion to the flat-top temperature tuning response as is seen in the measured results.

A simple experiment can prove or disprove this assertion. By simply focusing the laser beam more loosely, with a larger spot size, the angular components of the beam reduce becoming more like that of simple plane-waves. Figure 3.15 shows the measured harmonic power of a uniform PPLN device and the widest bandwidth flat-top device using a loose focus fundamental beam. Here the fundamental spot size was increased until no asymmetry could be observed on the temperature tuning response of the uniform PPLN device. It is clear from the plot of Figure 3.15(b) that no asymmetry can be observed in the response of the flat-top bandwidth device, thus proving that the asymmetry seen earlier is an effect of focusing and not an inherent flaw within the device design or fabrication.

This asymmetry effect has not been previously reported in other wide bandwidth devices, this can be attributed to the vast majority of the experimental work on such devices being performed in waveguide structures in an effort to maintain high conversion efficiencies [11, 29]. Of course in waveguides, assuming single mode operation, the fundamental beam can be considered to be plane-wave and thus does not suffer from the same effects as these focused interactions. The devices shown here would equally prove suitable for use in waveguides, allowing them to achieve higher efficiencies than focused interactions for the same fundamental power.

Despite the high conversion efficiencies offered by waveguide based devices, the power handling capabilities of such structures are considerably lower than for bulk interactions where, due to the tightly confined mode, damage occurs at lower input powers. Thus for high power operation bulk devices are essential, with tight focusing essential to achieve efficient operation. However, as demonstrated focusing has a detrimental effect on the power stability of wide bandwidth devices designed using plane-wave simulation techniques. As such in the following chapters a thorough investigation into the effects of focused interactions on both standard uniform QPM structures and complex wide bandwidth sinc structured devices is undertaken with the aim of designing wide bandwidth devices suitable for high power, high efficiency harmonic generation.

## 3.6 Conclusions

In conclusion, in this chapter a novel analytic simulation technique for analysing second harmonic generation in quasi-phase matched structures has been presented. With this technique providing advantages over more common numerical integration techniques in terms of the accuracy of the simulations, the computational efficiency of the calculations and its simple application, with no additional complexity even as conversion efficiency approaches 100%.

Further, using this analysis technique a new type of temperature stable, constant power output QPM device has been designed and simulated, with these new devices providing a 35 fold increase in temperature acceptance bandwidth compared to equivalent length uniform QPM. At these wide bandwidths efficiencies almost an order of magnitude greater than comparable bandwidth uniform QPM devices can be obtained. These characteristic make such structures ideally suited for packaged frequency conversion modules, with the usually strict temperature stabilisation requirements for efficient operation significantly reduced. Here, the increased device stability can lead to simplifications in packaging, with less consideration to thermal insulation required to maintain a constant power output. Additionally, these wide bandwidths can be well matched to the linewidths of cheap laser diode sources, which tend to have wide spectral bandwidths, allowing higher conversion efficiencies to be obtained than with uniform QPM devices.

These devices also benefit from constant poled domain sizes, offering high yield upon fabrication.

Finally, these simulated devices have been fabricated and optically tested and have been shown to offer wide flat-top temperature bandwidths in line with those predicted by theory. Although some deviation in performance from the plane-wave model is evident a likely cause for this has been presented and has been further investigated in the following chapters.

# References


[1] S. Matsumoto, E. J. Lim, H. M. Hertz, and M. M. Fejer. Quasiphase-matched second harmonic generation of blue light in electrically periodically-poled lithium tantalate waveguides. *Electron. Lett.*, 27(22):2040–2042, 1991.

[2] A. Djupsjöbacka. Novel type of broadband travelling-wave integrated-optic modulator. *Electron. Lett.*, 21:908–909, 1985.

[3] C. S. Hong, J. B. Shellan, A. C. Livanos, A. Yariv, and A. Katzir. Broad-band grating filters for thin-film optical waveguides. *Applied Physics Letters*, 31(4):276–278, 1977.

[4] J. P. van der Ziel, M. Ilegems, P. W. Foy, and R. M. Mikulyak. Phase-matched second harmonic generation in a periodic GaAs waveguide. *Applied Physics Letters*, 29(12):775–777, 1976.

[5] T. Suhara, H. Tazaki, and H. Nishihara. Measurement of reduction in shg coefficient of $LiNbO_3$ by proton exchanging. *Electron. Lett.*, 25(20):1326–1328, Sept. 1989.

[6] M. A. Arbore, A. Galvanauskas, D. Harter, M. H. Chou, and M. M. Fejer. Engineerable compression of ultrashort pulses by use of second-harmonic generation in chirped-period-poled lithium niobate. *Opt. Lett.*, 22(17):1341–1343, 1997.

[7] G. Imeshev, M. A. Arbore, M. M. Fejer, A. Galvanauskas, M. Fermann, and D. Harter. Ultrashort-pulse second-harmonic generation with longitudinally nonuniform quasi-phase-matching gratings: pulse compression and shaping. *J. Opt. Soc. Am. B*, 17(2):304–318, Feb 2000.

[8] T. Kartaloğlu, Z. G. Figen, and O. Aytür. Simultaneous phase matching of optical parametric oscillation and second-harmonic generation in aperiodically poled lithium niobate. *J. Opt. Soc. Am. B*, 20(2):343–350, 2003.

[9] G.-D. Xu, Y.-y. Zhu, S.-n. Zhu, and N.-b. Ming. Simultaneous generation of efficient three-primary-colors by using focused Gaussian beams in an optical superlattice. *Opt. Commun.*, 223(1–3):211–218, May 2003.

[10] B.-Y. Gu, B.-Z. Dong, Y. Zhang, and G.-Z. Yang. Enhanced harmonic generation in aperiodic optical superlattices. *Applied Physics Letters*, 75(15):2175–2177, 1999.

[11] J. Huang, X. P. Xie, C. Langrock, R. V. Roussev, D. S. Hum, and M. M. Fejer. Amplitude modulation and apodization of quasi-phase-matched interactions. *Opt. Lett.*, 31(5):604–606, 2006.

[12] T. Suhara and H. Nishihara. Theoretical analysis of waveguide second-harmonic generation phase matched with uniform and chirped gratings. *IEEE J. Quantum Electron.*, 26(7):1265–1276, July 1990.

[13] T. Umeki, M. Asobe, Y. Nishida, O. Tadanaga, K. Magari, T. Yanagawa, and H. Suzuki. Widely tunable 3.4 $\mu$m band difference frequency generation using apodized $\chi^{(2)}$ grating. *Opt. Lett.*, 32(9):1129–1131, 2007.

[14] A. Tehranchi and R. Kashyap. Design of novel unapodized and apodized step-chirped quasi-phase matched gratings for broadband frequency converters based on second-harmonic generation. *J. Lightwave Technol.*, 26(3):343–349, 2008.

[15] A. Tehranchi and R. Kashyap. Engineered gratings for flat broadening of second-harmonic phase-matching bandwidth in MgO-doped lithium niobate waveguides. *Opt. Express*, 16(23):18970–18975, 2008.

[16] J. Amin, V. Pruneri, J. Webjörn, P. S. J. Russell, D. C. Hanna, and J. S. Wilkinson. Blue light generation in a periodically poled Ti:$LiNbO_3$ channel waveguide. *Optics Communications*, 135(1-3):41 – 44, 1997.

[17] S. Nagano, M. Konishi, T. Shiomi, and M. Minakata. Study on formation of small polarization domain inversion for high-efficiency quasi-phase-matched second-harmonic generation device. *Jpn. J. Appl. Phys.*, 42(7A):4334–4339, 2003.

[18] Y. Chen, W. Yan, D. Wang, S. Chen, G. Zhang, J. Zhu, and Z. Wei. Submicron domain inversion in Mg-doped $LiNbO_3$ using backswitched poling with short voltage pulses. *Appl. Phys. Lett.*, 90(062908), 2007.

[19] K. Mizuuchi, A. Morikawa, T. Sugita, and K. Yamamoto. Efficient second-harmonic generation of 340-nm light in a 1.4 $\mu$m periodically poled bulk MgO:$LiNbO_3$. *Jpn. J. Appl. Phys.*, 42(2A):L90–L91, 2003.

[20] R. L. Jungerman, C. A. Johnsen, D. W. Dolfi, and M. Nazarathy. Coded phase-reversal $LiNbO_3$ modulator with bandwidth greater than 20 GHz at 1.3$\mu$m wavelength. *Electron. Lett.*, 23(4):172–174, 12 1987.

[21] M. Nazarathy, D. W. Dolfi, and R. L. Jungerman. Velocity-mis-match compensation in travelling-wave modulators using pseudorandom switched-electrode patterns. *J. Opt. Soc. Am. A*, 4:1071–1079, 1987.

[22] R. H. Barker. Group synchronizing of binary digital sequences. In *Communication Theory*, pages 273–287, 1953.

[23] J. Jedwab and S. Lloyd. A note on the nonexistence of Barker sequences. *Designs, Codes and Cryptography*, 2:93–97, 1992.

[24] M. Nazarathy and D. W. Dolfi. Spread-spectrum nonlinear-optical interactions: quasi-phase matching with pseudorandom polarity reversals. *Opt. Lett.*, 12(10):823–825, 1987.

[25] M. L. Bortz, M. Fujimura, and M. M. Fejer. Increased acceptance bandwidth for quasi-phasematched second harmonic generation in $LiNbO_3$ waveguides. *Electron. Lett.*, 30(1):34–35, Jan 1994.

[26] M. M. Fejer, G. A. Magel, D. H. Jundt, and R. L. Byer. Quasi-phase-matched 2nd harmonic-generation - tuning and tolerances. *IEEE J. Quantum Electron.*, 28:2631–2654, 1992.

[27] Z. Xianglong, C. Xianfeng, W. Fei, C. Yuping, X. Yuxing, and C. Yingli. Second-harmonic generation with broadened flattop bandwidth in aperiodic domain-inverted gratings. *Opt. Commun.*, 204:407–411, 2002.

[28] K. Mizuuchi, K. Yamamoto, M. Kato, and H. Sato. Broadening of the phase-matching bandwidth in quasi-phase-matched second-harmonic generation. *IEEE J. Quantum Electron.*, 30(7):1596–1604, Jul 1994.

[29] K. Mizuuchi and K. Yamamoto. Waveguide second-harmonic generation device with broadened flat quasi-phase-matching response by use of a grating structure with located phase shifts. *Opt. Lett.*, 23(24):1880–1882, 1998.

[30] J. A. Armstrong, N. Bloembergen, J. Ducuing, and P. S. Pershan. Interactions between light waves in a nonlinear dielectric. *Phys. Rev.*, 127(6):1918–1939, 1962.

[31] W. H. Press, S. A. Teukolsky, W. T. Vetterling, and B. P. Flannery. *Numerical recipies in C*. CAMBRIDGE UNIVERSITY PRESS, 1992.

[32] K. Rustagi, S. Mehendale, and S. Meenakshi. Optical frequency conversion in quasi-phase-matched stacks of nonlinear crystal. *IEEE J. Quantum Electron.*, QE-18(6):1029–1041, 1982.

[33] J. M. Manley and H. E. Rowe. Some general properties of non-linear elements. *Proc. Inst. Radio Engrs.*, 44(7):904–913, July 1956.

[34] D. Eimerl. High average power harmonic generation. *IEEE J. Quantum Electron.*, QE-23(5):575–592, 1987.

[35] D. Eimerl. Quadrature frequency conversion. *IEEE J. Quantum Electron.*, 23(8):1361–1371, 1987.

[36] A. Ashkin, G. D. Boyd, J. M. Dziedzic, R. G. Smith, A. A. Ballman, J. J. Levinstein, and K. Nassau. Optically-induced refractive index inhomogeneities in $LiNbO_3$ and $LiTaO_3$. *Appl. Phys. Lett.*, 9(1):72–74, 1966.

[37] L. Pálfalvi, J. Hebling, G. Almási, and K. Polgár. Refractive index changes in Mg-doped $LiNbO_3$ caused by photorefraction and thermal effects. *J. Opt. A-Pure Appl. Opt.*, 5:S280–283, 2003.

[38] G. D. Boyd and D. A. Kleinman. Parametric interaction of focused Gaussian light beams. *J. Appl. Phys.*, 39(8):3597–3639, 1968.

[39] D. A. Kleinman and R. C. Miller. Dependence of second-harmonic generation on the position of the focus. *Phys. Rev.*, 148(1):302–312, Aug 1966.

# Chapter 4

# Improved SHG Efficiency from Focussed Gaussian Beams

## 4.1 Introduction

High conversion efficiency is an essential requirement if the widespread deployment of nonlinear laser sources is to be achieved, with nonlinear interactions being the only viable route towards the generation of some highly desired laser wavelengths. For example the generation of high intensity pure green laser light for display purposes is impossible to directly achieve with known semiconductor materials [1], with second harmonic conversion being the only viable alternative. As was discussed in Chapter 2, many factors determine the conversion efficiency of a harmonic process, such as the magnitude of the nonlinear coefficients, interaction lengths, phase-matching and fundamental input intensity. In this chapter attention shall be given to the focused confinement of laser beams, specifically Gaussian beams, to increase laser intensity and thus the harmonic conversion efficiency. Although the alternative technique of nonlinear waveguide interactions can offer tighter confinement, and thus higher efficiency for a given power, bulk focussed interactions provide a large device aperture, which in contrast to the tight confinement in waveguides allow much greater power handling capabilities before intensity dependent damage occurs.

Studies into the effects of focussing on nonlinear interactions were carried out shortly after the initial experimental evidence for optical harmonic processes. The first theoretical work comprised of the study of finite parallel beams under the effects of double refraction in the near field [2], which followed on from the prior experimental works showing a link between focussed spot size and SHG conversion efficiency [3, 4]. Further work considered the situation of very tight focus,

where the nonlinear device length ($L$) is significantly greater than the confocal parameter ($b$), noting that at such extreme focus the $\Delta k$ phase-matching parameter for optimum efficiency does not correspond to the condition of $\Delta k = 0$ [5].

However, neither the work on very tight or loose focussing can suitably predict the conditions required for optimal focused efficiency. Not until 1968 would a rigourous analysis, by Boyd and Kleinman [6], provide expressions for the harmonic conversion process for the general case of arbitrary focussing, which would show that there is an optimum focusing ratio between the confocal parameter and nonlinear device length. This work further went on to show that in the case of extreme tight or loose focussing the analysis could be reduced to that of the previous studies.

In this seminal paper it was shown that for the case of second harmonic conversion assuming no walk-off, as is the case for non-critical birefringently phase-matched or standard QPM processes, an optimum focussing ratio of $\xi = L/b = 2.84$ gave peak conversion efficiency for any device length. This ratio can be thought of a compromise between the high intensities generated at tight focussing and the corresponding reduction in effective interaction length due to a short confocal parameter. Further, through their extensive analysis they were able to show that as the focus is tightened significant asymmetry can be observed on the sinc profile $\Delta k$ phase-matching tuning curve and, like in the previous works, that this was accompanied by a shift in the phase-matching conditions for optimal conversion efficiency.

In this chapter a rigourous analysis of focussed SHG interactions is undertaken, following the notation in [6], showing that the optimal focussing conditions determined by Boyd and Kleinman are only valid for linearly invariant nonlinear materials. By extending the analysis it shall be shown that improvements on the theoretical conversion efficiency can be achieved with the use of a nonlinear phase-matching condition. Here, the improvements are obtained through the compensation of a spatially varying phase advancement, known as the Gouy phase which is inherent to all focused waves, that acts to de-phase the interacting waves and thus prevent perfect phase-matching. Further, an expression defining the domain position for a suitably modified QPM structure is given. It shall also be shown, in addition to improvements in conversion efficiency, that compensation of the Gouy phase leads to a return to the symmetrical phase-matching tuning response and a shift in the peak phase-matching $\Delta k$ back to that of plane wave interactions.

This theoretical endeavour shall further be verified through experimental measurements on the temperature tuning characteristics of suitably modified QPM grating structures, designed for second harmonic generation under a range of focussing conditions, showing the return to

symmetry and a shift in phase-matching temperature, equating to a shift in peak $\Delta k$.

## 4.2 Gaussian beam interactions in a nonlinear media

In this analysis a complete mathematical representation of the process of second harmonic generation with Gaussian beams is undertaken building on and updating the work of Boyd and Kleinman. However, for brevity the effects of double refraction are ignored, having no role to play in the process of quasi-phase-matching, in addition absorption is also neglected. Starting with the assumption of a single mode $\mathrm{TEM}_{00}$ Gaussian beam the fundamental spatially varying electric field can be defined as

$$E_{\omega}\left(r,z,t\right)=\frac{E_{0\omega}}{2}\frac{w_{o}}{w\left(z\right)}e^{\frac{-r^{2}}{w^{2}(z)}}e^{i\Psi(z)}e^{-i\Phi(z)}e^{i(k_{\omega}z-\omega t)}+c.c. \tag{4.1}$$

with the following further definitions,

$$w\left(z\right) = w_{0}\left[1+\left(\frac{\lambda z}{\pi w_{0}^{2}n_{\omega}}\right)^{2}\right]^{1/2} \tag{4.2}$$

$$\Psi\left(z\right) = \frac{kr^{2}}{2z\left[1+\left(\frac{\pi w_{0}^{2}n_{\omega}}{\lambda z}\right)^{2}\right]} \tag{4.3}$$

Here, $E_{0\omega}$ is the peak electric field amplitude, $w\left(z\right)$ is an expression for the beam radius at a distance $z$ from the focus, $w_0$ is the focused spot size, $\lambda$ is the fundamental wavelength, $\Psi\left(z\right)$ defines the phase curvature of the wave-fronts and $\Phi\left(z\right)$ is an expression for the variation in phase front position along the length of the focussed beam known as the Gouy phase.

Before proceeding with the analysis it is useful at this point to clarify the role of the Gouy phase and the physical mechanisms for its existence. The Gouy phase shift is an inevitable consequence of any focused wave interaction, resulting in an advancement of the position of the fronts of constant phase in the wave. The Gouy phase has been experimentally observed in many situations from the initial studies in 1890 [7], to more modern techniques such as observations of carrier wave phase slippage in femto-second pulses [8] and the use of interferometers, with a focusing lens in one arm, to observe interference fringe variation upon focussing [9]. Additionally, the Gouy phase shift has a bearing on laser operation, with the phase advancement responsible for different resonant frequencies for various modes of oscillation [10], with the Gouy phase of higher order modes advancing more rapidly and further than lower order modes.

For a spherically focussed single mode wave the phase advancement has a value of $\pi$ radians, for a cylindrically focussed wave this value reduces to $\pi/2$, with the advancement occurring as the wave propagates from $-\infty$ to $\infty$ through a focused waist. For the case of Gausian beams,

as is seen most commonly in laser systems, the phase advancement can be described as

$$\Phi(z) = (m+n+1)\arctan\left(\frac{\lambda z}{\pi w_0^2 n}\right) \tag{4.4}$$

where $m, n$ reference the Hermite-Gaussian mode order.

Many theories have been presented for the origin of this phase advancement, such theories include simple geometrical properties of Gaussian beams [11], although this theory is incomplete being unable to account for the reduced phase shift seen in cylindrically focused beams, quantum geometric theories have also been proposed [12]. However, the Gouy phase shift is observable in all waves, including mechanical waves, so it would seem a quantum theory is not necessary. A recent proposal put forward considers the effect of transverse confinement and the influence of the uncertainty principle on the spread of transverse momenta within the wave [13], this relatively simple mechanism is valid for both spherical and cylindrically focussed waves and is equally applicable to quantum or classical waves.

Returning now to the nonlinear analysis significant simplifications can be made to Equation 4.1 with the following definitions;

$$\zeta = \frac{z}{z_R} = \frac{\lambda z}{\pi w_0^2 n_\omega} \tag{4.5}$$

$$e^{-i\Phi(z)} = \frac{1-i\zeta}{\sqrt{1+\zeta^2}} \tag{4.6}$$

here $z_R$ is the Rayleigh range and Equation 4.6 is obtained from the substitution of Equation 4.4. With the above substitutions Equation 4.1 can be re-written, with some rearranging, as

$$E_\omega(r,z) = \frac{E_{0\omega}}{2}\left(\frac{1}{1+i\zeta}\right) e^{\frac{-r^2}{w_0^2(1+i\zeta)}} e^{ik_\omega z} \tag{4.7}$$

To provide complete generality $\zeta$ is further replaced by $\tau$ to allow freedom in the positioning of the focused waist within the nonlinear device, with $\tau$ defined as

$$\tau = \frac{2(z-f)}{b} \tag{4.8}$$

Where $b = 2z_R$ is the confocal parameter and $f$ is the position of the focus. However, it was shown in [6] that for the case of zero loss it is always optimal to locate the focal position at the centre of the nonlinear device.

From the compact definition of the fundamental electric field in Equation 4.7 it is now possible to generate an expression for the induced polarisation. Using the same notation as in Equation 2.25 the following definition is obtained,

$$P_{2\omega}^{(2)}(r,z) = \frac{\epsilon_0}{2}\chi^{(2)}(2\omega;\omega,\omega)\left|E_\omega(r,z)\right|^2 \tag{4.9}$$

$$= \frac{\epsilon_0}{2}\chi^{(2)}(2\omega;\omega,\omega)E_{0\omega}^2\left[\frac{1}{(1+i\tau)}\right]^2 e^{\frac{-2r^2}{w_0^2(1+i\tau)}} e^{i2k_\omega z} \tag{4.10}$$

Now, to determine the generated harmonic wave in the far-field it is necessary to account for all point sources within the crystal and propagate their generated waves to the observation point $(x', y', z')$. By considering the nonlinear device as segments of infinitesimal length, $\mathrm{d}z$, it is possible to derive expressions for the incremental harmonic field from each of them, which can further result in the expression for total radiated harmonic field. The incremental field is described as

$$\begin{aligned} \mathrm{d}E_{2\omega}(r,z) &= i\frac{\mu_0 (2\omega)^2}{2k_{2\omega}} P^{(2)}_{2\omega}(r,z)\, e^{-ik_{2\omega}z}\mathrm{d}z \qquad (4.11) \\ &= i\frac{(2\omega)^2}{4k_{2\omega}c^2}\chi^{(2)}(2\omega;\omega,\omega)\, E_{0\omega}^2 \left(\frac{1}{1+i\tau}\right) e^{i2k_\omega z} \\ &\quad \times \left\{ \left(\frac{1}{1+i\tau}\right) e^{\frac{-2r^2}{w_0^2(1+i\tau)}} e^{-ik_{2\omega}z} \right\} \mathrm{d}z. \qquad (4.12) \end{aligned}$$

Here, it is noted that the bracketed expression in Equation 4.12 is in the form of a Gaussian wave, thus it can be assumed that it is this component of the field that propagates to the observer-ation point. This assumption has been proven valid with the use of Green's function analysis [5], furthermore for the more complex case of DFG and parametric amplification/oscillation Green's function analysis is an essential procedure with these modes of operation not enjoying the simplifications provided in SHG.

The simplification that makes the above assumption valid is that the focused spot size of the induced polarisation is, by nature of the SHG process, exactly $\sqrt{2}$ smaller than that of the fundamental. When this is combined with the generated harmonic field having twice the frequency of the fundamental it is found that both incident and generated waves have equal Rayleigh ranges. Thus, power will always flow from the fundamental to the harmonic in such a way as to preserve the Gaussian nature of the beams. However, it should be noted that if power transfers back from the generated harmonic field to the fundamental, through a phase-mismatch, distortions will occur to the Gaussian nature of the fundamental. This is due to the back-conversion process being DFG and therefore a mismatch in the mode overlap of the induced polarisation and the fundamental field arises, although at low powers this effect is insignificant resulting in negligible change to the Gaussian nature of the beams.

To obtain the final far-field harmonic power it is necessary to integrate over all the sources within the nonlinear material. Before the integration is carried out a change of co-ordinate system is required to ensure that only the Gaussian field expression in Equation 4.12 propagates to the observer. To achieve this $\tau$ is substituted, within the bracketed expression, for

$$\tau' = \frac{2(z'-f)}{b} \qquad (4.13)$$

resulting in a new expression for the incremental harmonic field outside the nonlinear material

$$\begin{aligned} \mathrm{d}E_{2\omega}\left(r',z'\right) &= i\frac{\left(2\omega\right)^2}{4k_{2\omega}c^2}\chi^{(2)}\left(2\omega;\omega,\omega\right)E_{0_\omega}^{\,2}\left(\frac{1}{1+i\tau}\right)e^{i2k_\omega z} \\ &\quad\times\left\{\left(\frac{1}{1+i\tau'}\right)e^{\frac{-2r'^2}{w_0^2(1+i\tau')}}e^{-ik_{2\omega}z}\right\}\mathrm{d}z \end{aligned} \tag{4.14}$$

Now, integrating over all sources within the material the following expression for the total generated harmonic field is obtained,

$$\begin{aligned} E_{2\omega}\left(r',z'\right) &= i\frac{\left(2\omega\right)^2}{4k_{2\omega}c^2}\chi^{(2)}\left(2\omega;\omega,\omega\right)E_{0_\omega}^{\,2}\left(\frac{1}{1+i\tau'}\right)e^{\frac{-2r^2}{w_0^2(1+i\tau')}} \\ &\quad\cdot\int_0^L\frac{e^{i\Delta kz}}{1+i\tau}\mathrm{d}z \end{aligned} \tag{4.15}$$

The final expression for the harmonic field in the far-field can be determined with the introduction of the limit

$$\tau'\to\infty. \tag{4.16}$$

With this assumption the Equation 4.15 can be greatly simplified by noting the following approximation,

$$\begin{aligned} \frac{1}{w_0^2\left(1+i\tau'\right)} &= \frac{\left(1-i\tau'\right)}{w_0^2\left(1+\tau'^2\right)} \\ &= \left[\frac{1-i\tau'}{w_0^2\tau'^2}\right]\left(1-\tau'^{-2}+\tau'^{-4}+\cdots\right) \\ \lim_{\tau'\to\infty} &\to \frac{1-i\tau'}{w_0^2\tau'^2} \end{aligned} \tag{4.17}$$

Further, with the following definitions,

$$s=\frac{x}{w_0\tau'},\qquad s'=\frac{y}{w_0\tau'} \tag{4.18}$$

it is possible to re-write the Gaussian power variation part of Equation 4.15 as

$$\frac{-2r'^2}{w_0^2\left(1+i\tau'\right)} \to -2s^2\left(1-i\tau'\right)-2s'^2\left(1-i\tau'\right) \tag{4.19}$$

Thus, the expression for the far-field harmonic field can be given as

$$\begin{aligned} E_{2\omega}\left(r',z'\right) &\to \frac{\left(2\omega\right)^2}{4k_{2\omega}c^2\tau'}\chi^{(2)}\left(2\omega;\omega,\omega\right)E_{0_\omega}^{\,2} \\ &\quad\cdot e^{-2\left(s^2+s'^2\right)\left(1-i\tau'\right)}\int_0^L\frac{e^{i\Delta kz}}{1+i\tau}\mathrm{d}z \end{aligned} \tag{4.20}$$

Now, with a change of variable in the integral in Equation 4.20, using $\tau=2\left(z-f\right)/b$ it is possible to obtain the following

$$\int_0^L\frac{e^{i\Delta kz}}{1+i\tau}\mathrm{d}z=\int_{\frac{-2f}{b}}^{\frac{2(L-f)}{b}}\frac{b}{2}\frac{e^{i\frac{\Delta kb\tau}{2}}e^{i\Delta kf}}{1+i\tau}\mathrm{d}\tau \tag{4.21}$$

With the introduction of the following variables,

$$\sigma = \Delta k b/2 \tag{4.22}$$

$$\xi = L/b \tag{4.23}$$

$$\mu = (L-2f)/L \tag{4.24}$$

this new integral can be simplified to

$$\frac{b}{2}e^{i\Delta k f}\int_{-\xi(1-\mu)}^{\xi(1+\mu)}\frac{e^{i\sigma\tau}}{1+i\tau}\mathrm{d}\tau \tag{4.25}$$

Further, following the procedure of Boyd and Kleinman an optimizable function $H(\sigma,\xi,\mu)$ is defined,

$$H(\sigma,\xi,\mu)=\frac{1}{2\pi}\int_{-\xi(1-\mu)}^{\xi(1+\mu)}\frac{e^{i\sigma\tau}}{1+i\tau}\mathrm{d}\tau \tag{4.26}$$

with this function providing a contraction in the notation of the far-field harmonic electric field:

$$E_{2\omega}(r',z')\rightarrow\frac{\pi b(2\omega)^2}{4k_{2\omega}c^2\tau'}\chi^{(2)}(2\omega;\omega,\omega)E_{0\omega}^2e^{-2\left(s^2+s'^2\right)\left(1-i\tau'\right)}e^{i\Delta k f}H(\sigma,\xi,\mu) \tag{4.27}$$

Note that the function $H(\sigma,\xi,\mu)$ has fewer degrees of freedom than that defined in [6], this is due to omitting the effects of absorption and double refraction. From these expressions a definition for the harmonic intensity distribution can be obtained.

$$\begin{aligned} I_{2\omega}(r',z') &= \frac{n_{2\omega}c\epsilon_0}{2}\left|E_{2\omega}(r',z')\right|^2 \\ &= \frac{n_{2\omega}c\epsilon_0}{2}\frac{\pi^2b^2(2\omega)^4}{16k_{2\omega}^2c^4\tau'^2}\chi^{(2)^2}E_{0\omega}^4\left|e^{-2(1-i\tau)\left(s^2+s'^2\right)}e^{i\Delta k f}H(\sigma,\xi,\mu)\right|^2 \\ &= \frac{(2\omega)^2}{32n_\omega^2n_{2\omega}c^3\epsilon_0\tau'^2}\chi^{(2)^2}P_\omega^2k_\omega^2e^{-4\left(s^2+s'^2\right)}\left|H(\sigma,\xi,\mu)\right|^2 \end{aligned} \tag{4.28}$$

Here, to obtain Equation 4.28, significant simplifications have been made with use of the following definitions,

$$P_\omega=\left(\frac{n_\omega c\epsilon_0}{2}\right)\left(\frac{\pi w_0^2}{2}\right)\left|E_{0\omega}\right|^2,\qquad w_0^2k_\omega=b \tag{4.29}$$

Finally, from this, an expression for the generated far-field harmonic power can be obtained by integrating over the intensity distribution

$$P_{2\omega}=\int\int_{-\infty}^{\infty}I_{2\omega}\mathrm{d}x\mathrm{d}y \tag{4.30}$$

But, first, it is important to note the change of variables introduced in Equation 4.18 resulting in a change of limits and integral variable

$$\mathrm{d}x=w_0\tau'\mathrm{d}\tau',\qquad \mathrm{d}y=w_0\tau'\mathrm{d}\tau' \tag{4.31}$$

$$P_{2\omega} = \frac{(2\omega)^2}{32n_\omega^2 n_{2\omega} c^3 \epsilon_0 \tau'^2} \chi^{(2)^2} P_\omega^2 k_\omega^2 w_0^2 \tau'^2 \int\int_{-\infty}^{\infty} e^{-4\left(s^2+s'^2\right)} \left|H\left(\sigma,\xi,\mu\right)\right|^2 \mathrm{d}s\mathrm{d}s' \quad (4.32)$$

$$= \frac{(2\omega)^2}{32n_\omega^2 n_{2\omega} c^3 \epsilon_0} \chi^{(2)^2} P_\omega^2 k_\omega b \int\int_{-\infty}^{\infty} e^{-4\left(s^2+s'^2\right)} \left|H\left(\sigma,\xi,\mu\right)\right|^2 \mathrm{d}s\mathrm{d}s' \quad (4.33)$$

To achieve the standard result, as given in [14], it is necessary to introduce a final function, $h\left(\sigma,\xi,\mu\right)$, which is commonly known as the Boyd and Kleinman focussing factor as discussed in Chapter 2. With this function defined as,

$$h\left(\sigma,\xi,\mu\right) = \frac{\pi^2}{\xi} \int\int_{-\infty}^{\infty} e^{-4\left(s^2+s'^2\right)} \left|H\left(\sigma,\xi,\mu\right)\right|^2 \mathrm{d}s\mathrm{d}s' \quad (4.34)$$

which, when substituted into Equation 4.33, provides the familiar result for total generated harmonic power as given in Equation 2.36

$$P_{2\omega} = \frac{(2\omega)^2}{32\pi^2 n_\omega^2 n_{2\omega} c^3 \epsilon_0} \left|\chi^{(2)}\left(2\omega;\omega,\omega\right)\right|^2 P_\omega^2 k_\omega L h\left(\sigma,\xi,\mu\right) \quad (4.35)$$

Where here it is again noted that the generated harmonic power is proportional to the nonlinear device length, not the quadratic length as is the case for plane wave interactions.

In their work, Boyd and Kleinman chose to optimise the focusing conditions for SHG through variation of the parameter $h\left(\sigma,\xi,\mu\right)$, which allows control of the phase matching conditions through the variable $\sigma$ and the focus waist position and size through $\mu$ and $\xi$ respectively. However, the assumption was made that the linear and nonlinear properties of the material were constant over the sample, resulting in the optimum focusing factor of $\xi = L/b = 2.84$ in the case of zero birefringence as is shown in Figure 4.1. It this this assumption that prevented the full optimisation of the focusing conditions, with a device of constant dispersion and nonlinearity unable to compensate for the phase slippage introduced by the Gouy phase.

Despite being unable to compensate for the deleterious effects of the Gouy phase Boyd and Kleinman did pursue studies into some of its more obvious effects, although never attributing these effects to it directly. In their studies it was shown that for increasingly tight focus the tuning response of a nonlinear device becomes increasingly asymmetric. For a loose focusing ratio of $\xi = 0.5$ it was shown that the response is almost that of a perfect sinc structure 4.2(a), but as the focus is tightened to a ratio of 2.84 significant asymmetries are observed along with a shift in the peak phase-matching condition, see Figure 4.2(b).

For weak focussing, $\xi \ll 1$, these results were obtained via a series expansion of the denominator in Equation 4.26. In the following analysis it will be shown that by spatially varying this denominator by using a carefully designed modified QPM grating structure, it is possible to completely negate the effects of the Gouy phase, achieving higher conversion efficiency at tighter focus in addition to a return to the symmetric sinc tuning response.

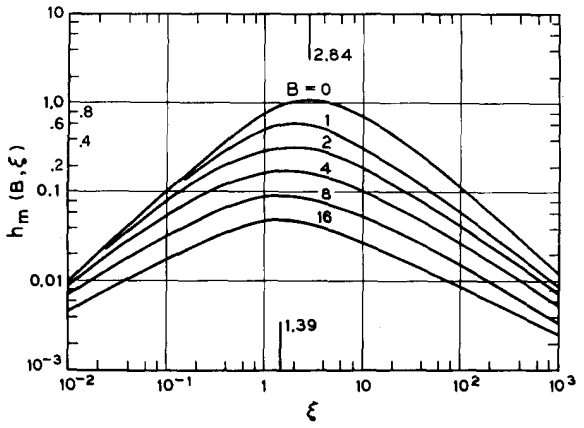


Figure 4.1: A plot of the magnitude of the focusing parameter h$(B, \xi)$, which is directly proportional to harmonic power, against the focusing ratio $\xi$. For the case of a linearly invariant material operating with non-critical birefringent phase-matching an optimum focus ratio of $\xi = 2.84$ is obtained. Figure from [6]

## 4.3 Compensating for the Gouy phase shift

In the proceeding analysis it was stated that the limiting factor on the conversion efficiency is the Gouy phase, which causes a phase slippage between the fundamental wave and the generated harmonic causing back conversion. However, without some minor modifications to the analysis it is difficult to see where the effects of the Gouy phase arise. To clarify this role it is necessary to re-write Equation 4.26 explicitly separating out the effects of the spatial phase variation, which can be achieved as follows

$$\begin{aligned} H(\sigma,\xi,\mu) &= \frac{1}{2\pi}\int_{-\xi(1-\mu)}^{\xi(1+\mu)} \mathrm{d}\tau \frac{e^{i\sigma\tau}}{1+i\tau} \\ &= \cdots \frac{e^{i\sigma\tau}}{1+i\tau}\cdot\frac{1-i\tau}{1-i\tau} \\ &= \cdots \frac{e^{i\sigma\tau}}{\sqrt{1+\tau^2}}\frac{1-i\tau}{\sqrt{1+\tau^2}} \end{aligned} \tag{4.36}$$

Here, it is clear to see, when compared with Equation 4.6, that the function H$(\sigma, \xi, \mu)$ has been separated into a term relating generated harmonic field with the scaled interaction length and a secondary term representing the Gouy phase. Explicitly solving this integral, for the simplistic case of $\Delta k = 0$, it is found that the function asymptotically approaches a value of $\pi$ for the case of $\xi \to \infty$. Where $\xi$ can approach infinity either through a reduction in spot size or an increase in the length of nonlinear media, although a lower limit on the value of $b$ is enforced through the paraxial approximation.

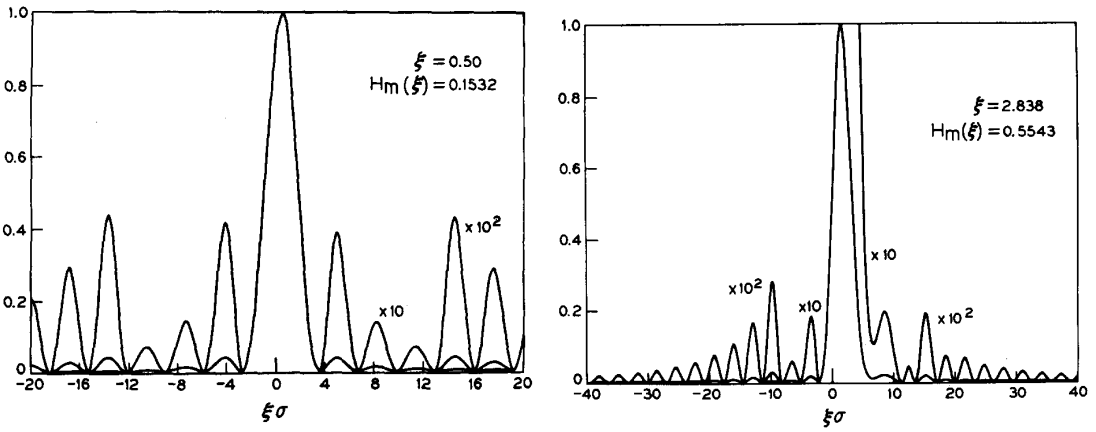


(a) (b)

Figure 4.2: (a) The $\Delta k$ tuning response, scaled with the focusing ratio, for loose focusing showing the sinc like structure observed under plane wave interactions. (b) Here, at optimal focusing conditions, significant asymmetry and peak phase-matching shift can be observed, both these effects are a result of the focused Gouy phase. Figure from [6]

It must be noted that although the function $\mathrm{H}(0, \xi, \mu)$ becomes constant for sufficiently tight focus, implying a conversion efficiency independent of increasingly tight focusing, this is counteracted by the reduction in Rayleigh range, the origins of which are clearly shown in Equation 4.25 and further emphasised in Equation 4.34. It is this scaling term that ultimately introduces a limit on the optimum focusing conditions. A plot of the variation in the magnitude of H with focusing parameter $\xi$ is shown in Figure 4.3 along with a plot of the resulting harmonic efficiency. Here, it is clear to see the asymptotic behaviour of the function H with increasing $\xi$, approaching a value of $\pi$. The reducing efficiency with tightening focus can be thought of physically as a shortening of the effective interaction length of the the high intensity focus, with the peak efficiency at $\xi = 1.4$ being a balance between the high intensities at the focused waist and a long interaction length.

However, as noted in the expansion of $H(\sigma, \xi, \mu)$ in Equation 4.36 the integral is highly dependent on the Gouy phase and as such it can be expected that removal of this term would lead to differing phase-matching conditions. When explicitly solving the integral above the simplification of constant $\Delta k = 0$ was made, it is this assumption that leads to the incorrect optimisation of the integral. To achieve the results outlined by Boyd and Kleinman it is necessary to optimise $\Delta k$ for each focus value, with this optimisation leading to the famous result of $\xi = 2.84$

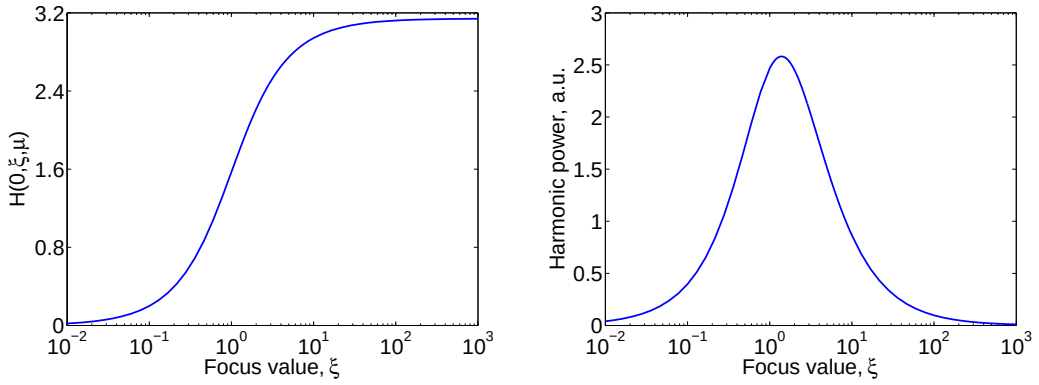


(a) (b)

Figure 4.3: (a) The theoretical variation in the magnitude of $H(0, \xi, \mu)$ for varying degrees of focusing at $\Delta k = 0$. (b) For constant phase-matching conditions, in this case fixed at $\Delta k = 0$, an optimum theoretical focused efficiency is obtained at $\xi \approx 1.4$

In their analysis Boyd and Kleinman took both the linear and nonlinear properties of the optical medium as fixed parameters with the only freedom allowed being the tuning of the total material dispersion, either by the application of heat, electric field or angle tuning. Using such a linear technique it is impossible to completely negate the phase advancement caused by the nonlinearly varying Gouy shift, with only a best fit correction being possible. Despite being only a partial compensation the results of this linear dispersion, and thus $\Delta k$ shift, are significant. Shown in Figure 4.4 are the curves of $H(\sigma, \xi, \mu)$ and harmonic power variation, as was plotted for the case $\Delta k = 0$, but here at each focus value $\Delta k$ has been optimised. As can be seen a large increase in power has been achieved, with the peak power now obtained at a tighter focus of $\xi = 2.84$.

An example of the Gouy phase and compensating linear dispersion phase required to achieve this peak efficiency is shown in Figure 4.5(a). It is necessary at this point to clarify what is meant by the dispersion phase, this is simply defined as the position advancement of a point on the coherence length of the dispersion tuned material compared with the same point on the coherence length of a perfect plane-wave interaction in the same material. Additionally, Figure 4.5(b) shows the phase errors that are still present for a range of focusing values despite best fit correction of the dispersion. As can be seen in plot (i) at very loose focus, here with a focus ratio of $\xi = 0.01$, their is negligible phase error after correction as at such loose focus the Gouy phase is to good approximation entirely linear and thus easily compensated for by a slight shift in operating conditions. However, as the focus is tightened to the optimal value

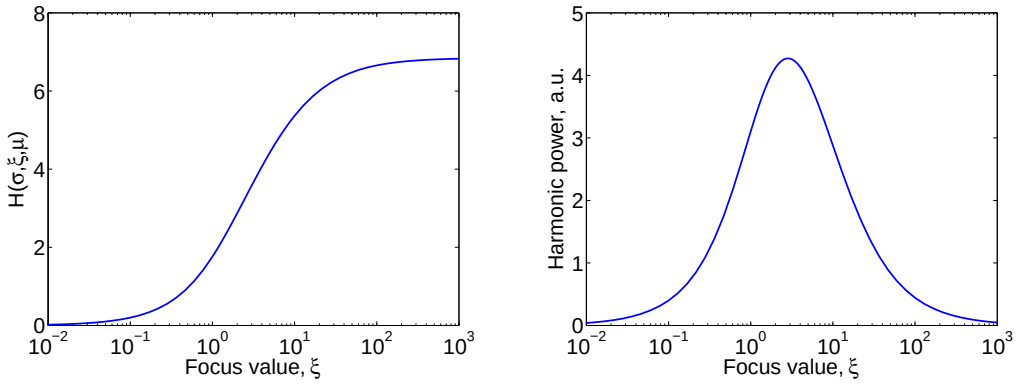


(a) (b)

Figure 4.4: (a) The theoretical variation in the magnitude of $H(\sigma, \xi, \mu)$ with focusing, here $\Delta k$ has been adjusted at each point for optimal efficiency. (b) With phase-matching optimised by a linear change in material dispersion peak harmonic power is obtained at $\xi \approx 2.84$.

of $\xi = 2.84$, as shown in plot (ii), significant phase errors are present with large regions of the focused interaction being far from phase-matched.

Physically, these phase errors are manifested in many ways that alter the expected response of focused parametric interactions. One of these effects highlighted by Boyd and Kleinman, and shown in Figure 4.2(b), is the asymmetric $\Delta k$ tuning response. Traditionally this effect has been attributed to a range of k-vector angles within the focused fundamental beam, with the z-direction resultant of two angled fundamental k-vectors matching with a shorter harmonic k-vector than in the non-focused case. This effect is explained diagrammatically in Figure 4.6, demonstrating the impossibility of the angled k-vectors combining to form a resultant longer than the unfocused vectors and thus preventing any variation from the sinc structure for $\Delta k > 0$. However, the alternative explanation given in this work can be expressed purely through the effects of the Gouy phase, although the Gouy phase and k-vector angle are intimately linked making either approach valid.

So, it is clear to see that to achieve perfect phase-matching for focused interactions it is necessary to compensate completely for the nonlinear Gouy phase shift. There are currently two known techniques to achieving such a result. One such method proposed concurrently but independently to the work detailed in this chapter is that of the formation of a spatially varying material dispersion, via application of localised temperature gradients [15], or via local application of electric fields to an electro-optic material. By carefully tuning the local dispersion to compensate for the Gouy phase shift perfect phase-matching should be achieved. However,

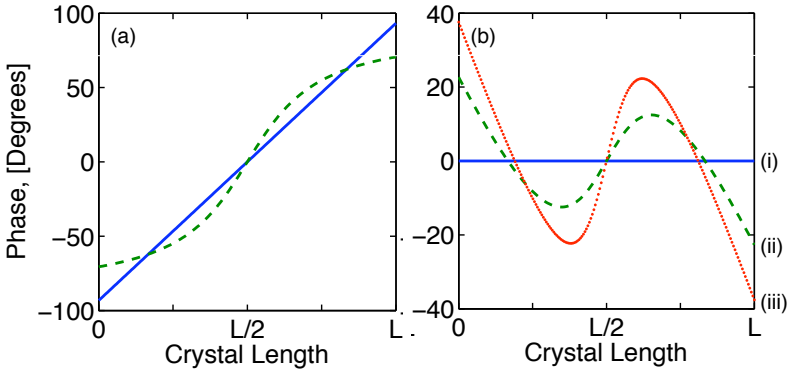


(a) (b)

Figure 4.5: (a) The theoretical plot of the Gouy phase of a focused beam (green) with a focus ratio of $\xi = 2.84$ and the best linear correcting phase achievable through adjustment of $\Delta k$. (b) A plot of the residual Gouy phase, after linear dispersion compensation, for focusing ratios of $\xi = 0.01$, 2.84 and 5.0 ( blue, green and red respectively).

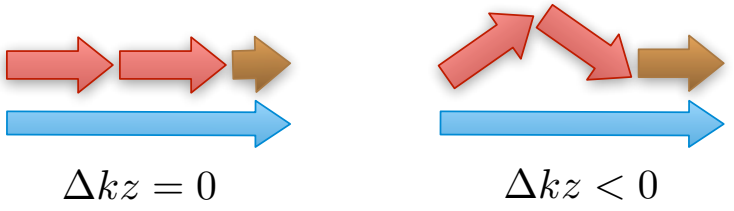


Figure 4.6: A representation of the k-vector angles in a QPM interaction for both plane-wave on axis propagation and for focused interactions where the k-vectors can be at an angle to the propagation direction, resulting in a shorter resultant k-vector. Here the grating k-vector must be enlarged in the focused case to allow adequate phase-matching.

this technique is for all intensive purposes impractical as controlling the temperature gradient through any useful thickness of material is highly challenging. Where, for example, in a sample of MgO(7%):$LiNbO_3$ variable control over a range of 0.5 °C is required along the length of the material with highly localised control to less than 0.1 °C necessary, which as is shown in Chapter 3 proves difficult to maintain in practical situations.

An alternative technique proposed in this work is the use of spatially modified effective nonlinearity, instead of a modified dispersion. Again, this process could be achieved through application of a localised electric field, this time interacting with a ferro-electric material. However, this technique is equally, if not more, difficult to implement with changes to both index and nonlinearity likely occurring. Instead, a much more robust technique is proposed that utilises

the power and flexibility of quasi-phase-matched (QPM) grating structures. Here it is proposed that by careful placement of the sections of re-oriented nonlinear polarisation, the positions of which traditionally only compensate for the phase mismatched caused by material dispersion, it should be possible to compensate for the Gouy phase allowing continuous addition of the generated harmonic wave.

This procedure can be expressed mathematically by returning to Equation 4.27 where here the nonlinearity, $\chi^{(2)}(-2\omega,\omega,\omega)$, is independent of $\tau$ and thus outside the optimisible function $H(\sigma,\xi,\mu)$. If however, the nonlinearity is now defined to be spatially varying with $\tau$ it can be taken inside the integral in $H(\sigma,\xi,\mu)$ and thus allows an extra term with which to negate the deleterious phase. From this a new function $H'(\sigma,\xi,\mu)$ is defined,

$$H'(\sigma,\xi,\mu) = \frac{1}{2\pi}\int_{-\xi(1-\mu)}^{\xi(1+\mu)} \frac{\kappa(\tau)\, e^{i\sigma\tau}}{1+i\tau}\mathrm{d}\tau \tag{4.37}$$

with $\kappa(\tau) = \pm\chi^{(2)}(\tau)$. Note that $\kappa(\tau)$ is a binary function, having only two values of nonlinearity relating to the direction of the local polarisation.

If initially the case of a plane-wave interaction is analysed, by allowing $\xi \to 0$, Equation 4.37 simplifies to the integral of the sinusoidally varying harmonic field along the crystal length. Using standard QPM this integral can be maximised by inverting the material nonlinearity at a period defined by the material dispersion to provide continuous growth of the second harmonic. This can be expressed mathematically as

$$\kappa(\tau) = \frac{\cos(\sigma\tau)}{|\cos(\sigma\tau)|} \tag{4.38}$$

This expression simply describes the standard form of a first-order QPM grating, where the nonlinearity is inverted with a frequency of $\Delta k$ corresponding to a period of $2\pi/\Delta k$.

For the more complex case of focused interactions, where $\xi$ is of the order 1.0 or greater, the Gouy phase is a significant factor that must be negated. This is achieved by adding a further term to the spatially varying nonlinearity which exactly cancels the Gouy term in Equation 4.37, this can be written as

$$\kappa(\tau) = \frac{\cos(\sigma\tau)}{|\cos(\sigma\tau)|} e^{i\tan^{-1}(\tau)} \tag{4.39}$$

Here, the spatially varying nonlinearity is simultaneously compensating for both the material dispersion and the nonlinear Gouy phase promoting continuous growth of the harmonic field. Of note here is that although the Gouy phase has been fully compensated it is however impossible to effectively compensate for the remaining term in the denominator of Equation 4.36. It is this term that accounts for the spatial variation in electric field along the axis of the focused beam due to diffraction, with a maximum value at $\tau = 0$ corresponding to the focused waist. Although

it is possible to further define the nonlinearity, $\kappa(\tau)$, to increase accordingly to compensate for this effect it is both counter productive, with best efficiency obtained by maximising the value of nonlinearity in all locations, and further impossible to achieve with standard QPM techniques.

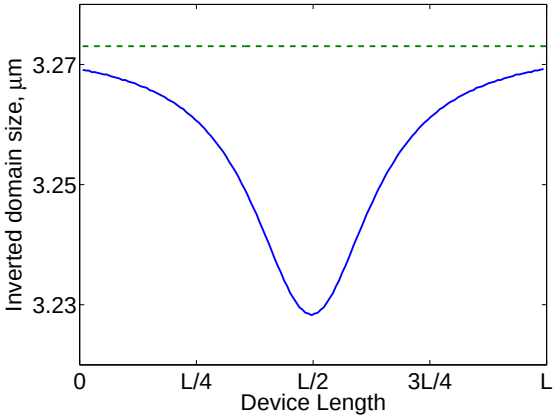


Figure 4.7: Inverted domain sizes for a 500 $\mu$m long, PPLN based, GQPM device (solid line), at a focus ratio of $\xi = 3.32$, compared with a standard QPM device (dashed line) for phase-matching the same interaction under plane-wave conditions with a phase-matching period of 6.548 $\mu$m.

Finally, by considering the complex conjugate of Equation 4.1 throughout the analysis, which for brevity has been ignored, a compact expression for the spatially varying nonlinearity can be defined as

$$\kappa(\tau) = \frac{\cos\left(\sigma\tau + \tan^{-1}[\tau]\right)}{\left|\cos\left(\sigma\tau + \tan^{-1}[\tau]\right)\right|} \tag{4.40}$$

Here, it is clear to see that for loose focusing values, where $\tau$ is large, the arctangent term has negligible effect simply offering a near linear phase offset in the QPM period. For tighter focusing the arctangent expression becomes highly nonlinear offering a more pronounced variation from the linear QPM grating structure. By directly comparing the dimensions of the inverted nonlinear polarisation sections of both QPM and Gouy adjusted QPM (GQPM) it is found that the period of the GQPM grating almost exactly matches that of standard QPM at either end of the device, only experiencing significant period alterations towards the centre.

For lengths of nonlinear material over 1mm in length and practical focusing conditions it is found that the variation in inverted section size and position is only of the order of a few nanometers compared with a standard QPM phase-matching the same nonlinear process. For more extreme focussing or very short device lengths the variation in inverted nonlinearity size becomes both large and rapid, an example of this is demonstrated in Figure 4.7 where the sizes of inverted nonlinearity have been calculated for a 500 $\mu$m long PPLN device and shown contrasted to the domain sizes in regular QPM.

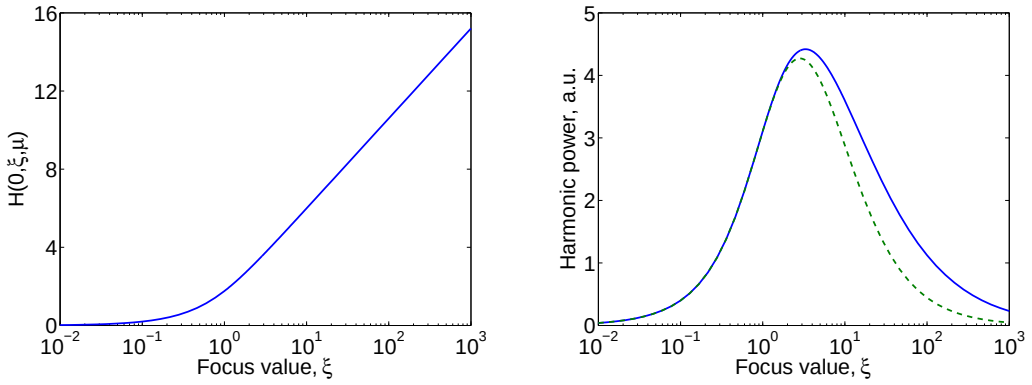


(a) (b)

Figure 4.8: (a) The variation in the magnitude of $H(\sigma, \xi, \mu)$ with focusing when the device nonlinearity is spatially varied to compensate for the Gouy phase. (b) With a Gouy compensated device (blue) peak harmonic power is obtained at the tighter focusing value of $\xi = 3.32$ providing 3.5% higher output power than linearly compensated devices (dashed green).

### 4.3.1 The advantages of Gouy compensated quasi-phase-matching

With a device structure suitable for compensating the deleterious effects of the Gouy phase it is now appropriate to analyse the theoretical benefits provided. Following on from the analysis of the harmonic efficiency verses focusing for a linearly Gouy compensated device the initial observation of a GQPM device is the higher efficiency that can be obtained. This result is perhaps unsurprising, with the corrected device providing a continuous forward transfer of power from the fundamental to the harmonic fields. As can be seen in Figure 4.8 for any focusing value a GQPM device will outperform a linearly compensated device, here it should be noted that at each focusing value a new GQPM device has been designed using Equation 4.40 to best match the resulting Gouy phase, with the linear QPM device $\Delta k$ tuned for optimum efficiency.

By analysing the response of the function $H(\sigma, \xi, \mu)$ for the GQPM structure, as shown in Figure 4.8(a), it is found that unlike for standard QPM devices the response is continuously increasing for tightening focus conditions. From this it is clear to see, when compared with Figure 4.3(a), the detrimental effect the Gouy phase has in uncompensated interactions. However, despite this continuous increase the final output power, Figure 4.8(b), is still limited to a peak conversion efficiency, this is due to the relatively slow increase in $H(\sigma, \xi, \mu)$ being surpassed by the more rapid reduction in Rayleigh range and thus lower average optical intensity as the focus is tightened.

Although the harmonic power has a peak focus efficiency, as is the case for standard QPM,

it is found that this peak is not at the famous $\xi = 2.84$ but at a tighter value of $\sim 3.32$. This result implies that the peak efficiency obtained for standard QPM and birefringent devices is not achieved at optimum power density along the length of the device but is in fact a compromise between the average power density and the detrimental effects of the Gouy phase shift de-phasing the fundamental and harmonic waves. Under such conditions the efficiency gain provided by tighter focusing, resulting from the higher electrical fields, is offset by the ever more nonlinear phase error creating a route for back conversion. In contrast, for a GQPM device the only limiting factor dictating optimal focusing conditions is the average power density. Further, at this tighter focusing value a gain in conversion efficiency over standard QPM devices is achieved, with the efficiency of a GQPM device at $\xi = 3.32$ being 3.5% greater than the efficiency of a standard QPM device at its peak at $\xi = 2.84$.

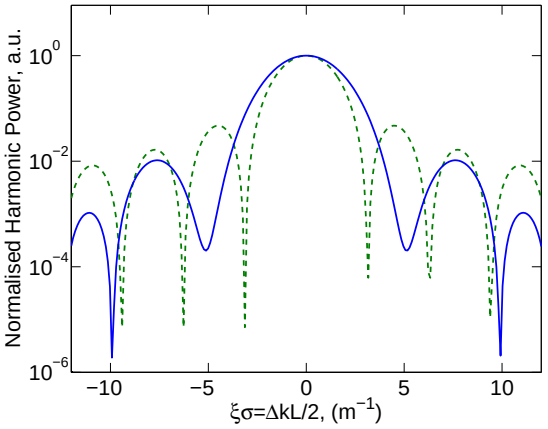


Figure 4.9: A plot of the normalised harmonic intensity for a sweep of $\Delta k$ values for both a GQPM device (solid line) and a plane-wave QPM interaction (dashed line). Unlike focused QPM the GQPM response is symmetric about $\Delta k = 0$, additionally the magnitude of the side lobes is reduced through an effective apodisation of the nonlinearity caused by the varying intensity along the focused beam axis.

An additional benefit of compensating the Gouy phase is the removal of any asymmetry in the $\Delta k$ tuning response, with this result being of particular use in synthesised response devices such as the wide-bandwidth flat-top temperature stable devices discussed in Chapter 3. Here, the Gouy phase introduced an unwanted asymmetry leading to power fluctuations on the otherwise flat-top tuning response. Figure 4.9 shows the $\Delta k$ tuning response of a GQPM device compared to that of a plane-wave device, with the normalised responses plotted on a logarithmic scale to highlight the excellent symmetry obtained. Note that any slight asymmetry observed in the depth of the sinc zeros is purely an artifact of rounding error and insufficient precision in performing the numerical integration of $H(\sigma, \xi, \mu)$. Here, it should be stressed that for such

figures of the calculated efficiency and phase-matching characteristics have been performed by numerical integration of the exact, low power, analytic expressions. In later chapters, Chapter 6, a fully numerical BPM model is applied to the case of high power analysis.

However, despite the excellent symmetry presented one obvious difference between the two plots is the wider bandwidth and partial suppression of the side lobes in the GQPM response. This change in bandwidth is purely related to the spatial variation in the fundamental power along the axis of the beam creating an effective interaction length shorter than that for the plane-wave interaction, with bandwidth being inversely proportional to device length [16]. Further, the side lobe suppression arises from the apodisation of the induced polarisation, caused again by the low intensity fundamental at the extremities of the device, which from standard Fourier analysis is well known to lead to a reduction in the frequency components in a signal and thus the magnitude of any side lobes.

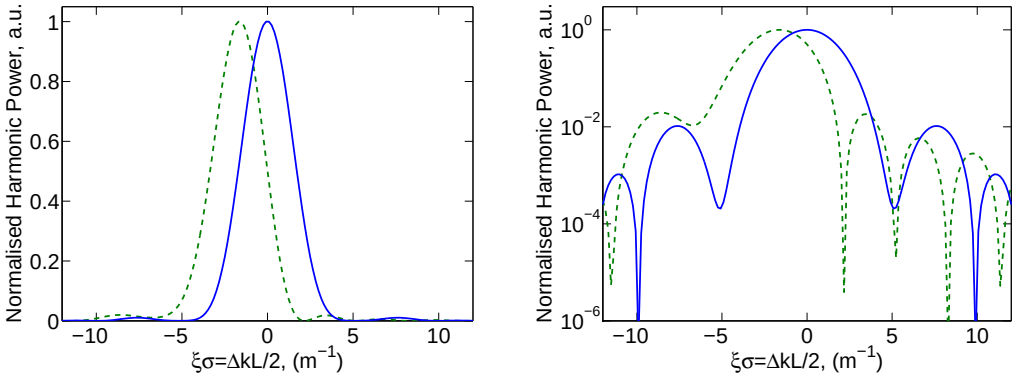


(a) (b)

Figure 4.10: Theoretical plots of the shift in phase-matching conditions for a uniform QPM device (green) operating at $\xi = 2.84$ relative to a GQPM device operating at $\xi = 3.32$ (blue), with the GQPM device phase-matching optimally at the plane-wave $\Delta k$ value. Also shown are the same data plotted on a logarithmic power scale highlighting the symmetric response in addition to the shifting phase-matching conditions.

Finally, the last observation after the removal of the Gouy phase influence is the return to plane-wave phase-matching conditions. As was discussed previously for standard QPM devices to achieve maximum efficiency the $\Delta k$ value of the nonlinear interaction must be carefully tuned, reaching maximum conversion efficiency when the difference between the nonlinear Gouy phase and the linear dispersive phase is minimised. The shift in the $\Delta k$ value is highly dependent on the focusing ratio, with tighter focusing or longer interaction lengths providing the larger shifts.

However, for the case of a GQPM device, when operating with a well matched focused beam, it is found that there is no offset in the $\Delta k$ value for peak focusing compared to that of a perfect plane-wave interaction. Figure 4.10 shows this effect clearly, here the standard QPM device operating at peak focusing of $\xi = 2.84$ has significant shift in the phase-matching position from the value predicted using plane-wave analysis. This is in contrast to the tuning response of the GQPM device, operating at its peak of $\xi = 3.32$, which has no shift in optimal phase-matching conditions from that of plane-wave devices. This lack of shift can of course be attributed to the complete compensation of the Gouy phase within the quasi-periodic grating structure, requiring no further adjustment through a change in the linear dispersion phase.

### 4.3.2 High order spatial modes and 3rd harmonic processes

At this point it is prudent to mention higher order spatial mode Gaussian beams and their effect on Gouy phase compensation. As noted in Equation 4.4 the Gouy phase of a Gaussian beam is highly dependent on the spatial mode-order, with multi-mode beams obtaining both a larger and more rapidly varying Gouy phase. Although not explicitly verified in this work, it can be readily extrapolated that by compensating for such additional phase advancements considerable performance gains can be made in the conversion of higher order modes, thus opening up the field of second harmonic generation to a wider range of laser sources.

Similar performance increases can be expected for higher order parametric mixing processes. For third harmonic generation, for example, it is readily accepted that high conversion efficiencies are prevented through a mismatch in the phases of the fundamental, second and third harmonic modes [17, 18]. This mismatch is of course attributable to the Gouy phase of the beams and with suitable compensation, through similar techniques as for SHG, it is expected that significant performance advancements can be accomplished.

## 4.4 Operational considerations for Gouy compensated QPM

Having described a procedure for effectively compensating the effects of the Gouy phase shift and highlighted some of the benefits gained through such a process it is useful to analyse the effectiveness of such a device in a real-world situation. This shall be achieved first by studying the effects of a non-optimal launch into the device followed by a study on the effects of errors in the size and position of the reversed nonlinear polarisation. For a basis of comparison these results shall be compared throughout with the results for standard QPM.

### 4.4.1 Sensitivity to non-optimal launch

There are two main factors that determine an optimal launch, these are position of the focused waist within the device and the focused spot size. If either of these two parameters do not match those used when fabricating a GQPM device the Gouy phase will not be perfectly compensated and may, in some cases, lead to a worsening of the very effects that such a device is meant to alleviate.

The first of these two parameters that shall be investigated is that of spot size as this is perhaps the more difficult of the two to achieve in practical experiments, with a change in spot size invariably leading to an unwanted shift in the position of the focused waist resulting in further optimisation steps. In contrast, positioning of the device centre relative to a known focused waist simply requires translation along the axis of the focused beam whilst tuning the $\Delta k$ value, by temperature or wavelength dispersion compensation, to achieve optimal efficiency.

To analyse the effects of a non-optimal spot size it is necessary to return to Equation 4.37 and again solve for varying focus values with the substitution of Equation 4.40. However, unlike previous calculations it is a requirement that the spatially varying nonlinearity function $\kappa(\tau)$ be fixed at a given focus value, thus emulating the effect of a fabricated GQPM device. Furthermore, it is now necessary to analyse the effects of a variation in the value of $\Delta k$, as it is no longer reasonable to assume that peak harmonic power will be generated at the plane-wave $\Delta k$ value due to the incorrectly compensated Gouy phase. Additionally, it should be noted that for this calculation it is initially assumed that despite the incorrect spot size the focal point is nevertheless centred within the GQPM device.

Figure 4.11(a) shows the theoretical power output for a GQPM device with a $\xi$ value fixed at the optimum of 3.32 plotted against both a standard uncompensated QPM structure and a GQPM device recalculated at each focus value. As can be seen at very loose focus the effect of incorrectly compensating the Gouy phase is negligible, with the variation in total power output between a GQPM device and that of a standard QPM device being insignificant compared with the peak power output obtained at optimal focus. Although the variation in power output between GQPM and QPM devices is small at such loose focus values the relative power variation can be of the order of a few percent in the favour of standard QPM. This is emphasised in Figure 4.11(b) which shows the percentage power variation for fixed GQPM and variable GQPM against a reference QPM structure for a range of realistic focus values.

This reduction in GQPM efficiency at loose focus can of course be attributed to the phase correction that has been fabricated within the GQPM device. At loose focus the Gouy phase of the fundamental beam is almost entirely linear with the result that the phase of the GQPM

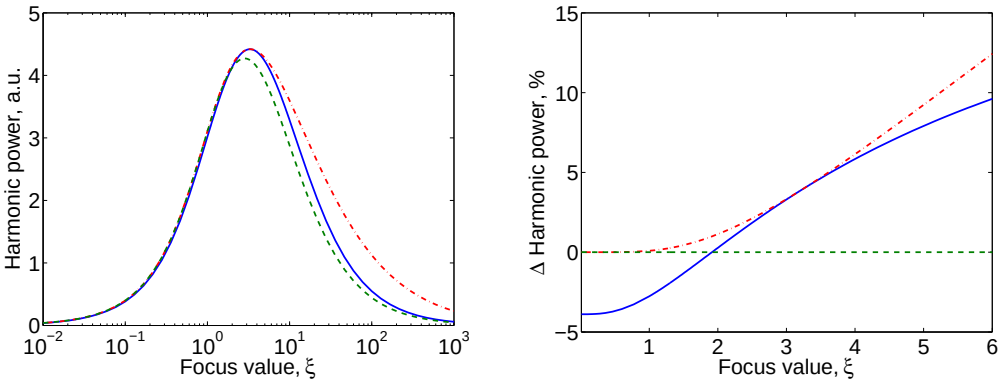


(a) (b)

Figure 4.11: (a) A plot of the variation in harmonic power output for QPM (green curve), GQPM recalculated for each focus (red curve) and GQPM fixed at $\xi = 3.32$ (blue) due to changes in spot size. (b) The percentage power difference of the same devices compared to standard QPM, here it can be seen above $\xi = 1.9$ GQPM will always outperform standard QPM.

device structure no longer reduces an existing phase error but instead creates an error equivalent to an inverted Gouy phase. This inverted phase can only be partially compensated for by a linear tuning of the grating k-vector, as is the case for compensating a genuine Gouy phase with a standard QPM device, leading to a reduction in efficiency.

However, as the focused spot size approaches the optimum value a complex interplay between the Gouy phase of the fundamental beam, the inverted Gouy phase of the grating and the linear dispersion phase occurs. At a focus value of approximately $\xi = 1.9$ it is found that by tuning the linear dispersion phase it is possible to overcome the residual error between the Gouy phase of the non-optimal fundamental beam and the inverted GQPM phase such that the overall power output is greater than that of an uncompensated QPM device.

This behaviour remains with tightening focusing, although the amount of linear dispersion compensation required reduces as is shown in Figure 4.12, up until the point that the optimum focus is achieved. Beyond this point the inverse Gouy phase of the GQPM grating is now insufficient to completely compensate the ever increasing nonlinearity of the focused Gouy phase and as such a linear dispersion is required to attempt to further reduce the error. Although at tight focus there is now a residual phase error, which cannot be compensated with linear tuning, the total error is still less than that of an uncompensated QPM device. The result of this is that a GQPM device, designed for optimal efficiency at $\xi = 3.32$, is more efficient than a standard QPM device for all focusing ratios in the range $\xi \geq 1.9$.

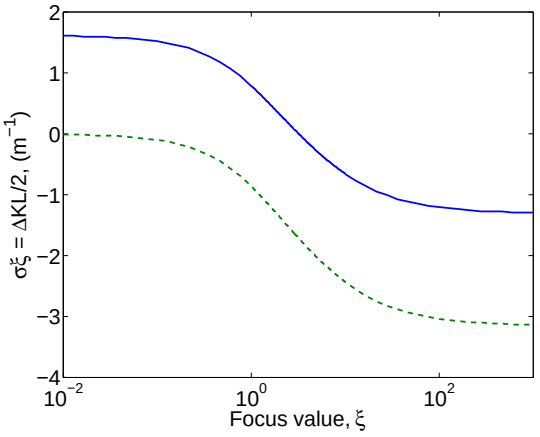


Figure 4.12: A plot of the variation in the peak phase-matching $\Delta k$, from the QPM plane-wave value, for varying degrees of focussing for both standard QPM (green curve) and a GQPM device optimised for $\xi = 3.32$ (blue curve). Here it can be seen the positive $\Delta k$, required to combat the inverted Gouy phase of the GQPM device at low focusing, reduces to zero at the optimal spot size before asymptotically decreasing for overly tight focusing.

Having shown that GQPM is relatively intolerant to the effects of an incorrectly sized focused waist, in terms of the power output compared to a QPM device, it is also necessary to investigate the effect of this spot size error on the symmetry of the phase-matching tuning curve, as this is perhaps a more desirable feature of such a focus compensated structure for many applications. Where, for example, the phase-matching tuning response is an essential component in determining the optical bandwidth, and distribution of frequencies within the bandwidth, of a frequency doubled laser system. This is especially true if long nonlinear samples are used to provide high conversion efficiencies, where the resulting narrow nonlinear bandwidth can closely match the bandwidth of the pump laser.

The effects of spot size variation on the symmetry of the $\Delta k$ tuning response is highlighted in Figure 4.13 which shows the normalised harmonic power output with $\Delta k$ for a range of focus ratios for both GQPM and QPM devices. Here, the error in focusing ratio has been set at $\pm 25\%$ from the optimal value, with the optimum values being $\xi = 3.32$ and $\xi = 2.84$ respectively. From these plots it can be seen that over such a large variation in spot size the symmetry of the GQPM device shown in Figure 4.13(a) is broken, with significant asymmetry returning for higher values of $\Delta k$ offset. In contrast the response of the standard QPM device in Figure 4.13(b), remains largely unaltered, with only a relatively minor increase in asymmetry for tighter focusing and, of course, a return towards symmetry for looser focusing.

However, despite this increase in asymmetry it can be seen that the GQPM device operating

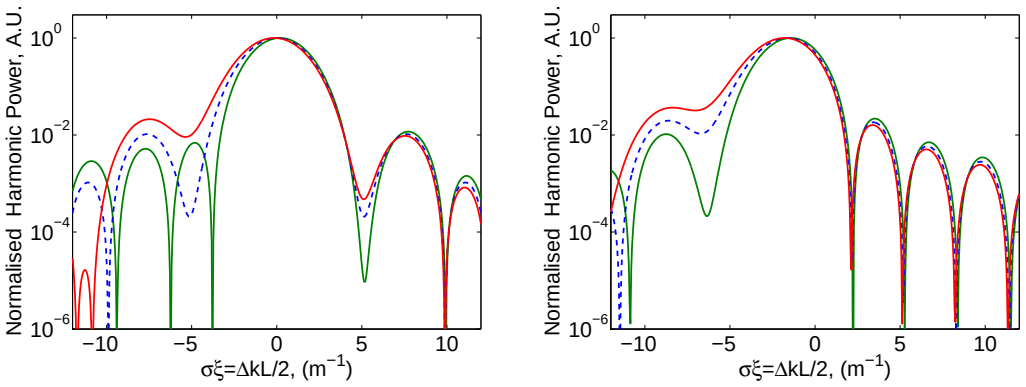


(a) (b)

Figure 4.13: Normalised power plots for GQPM (a) and QPM (b) devices showing the effects of an incorrect spot size on the $\Delta k$ tuning symmetry. For both plots optimal focusing is shown (blue dashed curve), which for GQPM is at $\xi = 3.32$ and for QPM at $\xi = 2.84$, along with plots for a 25% increase in focus ratio (red curve) and a 25% decrease in focus ratio (green curve)

with a focus ratio 25% too tight still maintains a more symmetric tuning response than that of a standard QPM device with equivalent focussing error. This is true despite the actual focusing ratio for the GQPM device being larger than for the QPM, which in itself would normally lead to greater asymmetry. Perhaps more surprising is that at this focusing value the GQPM device has a marginally higher degree of symmetry than that of even optimally focused QPM at $\xi = 2.84$. Further, by comparing the power levels of the side lobes for both GQPM and QPM structures it is clear to see that at equivalent focusing errors the GQPM device outperforms QPM, with much lower peaks and deeper zeros, resulting in a more efficient harmonic process with a cleaner frequency response.

From the results of these simulations it is clear that GQPM structures are remarkably insensitive to the focused spot size, maintaining both higher efficiency and better symmetry than standard QPM devices for quite large errors in the focusing ratio. Additionally, throughout these comparisons both the GQPM and QPM structures have been simulated for optimal harmonic power output, which for GQPM occurs at a smaller spot size resulting in a larger and faster varying Gouy phase than is the case for optimal QPM. If however, the proposed application requires a more symmetric response and not necessarily maximum efficiency it may be desirable to utilise a GQPM device designed for say $\xi = 2.84$, at this focusing ratio the device would be even less sensitive to focusing errors whilst still providing slightly higher efficiency and significantly better symmetry than a QPM device.

Having proven the merits of a GQPM device with a non-optimal spot size the analysis is now adapted to provide quantitative results for the performance characteristics of such a device when an optimally focused spot is launched into the device but with the waist offset from the centre. As is the case for standard QPM, and non-critically phase matched birefringent devices, it is reasonable to assume that the harmonic output power will reduce as the focused waist is translated from the centre. Here the main cause of the harmonic power reduction is due to a reduction in the average fundamental intensity along the crystal length. However, in a GQPM device this process is further complicated by the built in spatially varying phase compensation, which if misaligned with the phase of the fundamental beam can be expected to further reduce the conversion efficiency via back conversion. Thus it is necessary to explore at what degree of focus offset the advantages of a GQPM are negated, to give an efficiency equivalent to that of standard QPM, helping to determine the suitability of a such a device in a real world application.

The theoretical simulations of harmonic power output variation with focused waist location are shown in Figure 4.14. For this simulation it was chosen that both GQPM and QPM devices be analysed at their respective optimal focus conditions of $\xi = 2.84$ and $\xi = 3.32$. However, under such focusing conditions, even if there were no Gouy phase compensation, the GQPM device would be more sensitive to offset errors than the QPM device purely due to power density constraints. Where the more rapid diffraction provided by the tighter focus at $\xi = 3.32$ would directly lead to a lower average intensity when offset from the centre of the device.

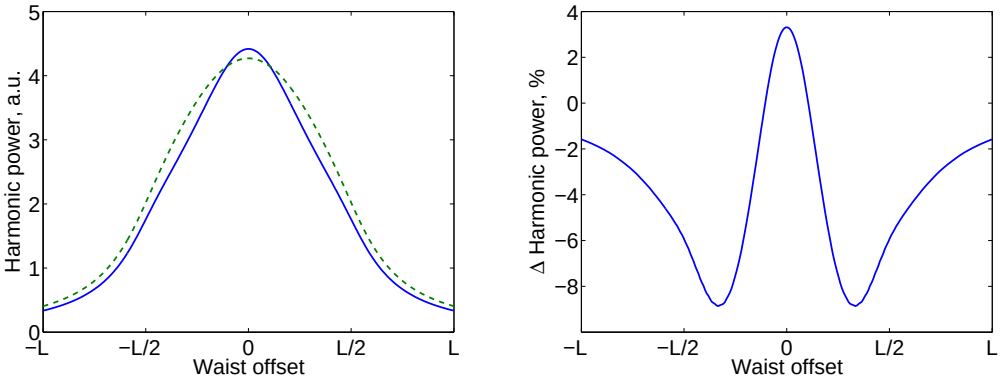


(a) (b)

Figure 4.14: (a) Theoretical plots of harmonic power for a GQPM device at $\xi = 3.32$ (blue) and a QPM device at $\xi = 2.84$ (green dashed) for varying degrees of waist offset from the device centres, (b) A plot of the percentage harmonic power difference of a GQPM device relative to a standard QPM device highlighting the gains of GQPM for well aligned systems.

As an be seen in Figure 4.14(a) when operating with a perfectly aligned launch the efficiency of GQPM outperforms standard QPM as was previously predicted. However, it is clear that the efficiency is more dependent on focus location in GQPM than QPM, with the rate of change of harmonic power being more rapid with small waist offsets. As a result of this more rapid variation it is found that any advantage in the output power of GQPM is quickly lost with offset error, with the efficiency dropping below that of standard QPM for waist positioning errors grater than approximately $\pm L/8$. This relative sensitivity to waist position is further emphasised in Figure 4.14(b) which re-plots the data of Figure 4.14(a) but now shown as the percentage difference in output power of the two devices. From this plot it is evident that at significant waist offset the power difference between the two devices can become quite severe, with GQPM performing almost 10% less efficiently than QPM. However, at this focus condition the overall power output is almost 50% down on the optimum of either GQPM or QPM and so this small loss in relative efficiency is likely of no significance if such a large output reduction can be tolerated. Further, for an actual device working with a low power CW laser source, the regime for which this simplistic no-depletion modelling is valid, to achieve reasonable efficiency it is common for the nonlinear device lengths to be in the region of a few centimetres in length. As such for a 20 mm long GQPM device to be less efficient than QPM the position error in the location of the focused waist must be approximately $\pm 2/3$ mm from the centre of the device, which is orders of magnitudes larger than the tolerances achievable with modern positioning systems or that of packaged devices.

The analysis now returns to bandwidth symmetry and any detrimental effects focus offset may have on it. Intuitively it would be expected that with an offset the GQPM response becomes asymmetric, with the response becoming more like that of QPM, as the Gouy phase of the focused fundamental beam and the inverted phase of the grating structure become misaligned allowing some level of back conversion. In such a scenario it is of course again necessary for a linear phase adjustment, created by dispersion tuning, to help minimise any residual phase error and thus maximise efficiency.

For more severe offset it would be expected that as the phase of the focused beam and the grating become ever more misaligned that the bandwidth response of GQPM becomes significantly more asymmetric than standard QPM. With this effect caused by a complex phase profile within the device as the near linear section of the grating phase, towards the extremities of the device, is combined with the highly nonlinear phase at the offset focused waist. However, such an offset is unlikely to occur in practical applications due to the significant power reduction associated with it.

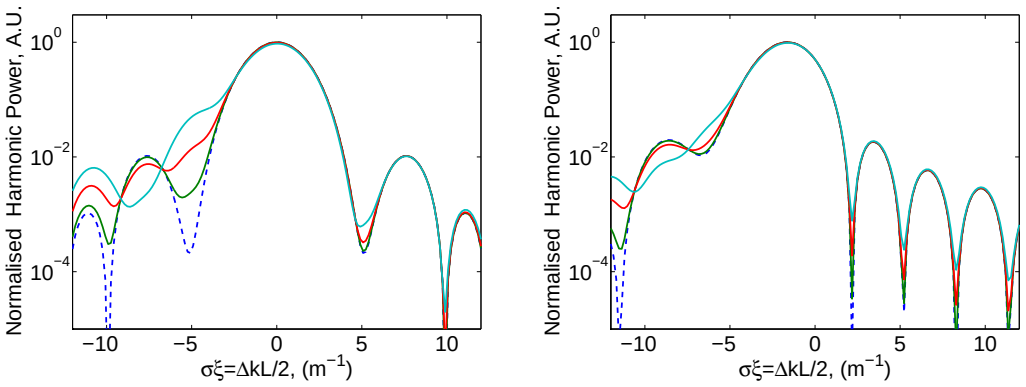


(a) (b)

Figure 4.15: Simulations of the effects of waist offset on the $\Delta k$ bandwidth of both GQPM (a) and QPM (b) devices with the following waist offsets from a central focus, 0% (dashed blue) 2% (green) 5% (red) 10% (light blue)

Instead the analysis shall consider only the more likely scenario of modest offset, such as was outlined above, where the output power is approaching its peak. Figure 4.15(a) shows the changing bandwidth response of an optimal GQPM device for varying degrees of waist offset, up to a maximum offset of 10% of the device length. The same set of simulations are also shown for QPM in Figure 4.15(b).

From these plots it is clear to see the high sensitivity of the bandwidth symmetry of GQPM devices to even slight changes in waist offset, with the sinc like symmetry quickly becoming more like that of standard focused QPM for offsets as small as 2% of the crystal length. As the offset approaches 10%, which is approximately the point at which the power output of GQPM reduces below that of QPM, the bandwidth becomes considerably worse than for QPM, with no sign of the initial minima of the sinc response. Thus significant care must be taken to achieve proper alignment of the device with the focused waist if bandwidth symmetry is of great importance, but again, this is a relatively trivial optimisation requiring simple translation of the device whilst optimising output power.

Finally, to complete the review of focus offset and spot size error these two effects shall be combined, as this is the most likely scenario in real applications. Here the parameter that shall be examined is the peak output power, although it is possible to analyse the change in bandwidth symmetry it is much harder to quantify what constitutes good symmetry and thus makes drawing conclusions difficult. To simplify the analysis both the spot size and waist offset are restricted to a small subset of realisable values, with the spot size limited to ensure it will physically fit

within the end apertures of a typical device without clipping and beam distortion. Of course depending on device length and operating wavelength this parameter can vary significantly.

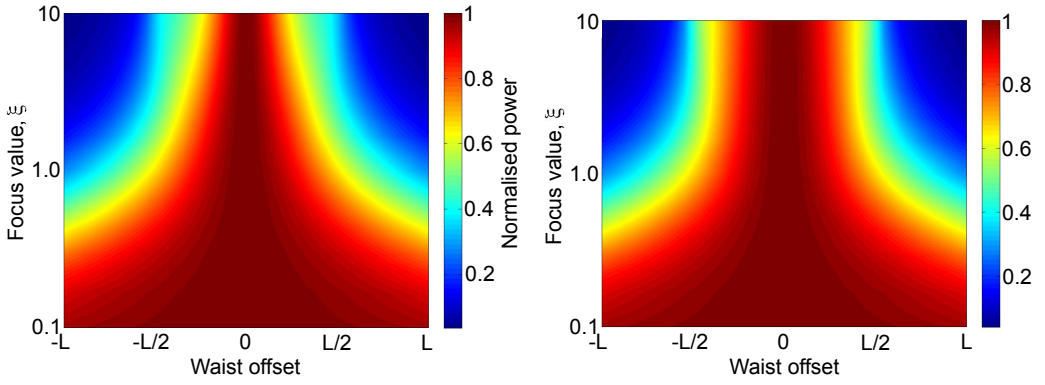


(a) (b)

Figure 4.16: Plots of normalised harmonic power output for errors in both the focused spot size and waist offset from the centre of the device for GQPM (a) and QPM (b) showing the greater sensitivity to waist position errors in GQPM devices. Note the power is normalised for each focus value.

The variation in harmonic power output with changing focus conditions are shown in Figure 4.16 for both GQPM and QPM devices. Here it should be noted that the plots have been normalised at each focus value; this normalisation was performed to aid in observing the variation in efficiency with offset, which without normalisation would be impossible to examine for all but the close to optimally focused conditions. When comparing the response of GQPM 4.16(a) with that of QPM 4.16(b) it is clear to see the higher sensitivity of GQPM to an offset. This result was predicted earlier for an optimal spot size with offset but it is now clear to see that the effect becomes more pronounced for over tight focusing. However, it must not be forgotten that for over tight focussing it was previously calculated that GQPM can offer substantial gains in output power when compared with QPM operating under the same conditions and thus may compensate for this sensitivity to offset errors.

A direct comparison of the output powers for GQPM and QPM for a range of spot sizes and waist locations is shown in Figure 4.17. Here the output power of GQPM is presented as a percentage of the output power obtained using standard QPM, showing the familiar 3.5% increase in efficiency at a focus of $\xi = 3.2$ under optimal alignment. Further it is clear to see that below approximately $\xi = 1.9$ GQPM is always less efficient than QPM irrespective of the alignment and that for offsets larger than $\pm L/8$ at the optimal spot size QPM again becomes more efficient. Both of these limiting cases were previously predicted. However, what is perhaps

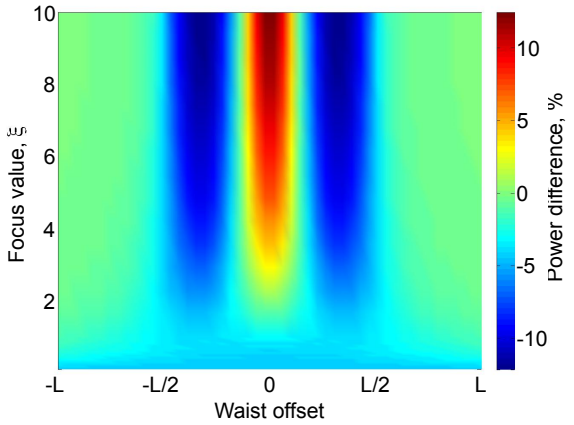


Figure 4.17: A plot of the percentage power difference of a GQPM device designed for $\xi = 3.32$ relative to a standard QPM device simulating the effects of both incorrect spot size and waist offset. Here it can be seen that if $\xi \geq 1.9$ and the waist offset is within the range of approximately $\pm L/8$ a GQPM 3.32 device will always outperform QPM.

surprising is that the constraint on the acceptable offset in waist position holds true for all focusing values. Despite the greater sensitivity GQPM has to offset errors at tighter focus this is almost exactly compensated by the greatly increasing efficiency of such a device in comparison with QPM.

In summary, this analysis has demonstrated the remarkable resilience of Gouy compensated QPM structures to errors in the optical launch. With such devices when operating with an incorrectly sized centrally located focus showing no worse than a 4% reduction in output power when compared to standard QPM at the same focus, with such a condition only occurring when the focus ratio is orders of magnitude too small. This modest reduction however is insignificant when compared with the loss in output power resulting from operating at such a loose focus compared to optimal focus, where for example a 1% reduction in power relative to QPM corresponds to a 15% reduction from the peak power obtainable at correct focus.

Further, it has been shown that only moderate care must be taken to align GQPM with the focused waist, with output powers higher than that achieved by QPM for the same offset obtainable when the focused waist is centrally located within a range of approximately 25% of the entire device length. However, if nonlinear bandwidth symmetry is of concern then more exacting care must be taken in alignment, with significant asymmetry returning to the bandwidth for offsets greater than approximately $\pm 5\%$ of the device length.

### 4.4.2 Sensitivity to fabrication errors

Having fully investigated the effects of a non-optimal optical launch the preceding analysis is now applied to investigate the effects of incorrectly fabricated GQPM devices on both the efficiency and bandwidth symmetry. For simplicity it is assumed that these poor quality grating structures are operating with a perfectly aligned optical system. The three effects that shall be modelled here are the effects of domain boundary position rounding error created by the minimum resolution of the photolithography mask, the effect of overgrowth of the polarisation inverted domains and finally the susceptibility of the device performance to random errors in the size and position of domains.

Previous work [16] has shown that QPM structures are relatively insensitive to such fabrication errors, showing only slight drops in efficiency for moderate errors. Additionally, it is quite possible to achieve nonlinear bandwidths in line with that predicted by QPM theory [19] demonstrating that, even with the inevitable fabrication errors, the overall periodicity of the QPM grating is the dominant factor in determining the response. Thus it can be expected that GQPM devices are equally as insensitive to fabrication errors, with the changing grating periodicity being the dominant factor in defining such a structure.

To enable this analysis the optimal positions of the domain boundaries have been calculated using Equation 4.40 and the midpoint of each domain determined. From this it is possible to simulate over or under sized domains as well as displace the centre of domains from the calculated midpoint in addition to varying the domain size. For this analysis a device length of 20 mm and a nominal period of 6.5 $\mu$m has been chosen to simulate the harmonic generation of 532 nm radiation from a 1064 nm Nd:YAG laser using the nonlinear material lithium niobate. With this length of device random position errors should have minimal effect on the functionality, with small errors being averaged out along the length. For short lengths this is not possible and such errors have a much larger influence on the device characteristics.

The results of the simulations for both over sized domains and random errors in the placement of the domain boundaries, from the calculated centre, are shown in Figure 4.18. For the over-sized domains all positively polarised domains have been set to be 20% larger than the optimal value and vice versa for negatively polarised sections. The situation of having all inverted domains over sized can be a common problem when fabricating a QPM structure in lithium niobate using electric field poling techniques. In simulating the random domain boundary positions the error has been allowed to randomly vary in an uniform distribution between $\pm 20\%$ of the nominal domain size, with the variation changing per domain. This technique can lead to conditions where the phase of an otherwise standard domain is offset or alternatively just create over or

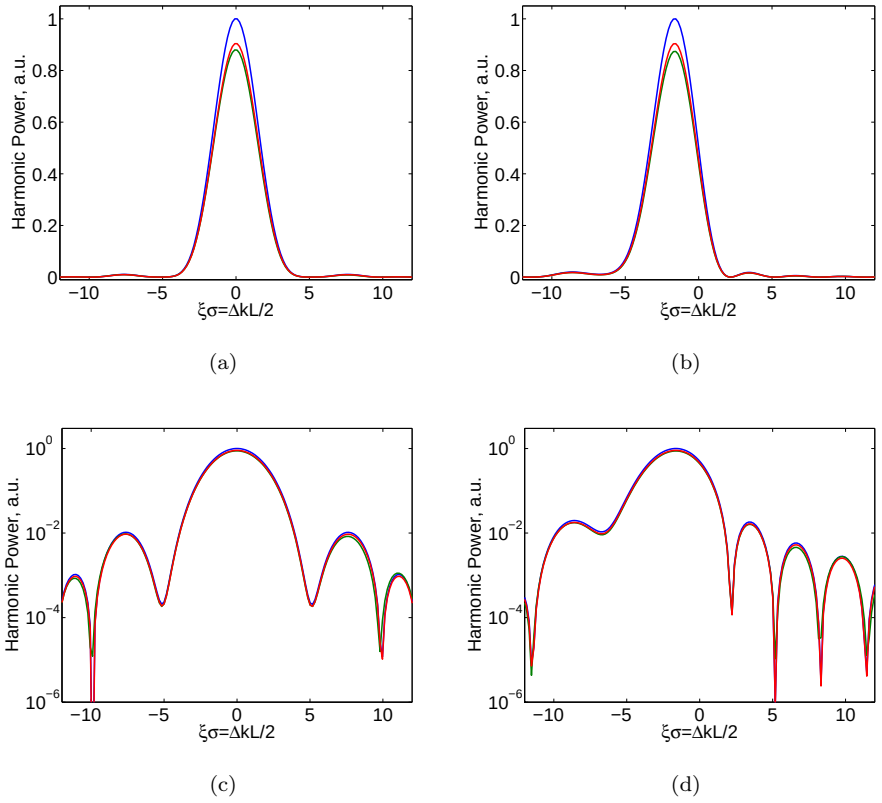


Figure 4.18: Simulation of the effects of 20% overgrowth of domain size (red) and domain boundary placement errors (green), using a random distribution of positioning errors of up to ±20% of the domain size, on the efficiency and symmetry of both GQPM (a)(c) and QPM (b)(d) devices compared with perfect GQPM and QPM (blue).

under-sized domains or even a combination of the two. As can be clearly seen from the linear plots of the GQPM bandwidth 4.18(a) there is no great penalty for either the over sized domains (red) or the randomly distributed domains (green), with the only noticeable effect being the slight reduction in efficiency. When this reduction is compared with the same simulations for standard QPM 4.18(b) it is found that the efficiency drop is indistinguishable, with this result confirming the earlier statement that the grating periodicity and not individual domains determine the device characteristics. What is also encouraging from these plots is the apparent lack of shift in the phase matching conditions, implying that the Gouy phase is still being correctly compensated despite the errors. This effect is further apparent in the logarithmic plots of the bandwidth where it can be seen that there is no discernible difference between the response of the over-sized domain simulation and that of perfect GQPM 4.18(c), with the same holding true for standard QPM

4.18(d).

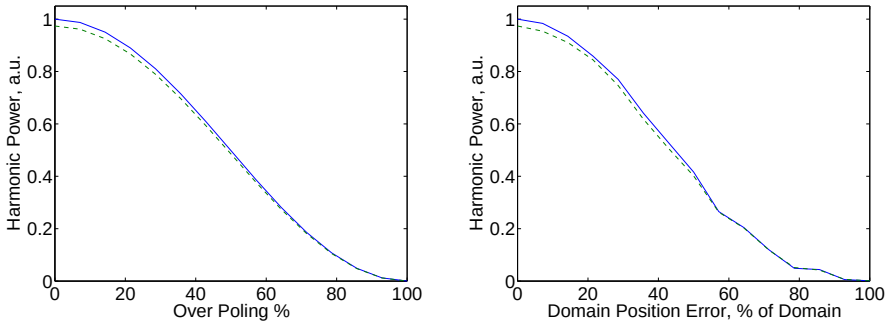


(a) (b)

Figure 4.19: Simulation of the effects of overpoling (a), and random domain placement errors (b), on the efficiency of both GQPM (blue) and QPM (green dashed) devices. Here both the over poling and random errors are as a percentage of the nominal domain size.

Finally, the analysis shall now look solely at the change in harmonic power of both GQPM and QPM for varying degrees of the two parameters from above. The plots in Figure 4.19 show the variation in harmonic power for both over-sized domains 4.19(a) and random domain positions 4.19(b), where the simulation has been performed for progressively more severe errors. As would be expected it is clear at 100% error in the domain size and position the output power for both devices is negligible as the grating structure has become a uniform domain and thus provides no phase-matching. Surprisingly however, GQPM is able to maintain the advantage in output power for both error types and for all degrees of error, never dropping below the peak power of standard QPM.

Thus, as is the case for standard grating structures, fabrication errors have relatively negligible effect on the behaviour of GQPM devices with any detrimental effects of these errors being common to both device types.

## 4.5 Experimental results

To test the real world performance of the theorised GQPM structures devices have been fabricated in the nonlinear material lithium niobate. This material was chosen as it provides excellent domain quality when fabricated using our electric field poling process as outlined in Chapter 2. For these experiments devices with a nominal grating period of approximately 6.5 $\mu$m, allowing frequency doubling of a 1064 nm Nd:YAG laser at a device temperature of 160 °C, were fabri-

cated. Further, these devices are based on a standard format of 20 mm in length and 0.5 mm in thickness, with such dimensions providing efficient harmonic signal generation and large apertures to accommodate the focused fundamental beam. Here, however, a compromise is made between longer device lengths, which provide stronger harmonic signals and crucially less stringent tolerances on alignment, and shorter lengths which help ensure high quality fabricated devices with a good yield. For ease of testing samples were manufactured to have numerous GQPM grating designs on a single lithium niobate device, with gratings capable of fully compensating the Gouy phase for focusing values of $\xi = 1.0$, 2.84, 3.32 and 5.0 and additionally, for comparison, a standard constant period QPM device.

Prior to testing accurate measurements of focused spot size and waist location and subsequent adjustment must be made. Spot size adjustments are made with the use of a adjustable afocal beam expander, comprising a pair of converging lenses and a single diverging lens providing approximately 1-2x magnification. With the first converging lens and the diverging lens providing the magnification and the final converging lens acting as a collimator, with the final focusing provided by an additional fixed converging lens close to the nonlinear sample.

### 4.5.1 Spot size measurement

Numerous measurement techniques were attempted to obtain accurate measurements of the focused spot size the first of which was the use of transmitting ruled gratings or Ronchi rulings. Such grating structures can be used to determine the spot size by observing the modulation depth of the transmitted laser power as a known period grating is translated perpendicularly through the beam [20]. Using a simple look-up table of the modulation depth between maximum and minimum transmittance for a given ruled grating period it is possible to readily obtain accurate values for the focused beam size. Here, maximum power is obtained when the focused spot is central to an opening on the grating structure and the minimum occurs when the centre of the beam is occluded by the high reflectivity grating. The advantage of this method compared with say the simple knife-edge technique is that there is no requirement to correlate the measured power with a translation position, which for the knife edge is essential to provided a scaling of the recorded power trace. Instead using the ruled grating technique all scaling is provided by the known period of the grating and as such these measurements can be performed without specialised precision translation stages. An example of the variation in modulation depth for a ruled grating, with a period of 20 lines per mm, for a range of spot sizes is given in Figure 4.20.

Despite the advantages such a rapid measurement technique provides it proved unsuitable for use in measuring the focused spot size. For the spot sizes required to provide optimal focusing for

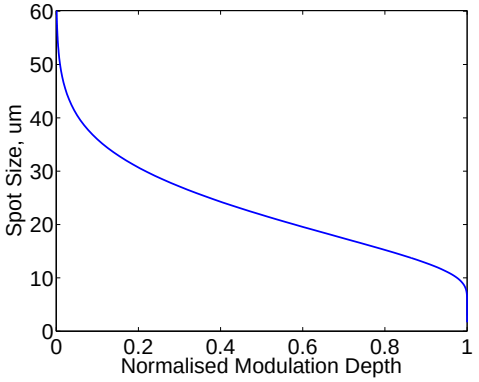


Figure 4.20: The theoretical variation in normalised transmitted power through a transmission ruled grating of 20 lines per mm for varying spot sizes. Here power is normalised to total laser power without a grating structure.

the lengths of material described above, approximately 23.4 $\mu$m at $1/e^2$ for $\xi = 2.84$ and 21.7 $\mu$m at $\xi = 3.32$, a ruled grating period of 20 lines per mm proves ideal. With a 25 $\mu$m spot equating to approximately a 50% modulation from full laser power. However, with such a fine period the ruled grating acts as a diffraction grating causing the very rapid divergence of the transmitted beam and thus preventing complete collection of the power at a detector. Although this prevents accurate determination of the actual spot size it does still allow for approximate positioning of the focused waist, by maximising the modulation depth of the zeroth order diffracted beam.

The technique finally used in this work for characterising the focused beam dimensions is that of the simple knife-edge. Here by translating a sharp, non-transmitting, straight edge through the beam and recording the power reaching the detector for known translation distances an error function curve is obtained. From simple analysis of the Gaussian distribution function this error function curve can readily be attributed to a spot size. Further to obtain an accurate measurement of the size and position of the focused waist it is necessary to take numerous readings of the beam radius along the axis of the focused beam, which by subsequent analysis can be correlated with the diffraction properties of Gaussian beams and a good estimate of spot size and location may be obtained. An example of the recorded error function curves for a focus spot size of approximately 23 $\mu$m corresponding to a focus ratio of $\xi = 2.84$ along with best fit theoretical plots is shown in Figure 4.21. These results are further correlated with the known variation in spot size due to diffraction in Figure 4.22 and thus give a good estimate of the focused spot parameters.

This technique, although simple and quite accurate, is labour intensive with many readings required for each spot size measurement. In this case, to maximise accuracy, power recordings

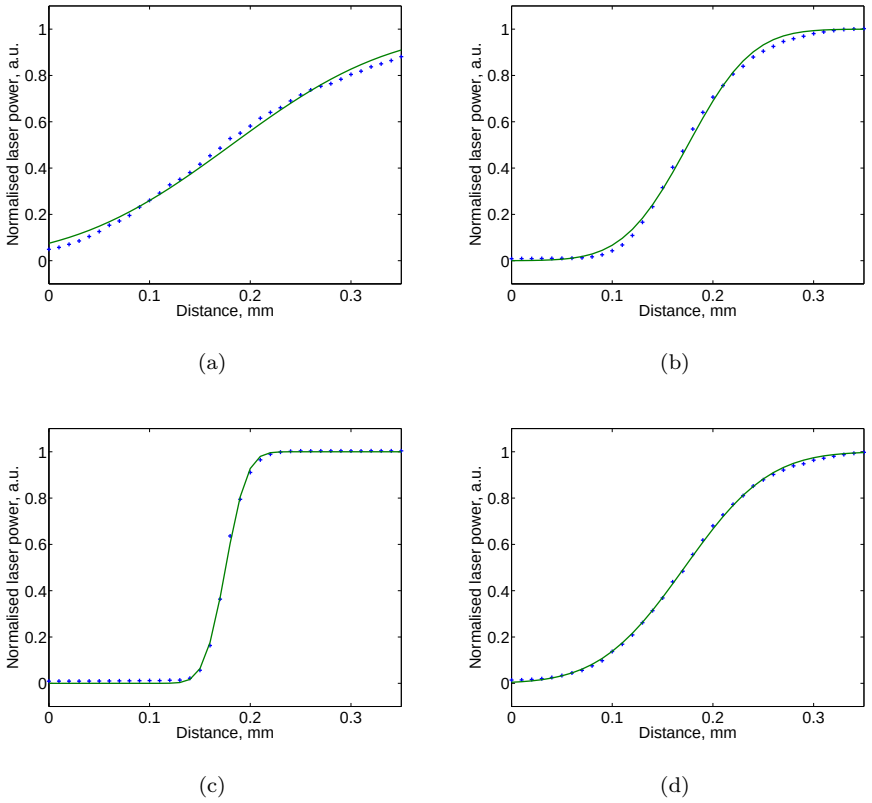


Figure 4.21: Measurements of transmitted power (dots) and best fit theoretical error function curves (green) for movements in the location of a knife edge through the focused beam at positions along the focus axis.

were taken over a 350 $\mu$m range in 10 $\mu$m increments through the beam, with this measurement repeated a further 25 times at 1 mm increments along the axis of the beam producing over 900 data points per spot size measurement. Despite this large number of data points it proved difficult to achieve reliable measurements without further steps to minimise errors. These included tightly aperturing the beam along the optical path to prevent stray back reflections from all the uncoated focusing optics reaching the detector and further aperturing of the knife-edge to prevent stray reflections from the knife blade.

Even with all the steps taken to achieve good quality beam measurements it is still clear from Figure 4.21(a) that discrepancies between the measurements and theory exist. Further, examining the variation in spot size with distance, as shown in Figure 4.22, it is found that although good agreement with theory can be obtained for the larger diffracted measurements the analysis breaks down close to the focus, with measured spot sizes being considerably tighter

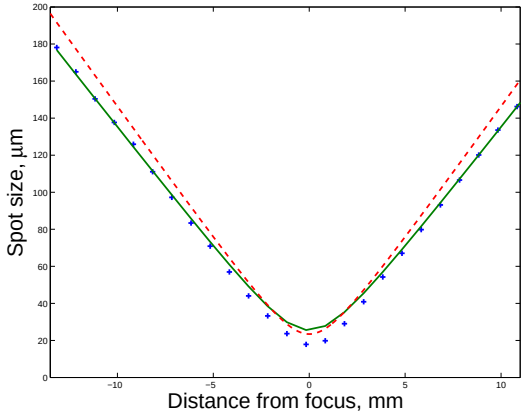


Figure 4.22: Measured spot size for positions along the focused beam (blue) and best fit Gaussian beam diffraction (green) corresponding to a focus of $\xi = 2.48$, also shown is the ideal spot size variation for a focus of $\xi = 2.84$ (red).

than predicted by the theoretical fitting. The reasons for this are likely two fold, the first and most influential being the insufficient number of data points on the most rapidly varying part of the recorded error functions, which allows for somewhat arbitrary fitting to theoretical plots. Secondly is non-uniformities in the straightness of the knife-edge, either through an unintended mounting angle from vertical or through possible fluctuations on the edge surface, both of which only need to be slight to have an impact with a 25 $\mu$m beam radius.

Finally, before characterisation of the GQPM samples can begin an adjustment must be made to the position of the focused spot to take into account the movement of the waist due to the changing of the beams radius of curvature as a result of the transition from the low refractive index of air into the much higher index of lithium niobate. This movement can be readily calculated by, among other methods, ray matrix analysis and shows a shift of approximately 4 mm for a 20 mm length sample of $LiNbO_3$. To facilitate in the alignment of the system this adjustment was accounted for in the spot size measurements by offsetting the knife edge from the ideal focal plane. This was achieved by modifying a mounting device, usually used to accurately locate the QPM samples, to hold a knife edge at the required offset distance. Thus once the focused waist is located a direct replacement of the modified mount with the mounted GQPM sample to be tested results in a near perfectly centred focus.

### 4.5.2 Harmonic power variations with temperature tuning

Finally, with the dimensions and location of the focused spot size determined temperature-tuned harmonic power output curves were recorded to verify the theorised characteristics of the GQPM samples, in particular the shifting peak phase-matching temperature and returning temperature-tuning symmetry.

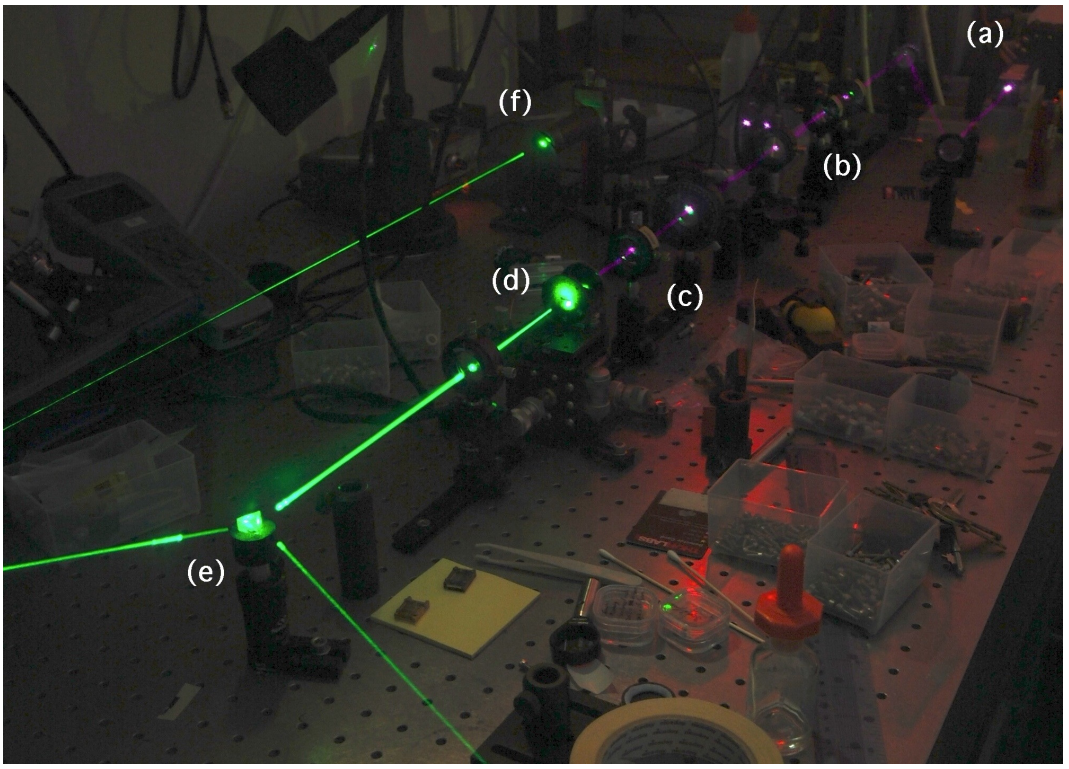


Figure 4.23: A long exposure photograph of the optical set-up used to measure the performance of the GQPM samples. Shown in this picture are the Nd:YAG laser (a), Beam expander telescope (b), focusing lens (c), Oven and GQPM sample (d), dispersive prism (e) and detector/lock-in amplifier (f). Note, the IR beam has been superimposed on the image to emphasise the optical path.

As stated previously the devices were designed to phase-match with a 1064nm Nd:YAG laser at an operating temperature of approximately 160 °C, with this high temperature operation essential to combat the effects of photorefractive damage [21]. For these experiments a single-longitudinal mode YAG laser, with a bandwidth of $< 10^{-5}$ nm and a power output of 100mW was used as the fundamental pump source. Although, due to the Fresnel reflections from the un-coated optics and other losses in the system the available power at the nonlinear device drops to approximately 65mW. Due to this relatively low optical power, which is reduced by a further 14% by the Fresnel reflection on entering the high index lithium niobate sample, and the desire to

observe the characteristics of the low power phase-matched side lobes, a lock-in amplifier is used to record the harmonic power. Control of the device temperature is performed using a standard resistive element PPLN oven attached to a computer controlled current source and custom PID control algorithm. A photograph of this optical setup is shown in Figure 4.23

Prior to the temperature tuning measurements the output power and output beam quality of both the fundamental and harmonic are optimised, by adjusting lateral grating position and tilt and rotation of the samples with the device temperature held close to the optimum value. However, it is found as a direct consequence of this precise alignment strong back reflections of both the fundamental and the harmonic beams, from the un-coated device facets, propagate back through the focusing optics into the laser cavity causing significant laser instability. In an attempt to overcome this fluctuating laser power, with these power spikes causing variations in the harmonic power of the order of the 3 times the steady state peak, isolation of the laser is provided through the use of a Faraday isolator. Despite this isolation, of the order of 40dB suppression of the back propagating fundamental, sporadic power fluctuations are still observed and thus in a further attempt to minimise these effects the nonlinear device is mounted so the end facet is at an angle from perpendicular to the beam.

With a relatively stable harmonic output power obtained temperature tuning curves were recorded for both QPM and GQPM devices, with the specific GQPM grating chosen to best match the current spot size. In an effort to obtain useful comparisons of the peak phase-matching temperature for both grating types the device temperature was held at a temperature 1 °C above the highest temperature point of interest for a minimum of 2 minutes, with the further constraint that the average temperature for this period vary by less than 0.05 °C from the set point, ensuring an uniform temperature across the sample. On reaching this steady state temperature the voltage applied to the resistive oven element is gradually reduced providing a temperature fall of approximately 0.6 °C/min. Measurement of the harmonic power was achieved first by collimating the output of the crystal and subsequently passing the collimated beam through a dispersive prism and separating out the fundamental and harmonic beams by propagating over a length of some meters. Finally, the now spatially isolated harmonic beam is passed through an optical chopper and onto a silicon photodiode, which to further increase the signal to noise ratio is isolated from room light and stray fundamental signal with the use of band pass filters and black out tubes.

The first recorded data for a GQPM device is shown in Figure 4.24, with this measurement taken using a close to optimal focus of approximately $\xi = 2.67$ and the GQPM2.84 grating structure. As can be seen in Figure 4.24(a) the recorded temperature tuning response is significantly

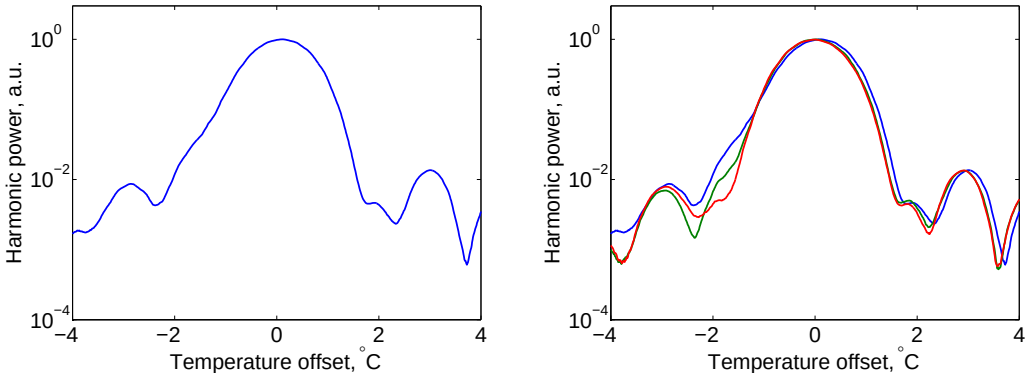


(a) (b)

Figure 4.24: (a) the initial measured Δk tuning response of a GQPM sample, here the sample has been placed at the optimum focus as determined by the spot size measurements. (b) Improvements in the measured symmetry for successive 100 $\mu$m shifts along the beam axis.

asymmetric, although less so than would be expected from a standard QPM device under the same conditions. Here some asymmetry can be expected from the incorrect spot size but further from possible misalignment of the focus with the device centre. The cause of this asymmetry was experimentally explored through slight movement of the GQPM sample relative to the expected waist position, with the results of this shown in Figure 4.24(b). Each plot in this figure represents a movement of 100 $\mu$m along the beam axis, with the movement in the direction of the laser propagation. What is evident is the reducing asymmetry with each successive movement, culminating in the highly symmetrical plot (shown red), giving credence to the original belief of a slight offset in the waist position leading to the significant asymmetry. If these results are compared with those predicted in Figures 4.13(a) and 4.15(a) it is clear that the changing asymmetry does indeed more closely resemble that for an incorrect waist position, although it should be stressed that these particular theoretical plots are for a focus of $\xi = 3.32$.

With the most symmetrical response obtained, via movement of the focus position, it is appropriate to compare the recorded response with that theorised from earlier calculations. Figure 4.25 shows the same measured response as above along with the theoretical response for both GQPM2.84 with a centrally located ideal focus of $\xi = 2.84$ and GQPM2.84 with a focus of $\xi = 2.67$, as was used for the measurements. Here it is evident that compared with the optimally focused device the response is remarkably symmetric, with the only slight asymmetry being the magnitude of the side lobes. However, with the theorised side lobes almost 2 orders of magnitude lower than the main peak this slight error in the second side lobe is perfectly acceptable. The

only significant deviation from theory is the missing first zero of the sinc oscillation, but with this zero being over 4 orders of magnitude lower than the peak it is perhaps not surprising. When compared with the theory for a $\xi = 2.67$ focus with GQPM2.84 it can be seen that it should be expected that the first zero of the response for lower temperatures become less defined. However, this is not true for higher temperatures so another mechanism must be affecting the measured response.

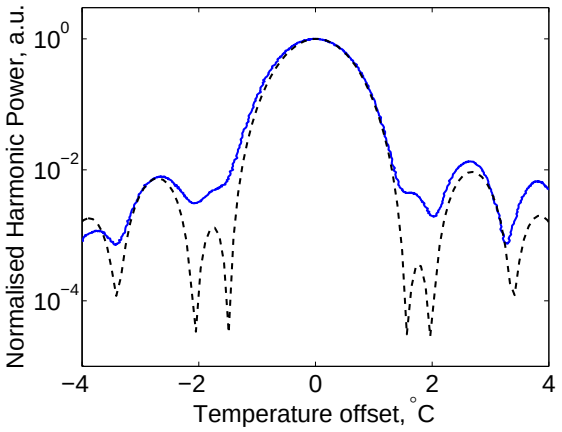


Figure 4.25: Log plots of the measured temperature tuning response of a 20mm GQPM2.84 sample (blue) and theoretical response of GQPM2.84 for focusing at $\xi = 2.67$.

One possible explanation for the poor definition of the first zero may be the non-Gaussian nature of the fundamental laser beam. It is likely that there are higher order spatial modes within the focussed beam which cannot be correctly phase matched by this structure, with the high order spatial modes having a more rapidly varying and larger Gouy phase. Further, it is unlikely that the poled structure is perfect and without domain flaws. Although it has been shown that poling errors have little effect on the overall device performance, when combined with the non-ideal mode of a real laser it is likely that strong zeros cannot in practice be obtained.

It should be stressed that it is at present unclear why the theoretical response for GQPM2.84 is so different from the plane wave response of QPM, with a much deeper first zero and varying period for the side lobes. Although the response of standard windowing techniques from Fourier analysis, which are similar to the Gaussian windowing applied to QPM structure by virtue of the focused intensity, can produce almost identical features.

Having demonstrated the generally good agreement of the measured temperature tuning response of GQPM2.84 with that predicted by theory it is now useful to compare this response with that of a measured standard QPM response under the same conditions. Figure 4.26(a)

shows the recorded temperature tuning profile of both these devices, here shown on a linear scale to highlight the significant shift in peak phase-matching temperature. Also shown in this plot are the theoretical plots of the expected shift in temperature for both devices, although these plots are difficult to differentiate from the measured data due to the very close agreement. To ensure accurate temperature readings for this measurement both device types are within the same physical sample, requiring only a sideways translation of the sample to change grating structure, thus maintaining the focal position. Further, as mentioned above, for both measurements the device temperature was stabilised to within 0.05 °C for a minimum of 2 minutes before beginning the temperature scan ensuring accurate temperature readings. From this temperature shift, in addition to the near symmetric tuning response, it can readily be inferred that the GQPM structure is indeed fully compensating for the Gouy phase of the focussed beam.

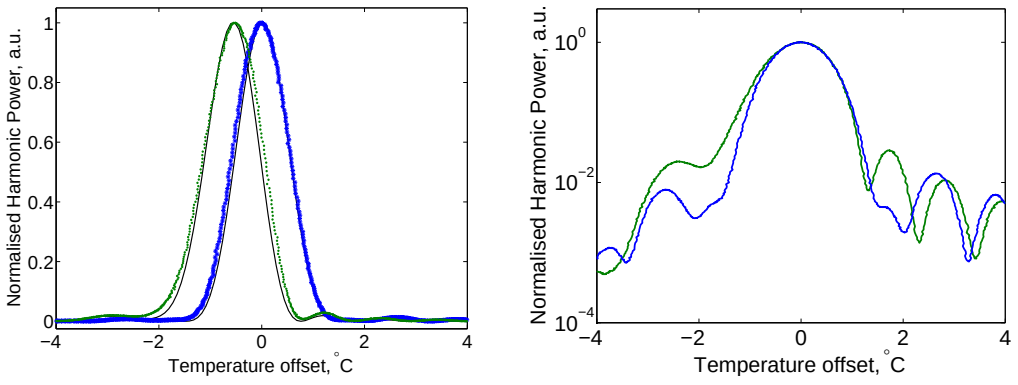


(a) (b)

Figure 4.26: (a) Measured temperature tuning responses for QPM (green) and GQPM2.84 (blue) and corresponding theoretical responses (black) for a focus ratio of $\xi = 2.84$. (b) Comparison of the measured responses of 20mm long samples of GQPM2.84 (blue) and QPM (green) at a focus of $\xi$ =2.84. Note QPM shifted to allow direct comparison of the asymmetry.

To highlight the detrimental effects that the Gouy phase has on standard focused QPM interactions Figure 4.26(b) re-plots the recorded data for both device types, but now on a logarithmic scale and with both curves overlaid, detailing the significant asymmetry in the tuning curve normally obtained for standard QPM interactions and the much narrower bandwidth that is achievable by compensating for the Gouy phase.

Although it has been shown that at the focus ratio of $\xi = 2.84$ all the detrimental effects of the Gouy phase variation can be negated it has so far not been possible to verify the performance enhancements offered by utilising the tighter focus compensated devices at $\xi = 3.3198$. On

attempting the characterisation of these devices significant feedback into the single mode laser cavity caused extensive power fluctuations in both the fundamental and harmonic power, with the SHG signal experiencing fluctuations of the order 300% above the steady state value. In an attempt to rectify this will be necessary to anti-reflection coat the samples thus preventing excessive optical feedback.

## 4.6 Conclusions

This chapter describes the interactions of focused Gaussian beams in nonlinear materials, particularly the parametric interaction of second harmonic generation. Building on the work carried out by Boyd and Kleinman in 1968 [6] this work extends their analysis to explicitly consider the detrimental effects of the Gouy phase, an inherent property of focused waves, on the nonlinear interaction. It is theoretically shown that the focusing condition of $\xi = 2.84$, proposed by Boyd and Kleinman and long regarded as the optimal for second harmonic power generation, is in fact a compromise with the Gouy phase shift offsetting the useful aspects of higher intensities at tighter focusing. It is further shown that by negating the effects of the Gouy phase it is possible to obtain higher output powers than standard uncompensated interactions for any focus value, with the optimal focusing conditions now occurring at a tighter value of $\xi = 3.3198$, providing a 3.5% increase in efficiency. Additionally by removing the effects of the Gouy phase it is possible to achieve fully symmetric $\Delta k$ tuning responses and a shift in the phase matching conditions back to that of plane wave interactions, with possible applications including creating narrow line frequency doubled laser sources. This work has also described how, by means of a simple modification to the periodicity of a standard QPM device, the Gouy phase can be counteracted. Further, using such a device the theoretical results of returning symmetry and shifting phase matching conditions have been experimentally verified.

# References


[1] W. P. Risk, T. R. Gosnell, and A. V. Nurmikko. *Compact Blue-Green Lasers*. Cambridge, 2003.

[2] G. D. Boyd, A. Ashkin, J. M. Dziedzic, and D. A. Kleinman. Second-harmonic generation of light with double refraction. *Phys. Rev.*, 137(4A):A1305–A1320, Feb 1965.

[3] P. D. Maker, R. W. Terhune, M. Nisenoff, and C. M. Savage. Effects of dispersion and focusing on the production of optical harmonics. *Phys. Rev. Lett.*, 8(1):21–23, 1962.

[4] A. Ashkin, G. D. Boyd, and J. M. Dziedzic. Observation of continuous optical harmonic generation with gas masers. *Phys. Rev. Lett.*, 11(1):14–17, Jul 1963.

[5] D. A. Kleinman, A. Ashkin, and G. D. Boyd. Second-harmonic generation of light by focused laser beams. *Phys. Rev.*, 145(1):338–379, May 1966.

[6] G. D. Boyd and D. A. Kleinman. Parametric interaction of focused Gaussian light beams. *J. Appl. Phys.*, 39(8):3597–3639, 1968.

[7] L. G. Gouy. Sur une propriete nouvelle des ondes lumineuses. *C. R. Acad. Sci. Paris*, 110:1251, 1890.

[8] F. Lindner, G. G. Paulus, H. Walther, A. Baltuška, E. Goulielmakis, M. Lezius, and F. Krausz. Gouy phase shift for few-cycle laser pulses. *Phys. Rev. Lett.*, 92(11), 2004.

[9] H. C. Kandpal, S. Raman, and R. Mehrotra. Observation of Gouy phase anomaly with an interferometer. *Opt. Laser Eng.*, 45(1):249–251, January 2007.

[10] H. Kogelnik and T. Li. Laser beams and resonators. *Appl. Optics*, 5(10):1550–1567, 1966.

[11] R. W. Boyd. Intuitive explanation of the phase anomaly of focused light beams. *J. Opt. Soc. Am.*, 70(7):877–880, July 1980.

[12] P. Hariharan and P. A. Robinson. The Gouy phase shift as a geometrical quantum effect. *J. Mod. Opt.*, 43(2):219–221, 1996.

[13] S. Feng and H. G. Winful. Physical origin of the Gouy phase shift. *Opt. Lett.*, 26(8):485–487, 2001.

[14] R. L. Byer. Parametric oscillators and nonlinear materials. In P. G. Harper and B. S. Wherrett, editors, *Nonlinear Optics*, pages 47–160. Academic Press, 1977.

[15] N. Lastzka and R. Schnabel. The Gouy phase shift in nonlinear interactions of waves. *Opt. Express.*, 15(12):7211–7217, June 2007.

[16] M. M. Fejer, G. A. Magel, D. H. Jundt, and R. L. Byer. Quasi-phase-matched 2nd harmonic-generation - tuning and tolerances. *IEEE J. Quantum Electron.*, 28:2631–2654, 1992.

[17] G.-D. Xu, T.-W. Ren, Y.-H. Wang, Y.-y. Zhu, S.-N. Zhu, and N.-b. Ming. Third-harmonic generation by use of focussed Gaussian beams in an optical superlattice. *J. Opt. Soc. Am. B*, 20(2):360–365, February 2003.

[18] S. Carrasco, B. E. A. Saleh, M. C. Teich, and J. T. Fourkas. Second- and third-harmonic generation with vector Gaussian beams. *J. Opt. Soc. Am. B*, 23:2134–2141, 2006.

[19] K. R. Parameswaran, J. R. Kurz, R. V. Roussev, and M. M. Fejer. Observation of 99% pump depletion in single-pass second-harmonic generation in a periodically poled lithium niobate waveguide. *Opt. Lett.*, 27(1):43–45, 2002.

[20] M. A. Karim. Measurement of Gaussian beam diameter using ronchi rulings. *Electron. Lett.*, 21(10):427–429, May 1985.

[21] F. S. Chen, J. T. LaMacchia, and D. B. Fraser. Holographic storage in lithium niobate. *Applied Physics Letters*, 13(7):223–225, 1968.

# Chapter 5

# Focus compensated Synthesised Gratings

## 5.1 Introduction

In Chapter 3 a study was undertaken to modify standard QPM devices to provide flat-top and wide bandwidth second harmonic temperature tuning responses, the purpose being for packaging with sources where either the operating temperature or fundamental pump wavelength are poorly constrained. Where a high degree of stability of these parameters is essential for the efficient operation of standard nonlinear devices. It was shown that by deliberately reducing the number of polarisation inverted regions over a given length of quasi-phase matched structure it is possible to create a predictable reduction in the effective nonlinearity for that region. Further with the introduction of $\pi$ phase shifts in the periodicity it is possible to create an effective negative nonlinearity.

Using a combination of these two techniques the effective nonlinearity of a QPM device could be altered to match arbitrary real mathematical functions, however with the one caveat that due to the limited number of possible sites of polarisation inversion for a given length of device the mathematical function could only be represented by quantised values. Despite this it proved possible to alter a QPM devices effective nonlinearity to broadly correspond to that of the mathematical function sinc. Here the sinc function is of particular importance as its frequency domain response is that of a perfect top-hat or flat-top, with the temperature or wavelength tuning response of device with a mathematically equivalent nonlinearity in turn becoming flat-top.

Throughout the design of such devices a high speed simulation technique was utilised to predict their conversion efficiency and temperature tuning response. However, such a technique was only ever intended to provide accurate simulations for plane-wave waveguide interactions. As a result, on the subsequent free-space focused beam experimental verification of the performance of these structures it was found that the tuning response although broadly similar to theory contained unexpected features. The most detrimental of which being the asymmetric tuning response which causes relatively large power fluctuations, above the acceptable design constraints, for variations in operating temperature. Here, a focused interaction is considered both for its reduced fabrication steps when compared with waveguide based devices and, additionally, as bulk focused interactions are of considerable interest for high power harmonic generation. With waveguide based devices severely power limited in comparison.

In this chapter a study into the effects of focused Gaussian beams on the temperature tuning response and efficiency of synthesised flat-top bandwidth quasi-phase matched structures is undertaken. This follows on from the work in Chapter 3, which demonstrated experimentally the detrimental effects of a focused fundamental beam on the symmetry of the temperature tuning response of a synthesised structure, and the work of Chapter 4 which highlights the cause of such an asymmetry, in standard nonlinear devices, as the Gouy phase [1, 2]. It shall be shown here that by compensating for the Gouy phase, using the technique detailed in Chapter 4, the asymmetry of the flat-top bandwidth can be removed and further that the shifted peak phase matching temperature that is associated with this effect can also be eliminated.

Additionally, this work proposes a method to overcome a narrowing of the phase-matching bandwidth of the synthesised structures which arises as a result of the non-uniform parametric interaction of the fundamental wave with the device nonlinearity, caused by the spatially varying Gaussian beam intensity. Where the higher intensities at the the focus waist interact with the near uniform high domain density at the crystal centre resulting in too large a response to be adequately compensated by the phase reversed sections of the synthesised devcie. The technique put forward to overcome this effect is fully compatible with both the initial design procedure proposed in Chapter 3 and importantly the Gouy phase compensation technique.

Finally, an investigation into the optimal focusing conditions of these complex structures is undertaken. Where due to the irregular distribution of the effective nonlinearity throughout the length of these synthesised devices it is not possible to assume that the standard focusing conditions, as used for uniform QPM structures, will provide optimal efficiency.

## 5.2 The effects of focusing on flat-top temperature tuning bandwidth

In Chapter 3 a thorough investigation of synthesised QPM devices for wide bandwidth, flat-top temperature stable second harmonic generation was undertaken. Throughout this work the design of such devices considered the case of plane wave parametric interactions, such as can be achieved with single-mode nonlinear waveguides. However, upon experimental testing of the synthesised devices using a loosely focused laser beam it was found that the measured temperature tuning response becomes asymmetric, creating an unacceptable variation in harmonic output power with changing temperature. With this power variation across the ideal flat-top severely reducing the bandwidth, defined as the temperature range over which power varies by less than 5% of the peak. This effect is further emphasised when operating close to the optimal focusing conditions for standard QPM devices of the same physical length, as shown in Figure 5.1. Here, the experimental data was taken using the optical launch described in the previous chapter, with the focus ratio measured as $\xi = 2.67$ corresponding to a spot size of $24.2\,\mu$m.

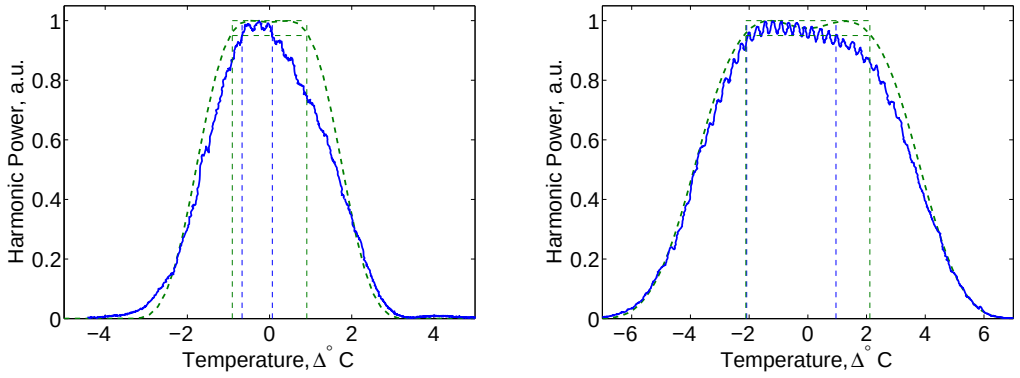


(a) (b)

Figure 5.1: Measured temperature tuning response of synthesised grating structures with sinc function effective nonlinearity ranging over $\pm 2\pi$ (a) and $\pm 6\pi$ (b) using a focused interaction (blue) showing asymmetric power output and the expected theoretical plane wave tuning response (green). The 95% flat-top bandwidth of both plane-wave and focused interactions are highlighted.

Figure 5.1(a) shows the measured temperature tuning response of a synthesised device, designed to provide approximately 1.81 °C of flat-top stability (as highlighted with the green dashed lines) when operating under plane wave conditions. As can be seen from the plot the 95% stability bandwidth of such a device when operating with a focused fundamental beam (highlighted

with blue dashed lines) is severely reduced, down to a bandwidth of only 0.74 °C, effectively negating the bandwidth advantages of such a device for focused interactions. However, as can be seen in Figure 5.1(b), which shows a synthesised device with a 4.23 °C flat-top plane wave bandwidth, the effect of focusing is less detrimental than for the more narrow bandwidth device with the bandwidth only dropping by 28% compared with 59% for the more narrow device.

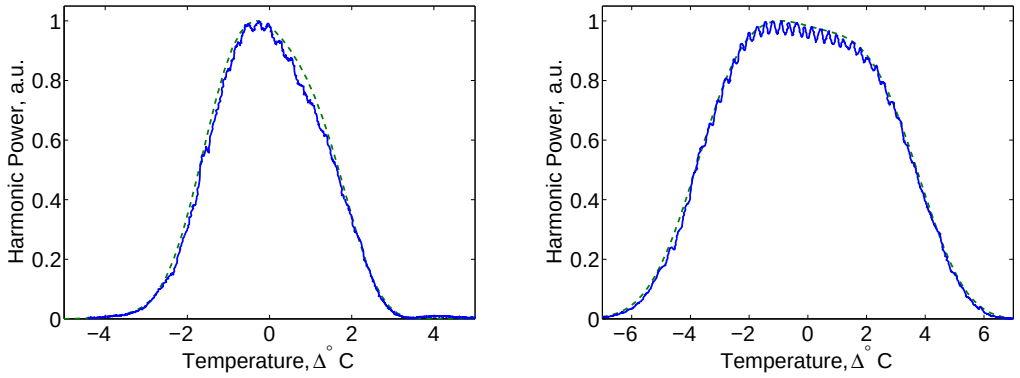


(a) (b)

Figure 5.2: Measured temperature tuning response of synthesised grating structures with an effective nonlinearity sinc function ranging over $\pm 2\pi$ (a) and $\pm 6\pi$ (b) using a focused interaction (blue) and the corresponding theoretical focused tuning response (green) for $\xi = 2.84$.

To investigate the cause of these effects the focus modelling technique developed in Chapter 4 is applied to these complex synthesised structures. The results of these simulations are shown in Figure 5.2, where initially the simulations are performed with a focus of $\xi = 2.84$. The theoretical results show strong asymmetry with an excellent agreement to the measured data, clearly showing that the asymmetry observed is indeed an artefact of the focused interaction and not an unexpected response due to say imperfect device fabrication or poor optical launch. Further, these results show an offset in the central operating temperature from that predicted by plane wave analysis, although due to the chosen temperature scaling this is not evident in the plots, with this offset moving the peak to lower temperatures indicating that these structures suffer strongly from the effects of the Gouy phase. Having identified the likely cause for the severe asymmetry it is now possible to provide a explanation for this and the resulting bandwidth reduction for the narrower bandwidth device.

The key physical difference between the two manufactured device types is the active nonlinear length, as shown in Figure 5.3, with the shorter active length device offering a greater flat-top bandwidth. Here the active length is the distance between the furthest polarisation inverted

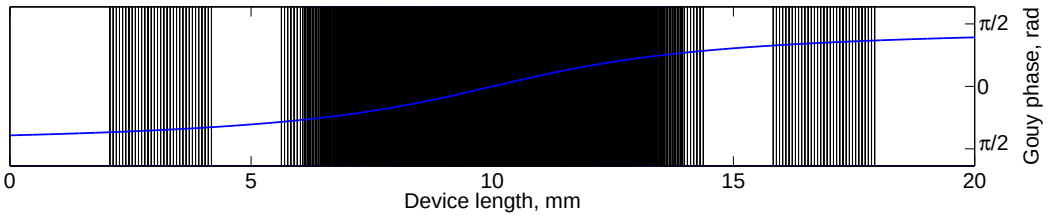


(a)

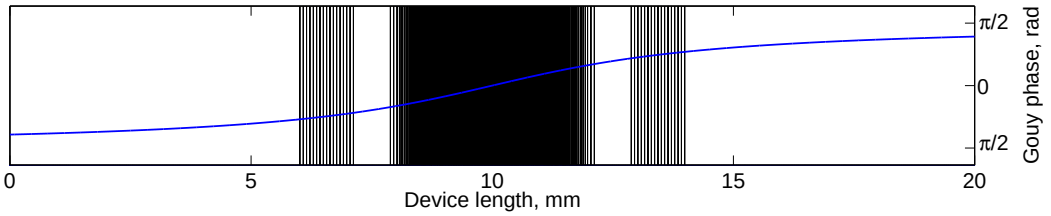


(b)

Figure 5.3: A graphical representation of the Gouy phase shift in 20 mm long synthesised grating structures. Here it is clear that for the narrower bandwidth device, (a), the Gouy phase is larger in value and less linear over the active grating region than in the wide bandwidth device (b).

periods, with any bulk material beyond these periods offering near zero net harmonic power due to the interactions cancelling out over multiples of the coherence length.

By superimposing the theoretical Gouy phase of a perfect Gaussian beam with a focus ratio of 2.84, matching that of the experimental and theoretical results, onto the grating patterns above it is clear that for the narrower bandwidth, longer active length device the variation of the Gouy phase is both much greater and more nonlinear than for the wider bandwidth device. The effect of this is twofold, firstly due to the larger phase variation a more pronounced linear dispersion compensation, provided by temperature offset, is required for efficient operation of the narrower devices. Secondly, and more importantly, due to the more nonlinear nature of the Gouy phase over the length of the longer active length device a linear $\Delta k$ compensation, as can be provided by temperature tuning, is unable to adequately counteract this phase advancement. This, as seen in Chapter 4, provides a route for raised efficiency operation at a temperature de-tuning below the central optimum. However, unlike for standard QPM devices where this raised efficiency occurs close to a zero on the sinc tuning profile and thus not altering the response significantly, the flat-top nature of these synthesised devices amplifies the effects of this raised efficiency resulting in a significantly asymmetric temperature tuning response and reduced flat-top bandwidth.

## 5.3 Compensating for the Gouy phase

Having demonstrated how the Gouy phase of a focused beam interacts with complex synthesised structures, producing an undesirable highly asymmetric, relatively narrow bandwidth temperature tuning response, the analysis now turns to mitigating these effects using the techniques pioneered in Chapter 4 with the aim of returning the response to that of plane-wave interactions.

Due to the deliberate design criteria that the domain size and period of the synthesised structures be unaltered compared with a standard QPM device phase matching the same nonlinear interaction the technique of compensating the Gouy phase, by subtly moving the position of the domains to maintain a phase lock between the grating and the propagating wave, is trivial to apply. This is made further apparent when it is considered that on designing the synthesised grating structure there is no concept of the phase-matching requirements of the proposed harmonic interaction other than a knowledge of the number of periods that can physically reside in the given device length. With instead the design simply consisting of a binary data set stating the existence or lack of polarisation inverted domains to match the required effective nonlinearity, with the exact positions of these domains only calculated later as needed for modelling or fabrication purposes. Here, as for compensating standard focused interactions, the position of each domain is calculated according to the position of zero crossings of the following

$$\kappa(\tau) = \cos(\sigma\tau + \arctan[\tau]), \tag{5.1}$$

with $\sigma = \Delta k b/2$, b is the confocal parameter and $\tau = 2(z-f)/2$ with $f$ the focal position within the device which is assumed to be central.

Now, by applying this technique to the designed synthesised gratings the following temperature tuning responses are obtained upon theoretical modelling with a focus ratio of $\xi = 2.84$, see Figure 5.4. As can be seen the theoretical responses have regained their symmetry and additionally, not shown, the central phase-matching temperature now corresponds exactly to the plane-wave value. Thus it is clear that the effects of the Gouy phase have been completely negated.

However, despite complete compensation of the deleterious effects of the Gouy phase the obtained flat-top bandwidth is still reduced compared with plane-wave theory. With a reduction of 40% for the narrowest bandwidth device and 17.1% for the larger bandwidth. Also evident from these simulations is a smoothing of the flat-top bandwidth, which from Fourier analysis can be attributed to a windowing or apodisation of the nonlinearity. With this windowing removing any discontinuity in the nonlinearity, resulting in a reduction of the oscillations across the flat-top which are caused by the finite nature of the sinc like nonlinearity.

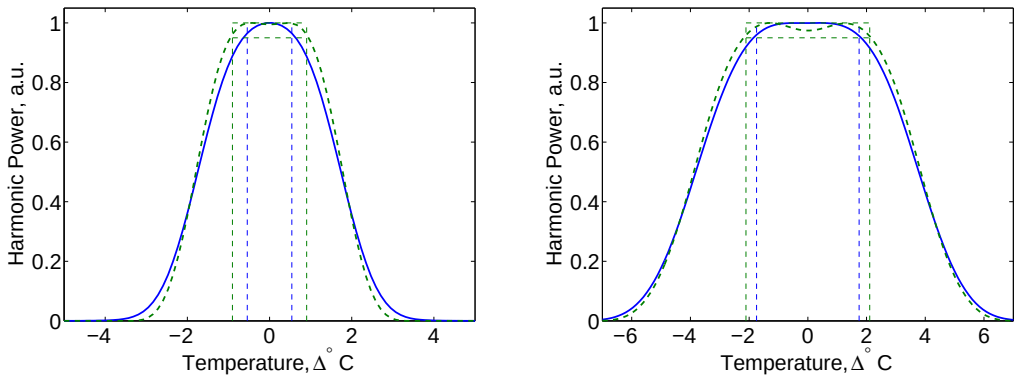


(a) (b)

Figure 5.4: Theoretical plots of Gouy compensated wide bandwidth structures under focused conditions (blue) demonstrating a return to temperature tuning symmetry. Note the Gouy compensated bandwidth is reduced compared with plane-wave (green), with this effect more pronounced for the less wide device.

Here the cause of both the reduced bandwidth and the smoothed flat-top response can be attributed to the spatially varying power density of the focused fundamental beam. With the focusing producing a weighting on the efficiency of the nonlinear interaction that is highest at the centre of the focus and rapidly reducing towards the device extremities. The effect of this weighting on the bandwidth is to reduce the influence of the phase inverted sinc side lobes, the function of which is to turn an otherwise simple apodisation of the nonlinearity which would not provide any useful bandwidth gain into the more broadband flat-top. This weighting has the effect of further reducing what little nonlinearity is available at the extremities of the device, which has already been intentionally reduced by a raised cosine apodisation in an effort to stop excessive ripple along the flat-top. In reducing this nonlinearity further all ripple along the flat-top is now removed, this proves detrimental for the particular devices under test as they have been carefully designed with some deliberate ripple, but below a 5% variation, with the intention of increasing the bandwidth.

## 5.4 Compensating for spatially varying focused fundamental power

To further improve the temperature tuning response of the synthesised structures under the effects of focusing, returning to the response achieved using plane wave simulations, a compensation for the spatially varying intensity of the focused Gaussian beam must be made. To correctly

compensate for this variation the exact properties of the focused beam must be known, specifically the Rayleigh range of the focused beam must be known so that an accurate mapping of the intensity within the synthesised device can be achieved. For this initial demonstration it shall be assumed that the focused beam has a Rayleigh range such that the focusing ratio is the familiar $\xi = 2.84$.

With knowledge of the focus ratio it is trivial to calculate the peak electric field of the focused mode at any point along its focus axis. Using this data it is possible to almost completely compensate for the effects of its variation by pre-biasing the strength of the effective nonlinearity such that the nonlinear regions with lowest applied electric field receive the highest value of effective nonlinearity. Of course with it being impossible to actively increase the nonlinearity of a QPM structure the procedure instead reduces the nonlinearity of sections of the grating that would otherwise have a high nonlinear efficiency due to the large focused intensity of the fundamental. This is achieved by deliberately removing regions of polarisation inversion. This technique is of course fully compatible with the previous technique of converting the nonlinearity to match the profile of a truncated sinc function, requiring only a simple multiplication of the desired sinc function, the windowing function required to achieve flat-top operation under plane-wave conditions and finally the scaled inverted variation of electric field.

In order to verify the validity of this technique an attempt has been made to compensate for all the effects of focusing present in a standard QPM interaction. As before, the simulations undertaken here utilise the non-depletion analysis tool decribed in Chapter 4 which is based on the analytic model developed by Boyd and Kleinman [3]. The plots of Figure 5.5(a) detail the negative impact focusing has on the temperature tuning response. In this figure are plots of an ideal plane wave interaction, shown in blue, a focused interaction at $\xi = 2.84$ shown in green and finally a Gouy phase compensated interaction also at $\xi = 2.84$ shown in red. Here it is clear to see the large shift in peak phase matching temperature and the asymmetry in the response of the standard QPM interaction as a result of the focused Gouy phase and the further removal of the negative features upon correct Gouy phase compensation. However, despite the Gouy compensation the tuning response of the GQPM device does not exactly match that of plane wave analysis, having a wider bandwidth and reduced side lobes. Here the reduced side lobes are as a result of the effective apodisation of the nonlinearity by the focused intensity, an effect identical to the smoothing of the ripple of flat-top synthesised structures. Further, the increased bandwidth can be attributed to an effective shortening of the device length with only a relatively short section of the grating gaining from the high intensity focused waist.

Thus, to reduce the bandwidth of a standard QPM device under focusing, back to that

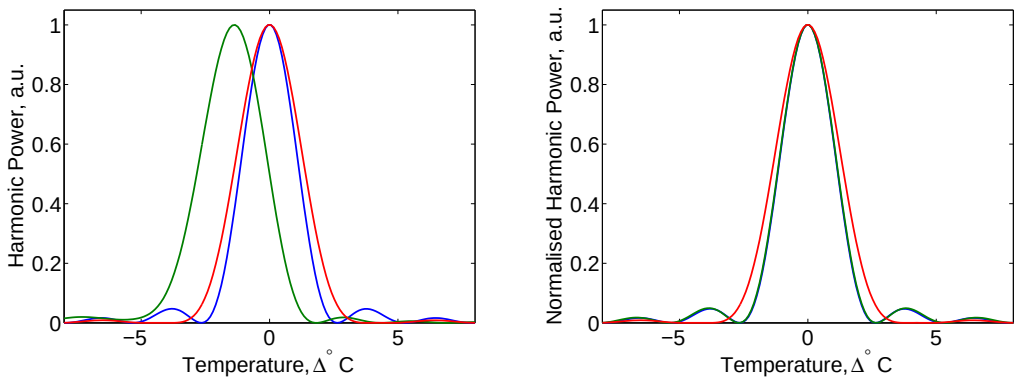


(a) (b)

Figure 5.5: (a) The theorised variation in temperature tuning bandwidth for a plane wave 8 mm PPLN device (blue), 8 mm device under focusing at $\xi = 2.84$ (green) and 20 mm GQPM (red). (b) temperature tuning bandwidth for plane-wave (blue), GQPM (red) and Gouy and spatial intensity compensated devices (green).

obtained under plane-wave, it is necessary to increase the effective length of the nonlinear interaction. This of course can be achieved by physically extending the length of the device, however doing so will change the focus ratio which will need further compensation. Instead using the technique detailed above a weighting is applied to the uniform QPM structure that is proportional to the inverse of the electric field thus increasing the length of equivalent nonlinear drive. This weighting is normalised such that the maximum weighting corresponds to a section of QPM with the highest domain density attainable, i.e. no missing polarisation inverted domains. Figure 5.6 shows the normalised weighting, or effective nonlinearity (blue plot), and the resulting domain structure that would be suitable for compensating for the focused electric field variation produced by a focus ratio of $\xi = 2.84$ in an 8 mm long QPM structure. Here the sample has been limited to 8 mm thus reducing the total domain number so that the slight variation in domain density can be visualised.

From this plot it is clear to see that a large reduction in domain density is required at the point of peak focused intensity, with the average domain number for a given length reducing by over 50% compared with standard uniform QPM. Of course, as a result, this technique would not be used for reducing the bandwidth of QPM under focused conditions due to the corresponding loss in efficiency. However, this is not a problem for synthesised devices as will be discussed briefly. Further, from this plot it is possible to identify why this technique was stated earlier as not being able to completely compensate for the intensity variation. Due to the limited periods

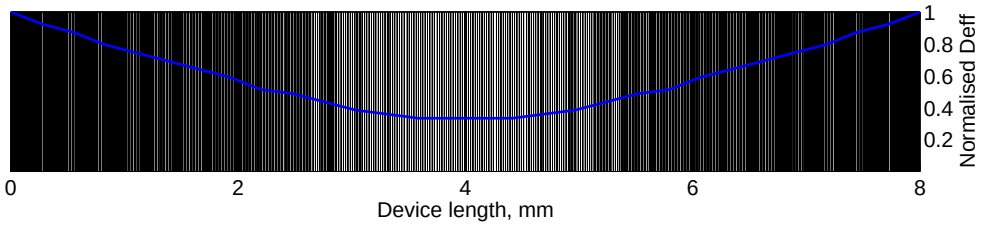


Figure 5.6: Domain density and normalised Deff of QPM that can compensate for the effects of non-uniform power density provided by a focused beam

within the QPM structure for a given length the variation in domain density must be quantised resulting in a non-ideal compensation. In this particular example 40 quantisation levels were found to provide a good compromise, with greater quantisation levels reducing the number of samples available along the length of the device thus preventing a good fit with the ideal value.

With an appropriately compensated structure the analysis now returns to the temperature tuning bandwidth performance, with the results shown in Figure 5.5(b). In this figure are the plots of a plane-wave interaction in an 8 mm long uniform QPM device (blue) the focused but Gouy compensated interaction through the same device (red) and finally the Gouy compensated, spatially varying intensity compensated focused interaction of the 8 mm long device of Figure 5.6 (green). Here, it can be seen that the temperature bandwidth of the fully compensated structure has almost completely returned to that of the standard 8 mm long uniform QPM plane-wave structure, with only the smallest of variation in the magnitude of the sinc side lobes. This minute variation can be attributed to the quantisation of the normalised effective nonlinearity and thus can be expected to be further improved with a longer device length or shorter wavelength interaction, both of which would provide more periods allowing finer quantisation control. From this result it is now clear that it is possible to almost completely compensate for all the detrimental effects of focused Gaussian beams and that such techniques should perform equally well for achieving the maximum flat-top bandwidth and efficiency of synthesised structures in focused beam interactions.

The techniques verified above shall now be applied to flat-top bandwidth structures in an effort to return the bandwidth back to that simulated under plane-wave conditions. However, at this point it is prudent to mention that for designing an optimal device for focused interactions, rather than attempt to design an optimal device under plane wave conditions and later adjust for the effects of focusing, a more efficient technique is to perform all the initial optimisations using focused interactions. This is evident from the results above on returning to plane-wave uniform bandwidth, where great care was taken to optimise the quantisation levels to ensure minimal

error. This freedom is not however available if the synthesised device has been pre-optimised for plane-wave, where a small change in the quantisation levels to achieve good control over the varying intensity can lead to drastic changes in the flat-top response.

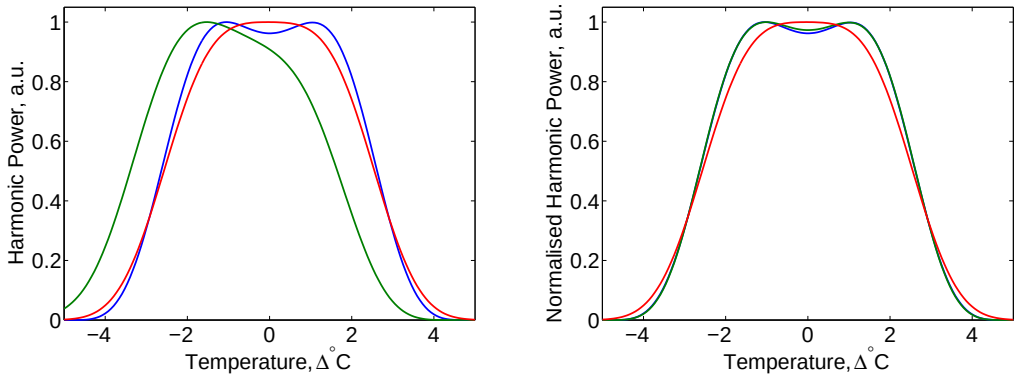


(a) (b)

Figure 5.7: (a) The theorised variation in temperature tuning bandwidth for a wide bandwidth device under plane-wave (blue), under focusing at $\xi = 2.84$ (green) and GQPM (red). (b) temperature tuning bandwidth for plane-wave (blue), GQPM (red) and Gouy and spatial intensity compensated devices (green).

Despite the difficulties in balancing the quantisation levels excellent results can still be achieved as will now be shown. Figure 5.7(a) shows a flat-top bandwidth device, designed under plane-wave conditions, providing a 95% bandwidth of 3.09 °C when operating with a theoretical plane-wave (blue). As for the uniform QPM device above also shown is the uncompensated response under a focus of $\xi = 2.84$ with a resulting bandwidth of 1.54 °C (green) and finally the Gouy compensated response with an improved bandwidth of 2.35 °C (red).

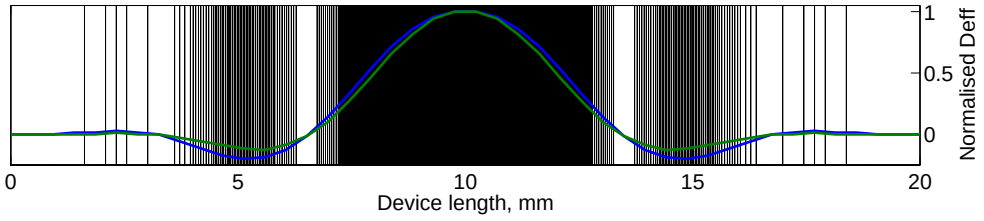


Figure 5.8: Graphic detailing the effective nonlinearity for an uncompensated wide bandwidth device (green) and the Gouy and spatial intensity compensated device (blue). Also shown is the grating pattern such an effective nonlinearity generates.

Now on compensating for the varying intensity, by applying a scaled windowing proportional

to the inverted focused electric field variation, the following synthesised QPM structure is obtained, see Figure 5.8. Also shown in this figure is the resulting normalised effective nonlinearity (blue). To highlight the slight change in the effective nonlinearity caused by the intensity compensation the plot of the fully compensated structure is contrasted with that of the optimal plane wave device (green).

As can be seen the overall change to the shape of the sinc like structure is minimal, with only a slight change in nonlinearity for all but the extremities of the device where the change is comparatively much larger. This of course is to be expected, with the inverted electric field weighting being strongest at the far limits of the device. One point of interest is that unlike for the fully compensated QPM structure of Figure 5.6 the overall efficiency of this fully compensated device should increase slightly over that of the same device with simple Gouy phase compensation. In the standard QPM device the compensation required an increase in the nonlinearity of the device at its extremities, with this impossible to achieve instead a reduction to the nonlinearity is made at the centre. Of course by reducing the nonlinearity the efficiency inevitably drops. However, due to the complex structure of the synthesised devices the nonlinearity at the extremities can be raised significantly without becoming greater than the nonlinearity required at the device centre, thus the overall average nonlinearity of such a device will be higher.

The temperature tuning results of this new structure are shown in Figure 5.7(b), where again the plane-wave results prior to any compensation are shown in blue, the bandwidth of the Gouy compensated focused interaction shown in red and the fully compensated focused interaction is shown in green. As can be seen the variation between the plane-wave result and the fully compensated result is again minute, with the 95% flat-top bandwidth increasing to 3.09 °C from 2.35 °C for the simple Gouy adjusted device, with this bandwidth exactly matching that of the plane-wave device. From this it is clear to see that even for a non-optimal device, with the initial optimisation performed assuming a plane-wave interaction, the detrimental effects of focusing can be compensated.

With this simple technique it is now possible to fully realise the potential of flat-top synthesised devices for non-waveguide applications, where the bulk focusing method may be more suitable due to high fundamental power levels that may lead to damage of the nonlinear material in a tightly confined waveguide structure. However, for these structures to achieve their ultimate performance, and become a viable substitute for waveguide based devices, a final optimisation of the focusing conditions must be made to maximise harmonic conversion efficiency.

## 5.5 Optimising focusing conditions for efficient operation

Throughout the analysis of focused interactions in these synthesised devices it has been assumed that good harmonic generation efficiency can be achieved with a focusing value at or close to that which is optimal for uniform QPM structures. However, it is clear from the plots of domain density and distribution in Figure 5.3 that the effective lengths of these complex structures are considerably shorter than the total device length and as such tighter focus is likely required to achieve optimal efficiency, this is especially true for the wider bandwidth devices with the correspondingly shorter active lengths. From this it is clear that there will be no one focusing condition that allows efficient operation in all synthesised structures of varying flat-top bandwidth and as such a dedicated study into the optimal focusing condition for each device of interest must be undertaken.

In an attempt to quantify the optimal focusing conditions a theoretical analysis of four flat-top devices has been undertaken, with the plane-wave flat-top bandwidths of these devices ranging from 2 °C up to a maximum of 7 °C. These four devices have been preselected for low level of flat-top oscillation in the hope that the temperature tuning responses remain stable under the various focusing conditions. The preliminary results of these uncompensated gratings are shown in Figure 5.9 where both the peak harmonic output power and the 95% stability flat-top bandwidth are presented. From the plot of harmonic power in Figure 5.9(a) it is clear to see that for all devices the uniform QPM optimal focusing condition of $\xi = 2.84$ is far from ideal, being at maximum only 60% as efficient as at the focus providing optimal power, with this value rapidly decreasing for the higher bandwidth devices. From this plot it is evident that the prior assumption of a tighter focus being required to achieve efficient operation as the flat-top bandwidth is increased is indeed correct. With a focus ratio of $\xi = 10$ and $\xi = 29$ being required for optimal efficiency of the narrowest and widest bandwidth devices respectively.

However, at these tighter focus values a significant compromise is encountered, with the 95% flat-top bandwidth of the devices reducing by over 50% from the plane wave maximum, as shown in Figure 5.9(b). This effect was of course highlighted earlier with both experimental and theoretical results obtained at a focus of $\xi = 2.84$ and can be attributed, at least partially, to the focused fundamental Gouy phase. What is perhaps surprising is that as the focus is further tightened it is found that the bandwidths of all devices begin returning to the plane wave value. This can be explained as the reduction in effective length leading to a general increase in bandwidth. Where the effective length is reduced by the now rapidly diffracting fundamental intensity only interacting efficiently with a very short section of the device.

The same analysis is now applied to the gratings after compensating for the Gouy phase shift,

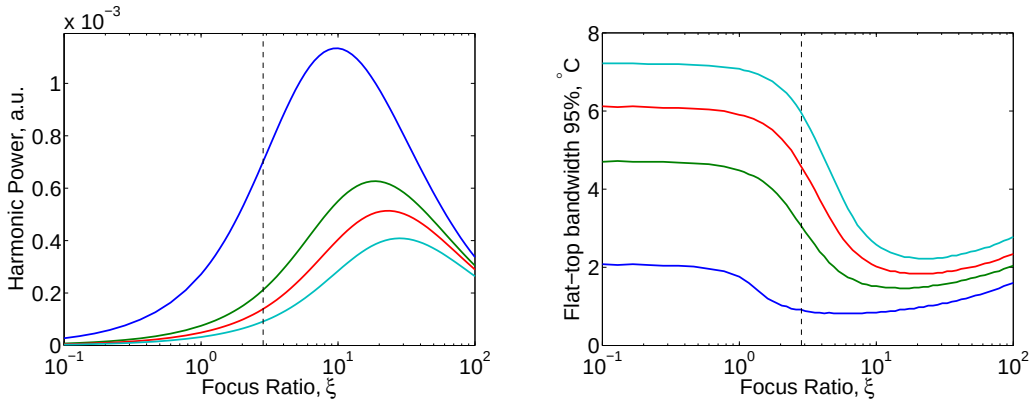


(a) (b)

Figure 5.9: (a) Theoretical plots of the power variation with focusing for un-compensated wide bandwidth devices, (b) flat-top bandwidth variation for changing focus value. For both plots device types are sinc like effective nonlinearity with range $\pm 2\pi$ (blue), $\pm 3\pi$ (blue), $\pm 4\pi$ (blue), $\pm 5\pi$ (blue).

where the shift is fully compensated at each focus point with the results shown in Figure 5.10(a). The results of these simulations are broadly in line with what is expected from the results on uniform gratings in Chapter 4. The most obvious such result being the tighter focus value required to achieve peak efficiency, this of course compares with the slight increase in optimal focussing achieved in uniform gratings.

Further, after compensating the Gouy phase it is clear from Figure 5.10(b) that the reduction in the flat-top bandwidth is less severe, where now the reduction is due solely to the effects of focused intensity. It is again seen that after an initial reduction, caused by the tighter focus only interacting strongly with the near uniform central grating region, the bandwidth again increases due to the previously mentioned reduced effective length.

Finally, the optimum focusing conditions for fully compensated structures are now investigated, where full compensation refers to simultaneously counteracting the effects of both the Gouy phase and spatially varying intensity. The first observation of these results is the drastic shift in optimum focus condition, with all device types operating at maximum efficiency at a much looser focus value. Where for example the narrowest bandwidth device has had its optimal focusing shift from $\xi = 10$ down to a much less severe value of $\xi = 5.5$. This effect is considerably more pronounced for the wider bandwidth devices with the 7 °C bandwidth device moving from $\xi = 37$ to a much more attainable value of $\xi = 16$, with the $1/e^2$ beam diameter at the device aperture dropping from 480 $\mu$m to a smaller 316 $\mu$m and the focused spot size increasing from 6.49 $\mu$m to 9.88 $\mu$m (assuming $LiNbO_3$ as the nonlinear material). Here these spot sizes can

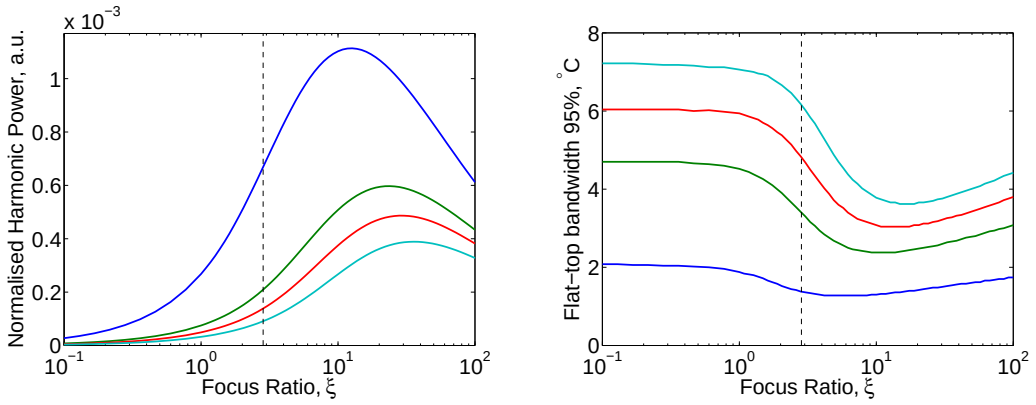


(a) (b)

Figure 5.10: (a) Theoretical plots of the power variation with focusing for Gouy compensated wide bandwidth devices, (b) flat-top bandwidth variation for changing focus value. For both plots device types are sinc like effective nonlinearity with range $\pm 2\pi$ (blue), $\pm 3\pi$ (blue), $\pm 4\pi$ (blue), $\pm 5\pi$ (blue). Here, Gouy compensation is recalculated at each focus value.

becoming quite limiting due to the limited aperture sizes of most QPM materials, with 500 $\mu$m being a common material thickness.

In addition to the reduction in the focus ratio it is also seen that these devices are more sensitive to variations in this ratio, than either uncompensated or Gouy compensated devices, with a small shift in focus conditions leading to a relatively large drop in harmonic output power. Before analysing the flat-top bandwidth characteristics of these devices the cause of this shift and increased sensitivity to focus ratio shall be investigated. On compensating for the spatial variation in fundamental intensity a weighting has been applied to the grating structure that is proportional to the inverse of the electric field strength. This weighting is of course more significant as the focus is tightened, with the effect on the grating structure being an increase in effective nonlinearity at the extremities which in turns creates an increase in effective device length. Thus it can be seen that the process is self enforcing with a tighter focus leading to higher peak electric fields and an increase in effective device length, both of which help drive the efficiency of the nonlinear process higher.

This explanation can explain the higher sensitivity to focus ratio below the peak but cannot account for the rolling over of efficiency with tightening focus and the subsequent rapid efficiency drop. Where it would be expected that the combination of increased electric field and longer effective interaction lengths would result in an ever increasing efficiency with tighter focus. This process would in fact be the correct result if it were possible to indefinitely increase the effective

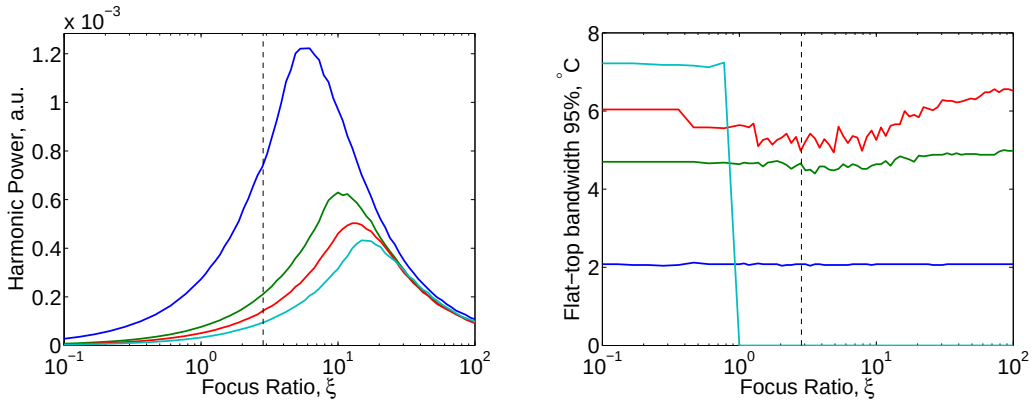


(a) (b)

Figure 5.11: (a) Theoretical plots of the power variation with focusing for Gouy and spatial intensity compensated wide bandwidth devices, (b) flat-top bandwidth variation for changing focus value. For both plots device types are sinc like effective nonlinearity with range $\pm 2\pi$ (blue), $\pm 3\pi$ (blue), $\pm 4\pi$ (blue), $\pm 5\pi$ (blue). Here, Gouy and spatial intensity compensation is recalculated at each focus value.

nonlinearity at the extremities of the device and thus increase the effective interaction length. However, as explained earlier the increase in nonlinearity is only an effective increase, with it being impossible to actively increase the nonlinearity of a QPM device above the natural nonlinearity. Instead the nonlinearity is effectively increased at the device extremities in proportion to the nonlinearity at the centre, examples of this redistribution of nonlinearity for various focusing values are given in Figure 5.12.

Here, for both figures - with Figure 5.12(a) being that of the 2 °C and Figure 5.12(b) being the 7 °C flat-top bandwidth device - effective nonlinearities are shown for a plane wave interaction (blue) and focusing values just above and below the optimum focusing condition (red and green respectively). From these plots it is clear that as the optimum focusing conditions are approached (green) the central region of the nominally sinc like strucure itself becomes broadened and flattened, with a large proportion of the device having close to maximum effective nonlinearity i.e. no missing domains. But, as can be seen for the tighter focusing condition (red) the weighting compensation for the focused intensity can increase more rapidly than the sinc function naturally decreases. This leads to the situation where the very centre of the sinc structure is no longer the region with highest effective nonlinearity and as such domains must be removed. Of course the very centre of the sinc is also the region with the highest focused intensity, so as domains are removed from this section the efficiency rapidly decreases.

Having explained the unexpected efficiency behaviour of the devices with focusing the analysis

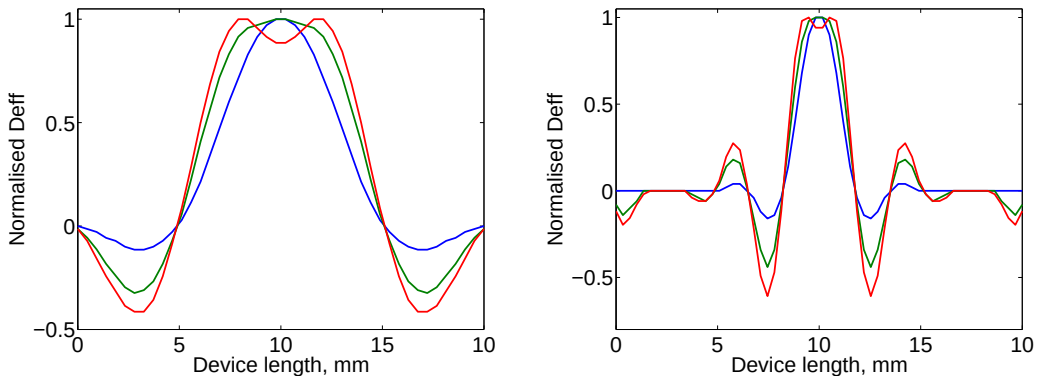


(a) (b)

Figure 5.12: The variation in the sinc like effective nonlinearity for 2 °C (a) and 7 °C (b) flat-top bandwidth devices for plane wave conditions (blue), optimal focusing with spatial intensity compensation applied (green) and for over tight focusing with intensity compensation.

now returns to Figure 5.11(b) and the effects of focusing on the flat-top bandwidth of these completely compensated devices. With the full compensation of the effects of focusing it should be expected that the bandwidth of these devices is unchanged no matter the level of focusing, with only the efficiency being of concern when choosing the optimum focusing conditions. Although this proposition holds true for some device types, in particular the lowest bandwidth devices (blue) which has a maximum of 5% deviation in bandwidth, it is not the case for all devices. Of particular note is the bandwidth variation of the most broadband device where it can be seen that for focusing over $\xi = 0.8$ the 95% bandwidth is 0 °C. Here a 0 °C bandwidth implies that an unacceptable variation in output power is achieved along the flat-top and as such the design must be rejected.

The reason for this breakdown in the compensation technique can again be explained by the limitation of using quantised values to represent the effective nonlinearity, where the number of quantisation levels has been predetermined to optimise the plane-wave response. The problem lies in that the optimisation of quantisation levels giving the best representation of the apodised plane-wave sinc structure does not always translate to the best representation of the inverted Gaussian intensity compensation. As such, although the effects of focusing can in principle be negated the compensation techniques must be utilised throughout the design procedure and not added as an afterthought to a plane-wave design. This however raises further difficulties in optimising the domain structures, with now four variables requiring adjustment to obtain the desired bandwidth response (sinc oscillations, quantisation levels, windowing function and

focusing value). Despite this, and as shown by the plots of Figure 5.12, an upper limit on focus ratio can be readily obtained by ensuring that the focus ratio is only increased for each design until the point that the centre of the sinc function is no longer at maximum effective nonlinearity. However, this technique will likely not hold for structures more complex than that of the simple apodised sinc, such as devices designed by simulated annealing or other self optimising methods.

## 5.6 Conclusion

In conclusion in this chapter an analysis of the effects of focusing on the symmetry of the temperature tuning response of synthesised QPM devices, designed for constant power operation across large temperature fluctuations, has been performed. It has been experimentally shown that when performing at close to optimum focusing conditions the flat-top temperature tuning response of a synthesised device becomes highly asymmetric, resulting in a significant drop in the temperature bandwidth over which constant power can be maintained. Using a simple low power analytic model of focused Gaussian beams these measured asymmetries have been shown to be entirely attributable to the Gouy phase shift of the focused beam. Further, using the Gouy compensation technique highlighted in Chapter 4 it has been theoretically demonstrated that this asymmetric response can be completely negated, with the compensation technique fully compatible with the complex grating design.

Despite compensation of the focused Gouy phase it was found that the response of the devices under focused interactions differed from the theoretical plane-wave simulations, with a reduction in temperature bandwidth observed for all device types. This effect was theoretically shown to be a consequence of the non-uniform power density along the axis of the focused beam, with the extremities of the devices contributing less than the device centre due to the reduced focused intensity. A correction for this effect has been proposed that pre-compensates for the spatial power variation through an increase in the effective nonlinearity of the device extremities to match the power variation of a focused Gaussian beam. This compensation has been shown, through simulation, to completely counteract the spatial power variation and, when combined with Gouy phase compensation, provides a tuning response almost exactly comparable to the plane-wave case.

Finally, an investigation has been undertaken to determine the optimum focusing conditions for these complex grating structures. With such gratings it is no longer reasonable to assume that the optimum focusing conditions for bulk and uniform QPM gratings apply due to the complex grating layout. It has been found that optimum focusing conditions for fully compensated devices, both Gouy phase and spatial power compensated, are considerably less tight than for

the uncompensated devices. Although, the optimum focusing is still considerably tighter in the compensated devices compared with the uniform or bulk devices due to the much shorter effective interaction length, with this being especially true for the greatest bandwidth devices.

# References

[1] H. E. Major, C. B. E. Gawith, and P. G. R. Smith. Gouy phase compensation in quase-phase matching. *Opt. Commun.*, 281(19):5036–5040, October 2008.

[2] R. W. Boyd. Intuitive explanation of the phase anomaly of focused light beams. *J. Opt. Soc. Am.*, 70(7):877–880, July 1980.

[3] G. D. Boyd and D. A. Kleinman. Parametric interaction of focused Gaussian light beams. *J. Appl. Phys.*, 39(8):3597–3639, 1968.

# Chapter 6

# Towards 100% focused efficiency in QPM structures

## 6.1 Introduction

For the creation of laser sources by means of nonlinear parametric interactions to become viable as an alternative to direct generation using solid-state or semi-conductor diode lasers many inherent limitations must be overcome. Many of these limitations, which in the common materials of lithium nobate and lithium tantalate include effects such as photorefractive damage, green induced infra-red absorption (GRIIRA) and relatively low power handling, have been somewhat negated with novel new material types. Where materials such as magnesium doped congruent lithium niobate (MgO:$LiNbO_3$) and lithium tantalate (MgO:$LiTaO_3$) have shown great promise in reducing the significance of these effects [1] and can result in improved working lifetimes under more favourable working conditions [2]. However, these factors aside a greater concern is the conversion efficiency of such a device for a given fundamental input power, where high efficiency at all input power levels is desirable. Here many factors determine the overall device efficiency and include the magnitude of the nonlinear coefficient, the phase-matching condition, device length and fundamental input intensity. Of course the nonlinear coefficient is dependent on the material type and cannot readily be improved upon. Instead, in this chapter attention shall be given to understanding the effects of fundamental input intensity, device length and phase-matching (specifically quasi-phase-matching) on the efficiency of the parametric interaction.

Many studies have previously been undertaken to determine the role of increased fundamental intensity in nonlinear interactions, with particular attention paid to understanding the processes

involved as 100% conversion efficiency is approached [3, 4, 5]. In these studies many differing regimes are often considered these include; the guided wave regime, where high intensities can be obtained even from relatively low input powers through tight modal confinement, focused bulk interactions where intensity enhancement is provided by constraining the power through tight focusing [6, 7] and intra-cavity regimes where the high intensity is provided by the large oscillated field [8]. A further regime encountered is that of unfocused bulk interactions, where the high power density provided by focussing is not desired as it can lead to optical damage in the nonlinear device with sufficiently high fundamental powers [9]. To date none of the theoretical analysises have been all encompassing, with some only treating focused beams as simple superpositions of plane-waves [10], whilst others although accounting for diffraction do not perform rigourous analysis of k-vector mismatch [7] and thus misinterpret the high power behaviour. Still more simulations are only valid for materials with constant nonlinearity, where more of the complex phase-matching conditions such as the Gouy phase [11, 12] and Rustagi phase-shift [13, 14] cannot be readily compensated. Although some of these works acknowledge the detrimental effect such sources of dephasing can have none have provided possible methods to correct for them.

In this chapter the majority of the analysis shall be aimed at focused parametric interactions, a regime more suited to high average fundamental power than waveguide devices. Further, it has been shown experimentally that 99% pump depletion has been achieved in waveguide based interactions [15] and as such it would appear that further theoretical investigation is not required. Despite this, some of the concepts discussed for high power focused interactions can equally be applied to waveguide interactions and provide possible explanations for some of the effects observed through experimentation as input power is increased. Using a modified beam propagation method (BPM), where parametric interactions have been included, a thorough analysis of the limiting effects of focused efficiency at high powers shall be undertaken. Here factors such as parametric dephasing [3, 5], fundamental bandwidth broadening by back conversion [16], the Gouy phase shift [11, 12], spatially non-uniform pump depletion and the intensity dependent Rustagi phase shift [13, 14] shall be considered.

Using BPM it shall be shown by modelling the complex parametric interactions occurring in realistic bandwidth fundamental beams that at higher conversion efficiencies compensating for the Gouy phase can result in reduced bandwidth broadening of both the fundamental and subsequently the harmonic beams. It shall further be shown that at very high pump depletion compensating for the standard Gaussian Gouy phase does not completely prevent back conversion, although it does allow higher efficiency and greater output powers before back conversion

occurs. Here a limit is placed on conversion efficiency, where due to complex effects such as non-uniform fundamental depletion the Gouy phase of an input Gaussian beam deviates from its low power value and thus requires a modified phase-matching structure. Further, the effects of diffractive 'healing' of the Gaussian beam shall be considered with the implications for higher efficiency parametric interactions discussed. Finally, the effects of the intensity dependent phase variation between fundamental and harmonic waves shall be investigated, where in very high power regimes such as created by femtosecond duration pulses the phase matching condition of even plane wave interactions varies along the device length and must be suitably compensated to prevent back conversion.

## 6.2 Beam Propagation Method with nonlinear coupling

In Chapter 4 a simple analysis technique was utilised to predict the behaviour of low power focused parametric interactions. However, this technique is limited to power regimes where the conversion efficiency of the nonlinear interactions is negligible and therefore cannot be utilised for investigating the effects of high power focused interactions. As such an alternative technique based on the split-step beam propagation method (BPM) has been developed to analyse the high power regime. Where by considering the spatial Gaussian profile of a focused beam and how this profile varies due to the effects of diffraction a more complete model of the harmonic processes can be developed.

Here a brief outline of the BPM technique shall be given. Returning to Equation 2.15 and re-writing in a form more readily applicable to BPM a description of the spatial variation of the optical electric field is given as

$$\nabla^2 \mathbf{E}\left(x,y,z\right) = -k^2 n^2\left(x,y,z\right)\mathbf{E}\left(x,y,z\right) - \mu_0 \omega^2 \mathbf{P}^{NL}\left(x,y,z\right) \tag{6.1}$$

Now by separating the electric field $\mathbf{E}\left(x,y,z\right)$ into two parts, the axially slowly varying envelope $\hat{\mathbf{E}}\left(x,y,z\right)$ and the rapidly varying term $e^{-ikn_o z}$, a new expression for the electric field is given as

$$\mathbf{E}\left(x,y,z\right) = \hat{\mathbf{E}}\left(x,y,z\right) e^{-ikn_o z} \tag{6.2}$$

Substituting this expression into Equation 6.1 a further expression can be obtained

$$\nabla^2 \hat{\mathbf{E}} - i2kn_0 \frac{\partial \hat{\mathbf{E}}}{\partial z} + k^2\left(n^2 - n_0^2\right)\hat{E} + \mu_0 \omega^2 \mathbf{P}^{NL} = 0 \tag{6.3}$$

Here simplifications have been made through application of the slowly varying envelope function and further re-defining $\nabla^2 = \frac{\partial^2}{\partial x^2} + \frac{\partial^2}{\partial y^2}$. Now by considering the weakly guiding condition

$\left(n^2 - n_0^2\right) \simeq 2n_0\left(n - n_0\right)$, Equation 4.26 can be written as

$$\frac{\partial \hat{\mathbf{E}}}{\partial z} = -\frac{i}{2kn_0}\nabla^2\hat{\mathbf{E}} - ik\left(n - n_0\right)\hat{E} - \frac{i\mu_0\omega^2}{2kn_0}\mathbf{P}^{NL} \tag{6.4}$$

Here, the weakly guiding approximation has been applied for consistency with the majority of literature on BPM although this is not necessary for the bulk interactions to be investigated here. When $n = n_0$ it is clear that only the first term on the right hand side governs the free space propagation of the electric field, with the second term defining guiding and the final term being an expression for the nonlinear polarisation. All these terms affect the electric field propagation simultaneously, however, the fundamental premise of the BPM technique is that on sufficiently small scales all these terms can be considered independent. Physically, this can be thought of as propagating the electric field over a small distance, $h$, and subsequently correcting for the spatial phase retardation caused by the refractive index variations. For the simulations employed here it is also necessary to calculate the nonlinear contributions over the step size. Here, a slight complication lies in that the step sizes required for high accuracy modeling of the nonlinear interactions is considerably shorter than that required for accurate free space propagation analysis.

For the case of a homogeneous optical medium, as is relevant to this work, Equation 6.4 can be expressed as

$$\frac{\partial \hat{\mathbf{E}}}{\partial z} = -\frac{i}{2kn_0}\nabla^2\hat{\mathbf{E}} - \frac{i\mu_0\omega^2}{2kn_0}\mathbf{P}^{NL} \tag{6.5}$$

By considering the nonlinear term as independent from the propagation this expression can be further spatially Fourier transformed, with respect to $x$ and $y$, to give

$$\frac{\partial \mathbf{\Psi}}{\partial z} = -\frac{k_x^2 + k_y^2}{2jk}\Psi \tag{6.6}$$

where $F\left\{\hat{\mathbf{E}}\left(x, y, z\right)\right\} = \mathbf{\Psi}\left(k_x, k_y, z\right)$. Solving this equation for an initial field, $\hat{\mathbf{E}}(x, y, 0)$ provides the paraxial transfer function $H(k_x, k_y; z)$:

$$H(k_x, k_y; z) = \frac{\mathbf{\Psi}(\mathbf{k_x}, \mathbf{k_y}; \mathbf{z})}{\mathbf{\Psi}(k_x, k_y; 0)} = exp\left[\frac{i\left(k_x^2 + k_y^2\right)z}{2k}\right] \tag{6.7}$$

By now expressing the full nonlinear interaction in terms of separable operators an understanding of the important BPM functions can be inferred. Defining

$$\frac{\partial \hat{\mathbf{E}}}{\partial z} = \left(D + S\right)\hat{\mathbf{E}} \tag{6.8}$$

where $D = \frac{1}{2ik_0}\nabla^2$ is the operator that accounts for free space propagation and $S$ is the nonlinear contribution term (for waveguide interactions $S$ would also contain the phase corrections

accounting for index variations). In reality these two operators act simultaneously, with the operator form of the solution to the above equation given as

$$\hat{\mathbf{E}}\left(x, y, z + \Delta z\right) = exp\left[\left(D + S\right)\Delta z\right]\hat{\mathbf{E}} \tag{6.9}$$

if $D$ and $S$ are considered independent of $z$. This assumption can be considered valid as the incremental steps in the z direction are sufficiently small that any change in these operators over a propagation step is negligible. Using the Baker-Hausdorff formula [17] the two independent, noncommuting operators $exp\left[\left(D + S\right)\Delta z\right]$ can be re-written as

$$exp\left(D\Delta z\right)exp\left(S\Delta z\right) = exp\left[D\Delta z + S\Delta z + \frac{1}{2}\left(DS - SD\right)\left(\Delta z\right)^2 + \ldots\right] \tag{6.10}$$

which for first order accuracy can be simplified to

$$exp\left[\left(D + S\right)\Delta z\right] \simeq exp\left(D\Delta z\right)exp\left(S\Delta z\right) \tag{6.11}$$

This now implies that the operator form of the equation governing the propagation of the electric field can be expressed to first order accuracy as

$$\hat{\mathbf{E}}\left(x, y, z + \Delta z\right) = exp\left(D\Delta z\right)exp\left(S\Delta z\right)\hat{\mathbf{E}} \tag{6.12}$$

with the free-space propagation now acting separately from the nonlinear coupling term (or even the refractive index induced phase correction, as would be encountered in non-homogeneous materials).

Now, with this separable form of the propagation equation it becomes possible to readily simulate the interacting fields in a nonlinear material. Noting that Equation 6.6, which is the free space propagator transfer function, is defined in the spatial frequency domain it is clear that performing the propagation step in the same domain is advantageous. However, the nonlinear coupling term is more readily solved in the spatial domain. As such the analysis must be performed as a two part process. Firstly, spatially Fourier transform the electric fields (numerically this is best performed using the discrete fast Fourier transform technique) and propagate the fields using the transfer function of Equation 6.6, with $z$ replaced by the desired propagation distance. Now, perform the inverse spatial Fourier transform to return to a coordinate system within which the nonlinear coupling between the fields can readily be calculated. Here, numerical integration offers the most straightforward approach. In this work the Runge-Kutta4(5) numerical integration technique has been applied, with the integration step performed over the same physical length as the earlier beam propagation step. A graphical representation of the required steps is shown in Figure 6.1.

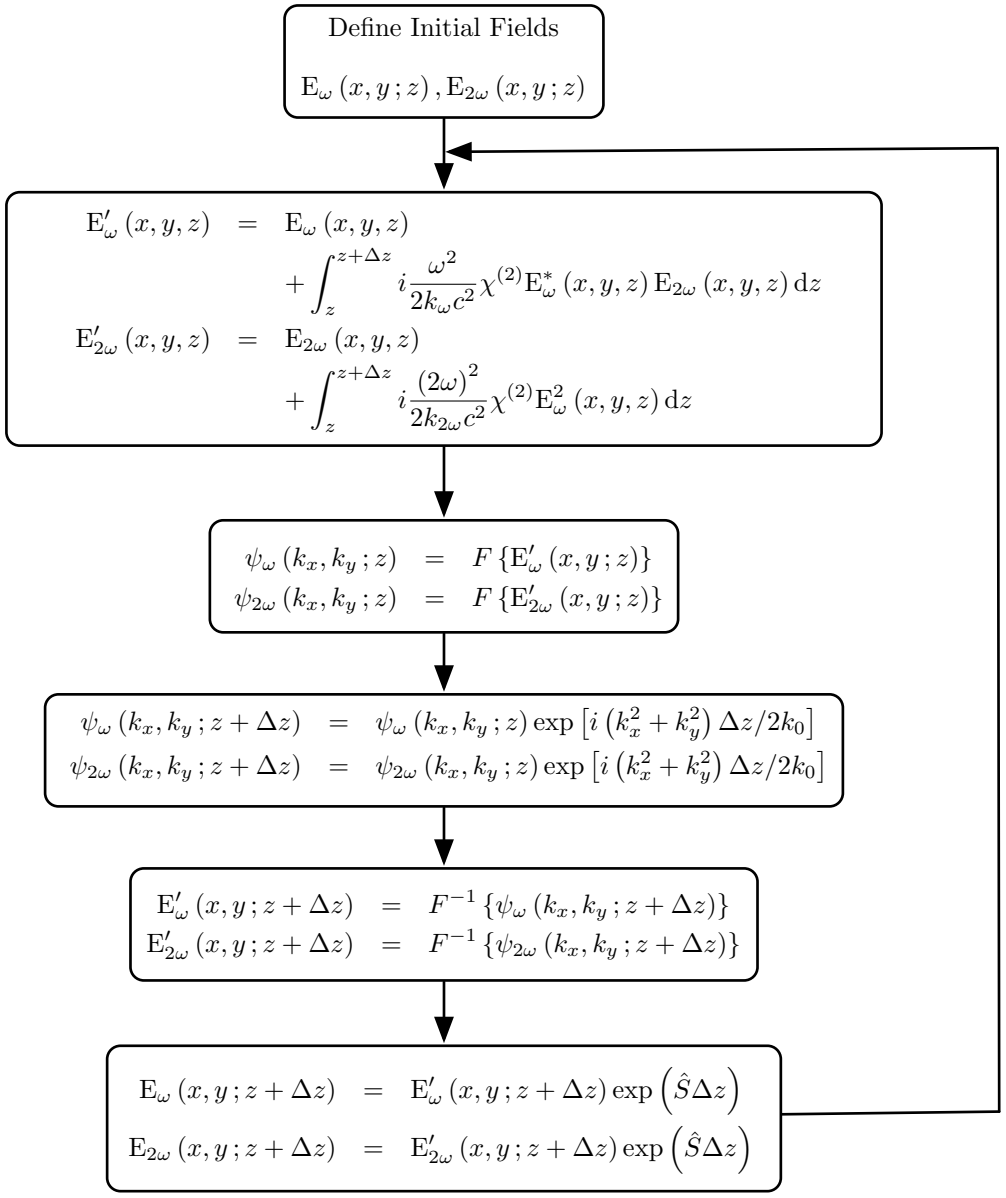


Figure 6.1: Flow chart of the steps for BPM with nonlinear coupling

A further enhancement to this technique is often utilised. Where, by performing a half step in the z direction, using the free space propagator, then correcting the phases of the fields and performing the nonlinear coupling for a full step and finally propagating the final half step provides higher accuracy in the simulation. This accuracy is obtained through a higher order expansion of Equation 6.10. In this work however, this enhancement has not been utilised. Due to the small steps required to correctly simulate the harmonic processes, steps which are considerably shorter than those required for beam propagation, performing the extra half steps

offer no tangible accuracy enhancement.

## 6.3 Limiting back conversion through Gouy Phase compensation

Achieving a highly efficient parametric process requires a high degree of phase matching, where even a small phase error between the interacting waves can result in significant back conversion of the generated harmonic field [3], with this requirement becoming even more essential as the nonlinear coupling between the waves increases. This is readily observed in the $\Delta k$ tuning curves for high power interactions, where as shown in Figure 6.2 a clear narrowing of the central phase-matching peak occurs as higher powers are utilised.

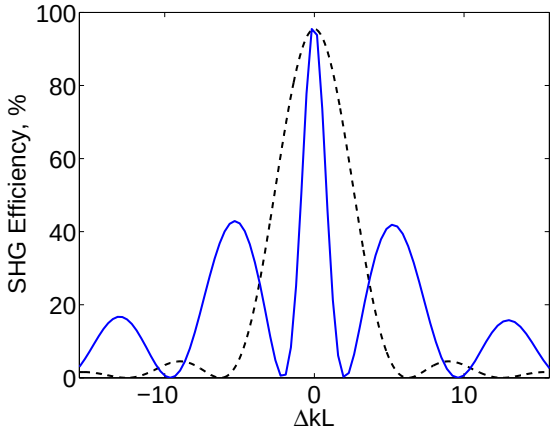


Figure 6.2: A numerical simulation of high efficiency second harmonic generation, showing the narrowing of the acceptance bandwidth and saturation of nonlinear drive resulting in high efficiency side lobes (blue). Also shown is the low power acceptance bandwidth (black).

Aside from the narrowed tuning response increasing the tolerances required for stable phase-matching, dephasing between the propagating waves and the compensating grating structure can have the undesired effect of broadening the bandwidth of the fundamental and, in turn, the harmonic waves. Here through small errors in the phase matching condition an interaction between the relatively high powers at the centre of the second harmonic bandwidth and the low power extremities of the spectral bandwidth of the fundamental wave can become efficiently phase-matched. At high fundamental power, and thus high second harmonic power, this interaction can lead to significant amounts of the harmonic beam being depleted into the side lobes of the fundamental, resulting in a reduced conversion efficiency. The sources of the dephasing

are numerous and include temperature offsets, wavelength drift, angled grating alignment and for focused interactions as discussed in Chapter 4 the Gouy phase shift. Here it was shown that the spatially varying phase of the fundamental beam at optimum focusing can only be approximately matched by the phase of uniform grating structures. As a result over large lengths of the nonlinear material a significant phase error exists providing a route for back conversion of the generated harmonic field.

As higher powers and greater efficiencies are demanded the effects of back conversion becomes more significant, where with a more intense second harmonic signal the efficiency of detrimental back conversion to new frequencies increases. Due to the high powers required to see this back conversion the simplistic non-depletion model developed in an earlier chapter was unable to model the effect. As such conclusions as to the effectiveness of compensating for the Gouy phase to prevent back conversion could not be made. Now however, using the modified nonlinear BPM analysis it is feasible to model the advantages Gouy phase compensation can provide.

### 6.3.1 Single longitudinal mode simulations

To investigate the effect of dephasing and back conversion it is useful to consider the most simplistic case of a theoretical single frequency or single-longitudinal mode (SLM) laser. Although using such a theoretical model it is impossible to simulate the effects of back conversion to new frequencies useful information can still be obtained on the general behaviour of nonlinear devices as fundamental input power is increased. Here two nonlinear QPM devices are simulated under the effects of focusing using the split-step BPM method, a standard PPLN based QPM device and a Gouy phase compensated QPM (GQPM) device. To provide maximum conversion efficiency both devices are simulated with focused Gaussian beams with the spot size chosen to provide the optimum focusing ratios of $\xi = 2.84$ and $\xi = 3.3198$ respectively. Here the focusing parameter $\xi$ is simply the ratio of the device length (L), which for both devices is 20 mm, to twice the Rayleigh range ($z_R$) of the focussed beams, i.e. $\xi = L/(2z_R)$.

For these calculations care must be taken in defining the spatial Gaussian properties of the interacting waves, with particular attention paid to the size of the spatial co-ordinate grids such that the furthest extent of significant power in the Gaussian mode is considerably smaller. Here, if too small a spatial grid is utilised, upon application of the Fourier transform 'reflections' from the spatial boundaries can occur leading to distorted mode propagation. In general defining the spatial boundaries to be approximately 5 times greater than that of the largest expected $1/e^2$ mode radius is sufficient to prevent distortions. A further consideration that must be made is that of the spatial resolution of the Gaussian mode, here it is essential that high resolution

is utilised to correctly model the full effects of focusing. Although at low spatial resolution the Gaussian mode can be seen to focus and subsequently diffract, after passing through the waist, the Gouy phase gained through focusing is incorrect. For a phase-matched interaction the exact phase of the propagating mode is important to provide accurate simulations, as such it is important to ensure the phase of the diffracted beam matches that of the analytic Gouy phase before attempting to model parametric processes. This problem becomes more severe for short device lengths where the optimal spot size is smaller and thus the diffraction rate is faster, here to ensure accurate representations of the focused beams very high spatial resolution is required. In general if the spatial co-ordinate system is set to be 5 times the maximum spot size a minimum axis resolution of $2^6$ data points is required. Here, the grid size is limited to powers of 2 as this provides the most computationally efficient fast Fourier transform. For shorter device lengths $< 2\,\text{mm}$ this figure needs increasing to $2^7$, giving rise to over 16,000 data points for which the Fourier transform, free space propagator, inverse transform and final Runge-Kutta integration must be performed. From this it is clear that a huge number of calculations must be performed to simulate the conversion efficiency of real devices, where this process is repeated multiple times per coherence length to achieve accurate results. As an example, to provide the conversion efficiency of a 20 mm long device phase-matching the SHG of 532 nm light at a single $\Delta k$ value over 550 million calculations must be performed, where here for simplicity it is assumed that the Fourier, free space propagator and Runge-Kutta steps are a single calculation.

The effects of back conversion in focused interactions have been investigated for a range of fundamental input powers, where the power has been raised to the point that maximum conversion efficiency occurs. At the point of maximum conversion efficiency further harmonic power increases are limited by back conversion, where even small errors in phase matching become a source of significant power loss. It is expected that a Gouy compensated device is capable of providing useful harmonic output at higher input powers than standard uniform QPM devices, where through the perfect compensation of the propagating phases back conversion is prevented.

The results of the BPM simulations are given in Figure 6.3(a) which shows the harmonic conversion efficiency for 20 mm long QPM (green) and GQPM (blue) PPLN based devices for increasing fundamental input powers. Also shown, Figure 6.3(b), is the percentage difference in output power for the two device types. Here it is clear that GQPM is able to provide a higher conversion efficiency for the majority of input powers when compared with standard QPM, as would be expected from the non-depletion analysis of Chapter 4. However, despite the compensation of the Gouy phase it is evident that even a GQPM device is incapable of completely preventing back conversion, with the conversion efficiency reducing at high nonlinear drive. It is

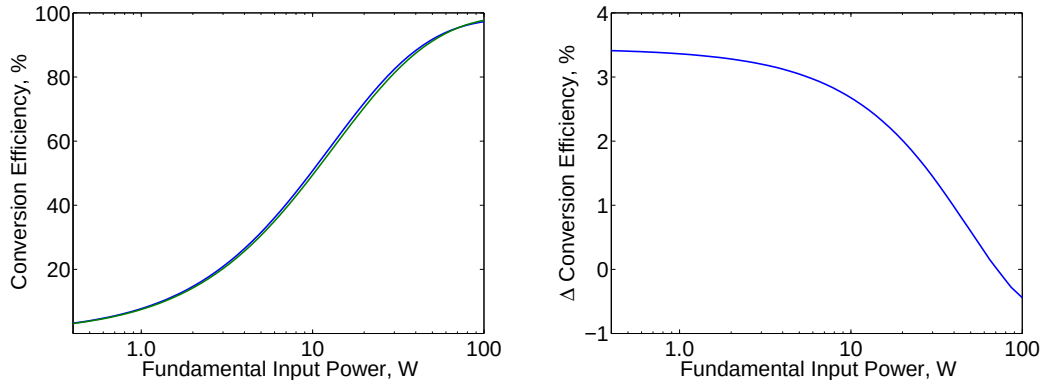


(a) (b)

Figure 6.3: (a) A theoretical plot of the conversion efficiency of both standard QPM (green) and Gouy compensated GQPM devices (blue) with increasing fundamental input power of a focused single longitudinal mode laser generated using split-step BPM. (b) The percentage increase in conversion efficiency of a GQPM device over standard uniform QPM. For both devices the focus was set to optimal i.e. $\xi = 2.84$ and 3.3198 for QPM and GQPM respectively with a device length of 20 mm. Further, to ensure maximum conversion efficiency the $\Delta k$ values were optimised at each power level.

further clear from Figure 6.3(b) that at very high nonlinear drive, where the conversion efficiency approaches 95%, that there is no advantage in utilising a Gouy compensated structure compared to a standard uniform QPM device and in fact such a device may prove detrimental for powers higher still. The cause for this limit on maximum input power is non-uniform pump depletion, an effect that modifies the Gaussian nature of the fundamental beam thus altering the Gouy phase [7]. The effect of non-uniform pump depletion shall be further investigated and possible remedies shall be offered that overcome its deleterious effects providing a route to 100% pump depletion even at high nonlinear drive.

### 6.3.2 Multi-longitudinal mode simulations

Having shown that for a single frequency laser a GQPM sample can provide moderate gains, of the order of 3.5%, over standard QPM for all but the highest nonlinear drives the effect of back-conversion on a real bandwidth, multi-longitudinal mode (MLM) laser input shall now be theoretically examined. Here it is expected that GQPM with its perfect low power phase-matching should limit the routes of back-conversion compared with uniform QPM, which due to the Gouy phase of the focused fundamental beam has significant phase mis-match along its length. By removing the source of de-phasing between the propagating waves and the grating

there is no longer a route for parametric back-conversion of the generated high power harmonic field into the tails of the fundamental bandwidth and as such the conversion efficiency of the GQPM based device should remain higher.

The effect of back-conversion has been simulated by defining the input harmonic field as a Lorentzian distribution of power across a range of wavelengths, centred at the wavelength of interest. To perform the split-step BPM analysis each frequency is defined as a Gaussian mode such that its focussed beam waist matches that of the ideal single frequency value, by propagating each mode individually it is possible to simulate a real bandwidth interaction. However, although the spatial propagation step is no more involved that for a single frequency simulation, apart from a greater number of modes to propagate using the Fourier transform technique, the complexity of the nonlinear coupling step is vastly increased. To fully simulate the effects of the nonlinear interaction and to allow all possible routes of back-conversion every mode must be allowed to interact with all other modes, this results in an huge increase in computation. In fact, if modelled fully, through nonlinear coupling an infinite number of frequencies will be generated. Where each new frequency mixes with existing frequencies, through SHG, SFG and DFG interactions, to generate yet more frequencies. To reduce this effect some constraints are placed on the modelling simulations, these include limiting the generated frequencies to lie within the transparency bandwidth of the material to be simulated, rounding of the generated frequencies (to a frequency resolution of 3.3 GHz or alternatively a wavelength resolution of 2 pm) such that only a small subset of new frequencies may be generated and finally limiting the data points in the fundamental bandwidth.

For the purpose of these simulations a 1064 nm wavelength multi-longitudinal mode laser has been simulated, with a FWHM Lorentzian bandwidth of 20 pm, the total fundamental frequency spread investigated is 160 pm. It must be noted at this stage that, for simplicity, all of the fundamental modes have been defined in-phase. That is, at the start of the crystal the electric fields of every mode is aligned, an effect analogous to a mode-locked laser pulse. The alternative is to assign an arbitrary phase to each frequency. However, in doing so for some sets of input phase the conversion efficiency would be considerably lower than the average. As such, to provide a realistic representation of the parametric interaction the calculation must be performed numerous times, each time with a random distribution of input phases, and the results averaged. This technique however is currently impractical with the simulation being too computationally intensive. Here, for example, in using the laser characteristics defined above 81 fundamental frequencies are generated, with these frequencies able to mix in over 3000 combinations. For the entire device this results in over 330 billion calculations of the coupled equations for a single

$\Delta k$ value. Here the maximum split-step resolution is determined by the criteria of total energy conservation, where overly large steps can result in a gain in the total system energy through numerical error. With current computing power a single calculation of the multi wavelength conversion efficiency takes approximately one month of continuous processing. From this it is clear that repeating the calculation for random input phases is not currently feasible.

In Figure 6.3(a) it was shown that at very high nonlinear drive the performance of GQPM suffered, with its efficiency gains over uniform QPM lost. However, for more modest input powers, resulting in approximately 60-70% conversion efficiency, it was clear that GQPM was still able to provide an advantage over QPM due the reduction in phase errors through Gouy phase compensation. From this it can be expected that the higher degree of phase matching along the entire length of the GQPM device, in contrast to the best fit average phase-matching of QPM, will limit the effects of back conversion. This has been tested using the multi-longitudinal mode laser model described above, where initially an input power of 1.25 W has been used with a 10 mm long device. Although the total fundamental power used for this calculation is low when compared with the results of Figure 6.3(a), producing only 20% efficiency for a device twice as long, due to the 'mode-locked' nature of this simulation the effective single frequency power is considerably higher. Here by having all input fields in phase the fundamental electric can be considered as the sum of all the separate fields, which provides an efficiency greater than any individual mode. If the total power is defined as $P$, and the number of separate frequency modes $m$ the difference in nonlinear drive between a SLM and a MLM calculation can be represented algebraically as:

$$\begin{aligned} E_{slm} &\propto \sqrt{P} \\ E_{mlm} &\propto \sqrt{(P/m)} \end{aligned}$$

where $E_{slm}$ and $E_{mlm}$ are the electric fields of each mode of the single longitudinal and multi-longitudinal mode sources respectively. Here it is assumed that the power is evenly distributed between all frequencies and that all modes are perfectly in-phase. From this it is clear that when coupling through the second order nonlinearity the effective nonlinear drive of the multi-mode mode-locked source is considerably larger and can be represented as:

$$\begin{aligned} P_{eff_s} &\propto |E_{slm}|^2 \\ &\propto P \\ P_{eff_m} &\propto \left|\sum E_{mlm}\right|^2 \\ &\propto mP \end{aligned}$$

Where, $P_{eff_s}$ is the single mode effective power and $P_{eff_m}$ the multi-mode. This would imply

that for the 81 mode simulation above the 1.25 W input power is in fact approximately equivalent to a 100 W source. However, the distribution of power between the modes of the simulation is not uniform and as such is likely much lower than this maximum value.

The results of the split-step BPM back conversion calculation for the multi-mode source using the 81 modes described above are given in Figure 6.4. Here back-conversion is determined through observation of the gain of the fundamental power at each frequency component and also the conversion efficiency of the total power at the end of the devices. For these simulations the device $\Delta k$ has been held constant at the low power peak value determined through the SLM simulations. Although this value may not provide the peak conversion efficiency, as described above it is computationally unfeasible to sweep $\Delta k$. Further, it was found that for moderate conversion efficiency, ∼60%, under SLM simulations the peak $\Delta$k value is almost unchanged from the lower power value for both GQPM and QPM.

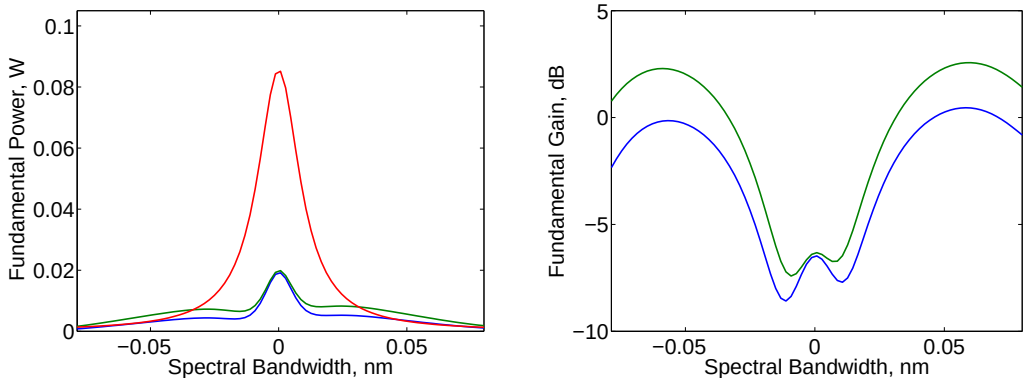


(a) (b)

Figure 6.4: (a) Theoretical plots of a 1.25 W mode-locked fundamental beam with a FWHM bandwidth of 0.02 nm prior to parametric conversion (red) and the resulting bandwidth at the end of 10 mm of uniform QPM (green) and GQPM (blue). (b) The resulting parametric gain of the fundamental bandwidth due to back conversion. Here it is clear that the GQPM device (blue) almost completely prevents back conversion giving 69.8% efficiency, in contrast at this power level the standard QPM sample allows considerable back conversion giving a lower efficiency of 56.9%.

Figure 6.4(a) shows the fundamental, Lorentzian distribution, wavelength bandwidth of the multi-mode source prior to propagation and parametric interactions (red). For comparison the total simulated bandwidth is 160 pm with a FWHM of 20 pm, and the FWHM bandwidths of the 10 mm long PPLN based devices are approximately 190 pm at this fundamental wavelength of 1064 nm. It is clear that the simulated multi-mode source fits completely within the device

bandwidth and as such the major source of dephasing is limited to the spatially varying Gouy phase. The resulting final fundamental power distributions at the exit of the devices for QPM (green) and GQPM (blue) are also shown, here it is evident that significant power has been converted from the fundamental frequency to the harmonic, with the conversion efficiency of the QPM and GQPM devices being approximately 57% and 70% respectively.

The favourable conversion efficiency of the GQPM device indicates that back-conversion has been suppressed, providing significantly higher performance enhancements than the 3.5% increase predicted using the low power non-depletion or even high power single frequency simulations. Now by comparing the parametric gain of each frequency component, Figure 6.4(b), the significance of the spatial Gouy compensation is clear. For the standard uniform QPM device (green), which has a considerable amount of phase error along its length, there are many routes for relatively efficient back conversion to the extremities of the fundamental bandwidth resulting in large spectral regions of net gain. In contrast the gain plot of the GQPM device (blue) shows that back-conversion has been almost completely suppressed with only a very small spectral bandwidth providing any net power gain.

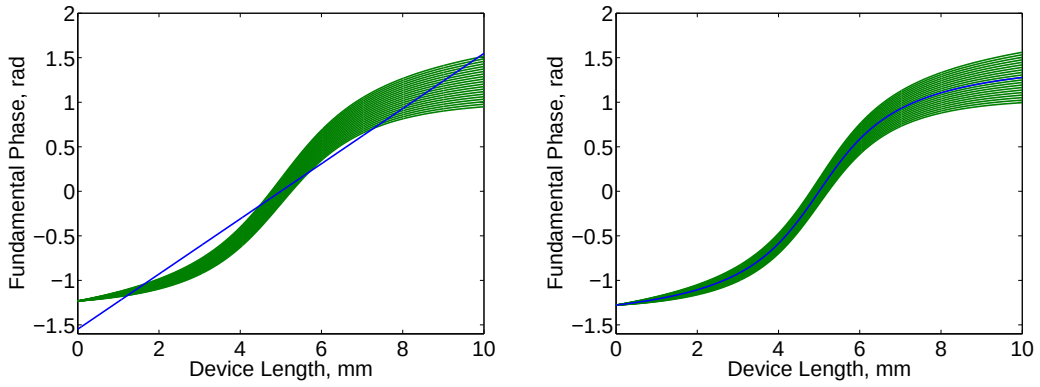


(a) (b)

Figure 6.5: (a) A theoretical plot of the Gouy phase variation of focused, 20 pm uniform bandwidth, multi-longitudinal mode fundamental source with a focus ratio of $\xi = 2.84$ and the corresponding best linear grating phase to provide maximum conversion efficiency. (b) The Gouy phase variation of the same theoretical source focused to give $\xi = 3.3198$ and the corresponding best non-linear grating phase with which to compensate.

By considering the phase of the propagating fundamental field and the corresponding phases of both the uniform QPM and the spatially varying GQPM devices an insight into the causes of back conversion can be obtained. With further consideration of the dispersion of the nonlinear

material the effects multi-longitudinal mode bandwidth can further be observed. The plots of Figure 6.5 show the phase variation of the focused multi-longitudinal modes of a theoretical 20 pm bandwidth laser source. Where here for simplicity it is assumed that the power within each mode is equal, resulting in a uniform top-hat power bandwidth distribution, additionally it is assumed that the phase of each mode is aligned at the start of the nonlinear device. From Figure 6.5(a), which shows the fundamental phase variation under a focus ratio of $\xi = 2.84$ in a uniform QPM device, it is clear that significant phase errors exist along the length of the device, with only very short regions of perfect phase-matching. In contrast, the plot of the GQPM sample, Figure 6.5(b), shows that only at the very far extent of the device is there any significant phase mismatch between the grating structure and the propagating waves. Here, dispersion is the sole cause of the mis-match and cannot be compensated for other than by using a narrower line laser or alternatively a wider bandwidth shorter physical device with less stringent phase-matching requirements. It is these regions of phase mis-match along the length of both devices that lead to back conversion of the harmonic signal at higher power levels.

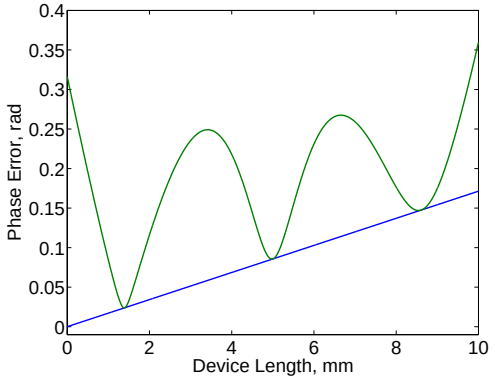


Figure 6.6: A plot of the average absolute phase error along the length of a 10 mm long QPM (green) and GQPM (blue) device for a focused multimode laser with a total bandwidth of 20 pm. Here it is assumed that the laser bandwidth has a uniform power distribution. It is clear that, although not perfectly phase matched with all longitudinal-modes, the GQPM sample has significantly lower phase-mismatch which results in reduced back-conversion.

Further, if one is to analyse the average absolute phase error of the numerous modes at each position along the length of both devices the advantages of GQPM in multi-longitudinal mode interactions becomes ever more clear, Figure 6.6(a) shows this result for both QPM (green) and GQPM (blue) devices. Here it is clear to see that the phase error of the Gouy compensated device is entirely linear and rate of growth of this error is solely determined by the dispersion properties of the material. Where if the total phase error becomes too large it merely indicates

that the device length is too long for the laser bandwidth. In contrast, although the phase error of the uncompensated device also has this linear dispersive offset, the dominating characteristics are the large oscillations occurring either side of the device centre and at the furthest extents of the device. The phase errors at the far limits of the device can largely be ignored for all but the highest fundamental input powers due to the low focused power density of the harmonic beam at these locations. However, the large oscillations either side of the device centre cannot be ignored due to the high harmonic intensities at these locations, in particular the oscillation after the focus where the harmonic field is likely to be the highest. It is this combination of relatively large phase error and very high harmonic intensity that create the conditions for the significant back conversion seen in Figure 6.4(a) and help to explain the 13% efficiency advantage of the GQPM device.

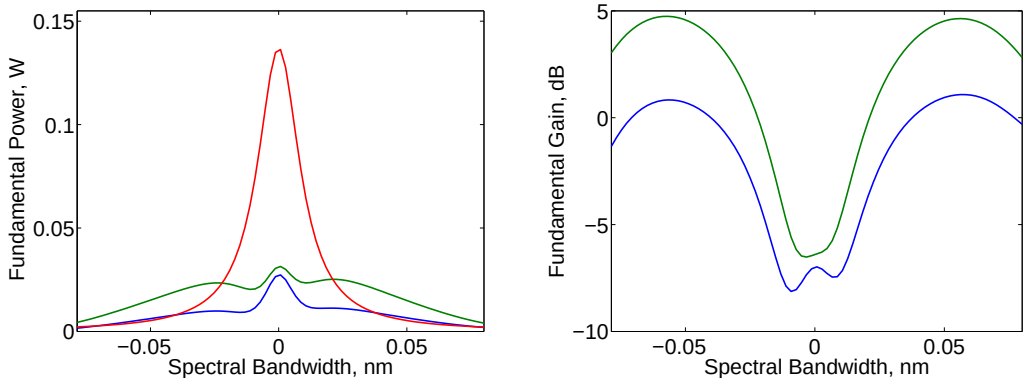


(a) (b)

Figure 6.7: (a) Theoretical plots of a 2 W mode-locked fundamental beam with a FWHM bandwidth of 0.02 nm prior to parametric conversion (red) and the resulting bandwidth at the end of 10 mm of PPLN based QPM (green) and GQPM (blue). (b) The resulting parametric gain of the fundamental bandwidth due to back conversion. Here the GQPM device (blue) largely prevents back conversion giving 65.3% efficiency. Although reduced when compared with the 1.25 W simulation in contrast at this power level the standard QPM sample allows considerable back conversion giving a significantly lower efficiency of 29.8%.

Finally to examine the performance of GQPM devices at very high depletion levels the fundamental input power of the multi-longitudinal mode laser source described above is increased to a total of 2 W. Again due to the multi-mode nature of the source the effective input power is considerably greater. Of course the 1.25 W source modelled previously, which was said to be equivalent a 100 W single frequency source assuming uniform power distribution within the

bandwidth, proved to provide efficiencies in line with a 10 W source; as such it is expected that a 2 W multi-mode source is likely equivalent to a 20 W single frequency source providing approximately 85-90% efficiency.

The fundamental power distribution across the bandwidth after propagation through both standard QPM and GQPM devices at this elevated power level are given in Figure 6.7(a). Here, it is clear as before that significant fundamental depletion has been achieved in both devices. However, the efficiencies of the device types are now markedly different with the QPM sample only providing 30% efficiency or 600 mW of harmonic output whilst the GQPM device provides over 65% efficiency or 1.3 W of harmonic power. Compared with the generated harmonic power at the earlier lower input power simulations for a 60% increase in input power the QPM sample provides a 16% *reduction* in output power whereas for the GQPM sample the same 60% increase in fundamental power results in a 48% increase in harmonic output. Further, on comparing both the plots of Figure 6.7(a) and 6.7(b) it is clear that significant amounts of back conversion into the sides of the fundamental bandwidth peak occurs for the uniform QPM device with significant net gain being present for a large range of wavelengths. This effect is almost completely suppressed in the GQPM device, although the back conversion gain at some wavelengths is higher than at the lower power level simulation. This increase in back conversion levels for the GQPM device may have two origins, the first is simply back conversion due dispersion which could be compensated for by reducing the device length. The second more complex mechanism is a variation in the Gouy phase of the focused fundamental beam from that of a standard Gaussian propagation such that the phase of the grating no longer provides correct compensation. Here, non uniform depletion of the fundamental Gaussian mode through the nonlinear interaction causes a variation in the propagation characteristics, with this effect being more pronounced at higher input powers.

## 6.4 Non-uniform pump depletion and diffractive healing

It has now been shown using a split-step BPM model that when operating at relatively low fundamental input powers Gouy phase compensated QPM structures can achieve the efficiency gains predicted by the non-depletion simulations of Chapter 4. Where by providing correct phase-matching between the propagating fields and the QPM grating an increase in efficiency of 3.5% over that of standard uniform QPM can be obtained for single frequency interactions. However, for both the single frequency and multi-longitudinal mode simulations it has been shown that as the fundamental input power is increased the performance advantages of Gouy compensation become reduced. Eventually resulting in lower efficiencies at high fundamental powers than with uniform QPM for SLM laser sources and further allowing back conversion to

the fundamental frequencies in the MLM simulations.

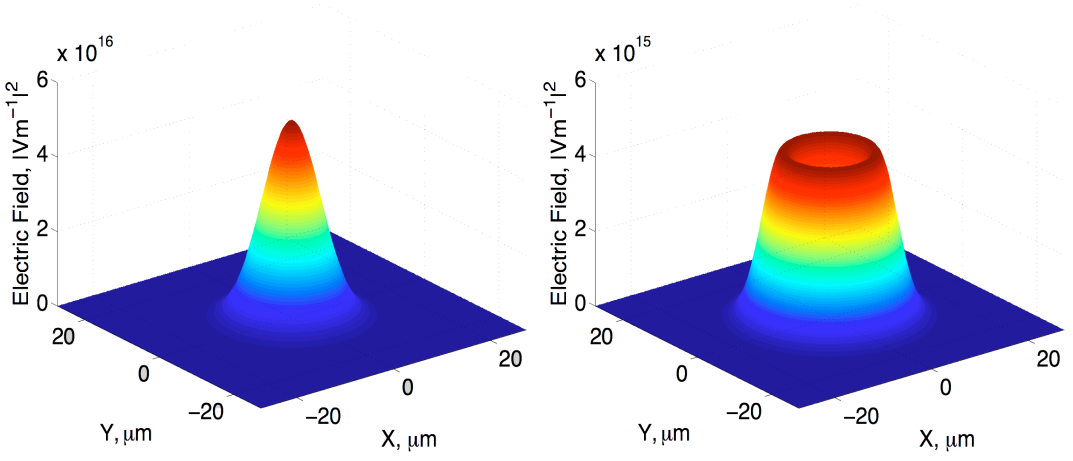


(a) (b)

Figure 6.8: Theoretical plots of the mode profile of a loosely focused Gaussian fundamental beam (a) as it propagates through a QPM device under the effects of high harmonic conversion efficiency, achieving over 80% conversion efficiency. Here the resulting 'doughnut' beam at the device output face (b) is created by non-uniform depletion of the initial Gaussian mode.

The cause of such effects can be attributed to the non-uniform depletion of the fundamental field. Through the nonlinear coupling, which is proportional to the magnitude of the fundamental field intensity, the high intensity centre of a Gaussian beam experiences a more rapid depletion than the lower intensity wings. Through this non-uniform depletion mechanism significant variations to the Gaussian mode profile can occur, with this effect becoming of much greater significance at higher fundamental powers. If left unchecked this depletion can lead to extensive distortions of the fundamental intensity profile, eventually resulting in the formation of 'doughnut' modes and further more complex structures as unphase-matched back conversion occurs, see Figure 6.8(b). This distortion of the Gaussian spatial properties of the fundamental mode of course has significant effects on the diffracting nature of the beam, with perhaps the most detrimental effect for the GQPM samples being the modification of the Gouy phase. Where, due to the depletion dependent Gouy phase variation a fixed GQPM device cannot be expected to provide correct compensation of the Gouy phase for all power levels.

Additionally, the formation of 'doughnut' modes significantly complicates the parametric process, where to achieve continued transfer of power from the remaining fundamental field to the harmonic the depleted mode centre must stay perfectly phase-matched else significant back-conversion in the mode centre can occur. Under such conditions there is a greater tendency for

out of phase power to convert back into the centre of the fundamental mode than forward power transfer from the remaining modal wings if any phase mismatch exists. This is as a result of the relatively high nonlinear drive at the centre of the fundamental mode, created by the now high intensity second harmonic mode which has maintained a more Gaussian like mode profile than the fundamental even at very high conversion efficiencies.

Despite the tendency for the formation of doughnut modes at extreme levels of nonlinear drive, either through very high pump power or a high nonlinear coefficient, the effect is somewhat suppressed for less severe regimes. For low input powers, where fundamental depletion is negligible, diffraction effects counteract the non-uniform depletion mechanism and redistribute power across the mode profile such that the $M^2$ value of the fundamental beam can stay almost unchanged. The same effect equally occurs as the nonlinear drive is increased, although the ability of the diffraction mechanism to completely 'heal' the beam is diminished.

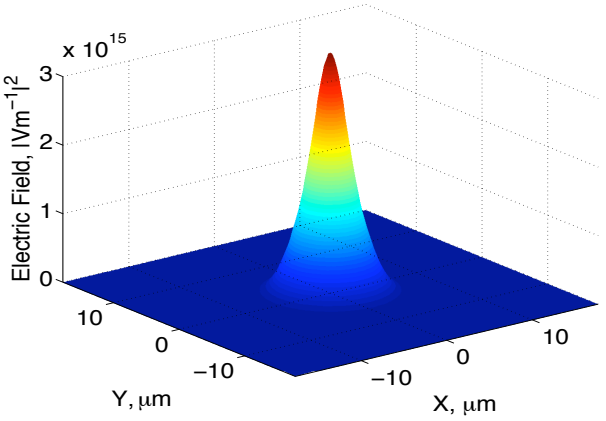


Figure 6.9: Under focusing conditions, here at a focus of $\xi = 2.84$, diffraction counteracts the effects of non-uniform pump depletion acting so as to 'heal' the mode. At this high conversion efficiency of 80%, however, this level of diffraction is insufficient to fully heal the mode, with the Gaussian profile becoming more like a Lorentzian mode.

Although unable to maintain a perfect Gaussian mode the effects of diffraction can be seen to prevent the formation of the doughnut mode, instead maintaining a modal distribution more similar to a Lorentz function. This effect is shown in Figure 6.9 where a focused Gaussian fundamental beam of focus ratio $\xi = 2.84$ has been distorted by the parametric processes resulting in this Lorentzian like mode profile at the end of the 20 mm device. The advantage of this diffractive healing is that the highest fundamental field is kept in the centre of the mode profile, maintaining a good mode overlap with the near Gaussian harmonic mode and thus providing

greater nonlinear coupling. However, although diffraction can help maintain a good overlap between the interacting fields, due to its inability to conserve the Gaussian mode profile the resulting Gouy phase variation differs from the standard single mode Gaussian model. It is of course this non-standard phase variation that prevents continuous phase matching with GQPM samples designed for low power use and explains the reduced efficiency and back-conversion characteristics seen at high input powers.

### 6.4.1 Variation in spot size and Gouy phase due to non gaussian mode

From the above theoretical plots of mode deformation due to non-uniform pump depletion it is clear that significant variations in the beam diameter can occur, with output beams significantly larger than would be expected through Gaussian beam propagation. In an attempt to demonstrate the adverse effect non-uniform depletion can have on the propagation characteristics of the fundamental beam at high power a brief outline of spot size and Gouy phase variation is now given.

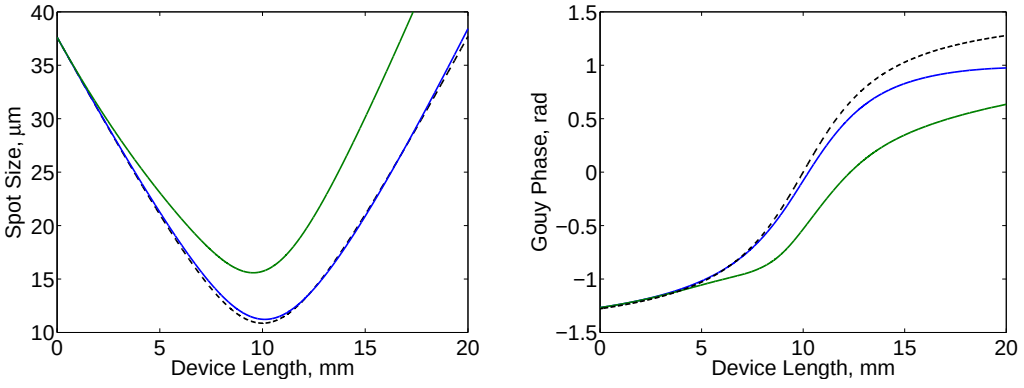


(a) (b)

Figure 6.10: (a) The simulated variation in the focused fundamental spot size in a GQPM device at moderate power (blue curve) and when generating the second harmonic at high efficiency ∼85% (green curve) compared with theoretical propagation. (b) As a result of the non-Gaussian nature the Gouy phase of the high power fundamental (green) significantly differs from the theoretical Gaussian propagation (dashed). Further, even the moderate power beam (blue), which shows very little spot size discrepancy, shows quite considerable Gouy phase variation from the theoretical case.

As demonstrated in Figures 6.8(b) and 6.9 at high nonlinear drive the spot size of the focused fundamental beam can vary quite significantly from the theoretical Gaussian mode by the end of the nonlinear interaction. To analyse how this distortion to the beam evolves it is useful to

obtain a numerical figure of merit of the beam shape throughout the parametric interaction, one possible figure of merit is to measure the beam radius. Figure 6.10(a) shows the evolution of the theoretical spot size throughout the nonlinear material calculated by measuring the second moment of the beam intensity [18]. This theoretical plot details the spot size variation with propagation distance for a focused beam with an initial radius of curvature chosen such that a focus ratio of $\xi = 2.84$ is achieved with the focused spot centred in the nonlinear material. The variation of a fundamental beam spot size achieved under minimal nonlinear drive conditions is given by the dashed curve. Here it should be noted that the spot size is characterised not by the $1/e^2$ radius, $\omega_0$, but alternatively by the sigma value of the second moment of the beam, with $w_0 = 2\sigma$. The further two plots shown in this figure are those of the spot size variation at a final conversion efficiency of 60% (blue plot) and 85% (green plot). Here it can be seen that at the lower of the two fundamental powers there is little variation in the overall spot dimensions from that of the low power values, although a slightly tighter focus is obtained offset from the centre of the device. For the higher power fundamental interaction it is clear that significant spot size variation is encountered, with a considerably larger focused spot size occurring, albeit with a much larger rate of diffraction. This contradiction of a large spot size with a rapid diffraction rate indicates the formation of a highly non Gaussian mode structure, with an $M^2$ value considerably greater than 1.0. Similar effects have been observed in OPA systems, where with increasing pump power it has been found that gain induced diffraction effects lead to a reduction in the system gain [19].

A further measure of beam propagation that is more sensitive to the modal properties of the fundamental beam is that of the Gouy phase. Measuring the phase gained at the centre of the fundamental mode can give an insight into the modal structure, with the Gouy phase being defined by the squeezing of the modal k-vectors during focusing. By now comparing the plots of Figure 6.10(b), which show the Gouy phase variation at the power levels mentioned above, it is clear that even for low distortion of the measured spot size significant variations in the Gouy phase are observed. It is this deviation in the Gouy phase, from the low power case (shown dashed), that causes the reduced efficiency for the Gouy phase adjusted devices in both SLM and MLM simulations. At these higher power levels the phase compensation defined in the grating structure is unable to adequately adjust for the power dependent Gouy phase introducing sources of dephasing which can lead to back conversion and reduced efficiency. In fact at the highest power level shown here it can be seen that a linear phase adjustment, offered by a simple uniform QPM grating, would provide significantly reduced overall phase error compared with a GQPM sample.

A final observation of nonlinear spot size variation that is prudent to mention here is that of the self trapping or soliton mode propagation. Here, with the correct coupling between the fundamental and harmonic modes, through phase-matching and power adjustment, it is possible to completely counteract the effects of diffraction, obtaining constant size mode propagation. Such second order nonlinearity induced soliton propagation has been both theoretically predicted [20] and experimentally observed in PPLN based QPM devices [21]. At first thought it would seem advantageous to have a non-diffracting beam for harmonic conversion, with the soliton gaining from a spatial confinement not dissimilar to waveguide structures. Here however, to obtain the soliton modes it is in fact necessary to detune the phase-matching characteristics of the nonlinear interaction to obtain balanced power transfer between the harmonic and fundamental modes. The effect of which is, of course, zero net gain in the conversion efficiency. One possible use however for such nonlinear soliton formation could be in obtaining mode locking of a laser cavity, where a spatial filter could be utilised to only accept the non-diffracting high intensity mode of a soliton. This however is outside the scope of this work and is not considered further.

## 6.5 Self optimised grating structure

Having predicted an alteration to the Gouy phase of the propagating fundamental beam caused by parametric depletion it is clear that a standard Gouy compensated grating, with a grating structure defined by Equation 4.40, is unsuitable for efficient operation. As such in an effort to produce the most efficient QPM device for high power operation a self-optimised structure has been developed. Here self-optimised refers to the automatic positioning of polarisation reversed domains such that maximum conversion efficiency is obtained every coherence length. This process is achieved by stepping the BPM analysis through the nonlinear device using intervals considerably shorter than the plane-wave coherence length and monitoring the generated harmonic power. At the point in the device where destructive interference of the harmonic waves is encountered, with subsequent steps leading to the reduction of the harmonic power, a polarisation inversion is applied ensuring the continued growth of the harmonic field.

At low power/depletion levels in a focused interaction such a self optimised structure will simply revert back to the GQPM description of Equation 4.40, with such a structure of course providing the optimal phase-matching conditions. However, at higher powers the designed grating structure will now automatically place the polarisation reversals such that the compensating grating phase correlates with the now non-Gaussian Gouy phase variation. By ensuring continuous phase matching between the propagating waves and the grating structure it would be expected that higher efficiencies can be achieved for a given power input than for either uniform

QPM or GQPM. Further at these high power levels the removal of phase-mismatch should almost completely eliminate sources of back conversion to new wavelengths and as such offer significant efficiency enhancements for MLM laser sources.

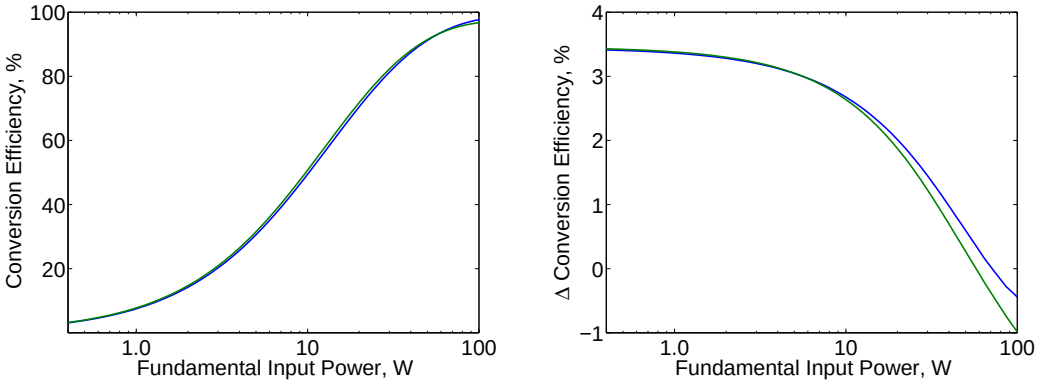


(a) (b)

Figure 6.11: (a) A theoretical plot of the conversion efficiency of a self optimised QPM structure for a range of fundamental input powers at a fixed focus of $\xi = 3.3198$. Where the position of the polarisation rotated domains have been determined to provide constant power transfer. (b) Also shown are the theoretical efficiency increases of the self optimised device (green) and a standard GQPM 3.3198 device (blue) relative to uniform QPM.

An example of the self-optimised conversion efficiencies predicted for a range of power levels in a focused interaction is given in Figure 6.11(a) (blue). Here a device length of 20 mm has been chosen and a focusing ratio of $\xi = 3.3198$, the optimal low power ratio, has been applied to the input fundamental beam. For each fundamental power value a new self optimised grating structure is generated ensuring optimal conversion efficiency. Also shown in this plot is the theorised conversion efficiencies of a uniform QPM (blue) sample as reported earlier. Due to the relatively small changes in overall conversion efficiency between the optimal device and the uniform QPM device Figure 6.11(b) shows the percentage differences in efficiency at each power level.

At low powers it is clear from Figure 6.11(b) that the self-optimsied grating structure offers no advantage over the standard GQPM device, providing the expected 3.5% conversion efficiency advantage over QPM. As the fundamental power is increased the self optimised grating structure is able to provide a slight performance improvement over both QPM and GQPM devices, as would be expected by its ability to maintain correct phase matching despite non-uniform beam deformation. However, as the input power is increased further, with conversion efficiencies

approaching 60%, the self-optimised devices unexpectedly result in reduced conversion efficiencies compared with either the uniform QPM or GQPM devices.

At first the reduction in efficiency for the self optimised structures at high nonlinear drive appears counter intuitive. However, this unexpected result can be simply explained. For the uniform QPM and GQPM devices when operating at high power the peak theoretical conversion efficiency is calculated by sweeping the grating response across a range of $\Delta k$ values - either through temperature or wavelength tuning. Here by allowing a shift from the plane wave phase matching conditions the rate of depletion of the fundamental field can be reduced, through a phase mismatch, such that the remaining un-depleted fundamental field propagates in a more Gaussian manner. As such at the expense of local conversion efficiency, on the order of a single coherence length, overall device efficiency can be increased. In contrast, the self-optimsed structure does not have the freedom to optimise to the long range efficiency. Thus, by being too locally efficient significant distortions to the propagating mode occur resulting in reduced nonlinear coupling.

Despite this slightly reduced conversion efficiency at higher power levels it must be remembered that the self-optimised grating structure is now correctly phase-matching the nonlinear interaction along the entire device length. As discussed before, this continuous phase-matching removes possible routes of back-conversion and thus can be expected to provide higher conversion efficiencies with real bandwidth laser sources.

### 6.5.1 Optimal high power focussing conditions

Throughout the analysis of high power second harmonic generation in this chapter it has been assumed that the optimal focusing conditions parallel that of low power interactions, with an optimal focusing ratio of $\xi = 2.84$ for uniform gratings and the tighter $\xi = 3.32$ for Gouy compensated gratings. However, as just demonstrated, the very behaviour of perfect phase matching and tighter confinement offered by Gouy compensated devices can become detrimental to the overall high power performance. Thus, it is reasonable to assume that by altering the focusing conditions to reduce the average spatial confinement along the length of the nonlinear device, thus reducing the local conversion efficiency, that higher overall efficiencies may be obtained.

It was shown in Chapter 4 that a focus ratio of $\xi = 3.3198$ provides the greatest power density along the length of the nonlinear device, with tighter focussing offering higher peak intensities at the focused waist but at the expense of reduced interaction lengths through the rapidly diffracting mode diameter. It is therefore reasonable to assume that at the higher power levels of interest in this chapter utilising either a more loosely or more tightly focused beam than

the optimal $\xi = 3.3198$ should provide enhancements to the overall efficiency by reducing the local efficiency and allowing the fundamental beam to maintain its Gaussian profile.

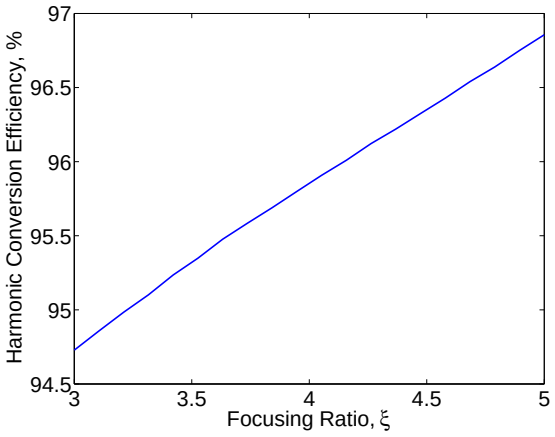


Figure 6.12: The theoretical change in conversion efficiency for a 20 mm long self optimised PPLN based grating at a range of focusing values. Here, for a 90 W fundamental mode it can be seen that higher efficiencies can be obtained by moving to a more tightly focused regime, where diffractive healing and a more gradual mode depletion allow greater overall efficiency.

At first thought it may be assumed that using a loosely focused beam is the preferred choice for high efficiency operation due to its lower power densities at any point along the device. However as was shown in Section 6.4 at looser focus the effect of diffraction is unable to adequately 'heal' the Gaussian mode resulting in the formation of doughnut modes. To overcome such an effect the mode diameter must be must be significantly increased to the point that the non-uniform mode depletion mechanisms are suppressed. Here the suppression is only ensured by the reduced power density and thus significantly reduced conversion efficiency for a given fundamental power. Alternatively, by moving to a tighter focus regime the benefits of reduced average power density and a high peak intensity are coupled with a strong diffractive healing mechanism and should result in a more Gaussian like mode and higher conversion efficiencies.

The verification of this is given in Figure 6.12 and further emphasised in Figure 6.13. Here a 20 mm long PPLN based device is modelled using the BPM simulation technique with a fundamental input power of 90 W. To investigate the effects of the focused spot size on the high power efficiency a range of focusing ratios have been examined, from a low value of $\xi = 3$ up to a value of $\xi = 5$, using the self-optimising grating technique. The initial input power has been chosen to correspond to approximately 95% conversion efficiency, the maximum value achieved with previous self optimised device at a focus ratio of $\xi = 3.3198$.

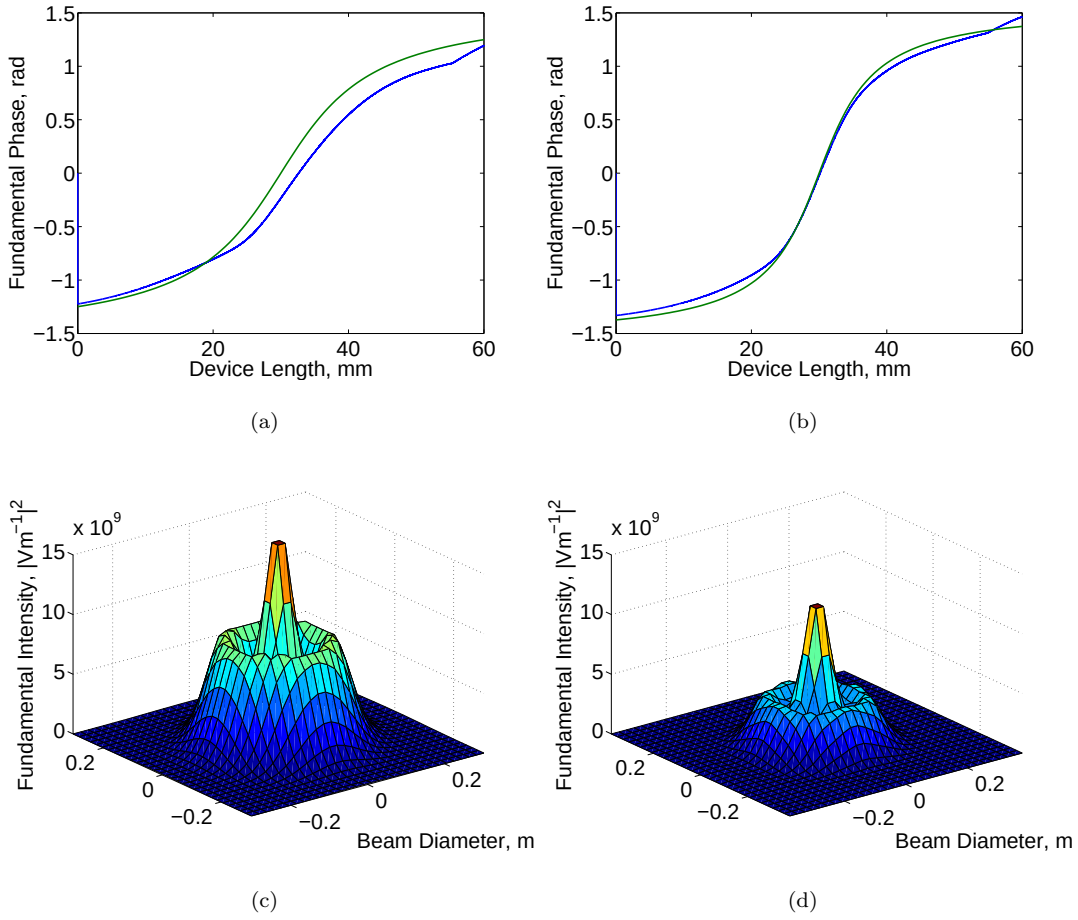


Figure 6.13: (a), (b) Theoretical plots of the phase of the fundamental mode centre for focus ratios of $\xi = 3$ and $\xi = 5$ respectively for low power interactions (green) and 95% fundamental power depletion (blue) in a 20 mm long PPLN based device. (c), (d) the resulting fundamental mode profiles at the device exit face for loose and tight focusing respectively, showing significant mode deformation through non-uniform depletion mechanisms

From Figure 6.12 it is clear that for a more loosely focused fundamental beam the final conversion efficiency is indeed lower than the earlier simulations performed at the low power optimal focusing condition of $\xi = 3.3198$. This agrees with the prior assumption that at looser focus the diffractive healing mechanism is less efficient resulting in significant distortions to the propagating mode. This is further clarified in Figures 6.13(a) and 6.13(c), which respectively show the focused Gouy phase throughout the device and mode intensity of the fundamental beam at the exit face of the device for a focus of $\xi = 3$. Here it is clear that at such extreme power levels diffraction is unable to heal the beam and a doughnut mode has been formed, this

has then further experienced back conversion into the depleted centre. By comparing the Gouy phase at the centre of the propagating beam (blue) with the theoretical Gaussian Gouy phase (green) it is clear that significant variation to the modal propagation has occurred.

In contrast, at tighter focusing Figure 6.12 clearly shows that higher conversion efficiencies can be obtained indicating that diffractive healing is able to somewhat limit the detrimental effects of non-uniform pump depletion. Now, by comparing the Gouy phase of the propagated beam at the tighter focus of $\xi = 5$, as shown in Figure 6.13(b), it is clear that the actual phase (blue) much more closely follows that of the theoretical Gaussian phase indicating a more Gaussian like modal propagation. Further, comparing the intensity distribution of the tighter focused mode in Figure 6.13(d) with its loose focus counterpart it is evident that, although by no means Gaussian in nature, the transfer of power from the Gaussian side lobes has been more significant before back conversion occurs. However, it must be noted that due to the tighter focusing, and thus more rapid diffraction, that the intensity of the fundamental mode at the device exit face is reduced compared with the looser focus and thus contributes to the lower intensity side lobes in the device profile.

Finally, it is clear from Figure 6.12 that there is no sign of roll-off in the conversion efficiency with increasing focus ratio, indicating that still higher conversion efficiencies may be obtained by going to yet tighter focusing conditions. The effects of increased power and tighter focusing shall now be fully examined, using the self optimised grating structures, again assuming a PPLN based device. It is important to note that by utilising a different material type, operating wavelength, or device length in these calculations that the peak focusing conditions may be greatly varying. With the rates of diffraction, and thus the efficiency of diffractive healing, varying with wavelength and material. Further, the nonlinear drive will of course vary between materials, greatly changing the powers at which non-uniform depletion mechanisms become important.

In an effort to determine the optimal focussing conditions under a high pump depletion regime an investigation into the maximum focused conversion efficiency for a 20 mm length of $LiNbO_3$ based QPM material has been undertaken. Here it is assumed that a fundamental Gaussian beam with a 1064 nm wavelength is input into the device, the power and focusing of which are freely varying parameters. Again for simplicity the QPM structure has been chosen to be self-optimising. With this allowing a rapid investigation into the maximum conversion efficiency without having to sweep $\Delta k$ space to find the peak phase matching conditions at each focus and power value.

The results of this investigation are shown in Figure 6.14. Here it is clear to see that the

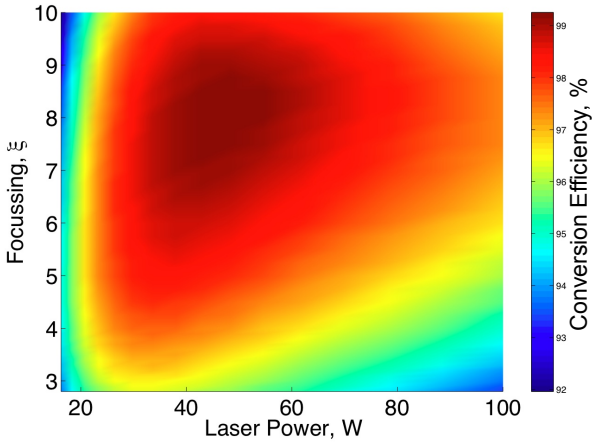


Figure 6.14: A theoretical plot of conversion efficiency, with darker colours indicating high efficiency, for a sweep of both fundamental input power and focusing ratio. Here it is clear that at high power optimum focusing is achieved at a significantly higher value than classically predicted at low power,

optimum conversion efficiency occurs at a focus ratio considerably tighter than that of low power interactions, with the peak focus ratio being approximately $\xi = 8.25$, corresponding to a focused spot size of $14\,\mu$m. Further, the peak conversion efficiency of over 99% is achieved with an input fundamental power of 45 W which corresponds to a peak power density of approximately $14.5\,\mathrm{MWcm^{-2}}$. Although this power density is high, such values can readily be obtained using picosecond duration pulses, or even pulses in the low nanosecond regime, whilst maintaining a energy density well below the accepted limit of $2\,\mathrm{Jcm^{-2}}$ for optical damage in $LiNbO_3$ [22]. A further limitation which may be necessary to consider to fully model the effects of high power CW interactions is that of thermal lensing. Here, due to effects such as two photon absorption [23], not insignificant optical power can be absorbed by the crystal lattice and result in regions of localised heating and consequently refractive index variation. Such localised index changes will of course vary the propagation characteristics of the focused beam and thus require different compensating grating structures. This effect will further be more prevalent at tight focus, where the high power density will of course result in greater heating. As such the results offered in Figure 6.14 should be considered as appropriate only for quasi-CW pulses in the low nano-second or pico-second regimes where heating effects are less of a concern.

This result clearly highlights the ability for diffractive healing of the fundamental beam to play a significant role in achieving high levels of conversion efficiency. Perhaps of more importance is that this work refutes the common held belief that it is impossible to achieve efficiencies approaching 100% in bulk interactions. With many works [15] incorrectly citing the papers by

Eimerl on high power bulk interactions as proof of this [9, 5]. However, these papers specifically address the highly unusual case of frequency converting laser beams with energies of 100 kJ and above. Here, the object of the work is not solely set on reaching high efficiencies (although this is indeed important) but is instead aimed at obtaining huge laser powers, $> 100$ TW, at UV wavelengths for the purpose of laser confinement nuclear fusion. At such extreme input powers it is clear that nonlinear depletion effects will become severe and ultimately place an artificial limit on conversion efficiency as a result of driving the interaction too hard.

This work has highlighted that for the particular case of producing green second harmonic light in a 20 mm long $LiNbO_3$ crystal an optimum efficiency can be obtained with a 40 W input source focused to a ratio of $\xi = 8.25$. However, this result is by no means universal and as such cannot be taken as the definitive operating conditions for all nonlinear interactions, even for interactions with identical fundamental power. This is in stark contrast to previous works on optimising the conversion efficiency of focused beams [24], where a single universal optimum focusing condition has been provided for any second harmonic interaction, regardless of wavelength, material type or length.

Here, at high powers, no single optimal result can be provided due to the differing rates of diffraction and the associated ability to heal the fundamental beam. For example, at shorter wavelengths in $LiNbO_3$ the rate of diffraction is higher than at longer wavelength and as such a looser focus ratio can provide the same degree of beam healing as a much tighter focus at longer wavelengths. Similar conditions arise for variations in device length, where a focus ratio of $\xi = 3$ in a 40 mm long crystal has a much lower rate of diffraction than an equal focus ratio in a 10 mm long crystal and as such a reduced ability to heal the Gaussian profile. Of course, with the greater interaction lengths provided by a 40 mm long device lower fundamental powers can be used to obtain high levels of pump depletion. With the lower powers and reduced rate of conversion efficiency somewhat negating the effects of nonlinear depletion.

## 6.6 Intensity dependent phase shifts

Thus far, throughout the analysis of high power parametric interactions the detrimental effects observed, such as the Gouy phase and beam deformation, have been common to all types of bulk phase-matching, be it QPM or birefringent. Although, the compensating techniques discussed have only been applicable to grating based structures, with their greater flexibility allowing a higher degree of control over the nonlinear interactions. Now however, having highlighted the benefits nonlinear grating based structures can provide at high power operation a further detrimental effect shall be discussed that is only of significant concern in quasi-phase-matched

interactions.

Returning to Equation 3.5 from the earlier work on an analytic solution to the coupled plane-wave equations of second harmonic generation (repeated here as Equation 6.13) it can be seen that there is an intensity dependent phase-shift between the two interacting waves along the direction of propagation.

$$\frac{\mathrm{d}\theta}{\mathrm{d}z} = \Delta k - \frac{\cos\theta}{\sin\theta}\frac{\mathrm{d}}{\mathrm{d}z}\ln\left(\rho_{\omega}^{2}\rho_{2\omega}\right) \tag{6.13}$$

Here $\rho_{\omega}$ and $\rho_{2\omega}$ are the real magnitudes of the fundamental and harmonic fields respectively and $\theta$ is the phase difference between the two propagating waves. At low powers it is clear that the rate of change of the phase of the two propagating fields is dominated by dispersion. However, as the fundamental input field is increased in magnitude it becomes evident that a significantly more complex variation in the phase of the two waves occurs, with the rate of phase change becoming linked to both the current phase and the field magnitudes.

Using the technique of quasi-phase matching it is clear that at low fundamental drive determining the optimum position of nonlinearity reversals to maintain a phase lock between the two waves is trivial. For high nonlinear drive however, the process becomes significantly more involved, with no one correct domain position satisfying all power levels. To aid in the analysis Equation 6.13 can be re-written as

$$\frac{\mathrm{d}\theta}{\mathrm{d}z} = \Delta k - 4\omega^{2}K\left(\frac{\rho_{2}}{k_{1}} - \frac{\rho_{1}^{2}}{\rho_{2}k_{2}}\right)\cos\theta \tag{6.14}$$

where $K$ is a definition of the second order nonlinearity coefficient and $k_1$ and $k_2$ are the fundamental and harmonic k-vectors respectively, this expression is fully derived in Appendix A. From the above expression it can be seen that the rate of change of phase between the two waves is strongly tied to the field of the fundamental wave, the consequence of which is an increase in the rate at which the two interacting waves lose phase lock at higher fundamental power levels. This can simply be thought of a shortening of the coherence length of the nonlinear interaction as fundamental power is increased. This effect was first highlighted in QPM interactions by Rustagi et. al [13] in 1982, although no efforts were made to compensate for its effects.

This shortening of the coherence length can of course be accounted for with a simple adjustment of the phase-matching period, through wavelength or temperature tuning, thus providing continuous growth of the fundamental field. However, at higher levels of nonlinear drive, through higher fundamental field or through larger nonlinear coefficient, it cannot be assumed that the phase variation generated over each coherence length is equal. At higher nonlinear drive the magnitude of $\rho_1$ is of course no longer constant, due to depletion of the fundamental through the nonlinear interaction. As such the magnitude of the phase addition is not constant along

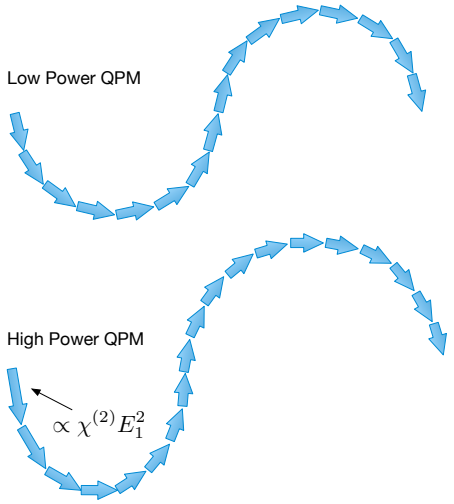


Figure 6.15: A representation of the effects of high power dephasing. Here it can be seen that at high power significant depletion of the fundamental beam results in an effective shortening of the k-vector as the harmonic is generated, this in turn results in a reduced coherence length which must be compensated for with a spatially varying QPM period.

the device length resulting in an expansion of the coherence length back towards that of the low power value. At extreme electric field magnitudes, as may be encountered in femtosecond pulsed interactions, the variation in the phase can become so rapid that the effects can become apparent over single coherence lengths. In such a regime it is possible to achieve not insignificant depletion of the fundamental over a single coherence length leading to significantly nonlinear variations in phase from QPM period to period. This effect can be visualised with the use of k-vector diagrams of the phase matching process as shown in Figure 6.15. As can be seen from the figure, due to depletion of the fundamental beam, a phase error is introduced whereby later parametric contributions are insufficient to counteract the phase of the earlier, higher power interactions.

This nonlinear variation in coherence length is remarkably similar in nature to the Gouy phase shift encountered in earlier chapters, although this new effect is much more subtle with considerably smaller shifts in the phase-matching characteristics. The result of this intensity dependent phase shift of course has similar consequences to that of the Gouy phase, resulting in dephasing of the propagating fields and subsequent back conversion of the generated harmonic field. Here however, as fundamental power is increased, in an effort to gain greater conversion efficiency, the phase variation becomes more severe. As for the Gouy phase shift, at higher fundamental and harmonic powers, this phase error may lead to the generation of new unwanted frequencies causing bandwidth broadening and reduced conversion efficiency.

Figure 6.16 is a theoretical plot of the conversion efficiency of a plane-wave SHG interaction

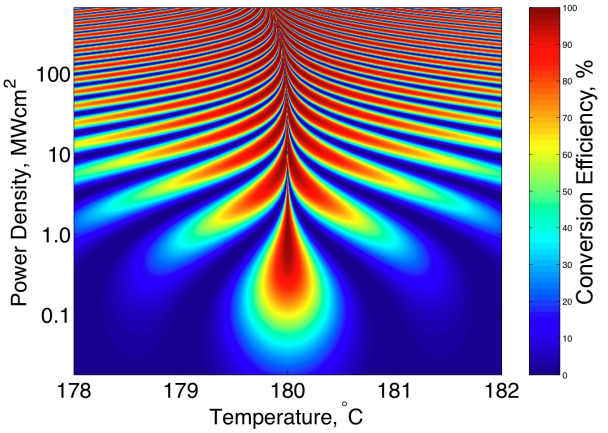


Figure 6.16: A plot of the conversion efficiency of a plane wave interaction for variation in the phase matching condition, shown here as a temperature offset, and the fundamental power density. Here it can be seen that at high intensities the phase-matching peak becomes significantly narrowed. But, also, as the intensity is pushed still higher it is clear that the peak phase-matching condition shifts, with this being a result of the intensity dependent phase-shift.

for varying fundamental power and phase-matching parameters in a uniform QPM structure which highlights some of the effects this phase shift may have. By taking a horizontal slice through this plot, at the lowest power level, the familiar sinc squared phase matching curve can be obtained. However, with increasing fundamental power it is clear to see that this sinc squared curve becomes severely narrowed, with this effect being a direct consequence of the intensity dependent phase shift. At still higher input powers the central phase matching lobe becomes so narrowed that it becomes impractical to operate efficiently at this value, with minute variations in operating temperature or fundamental wavelength resulting in large reductions in generated harmonic power. However, it is clear that at these higher drive levels the side lobe efficiency has raised significantly such that high harmonic powers can be obtained through deliberate detuning of the phase-matching characteristics. It is quite likely that experimentally at high powers the optimum efficiency is obtained from one of these side lobes and not the central lobe as would be expected.

Aside from the narrowed phase-matching response at the highest input powers, as can routinely be achieved with femtosecond pulsed lasers, it is evident that a shift in the peak phase matching condition to lower temperature values occurs. This shifting phase matching condition is as a result of tuning the grating to provide the best average phase-matching to compensate for the spatially varying coherence length of the nonlinear interaction. Although this shift appears

somewhat insignificant it has been shown, independently from this work, that such a phase error can have detrimental effects on pulsed light, leading to frequency chirps, wavefront tilt and focusing distortions [14].

As for the case of Gouy phase compensated gratings it should in theory be perfectly possible to create QPM gating structures that can compensate for the effects of intensity dependent phase shifts, resulting in reduced back conversion, lessened frequency distortion of the harmonic temporal pulses and overall higher conversion efficiencies. Here however, no single device will be able to adequately compensate a range of interactions. With instead each laser source, with a known output power, requiring an individually tailored grating structure to provide optimum performance.

As for high power Gouy compensation it should be possible to generate a suitable grating structure using a self optimising BPM algorithm, although the simulations used in this chapter would likely need extending to account for temporal effects of short pulse interactions including group velocity mismatch (GVM) and non-uniform depletion of the temporal profile. Finally, with such a bespoke design it now becomes essential to include in the simulations the effects of absorption and local heating, green induced infra-red absorption (GRIIRA) and the changes these factors will have on the local characteristics of the nonlinear material.

## 6.7 Conclusions

In this chapter a purely theoretical analysis of high efficiency second harmonic generation has been undertaken. Using a modified split-step beam propagation method, which takes into account nonlinear coupling of propagating fields through the second order nonlinearity, an investigation into the effects of the Gouy phase of focused Gaussian beams on the conversion efficiency has been undertaken. It has been shown that, for moderate fundamental depletion and single frequency operation, the Gouy phase shift can reduce the conversion efficiency of harmonic interactions and that compensating for this phase error with a modified QPM structure can result in improvements in efficiencies of up to 3.5%.

Further, using a more complicated BPM simulation, which can concurrently model the effects of many hundreds of coupled propagating fields in a grating structure, it has been shown that compensating for the Gouy phase of focused beams can lead to significant performance enhancements. Simulating a 20 pm Lorentzian bandwidth laser source it has been shown that using a Gouy compensated QPM device efficiencies a factor of two greater than a comparable uniform QPM device can readily be achieved through limiting back conversion at high input powers.

Using this extended BPM simulation tool it has been demonstrated that at higher funda-

mental power levels it is insufficient to compensate for the theoretical Gouy phase of a Gaussian beam, with non-uniform beam deformation causing a modification in the propagation characteristics of the fundamental mode. This deformation has been identified as the source of unexpected back-conversion of Gouy compensated devices at higher fundamental powers. From this a further simulation tool was developed to create self optimised grating structures that could actively maintain perfect phase lock between the propagating fields and the grating. However, it was found that for single frequency simulations at very high power levels such a grating structure resulted in a reduced conversion efficiency than either uniform QPM or standard GQPM devices. Here, it is believed that the more efficient phase matching provided by this structure led to a more rapid spatial depletion of the fundamental beam which cannot be compensated for with simple 1 dimensional grating structures. Due to computational limitations a self optimised multiple frequency simulation has not been performed although it is believed that it would show considerable efficiency gains over either QPM or GQPM at higher power levels.

Additionally, an investigation was undertaken into the optimal SLM focusing conditions at high fundamental power. It has been found that unlike for low power negligible depletion interactions the optimum focusing condition is not at the famous Boyd and Kleinman $\xi = 2.84$ [24] or even at the improved $\xi = 3.3198$, proposed by this author for low power interactions [11], but is found to be a much tighter value. Here operating at tighter focusing enables an effect termed 'diffractive healing' to occur, with this process actively repairing the depleted fundamental mode through diffraction. The result of this healing is a mode with a greater modal overlap with the near perfect Gaussian distribution second harmonic mode, providing a higher degree of nonlinear coupling and thus greater efficiency.

By compensating for these numerous effects it has been shown theoretically that there are no restrictions preventing nominally 100% fundamental depletion. This is in contrast to often quoted articles that claim efficiencies over 90% are impossible to obtain without the use of multiple orthogonal nonlinear devices [5].

# References


[1] Y. Furukawa, K. Kitamura, A. Alexandrovski, R. Route, M. M. Fejer, and G. Foulon. Green-induced infrared absorption in MgO doped $LiNbO_3$. *Appl. Phys. Lett.*, 78(14):1970–1972, 2001.

[2] N. Pavel, I. Shoji, T. Taira, K. Mizuuchi, A. Morikawa, T. Sugita, and K. Yamamoto. Room-temperature, continuous wave 1-W green power by single-pass frequency doubling in a bulk periodically poled MgO:$LiNbO_3$ crystal. *Opt. Lett.*, 29(8):830–832, 2004.

[3] J. A. Armstrong, N. Bloembergen, J. Ducuing, and P. S. Pershan. Interactions between light waves in a nonlinear dielectric. *Phys. Rev.*, 127(6):1918–1939, 1962.

[4] R. C. Eckardt and J. Reintjes. Phase matching limitations of high efficiency second harmonic generation. *IEEE J. Quantum Electron.*, QE-20(10):1178–1187, 1984.

[5] D. Eimerl. Quadrature frequency conversion. *IEEE J. Quantum Electron.*, 23(8):1361–1371, 1987.

[6] M. A. Dreger and J. K. McIver. Second-harmonic generation in a nonlinear, anisotropic medium with diffraction and depletion. *J. Opt. Soc. Am. B*, 7(5):776–784, 1990.

[7] S.-C. Sheng and A. Siegman. Nonlinear-optical calculations using fast-transform methods: Second-harmonic generation with depletion and diffraction. *Phys. Rev. A*, 21(2):599–606, 1980.

[8] I. Jovanovic, B. J. Comaskey, and D. M. Pennington. Angular effects and beam quality in optical parametric amplification. *J. Appl. Phys.*, 90(9):4328–4337, 2001.

[9] D. Eimerl. High average power harmonic generation. *IEEE J. Quantum Electron.*, QE-23(5):575–592, 1987.

[10] S. K. Wong, G. Fournier, P. Mathieu, and P. Pace. Beam divergence effects on nonlinear frequency mixing. *J. Appl. Phys.*, 71(3):1091–1101, 1992.

[11] H. E. Major, C. B. E. Gawith, and P. G. R. Smith. Gouy phase compensation in quase-phase matching. *Opt. Commun.*, 281(19):5036–5040, October 2008.

[12] N. Lastzka and R. Schnabel. The Gouy phase shift in nonlinear interactions of waves. *Opt. Express.*, 15(12):7211–7217, June 2007.

[13] K. Rustagi, S. Mehendale, and S. Meenakshi. Optical frequency conversion in quasi-phase-matched stacks of nonlinear crystal. *IEEE J. Quantum Electron.*, QE-18(6):1029–1041, 1982.

[14] A. V. Smith and M. S. Bowers. Phase distortions in sum- and difference-frequency mixing in crystals. *J. Opt. Soc. Am. B*, 12(1):49–57, 1995.

[15] K. R. Parameswaran, J. R. Kurz, R. V. Roussev, and M. M. Fejer. Observation of 99% pump depletion in single-pass second-harmonic generation in a periodically poled lithium niobate waveguide. *Opt. Lett.*, 27(1):43–45, 2002.

[16] D. Taverner, P. Britton, P. G. R. Smith, D. J. Richardson, G. W. Ross, and D. P. Hanna. Highly efficient second-harmonic and sum-frequency generation of nanosecond pulses in a cascaded erbium-doped fiber:periodically poled lithium niobate source. *Opt. Lett.*, 23(3):162–164, 1998.

[17] G. H. Weiss and A. A. Maradudin. The Baker-Hausdorff formula and a problem in crystal physics. *Journal of Mathematical Physics*, 3(4):771–777, 1962.

[18] A. E. Siegman, G. Nemes, and J. Serna. How to (maybe) measure laser beam quality. In *DPSS (Diode Pumped Solid State) Lasers: Applications and Issues*, volume 17 of *OSA Trends in Optics and Photonics*. Optical Society of America, 1998.

[19] C. Kim, R.-D. Li, and P. Kumar. Deamplification response of a traveling-wave phase-sensitive optical parametric amplifier. *Opt. Lett.*, 19(2):132, 1994.

[20] L. Torner and G. I. Stegeman. Soliton evolution in quasi-phase-matched second-harmonic generation. *J. Opt. Soc. Am. B*, 14(11):3127–3133, Nov 1997.

[21] B. Bourliaguet, V. Couderc, A. Barthélémy, G. W. Ross, P. G. R. Smith, D. C. Hanna, and C. De Angelis. Observation of quadratic spatial solitons in periodically poled lithium niobate. *Opt. Lett.*, 24(20):1410–1412, Oct 1999.

[22] S. Brosnan and R. L. Byer. Optical parametric oscillator threshold and linewidth studies. *IEEE J. Quantum Electron.*, QE-15(6):415–431, 1979.

[23] W. Kaiser and C. G. B. Garret. Two-photon excitation in $CaF_2$:$Eu^{2+}$. *Phys. Rev. Lett.*, 7(229), 1961.

[24] G. D. Boyd and D. A. Kleinman. Parametric interaction of focused Gaussian light beams. *J. Appl. Phys.*, 39(8):3597–3639, 1968.

# Chapter 7

# Conclusions and Future Work

## 7.1 Increased temperature bandwidth QPM devices

Synthesised response QPM grating structures have shown considerable promise as systems for stable, relatively efficient, production of optical harmonics. Such devices have proven effective in providing highly temperature and wavelength stable constant optical power output. With this stability extending up to 35 times greater than standard uniform QPM devices. Unfortunately, at such extremes of stability the relative conversion efficiency of such devices, when compared with unmodified periodic structures, is considerably lower. This of course is an unavoidable physical effect of the nonlinear interaction and cannot readily be improved on. Notwithstanding, although a significant reduction in optical efficiency is encountered with such devices, the reduction is considerably lower than the alternative method of utilising shorter periodic devices. For uniform devices an increase in temperature or wavelength bandwidth can be accomplished with shorter device lengths, with the bandwidth varying proportionally with the inverse of device length. This however is matched with a corresponding loss in conversion efficiency which is proportional to the inverse of the square of the device length. In contrast, the devices designed and fabricated as part of this research have been able to maintain an almost linear relationship between bandwidth and efficiency, resulting in almost an order of magnitude greater efficiency at some bandwidths.

As a technique for the large scale production of temperature stable QPM devices the method demonstrated in Chapter 3 has proven to be highly successful in $LiNbO_3$. By ensuring uniformly sized poled domains in the quasi-periodic structure a very high fabrication yield has been achieved, rivalling that of uniform QPM structures. It is this advantage in high yield fabrication that sets such a bandwidth enhancement technique apart from the numerous others, many of which have been shown to provide efficiencies rivalling the devices detailed here.

With initial experimental verification of such a device type being based on early, un-optimised designs there is considerable scope for improving the performance of such devices. Future work on these devices will likely lead to much greater efficiencies than currently achieved. Using more complex design tools, such as simulated annealing [1], whilst maintaining a constant poled domain size should result in considerable efficiency enhancements.

## 7.2 Analytic simulations of nonlinear interactions

The modelling technique utilised throughout Chapter 3, which is based on analytic solutions to the coupled parametric equations, has proven to be a highly effective tool. Capable of providing exact analytic answers to the most complex of plane-wave interactions such a tool has proven invaluable. In particular, for the wide bandwidth devices detailed such a modelling technique has allowed very rapid yet highly accurate analysis. Taking advantage of the relatively large regions of constant nonlinearity within such structures the Armstrong [2] based simulation tool, which is able to determine the contribution of such regions in a single calculation, has proven many times faster than alternative methods such as Runge-Kutta.

However, although precise and relatively rapid in use, the underlying computer coding of this tool is far from optimised. Currently the simulation times are limited by the large number of computations required to solve the Jacobi elliptic function of Equation 3.25. By reducing this time, through optimisation of the Jacobi solver, further performance gains can likely be achieved making this tool the standard modelling technique of choice for plane-wave SHG interactions. This technique can further be readily adapted for the more complex three wave mixing processes, allowing for more detailed analysis of effects such as difference frequency mixing and the associated back conversion of the SHG signal.

## 7.3 Compensation of the Gouy phase with domain engineering

The work of Chapter 3 highlighted an often overlooked phenomenon of parametric interactions. Specifically, under focused Gaussian beam interactions the operation of nonlinear devices differ quite markedly from the more readily analysed plane-wave interactions, as are produced in single mode waveguide devices for example. The more obvious of such differences being a shifted phase-matching parameter and asymmetric power output for changes in this parameter. For the majority of applications these effects are of little significance and as such are generally

considered of no interest and thus ignored. However, as shown in the tuning characteristics of the wide bandwidth devices discussed above, these effects, in particular the asymmetric tuning response, can have dramatic unwanted consequences.

The effects of focussed Gaussian beam interactions in nonlinear devices have previously been considered, with a thorough analysis of SHG, SFG and DFG undertaken [3]. For SHG this analysis verified the observed asymmetries and phase-shifts as effects of the focused beams and further went on to provide an analytically derived optimum operating condition for maximum optical conversion efficiency. However, throughout this analysis, and ever since, there have been no real efforts undertaken to fully explain the causes of these effects and thus there has been no possible routes to overcome them.

In Chapter 4, in an effort to explain the unwanted effects observed in the flat-top temperature stable devices of Chapter 3 the analysis of Boyd and Kleinman has been revisited. Subsequently it has been found that a spatially varying phase advancement, along the optical axis, occurs in focused interactions. This non-uniform phase, first identified by Gouy in 1890 [4], is directly responsible for the deleterious effects of focusing, specifically the phase-shift and asymmetric tuning response. Further it has been shown theoretically that by negating this spatially varying Gouy phase both these effects can be fully suppressed, returning the device performance back to that of a plane-wave interaction.

A further, unexpected consequence of removing this phase advancement is an increase in optical conversion efficiency. By providing constant phase-matching between the interacting fundamental and harmonic fields it has been shown that at any focused spot size higher efficiencies could be obtained through compensating for the Gouy phase. Additionally, it has been demonstrated that the optimum focusing condition provided by Boyd and Klienman over 40 years ago is in fact too loose, with higher efficiencies obtainable at tighter focusing.

Finally, a route to achieve Gouy phase compensation through domain engineered QPM has been both theoretically demonstrated and experimentally verified. By compensating for the phase advancement, through subtle shifts in the grating period, devices have been fabricated in $LiNbO_3$ and optically tested and have shown a return to a symmetric phase-matching tuning response and a shift in peak phase-matching condition back to that of plane-wave.

### 7.3.1 Focus compensated Flat-top devices

Using the technique of Gouy phase compensation new temperature stable QPM devices have been simulated, with such devices now providing perfectly symmetric phase-matching characteristics. Despite this compensation, however, it has been shown that the response under focusing is still

not directly comparable to plane-wave interactions, with the obtained bandwidths being reduced and the flat-top response becoming softened. Both of these effects have subsequently been shown to be entirely attributable to the spatially varying optical intensity in a focused beam, with such variation leading to an apodisation of the spatial structure which in turn causes a smoothing of the spectral response. Further, by pre-compensating for this effect in the effective nonlinearity of the wide bandwidth devices it has been shown that all of the deleterious effects of focused interactions can be completely overcome, resulting in optical characteristics indistinguishable from waveguide interactions.

Such focus compensation techniques may now allow for complex phase-matching characteristics in bulk focused devices, where previously they may have been restricted to the more controllable waveguide interactions. Utilising such structures in bulk focused interactions would allow significantly higher power handling than in waveguide devices.

## 7.4 High power SHG

Following on from the work on Gouy phase compensation at low power and negligible pump depletion a further study on the effects of focus induced phase mismatch under intense optical fields has been undertaken. Using a split-step beam propagation technique simulations of 3-D coupled wave equations defining SHG interactions have been performed. Through these simulations it has been shown that for narrow line width lasers, such as single longitudinal mode sources, there is unfortunately no greater benefit to utilising Gouy compensated QPM samples than at low power. With only a 3.5% increase in efficiency being achieved over the uniform QPM devices.

Further, it has been shown that at very high nonlinear drives, where fundamental pump depletion approaches 90%, GQPM samples are no longer able to compensate adequately the Gouy phase shift, resulting in a reduced efficiency compared with standard QPM. This reduction can been attributed to a variation in the propagation characteristics of the fundamental mode through a process known as non-linear depletion. Here, the high intensity centre of the Gaussian mode depletes more rapidly than the lower intensities wings, resulting in significantly altered propagation for which the GQPM grating cannot compensate.

However, for multi-longitudinal mode lasers, with bandwidths approaching that of the nonlinear devices, GQPM structures have shown considerable performance enhancements over QPM devices. Using a more complex BPM simulation, which models the interactions of hundreds of coupled modes, it has been shown that GQPM samples can limit back-conversion of the high intensity SHG signal to fundamental frequencies by removing possible phase-matching conditions.

Preliminary theoretical results have predicted an almost 100% enhancement in harmonic output power using GQPM samples for some high power interactions.

In an effort to produce GQPM designs suitable for the most intense parametric interactions a further self optimising BPM simulation tool has been developed. With the ability to optimise domain positions within the GQPM structure such a tool offers the promise of near perfectly phase-matched interactions even at the highest levels of nonlinear drive. Such a design has be used in conjunction with the effect of diffractive healing to maximise the conversion efficiency for a given fundamental power, providing theoretical conversion efficiencies of over 99%.

Thus far there has been no experimental verification of these concepts, with experimental testing of Gouy compensated devices limited to low fundamental powers. However, it is useful to highlight possible experiments that can be undertaken to verify the claims of this work. The simulations in this work suggest that the majority of high power SHG experiments performed in PPLN are performed in a regime significantly too energetic for high fundamental depletion to occur, with femtosecond and even picosecond regimes producing too high a nonlinear drive. Instead, utilising long pulse or cw laser sources it is possible to use long QPM devices, with the laser bandwidth now being considerably reduced compared with short pulse systems, allowing a slow growth of the harmonic field thus overcoming the nonlinear mode depletion mechanisms. To achieve conversion efficiencies approaching 100% in bulk interactions theory suggests peak powers no higher than 500 W in as long a self optimised QPM structure as physically possible. Such a regime reduces the detrimental effects of non-uniform deformation, both spatial and temporal, and will of course prevent back conversion to parasitic frequencies as observed in many high power experiments to date [5].

## 7.5 Future Work - Massively multimode waveguides

The demand for high power harmonic generation, particularly for producing visible green light, is high. However, as shown in Chapter 6, to obtain efficient harmonic conversion considerable optical intensities are required. There are numerous routes to obtaining high optical intensities, with one of the most common being the use of waveguide structures. With the use of single mode nonlinear waveguides it is routinely possible to achieve power conversion of over 50% [6], with the non depletion figure for conversion efficiency for a given length of $LiNbO_3$ being of the order of $150\,\%W^{-1}cm^{-1}$ [7, 8, 9]. In contrast, in unguided devices of the same material the accepted conversion efficiency is given as $4\,\%W^{-1}cm^{-1}$. From this it is clear that for efficient generation of harmonic light sources it is highly desirable to utilise waveguide structures, especially when the fundamental pump source is low power and CW.

However, there comes a problem with waveguide devices as attempts are made to scale the harmonic power to greater levels. Due to the very large optical intensities, which are necessary for the high conversion efficiency, waveguide based parametric conversion devices are prone to optical damage mechanisms. These damage effects, such as photo-refractive [10, 11, 12], GRIIRA [13] and BLIIRA [14] restrict the fundamental input power, with higher power levels leading to significant degradation of the nonlinear material. Single mode nonlinear waveguide experiments to date have shown a limited harmonic power output of the order 100 mW CW, with the greater number reporting values significantly lower [15, 16].

An obvious route to overcome such damage effects is to increase the mode area of the waveguide such that the optical field intensities are reduced. This technique however has highly undesirable effects that can lead to a significantly reduced conversion efficiency. By utilising a physically larger waveguide core, whilst maintaining the same index contrast, the nature of the guiding region can quickly become multi-mode. This multi-mode nature has significant implications for the harmonic generation process, with poor modal overlap reducing the nonlinear coupling [17] or even preventing any harmonic generation if the fundamental mode is even and the harmonic mode is odd [18]. Further, the propagation k-vector of each mode differs and leads to phase-matching errors, which can result in back conversion and parasitic depletion effects.

From this it can be seen that there is no simple method for efficiently generating moderate power harmonic light sources. With single mode waveguides providing no more than 100 mW CW power, albeit at very high efficiency, and bulk devices requiring significantly greater fundamental power to achieve 100 mW output. At this power level bulk devices are very inefficient resulting in significant power wastage which may be of considerable importance in compact, miniaturised systems for example.

An alternative concept that is proposed here, and an area of ongoing research, is the use of massively multimode large area waveguide structures. Here by deliberately utilising highly multimode structures, where there are 100's of spatial modes, many of the deleterious effects observed in multimode waveguides can be suppressed. Firstly, with sufficiently numerous fundamental and harmonic modes the issues of modal overlap are significantly reduced, with the high mode numbers providing a near uniform distribution of harmonic and fundamental power. Secondly, with many 100's of modes the standard deviation of k-vector values is reduced, with the consequence that phase-mismatch is minimised and back-conversion at higher powers is suppressed. A further practical advantage of multimode waveguides is the relative ease with which they can be fabricated, here air clad ridge waveguides in lithium niobate are considered as possible devices.

Traditionally, air clad ridge waveguides in $LiNbO_3$ are not often utilised due to the extremely

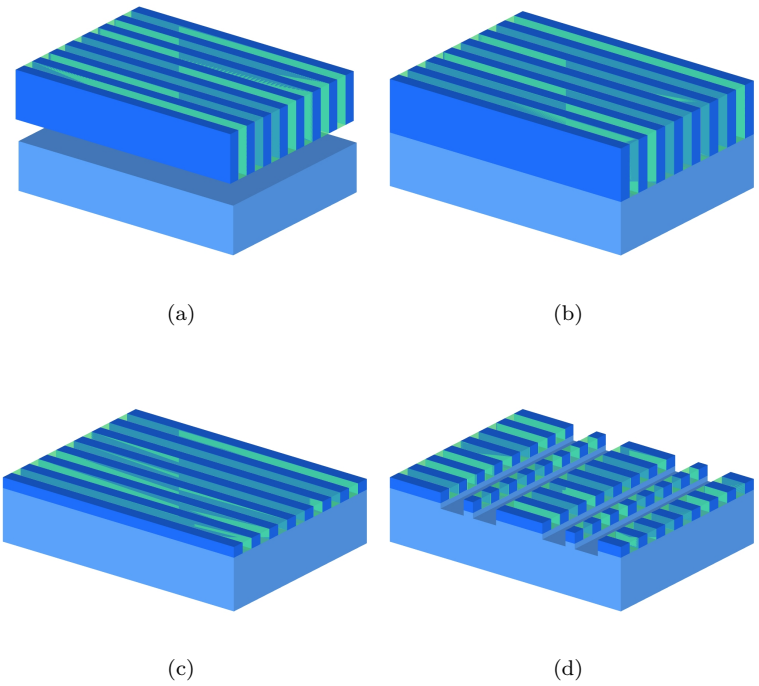


Figure 7.1: A schematic representation of the main steps of direct bonded PPLN ridge waveguides. (a) Poled $LiNbO_3$ wafer and substrate $LiTaO_3$ prior to direct bonding. (b) Samples combined using direct bonding. (c) PPLN layer polished back to 10's $\mu$m thickness. (d) Ridge waveguides formed using precision dicing saw.

high number of modes supported by the large step index contrast, with $LiNbO_3$ having an index of $\sim$2.15 at 633 nm. However, for this particular application this feature is highly desirable. There have been numerous proposed methods for fabricating ridge waveguides in this material, including utilising the differing etch rates for poled and unpoled domains [19]. In this work the robust technique of polishing and dicing is assumed as the basis for the devices. The process for the fabrication of such devices is outlined in Figure 7.1. Initially a sample of standard $LiNbO_3$ or MgO:$LiNbO_3$ is periodically poled for the desired phase-matching interaction using electric field poling techniques, as detailed in Chapter 2. This substrate is then bonded to a second lower index material, in this case $LiTaO_3$, using an adhesive free bonding technique. Here, with sufficiently flat and defect free optical surfaces two substrates can be permanently bonded together through only atomic forces [20]. Subsequently, the bonded poled layer is polished back to the desired thickness, nominally 10's of microns, to provide a degree of vertical confinement before a high precision dicing saw is used to machine a free-standing ridge structure.

A investigation into the expected conversion efficiency for a given waveguide core dimension

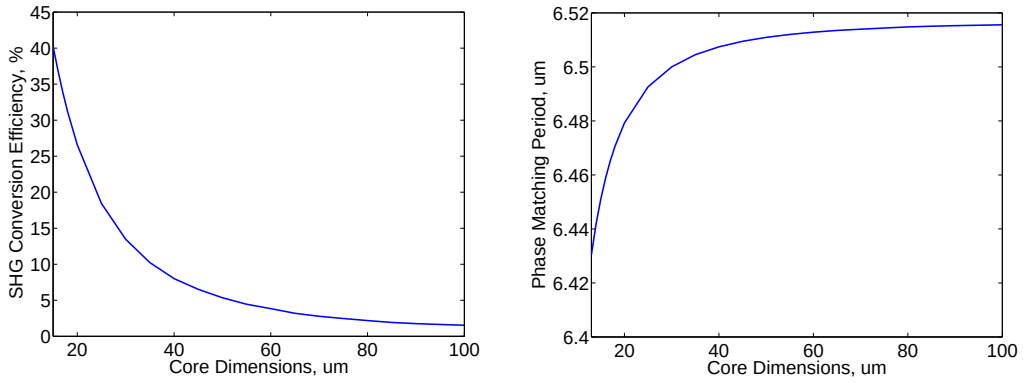


(a) (b)

Figure 7.2: (a) A theoretical plot of conversion efficiency against waveguide dimensions calculated using BPM, (b) The change in predicted phase-matching period for changing guide dimensions, here the effective index begins to alter the phase-matching characteristics.

has been undertaken numerically. Using a modified version of the nonlinear beam propagation technique developed in Chapter 6 approximate conversion efficiency measurements have been made. Here, the BPM software has been enhanced to account for the effects of the 2-D spatially varying index of the guide structure. It must be stressed that the simulation is by no means rigourous, with BPM generally considered unsuitable for high index contrast waveguides. Further, being a non-vectorial simulation technique, ignoring polarisation effects, exact mode propagation characteristics cannot be determined.

Despite the limitations of the BPM simulation it is still possible to obtain information on the expected conversion efficiency for a given core dimension. The results of these simulations are provided in Figure 7.2. For these results an input power of 1 W at 1064 nm wavelength is assumed with a device length of 10 mm, the core dimensions are defined to be square. From Figure 7.2(a) it is clear that considerable gains over bulk interactions can be obtained, with a 50 x 50 $\mu$m core being the maximum size before bulk interactions begin to become comparable in efficiency. It should be noted that for a bulk interaction in a 10 mm long device a focused beam diameter of $\sim$33 $\mu$m provides optimal conversion efficiency at 4% $W^{-1}\,cm^{-1}$. Using the same focusing optics a 30 $\mu$m waveguide would accept the majority of the focused spot but provide a conversion efficiency of 14% $W^{-1}\,cm^{-1}$. Shown in Figure 7.2(b) is the expected variation in phase matching period with changing core dimensions. Here, as the core dimension is reduced the effective index for the fundamental modes reduces more rapidly than for the harmonic modes resulting in a shift to shorter phase matching periods.

In conclusion, massively multimode waveguides show promise for obtaining relatively efficient harmonic output, being over 3.5 times as efficient as bulk devices, whilst maintaining high power handling capabilities. Such devices may prove useful in spanning the current divide between high efficiency single mode waveguide and high efficiency bulk devices. With single mode waveguides providing high efficiency but limited power output and bulk devices only providing high efficiency at the highest power levels. Future work would be the production and test of these devices with the aim of integration with inexpensive multi-watt level diode bars resulting in compact high power sources of visible laser light.

# References


[1] D. T. Reid. Engineered quasi-phase-matching for second-harmonic generation. *J. Opt. A-Pure Appl. Opt.*, 5:S97–S102, 2003.

[2] J. A. Armstrong, N. Bloembergen, J. Ducuing, and P. S. Pershan. Interactions between light waves in a nonlinear dielectric. *Phys. Rev.*, 127(6):1918–1939, 1962.

[3] G. D. Boyd and D. A. Kleinman. Parametric interaction of focused Gaussian light beams. *J. Appl. Phys.*, 39(8):3597–3639, 1968.

[4] L. G. Gouy. Sur une propriete nouvelle des ondes lumineuses. *C. R. Acad. Sci. Paris*, 110:1251, 1890.

[5] D. Taverner, P. Britton, P. G. R. Smith, D. J. Richardson, G. W. Ross, and D. P. Hanna. Highly efficient second-harmonic and sum-frequency generation of nanosecond pulses in a cascaded erbium-doped fiber:periodically poled lithium niobate source. *Opt. Lett.*, 23(3):162–164, 1998.

[6] Y. Nishida, H. Miyazawa, M. Asobe, O. Tadanaga, and H. Suzuki. 0-db wavelength conversion using direct-bonded QPM-Zn : $LiNbO_3$ ridge waveguide. *Photonics Technology Letters, IEEE*, 17(5):1049–1051, May 2005.

[7] M. Yamada, N. Nada, M. Saitohand, and K. Watanabe. First-order quasi-phase matched $LiNbO_3$ waveguide periodically poled by applying an external field for efficient blue second-harmonic generation. *Appl. Phys. Lett.*, 62(5):435–436, 1993.

[8] S. Kurimura, Y. Kato, M. Maruyama, Y. Usui, and H. Nakajima. Quasi-phase-matched adhered ridge waveguide in $LiNbO_3$. *Appl. Phys. Lett.*, 89(191123):1–3, 2006.

[9] K. R. Parameswaran, J. R. Kurz, R. V. Roussev, and M. M. Fejer. Observation of 99% pump depletion in single-pass second-harmonic generation in a periodically poled lithium niobate waveguide. *Opt. Lett.*, 27(1):43–45, 2002.

[10] Y. Furukawa, K. Kitamura, S. Takekawa, A. Miyamoto, M. Terao, and N. Suda. Photorefraction in $LiNbO_3$ as a function of [Li]/[Nb] and MgO concentrations. *Appl. Phys. Lett.*, 77(16):2494–2496, 2000.

[11] A. Ashkin, G. D. Boyd, J. M. Dziedzic, R. G. Smith, A. A. Ballman, J. J. Levinstein, and K. Nassau. Optically-induced refractive index inhomogeneities in $LiNbO_3$ and $LiTaO_3$. *Appl. Phys. Lett.*, 9(1):72–74, 1966.

[12] L. Pálfalvi, J. Hebling, G. Almási, and K. Polgár. Refractive index changes in Mg-doped $LiNbO_3$ caused by photorefraction and thermal effects. *J. Opt. A-Pure Appl. Opt.*, 5:S280–283, 2003.

[13] Y. Furukawa, K. Kitamura, A. Alexandrovski, R. Route, M. M. Fejer, and G. Foulon. Green-induced infrared absorption in MgO doped $LiNbO_3$. *Appl. Phys. Lett.*, 78(14):1970–1972, 2001.

[14] J. Hirohashi, V. Pasiskevicius, S. Wang, and F. Laurell. Picosecond blue-light-induced infrared absorption in single-domain and periodically poled ferroelectrics. *J. Appl. Phys.*, 101(3):033105, 2007.

[15] K. Mizuuchi, K. Yamamoto, and T. Taniuchi. Second-harmonic generation of blue light in a $LiTaO_3$ waveguide. *Appl. Phys. Lett.*, 58(24):2732–2734, June 1991.

[16] K. Yamamoto, K. Mizuuchi, Y. Kitaoka, and M. Kato. High power blue light generation by frequency doubling of a laser diode in a periodically domain-inverted litao3 waveguide. *Appl. Phys. Lett.*, 62(21):2599–2601, May 1993.

[17] L. Ming, C. B. E. Gawith, K. Gallo, M. V. O'Connor, G. D. Emmerson, and P. G. R. Smith. High conversion efficiency single-pass second harmonic generation in a zinc-diffused periodically poled lithium niobate waveguide. *Opt. Express.*, 13(13):4862–4868, 2005.

[18] J. R. Kurz, X. P. Xie, and M. M. Fejer. Odd waveguide mode quasi-phase matching with angled and staggered gratings. *Opt. Lett.*, 27(16):1445–1447, 2002.

[19] I. E. Barry, G. W. Ross, P. G. R. Smith, R. W. Eason, and G. Cook. Microstructuring of lithium niobate using differential etch-rate between inverted and non-inverted ferroelectric domains. *Mater. Lett.*, 37:246–254, 1998.

[20] C. B. E. Gawith, D. P. Shepherd, J. A. Abernethy, D. C. Hanna, G. W. Ross, and P. G. R. Smith. Second harmonic generation in a direct-bonded periodically poled $LiNbO_3$ buried waveguide. *Opt. Lett.*, 24(7):481–483, 1999.

# Appendix A

# Armstrong Derivation

$$\begin{aligned} E_1 &= \Re\left[A_1(z)\, e^{i(k_1 z-\omega_1 t)}\right] \\ &= \rho_1(z)\cos\left[k_1 z-\omega_1 t+\phi_1(z)\right] \end{aligned}$$

$$\frac{\mathrm{d}A_1}{\mathrm{d}z} = -i\left(\frac{2\omega^2 K}{k_1}\right) A_2 A_1^* e^{-i(2k_1-k_2)z} \tag{A.1}$$

$$\frac{\mathrm{d}A_2}{\mathrm{d}z} = -i\left(\frac{4\omega^2 K}{k_2}\right) A_1^2 e^{i(2k_1-k_2)z} \tag{A.2}$$

Here $K = \frac{2\pi\chi^{(2)}}{c^2}$ is the device nonlinearity. Using $A_1 = \rho_1 e^{i\phi_1}$ and $A_2 = \rho_2 e^{i\phi_2}$ the above equations can be re-written as:

$A.1 \Rightarrow$

$$\begin{aligned} \frac{\mathrm{d}}{\mathrm{d}z}\left(\rho_1 e^{i\phi}\right) &= -i\left(\frac{2\omega^2 K}{k_1}\right)\rho_2 e^{i\phi_2}\rho_1 e^{-i\phi_1} e^{-i(2k_1-k_2)z} \\ \frac{\mathrm{d}\rho_1}{\mathrm{d}z}e^{i\phi_1} + i\rho_1\frac{\mathrm{d}\phi_1}{\mathrm{d}z}e^{i\phi_1} &= -i\left(\frac{2\omega^2 K}{k_1}\right)\rho_2\rho_1 e^{-i((2k_1-k_2)z+\phi_1-\phi_2)} \\ &= -i\left(\frac{2\omega^2 K}{k_1}\right)\rho_2\rho_1\left[\cos\theta - i\sin\theta\right] \end{aligned}$$

Real part

$$\frac{\mathrm{d}\rho_1}{\mathrm{d}z} = -\left(\frac{2\omega^2 K}{k_1}\right)\rho_2\rho_1\sin\theta \tag{A.3}$$

Imaginary part

$$\rho_1\frac{\mathrm{d}\phi_1}{\mathrm{d}z} = -\left(\frac{2\omega^2 K}{k_1}\right)\rho_2\rho_1\cos\theta \tag{A.4}$$

$A.2 \Rightarrow$

$$\begin{aligned}
\frac{\mathrm{d}}{\mathrm{d}z}\left(\rho_2 e^{i\phi_2}\right) &= -i\left(\frac{4\omega^2 K}{k_2}\right)\rho_1^2 e^{i2\phi_1} e^{i(2k_1-k_2)z} \\
\frac{\mathrm{d}\rho_2}{\mathrm{d}z}e^{i\phi_2} + i\rho_2\frac{\mathrm{d}\phi_2}{\mathrm{d}z}e^{i\phi_2} &= -i\left(\frac{4\omega^2 K}{k_2}\right)\rho_1^2 e^{i((2k_1-k_2)z+2\phi_1)} \\
&= -i\left(\frac{4\omega^2 K}{k_2}\right)\rho_1^2\left[\cos\theta + i\sin\theta\right]
\end{aligned}$$

Real part

$$\frac{\mathrm{d}\rho_2}{\mathrm{d}z} = \left(\frac{4\omega^2 K}{k_2}\right)\rho_1^2 \sin\theta \tag{A.5}$$

Imaginary part

$$\rho_2\frac{\mathrm{d}\phi_2}{\mathrm{d}z} = -\left(\frac{4\omega^2 K}{k_2}\right)\rho_1^2 \cos\theta \tag{A.6}$$

combining A.4 and A.6 a single equation for the imaginary terms can be obtained:

$$2 \times \frac{A.4}{\rho_1} - \frac{A.6}{\rho_2}$$

$\Rightarrow$

$$\begin{aligned}
2\frac{\mathrm{d}\phi_1}{\mathrm{d}z} - \frac{\mathrm{d}\phi_2}{\mathrm{d}z} &= -\left(\frac{4\omega^2 K}{k_1}\right)\rho_2\cos\theta + \left(\frac{4\omega^2 K}{k_2}\right)\frac{\rho_1^2}{\rho_2}\cos\theta \\
&= -\left(4\omega^2 K\right)\left(\frac{\rho_2}{k_1} - \frac{\rho_1^2}{\rho_2 k_2}\right)\cos\theta \\
\frac{\mathrm{d}}{\mathrm{d}z}\left(2\phi_1 - \phi_2\right) + \Delta k &= \Delta k - \left(4\omega^2 K\right)\left(\frac{\rho_2}{k_1} - \frac{\rho_1^2}{\rho_2 k_2}\right)\cos\theta
\end{aligned}$$

using

$$\frac{\mathrm{d}}{\mathrm{d}z}\left(2\phi_1 - \phi_2 + 2k_1 z - k_2 z\right) = \frac{\mathrm{d}\theta}{\mathrm{d}z}$$

the following real equations can further be obtained.

$$\frac{\mathrm{d}\rho_1}{\mathrm{d}z} = -\left(\frac{2\omega^2 K}{k_1}\right)\rho_1\rho_2\sin\theta \tag{A.7}$$

$$\frac{\mathrm{d}\rho_2}{\mathrm{d}z} = \left(\frac{4\omega^2 K}{k_2}\right)\rho_1^2\sin\theta \tag{A.8}$$

$$\frac{\mathrm{d}\theta}{\mathrm{d}z} = \Delta k - 4\omega^2 K\left(\frac{\rho_2}{k_1} - \frac{\rho_1^2}{\rho_2 k_2}\right)\cos\theta \tag{A.9}$$

Rearranging A.7 and A.8

$$A.7 \Rightarrow \frac{\rho_2}{k_1} = \frac{-1}{2\omega^2 K\sin\theta\rho_1}\frac{\mathrm{d}\rho_1}{\mathrm{d}z}$$

$$\frac{A.8}{\rho_2} \Rightarrow \frac{\rho_1^2}{\rho_2 k_2} = \frac{1}{4\omega^2 K\sin\theta\rho_2}\frac{\mathrm{d}\rho_2}{\mathrm{d}z}$$

$\Rightarrow$

$$\frac{\mathrm{d}\theta}{\mathrm{d}z} = \Delta k - 4\omega^2 K\left(\frac{-1}{2\omega^2 K\rho_1}\frac{\mathrm{d}\rho_1}{\mathrm{d}z} - \frac{1}{4\omega^2 K\rho_2}\frac{\mathrm{d}\rho_2}{\mathrm{d}z}\right)\frac{\cos\theta}{\sin\theta} \tag{A.10}$$

$$= \Delta k + \left(\frac{2}{\rho_1}\frac{\mathrm{d}\rho_1}{\mathrm{d}z} + \frac{1}{\rho_2}\frac{\mathrm{d}\rho_2}{\mathrm{d}z}\right)\frac{\cos\theta}{\sin\theta} \tag{A.11}$$

$$= \Delta k + \frac{\mathrm{d}}{\mathrm{d}z}\ln\left(\rho_1^2\rho_2\right)\frac{\cos\theta}{\sin\theta} \tag{A.12}$$

$$\frac{\mathrm{d}\rho_1}{\mathrm{d}z} = -\left(\frac{2\omega^2 K}{k_1}\right)\rho_1\rho_2\sin\theta \tag{A.13}$$

$$\frac{\mathrm{d}\rho_2}{\mathrm{d}z} = \left(\frac{4\omega^2 K}{k_2}\right)\rho_1^2\sin\theta \tag{A.14}$$

$$\frac{\mathrm{d}\theta}{\mathrm{d}z} = \Delta k + \frac{\mathrm{d}}{\mathrm{d}z}\ln\left(\rho_1^2\rho_2\right)\frac{\cos\theta}{\sin\theta} \tag{A.15}$$

Using the Manely-Rowe relations:

$$\frac{k_1}{\omega_1}|E_1|^2 + \frac{k_2}{\omega_2}|E_2|^2 = \text{constant}$$

$$\frac{k_1}{\omega}\rho_1^2 + \frac{k_2}{2\omega}\rho_2^2 = \text{constant}$$

$\Rightarrow$

$$W = \frac{c^2}{8\pi\omega}\left(k_1\rho_1^2 + \frac{k_2}{2}\rho_2^2\right) \tag{A.16}$$

To obtain Eq.(5.5) in Armstrong-Bloembergen use the following substitutions:

$$u = \left(\frac{c^2 k_1}{8\pi\omega W}\right)^{1/2}\rho_1 \Rightarrow \rho_1 = \left(\frac{8\pi\omega W}{c^2 k_1}\right)^{1/2} u$$

$$v = \left(\frac{c^2 k_2}{16\pi\omega W}\right)^{1/2}\rho_2 \Rightarrow \rho_2 = \left(\frac{16\pi\omega W}{c^2 k_2}\right)^{1/2} v$$

$$\zeta = \left(\frac{2\omega^2 K}{k_1}\right)\left(\frac{16\pi\omega W}{c^2 k_2}\right)^{1/2} z \Rightarrow z = \left(\frac{k_1}{2\omega^2 K}\right)\left(\frac{c^2 k_2}{16\pi\omega W}\right)^{1/2}\zeta$$

$$\frac{\mathrm{d}\rho_1}{\mathrm{d}z} = \left(\frac{8\pi\omega W}{c^2 k_1}\right)^{1/2}\frac{\mathrm{d}u}{\mathrm{d}z}$$

$$\frac{\mathrm{d}\rho_2}{\mathrm{d}z} = \left(\frac{16\pi\omega W}{c^2 k_2}\right)^{1/2}\frac{\mathrm{d}v}{\mathrm{d}z}$$

$$\frac{\mathrm{d}z}{\mathrm{d}\zeta} = \left(\frac{k_1}{2\omega^2 K}\right)\left(\frac{c^2 k_2}{16\pi\omega W}\right)^{1/2}$$

$\Rightarrow$

$$\frac{\mathrm{d}\rho_1}{\mathrm{d}z} \Rightarrow \left(\frac{8\pi\omega W}{c^2 k_1}\right)^{1/2}\frac{\mathrm{d}u}{\mathrm{d}z} = -\left(\frac{2\omega^2 K}{k_1}\right)\left(\frac{8\pi\omega W}{c^2 k_1}\right)^{1/2}\left(\frac{16\pi\omega W}{c^2 k_2}\right)^{1/2} uv\sin\theta$$

$$\frac{\mathrm{d}u}{\mathrm{d}z} = -\left(\frac{2\omega^2 K}{k_1}\right)\left(\frac{16\pi\omega W}{c^2 k_2}\right)^{1/2} uv\sin\theta$$

$$\begin{aligned}
\frac{\mathrm{d}u}{\mathrm{d}\zeta} &= \frac{\mathrm{d}u}{\mathrm{d}z}\frac{\mathrm{d}z}{\mathrm{d}\zeta} \\
&= -\left(\frac{2\omega^2 K}{k_1}\right)\left(\frac{16\pi\omega W}{c^2 k_2}\right)^{1/2} uv\sin\theta\left(\frac{k_1}{2\omega^2 K}\right)\left(\frac{c^2 k_2}{16\pi\omega W}\right)^{1/2} \\
\frac{\mathrm{d}u}{\mathrm{d}\zeta} &= -uv\sin\theta
\end{aligned}$$

$$\begin{aligned}
\frac{\mathrm{d}\rho_2}{\mathrm{d}z} \Rightarrow \left(\frac{16\pi\omega W}{c^2 k_2}\right)^{1/2}\frac{\mathrm{d}v}{\mathrm{d}z} &= \left(\frac{4\omega^2 K}{k_2}\right)\left(\frac{8\pi\omega W}{c^2 k_1}\right)u^2\sin\theta \\
\frac{\mathrm{d}v}{\mathrm{d}z} &= \left(\frac{4\omega^2 K}{k_2}\right)\left(\frac{8\pi\omega W}{c^2 k_1}\right)\left(\frac{c^2 k_2}{16\pi\omega W}\right)^{1/2} u^2\sin\theta
\end{aligned}$$

$$\begin{aligned}
\frac{\mathrm{d}v}{\mathrm{d}\zeta} &= \frac{\mathrm{d}v}{\mathrm{d}z}\frac{\mathrm{d}z}{\mathrm{d}\zeta} \\
&= \left(\frac{4\omega^2 K}{k_2}\right)\left(\frac{8\pi\omega W}{c^2 k_1}\right)\left(\frac{c^2 k_2}{16\pi\omega W}\right)^{1/2} u^2\sin\theta\left(\frac{k_1}{2\omega^2 K}\right)\left(\frac{c^2 k_2}{16\pi\omega W}\right)^{1/2} \\
&= 2\frac{k_1}{k_2}\left(\frac{8\pi\omega W}{c^2 k_1}\right)\left(\frac{c^2 k_2}{16\pi\omega W}\right)u^2\sin\theta \\
\frac{\mathrm{d}v}{\mathrm{d}\zeta} &= u^2\sin\theta
\end{aligned}$$

$$\begin{aligned}
\frac{\mathrm{d}\theta}{\mathrm{d}z} &= \Delta k + \frac{\cos\theta}{\sin\theta}\left(\frac{2}{\rho_1}\frac{\mathrm{d}\rho_1}{\mathrm{d}z} + \frac{1}{\rho_2}\frac{\mathrm{d}\rho_2}{\mathrm{d}z}\right) \\
&= \Delta k + \frac{\cos\theta}{\sin\theta}\left(\frac{2}{\left(\frac{8\pi\omega W}{c^2 k_1}\right)^{1/2} u}\left(\frac{8\pi\omega W}{c^2 k_1}\right)^{1/2}\frac{\mathrm{d}u}{\mathrm{d}z} + \frac{1}{\left(\frac{16\pi\omega W}{c^2 k_2}\right)^{1/2} v}\left(\frac{16\pi\omega W}{c^2 k_2}\right)^{1/2}\frac{\mathrm{d}v}{\mathrm{d}z}\right) \\
&= \Delta k + \frac{\cos\theta}{\sin\theta}\left(\frac{2}{u}\frac{\mathrm{d}u}{\mathrm{d}z} + \frac{1}{v}\frac{\mathrm{d}v}{\mathrm{d}z}\right) \\
&= \Delta k + \frac{\cos\theta}{\sin\theta}\frac{\mathrm{d}}{\mathrm{d}z}\ln\left(u^2 v\right)
\end{aligned}$$

$$\begin{aligned}
\frac{\mathrm{d}\theta}{\mathrm{d}\zeta} &= \frac{\mathrm{d}\theta}{\mathrm{d}z}\frac{\mathrm{d}z}{\mathrm{d}\zeta} \\
&= \Delta k\left(\frac{k_1}{2\omega^2 K}\right)\left(\frac{c^2 k_2}{16\pi\omega W}\right)^{1/2} + \frac{\cos\theta}{\sin\theta}\frac{\mathrm{d}}{\mathrm{d}z}\ln\left(u^2 v\right)\frac{\mathrm{d}z}{\mathrm{d}\zeta} \\
&= \Delta S + \frac{\cos\theta}{\sin\theta}\frac{\mathrm{d}}{\mathrm{d}\zeta}\ln\left(u^2 v\right)
\end{aligned}$$

where

$$\Delta S = \frac{\Delta k}{\left(\frac{2\omega^2 K}{k_1}\right)\left(\frac{16\pi\omega W}{c^2 k_2}\right)^{1/2}}$$

Rearranging $W$ in terms of $u$ and $v$

$$\begin{aligned} W &= \frac{C^2}{8\pi\omega}\left(k_1\rho_1^2 + \frac{k_2}{2}\rho_2^2\right) \\ &= \frac{C^2}{8\pi\omega}\left[k_1\left(\frac{8\pi\omega W}{c^2 k_1}\right)u^2 + \frac{k_2}{2}\left(\frac{16\pi\omega W}{c^2 k_2}\right)v^2\right] \\ &= \left(\frac{c^2}{8\pi\omega}\right)\left(\frac{8\pi\omega W}{c^2}\right)\left[u^2+v^2\right] \\ W &= W\left[u^2+v^2\right] \end{aligned}$$

thus $u^2 + v^2 = 1$.

So finally the three equations from Armstrong-Bloembergen are:

$$\frac{\mathrm{d}u}{\mathrm{d}\zeta} = -uv\sin\theta \tag{A.17}$$

$$\frac{\mathrm{d}v}{\mathrm{d}\zeta} = u^2\sin\theta \tag{A.18}$$

$$\frac{\mathrm{d}\theta}{\mathrm{d}\zeta} = \Delta S + \frac{\cos\theta}{\sin\theta}\frac{\mathrm{d}}{\mathrm{d}\zeta}\ln\left(u^2 v\right) \tag{A.19}$$

First it is necessary to consider the case of perfect phase matching. Integrating Eq. A.19 whilst setting $\Delta S = 0$ gives,

$$\begin{aligned} \int \frac{\sin\theta}{\cos\theta}\frac{\mathrm{d}\theta}{\mathrm{d}\zeta}d\zeta &= \int \frac{\mathrm{d}}{\mathrm{d}\zeta}\ln\left(u^2 v\right)d\zeta \\ \int \tan\theta d\theta &= \int d\ln\left(u^2 v\right) \\ -\ln|\cos\theta| + c_1 &= \ln\left(u^2 v\right) + c_2 \\ \ln\left(u^2 v\right) + \ln|\cos\theta| &= c_3 \\ \ln\left(u^2 v\cos\theta\right) &= \ln\left(\Gamma\right) \\ u^2 v\cos\theta &= \Gamma \end{aligned}$$

Now evaluating $\Gamma$ at $z = \zeta = 0$

$$\begin{aligned} \Gamma &= \left(\frac{c^2 k_1}{8\pi\omega W}\right)\left(\frac{c^2 k_2}{16\pi\omega W}\right)^{1/2}\rho_1^2(0)\,\rho_2(0)\cos\left[2\phi_1(0) - \phi_2(0)\right] \\ &= 2k_1 k_2^{1/2}\left(\frac{c^2}{16\pi\omega W}\right)\left(\frac{c^2}{16\pi\omega W}\right)^{1/2}\rho_1^2(0)\,\rho_2(0)\cos\left[2\phi_1(0) - \phi_2(0)\right] \\ &= \frac{2k_1}{k_2}\left(\frac{c^2 k_2}{16\pi\omega W}\right)^{3/2}\rho_1^2(0)\,\rho_2(0)\cos\left[2\phi_1(0) - \phi_2(0)\right] \end{aligned}$$

giving the same as Eq 5.8 in Armstrong-Bloembergen.

Now to obtain an expression for $\zeta$ as in Eq 5.9 utilise both the facts $u^2 + v^2 = 1$ and $\Gamma = u^2 v \cos\theta$

$$\begin{aligned}
\frac{\mathrm{d}v}{\mathrm{d}\zeta} &= u^2 \sin\theta \\
v\frac{\mathrm{d}v}{\mathrm{d}\zeta} &= u^2 v \sin\theta \\
\frac{1}{2}\frac{\mathrm{d}\left(v^2\right)}{\mathrm{d}\zeta} &= u^2 v \sin\theta \\
\left(\frac{\mathrm{d}\left(v^2\right)}{\mathrm{d}\zeta}\right)^2 &= 4u^4 v^2 \sin^2\theta \\
&= 4u^4 v^2 \left(1 - \cos^2\theta\right) \\
&= 4\left(u^4 v^2 - u^4 v^2 \cos^2\theta\right) \\
&= 4\left(u^4 v^2 - \Gamma^2\right) \\
\frac{\mathrm{d}\left(v^2\right)}{\mathrm{d}\zeta} &= \pm 2\left[\left(1 - v^2\right)^2 v^2 - \Gamma^2\right]^{1/2} \qquad \text{(A.20)} \\
d\zeta &= \pm\frac{1}{2}\left[\left(1 - v^2\right)^2 v^2 - \Gamma^2\right]^{-1/2} dv^2 \\
\zeta &= \pm\frac{1}{2}\int_{v^2(0)}^{v^2(\zeta)} \frac{d\left(v^2\right)}{\left[\left(1 - v^2\right)^2 v^2 - \Gamma^2\right]^{1/2}} \qquad \text{(A.21)}
\end{aligned}$$

At this point notation is introduced to allow the denominator of Eqn. A.21 to be written as an expression of its roots. To clarify, the roots of the denominator are the roots of Eqn. A.20 which are, of course, the $\zeta$ positions at which the gradient of $v^2$ is zero, i.e a maxima, minima or point of inflection. Physically $v^2$ is constrained to only exist between 0 and 1, therefore there must be both a minimum and a maximum to prevent $v^2$ escaping its bounds. The third root can be an unphysical solution, the variation of $v$ is periodic and such requires the last maxima/minimum to feed into the first, e.g if there is no harmonic initially $\Gamma = 0$ and the roots of $v^2(1 - v^2)^2 - \Gamma^2$ are 0 & 1 twice. If however the third root is not a repeated root it is unphysical and thus ignored.

With this in mind define the roots of the cubic as $v_c^2 \geq v_b^2 \geq v_a^2$, from this an expression for the period at which $v^2$ oscillates between its lowest roots, also known as the coherence length, can be generated.

$$\Pi_\zeta = \int_{v_a^2}^{v_b^2} \frac{\mathrm{d}\left(v^2\right)}{\left[v^2(1 - v^2)^2 - \Gamma^2\right]^{1/2}}.$$

Now consider the situation that only a fundamental beam is input i.e $\Gamma = 0$ this as above implies

$v_a^2 = 0$ and $v_b^2 = 1$ giving:

$$\begin{aligned}\zeta &= \frac{1}{2}\int_{v^2(0)}^{v^2(\zeta)} \frac{\mathrm{d}\left(v^2\right)}{\left[v^2\left(v^2 - v_a^2\right)\left(v^2 - v_b^2\right)\right]^{1/2}} \\ &= \frac{1}{2}\int_{v^2(0)}^{v^2(\zeta)} \frac{\mathrm{d}\left(v^2\right)}{\left[v^2\left(v^2 - 1\right)\left(v^2 - 1\right)\right]^{1/2}}\end{aligned}$$

Now, let $v^2 - 1 = p$, $\Rightarrow \mathrm{d}\left(v^2\right) = \mathrm{d}p$

$$\begin{aligned}\zeta &= \frac{1}{2}\int_{v^2(0)-1}^{v^2(\zeta)-1} \frac{\mathrm{d}p}{\left[\left(p+1\right)p^2\right]^{1/2}} \\ &= \frac{1}{2}\int_{v^2(0)-1}^{v^2(\zeta)-1} \frac{\mathrm{d}p}{p\sqrt{p+1}}\end{aligned}$$

Substituting back with $p = v^2 - 1$ and $\mathrm{d}p = 2v\mathrm{d}v$

$$\begin{aligned}\zeta &= \frac{1}{2}\int_{v^2(0)}^{v^2(\zeta)} \frac{2v\mathrm{d}v}{\left(v^2-1\right)v} \\ &= \int_{v^2(0)}^{v^2(\zeta)} \frac{\mathrm{d}v}{\left(v^2-1\right)} \qquad \text{(A.22)} \\ &= \int_{0}^{v^2(\zeta)} \frac{\mathrm{d}v}{\left(v^2-1\right)} - \int_{0}^{v^2(0)} \frac{\mathrm{d}v}{\left(v^2-1\right)} \qquad \text{(A.23)}\end{aligned}$$

Defining

$$\zeta_1 = \int_{0}^{v^2(\zeta)} \frac{\mathrm{d}v}{\left(v^2-1\right)}$$

and

$$\zeta_0 = \int_{0}^{v^2(0)} \frac{\mathrm{d}v}{\left(v^2-1\right)}$$

it is possible to write

$$\zeta + \zeta_0 = \zeta_1.$$

Now, from the definition of $\tanh^{-1}(x)$ in log form the following is obtained,

$$\begin{aligned}\frac{\mathrm{d}}{\mathrm{d}x}\tanh^{-1}(x) &= \frac{\mathrm{d}}{\mathrm{d}x}\left(\frac{1}{2}\ln\left[\frac{1+x}{1-x}\right]\right) \\ &= \frac{1}{2}\left(\frac{1-x}{1+x}\right)\left(\frac{(1)(1-x)-(-1)(1+x)}{(1-x)^2}\right) \\ &= \frac{1}{2}\left(\frac{1}{1+x}\right)\left(\frac{(1-x)+(x-1)}{1-x}\right) \\ &= \frac{1}{(1+x)(1-x)} \\ &= \frac{-1}{x^2-1} \qquad \text{(A.24)}\end{aligned}$$

Comparing Eqn. A.23 and Eq. A.24 it can thus be seen

$$\zeta + \zeta_0 = -\tanh^{-1}\left(\sqrt{v^2_{\Gamma=0}(\zeta)}\right).$$

Therefore,

$$\begin{aligned} v_{\Gamma=0}(\zeta) &= \tanh(\zeta+\zeta_0) && \text{(A.25)} \\ u_{\Gamma=0}(\zeta) &= \sqrt{1-\tanh^2(\zeta+\zeta_0)} \\ &= \operatorname{sech}(\zeta+\zeta_0) && \text{(A.26)} \end{aligned}$$

From this it is clear that as device length ($\zeta$) tends towards $\infty$ the harmonic power tends towards 100%.

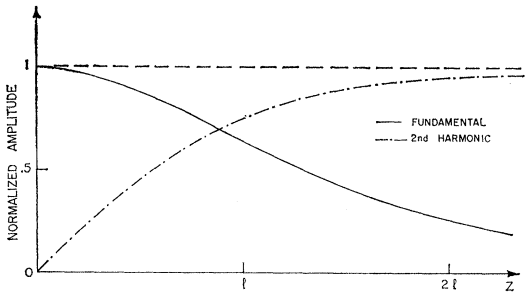


FIG. 3. The growth of the normalized second-harmonic amplitude and decrease of the normalized fundamental amplitude for perfect phase matching, if the second harmonic builds up from zero.

Now it is necessary to re-write Eqn. A.21 in a form directly comparable with that of a Jacobi elliptic function. Starting from, Eq. A.21 the denominator can be written in terms of its roots

$$\begin{aligned} \zeta &= \frac{1}{2}\int_{v^2(0)}^{v^2(\zeta)} \frac{\mathrm{d}\left(v^2\right)}{\left[v^2\left(1-v^2\right)^2-\Gamma^2\right]^{1/2}} \\ \zeta &= \frac{1}{2}\int_{v^2(0)}^{v^2(\zeta)} \frac{\mathrm{d}\left(v^2\right)}{\left[\left(v^2-v_a^2\right)\left(v^2-v_b^2\right)\left(v^2-v_c^2\right)\right]^{1/2}} \end{aligned}$$

$$\times \frac{v_b^2-v_a^2}{\sqrt{v_b^2-v_a^2}\sqrt{v_b^2-v_a^2}}$$

$$\zeta = \frac{1}{2}\int_{v^2(0)}^{v^2(\zeta)} \frac{\mathrm{d}\left(v^2\right)}{\sqrt{\frac{v^2-v_a^2}{v_b^2-v_a^2}}\left(v_b^2-v_a^2\right)\sqrt{\frac{\left(v^2-v_b^2\right)\left(v^2-v_c^2\right)}{v_b^2-v_a^2}}}$$

Now, making the substitutions

$$y^2 = \frac{v^2-v_a^2}{v_b^2-v_a^2}$$

$$\begin{aligned} v^2 &= y^2\left(v_b^2 - v_a^2\right) - v_a^2 \\ \mathrm{d}\left(v^2\right) &= 2\left(v_b^2 - v_a^2\right) y\,\mathrm{d}y \\ &= 2\left(v_b^2 - v_a^2\right)\sqrt{\frac{v^2 - v_a^2}{v_b^2 - v_a^2}}\,\mathrm{d}y \end{aligned}$$

giving,

$$\begin{aligned} \zeta &= \frac{1}{2}\int_{v^2(0)}^{v^2(\zeta)} \frac{2\sqrt{\frac{v^2-v_a^2}{v_b^2-v_a^2}}\left(v_b^2 - v_a^2\right)\,\mathrm{d}y}{\sqrt{\frac{v^2-v_a^2}{v_b^2-v_a^2}}\left(v_b^2 - v_a^2\right)\sqrt{\frac{\left(v^2-v_b^2\right)\left(v^2-v_c^2\right)}{v_b^2-v_a^2}}} \\ &= \int_{y(0)}^{y(\zeta)} \frac{\mathrm{d}y}{\left[\frac{\left(v^2-v_b^2\right)\left(v^2-v_c^2\right)}{v_b^2-v_a^2}\right]^{1/2}} \end{aligned}$$

For ease of reading only the denominator of the integrand is written out fully. Now, split the fraction,

$$\begin{aligned} \left[\frac{\left(v^2 - v_b^2\right)\left(v^2 - v_c^2\right)}{v_b^2 - v_a^2}\right]^{1/2} &= \left[\left(\frac{-v^2 + v_b^2}{v_b^2 - v_a^2}\right)\left(-v^2 + v_c^2\right)\right]^{1/2} \\ &= \left[\left(\frac{v_a^2 - v^2 + v_b^2 - v_a^2}{v_b^2 - v_a^2}\right)\left(-v^2 + v_c^2\right)\right]^{1/2} \\ &= \left[\left(1 - \frac{v^2 - v_a^2}{v_b^2 - v_a^2}\right)\left(-v^2 + v_c^2\right)\right]^{1/2} \\ &\quad \times \frac{v_c^2 - v_a^2}{v_c^2 - v_a^2} \end{aligned}$$

$$\begin{aligned} &= \left[\left(1 - \frac{v^2 - v_a^2}{v_b^2 - v_a^2}\right)\left(\frac{-v^2 + v_c^2}{v_c^2 - v_a^2}\right)\left(v_c^2 - v_a^2\right)\right]^{1/2} \\ &= \left[\left(1 - \frac{v^2 - v_a^2}{v_b^2 - v_a^2}\right)\left(\frac{v_a^2 - v^2 + v_c^2 - v_a^2}{v_c^2 - v_a^2}\right)\left(v_c^2 - v_a^2\right)\right]^{1/2} \\ &= \left[\left(1 - \frac{v^2 - v_a^2}{v_b^2 - v_a^2}\right)\left(1 - \frac{v^2 - v_a^2}{v_c^2 - v_a^2}\right)\left(v_c^2 - v_a^2\right)\right]^{1/2} \\ &= \left[\left(1 - \frac{v^2 - v_a^2}{v_b^2 - v_a^2}\right)\left(1 - \frac{v^2 - v_a^2}{v_b^2 - v_a^2}\left(\frac{v_b^2 - v_a^2}{v_c^2 - v_a^2}\right)\right)\left(v_c^2 - v_a^2\right)\right]^{1/2} \end{aligned}$$

Finally, define:

$$\gamma^2 = \frac{v_b^2 - v_a^2}{v_c^2 - v_a^2}$$

giving,

$$\left[\frac{\left(v^2 - v_b^2\right)\left(v^2 - v_c^2\right)}{v_b^2 - v_a^2}\right]^{1/2} = \left[\left(1 - y^2\right)\left(1 - \gamma^2 y^2\right)\left(v_c^2 - v_a^2\right)\right]^{1/2}$$

Putting this result back in as the denominator of the integrand the following is obtained,

$$\zeta = \frac{\pm 1}{\left(v_c^2 - v_a^2\right)^{1/2}} \int_{y(0)}^{y(\zeta)} \frac{dy}{\left[\left(1-y^2\right)\left(1-\gamma^2 y^2\right)\right]^{1/2}}$$

Noting that the definition of an elliptic integral of the first kind is

$$\begin{aligned} u &= \int_0^x \frac{dx}{\sqrt{1-x^2}\sqrt{1-k^2x^2}} \\ &= \mathrm{sn}^{-1}\left(x,\, k\right) \\ x &= \mathrm{sn}\left(u,\, k\right) \end{aligned}$$

and that

$$\int_{x_0}^{x_1} \frac{dx}{\sqrt{1-x^2}\sqrt{1-k^2x^2}} = \int_0^{x_1} \frac{dx}{\sqrt{1-x^2}\sqrt{1-k^2x^2}} - \int_0^{x_0} \frac{dx}{\sqrt{1-x^2}\sqrt{1-k^2x^2}}$$

letting

$$u_1 = \int_0^{x_1} \frac{dx}{\sqrt{1-x^2}\sqrt{1-k^2x^2}}$$

and

$$u_0 = \int_0^{x_0} \frac{dx}{\sqrt{1-x^2}\sqrt{1-k^2x^2}}$$

it is possible to write

$$u + u_0 = u_1,$$

which provides the following definition:

$$\zeta + \zeta_0 = \frac{\pm 1}{\left(v_c^2 - v_a^2\right)^{1/2}} \int_{0)}^{y(\zeta)} \frac{dy}{\left[\left(1-y^2\right)\left(1-\gamma^2 y^2\right)\right]^{1/2}} \tag{A.27}$$

$$\left(\zeta + \zeta_0\right)\left(v_c^2 - v_a^2\right)^{1/2} = \int_0^{y(\zeta)} \frac{dy}{\left[\left(1-y^2\right)\left(1-\gamma^2 y^2\right)\right]^{1/2}} \tag{A.28}$$

$$\left(\zeta + \zeta_0\right)\left(v_c^2 - v_a^2\right)^{1/2} = \mathrm{sn}^{-1}\left(y\left(\zeta\right),\, \gamma\right) \tag{A.29}$$

$$y\left(\zeta\right) = \mathrm{sn}\left[\left(\zeta + \zeta_0\right)\left(v_c^2 - v_a^2\right)^{1/2},\, \gamma\right] \tag{A.30}$$

$$y^2\left(\zeta\right) = \mathrm{sn}^2\left[\left(\zeta + \zeta_0\right)\left(v_c^2 - v_a^2\right)^{1/2},\, \gamma\right] \tag{A.31}$$

$$v^2\left(\zeta\right) = v_a^2 + \left(v_b^2 - v_a^2\right)\mathrm{sn}^2\left[\left(\zeta + \zeta_0\right)\left(v_c^2 - v_a^2\right)^{1/2},\, \gamma\right] \tag{A.32}$$

## A.1 Non-phase-matched case

Now consider the situation where phase-matching is imperfect, for example when efficient harmonic generation is achieved via quasi-phase-matching (QPM). In this situation the only difference in the analysis is in the definition of $\Gamma$, as can be inferred from Eq. A.19. As $\Delta k$ is no

longer zero, and thus $\Delta S \neq 0$ the integration of Eq. A.19 is no longer trivial, in the Armstrong-Bloembergen paper it is suggested that this integration can be performed via the method of variation of the parameter. However, it has proved difficult to replicate the method described, so instead, working backwards from the final solution (ABDP Eq. 5.15) Eq. A.19 shall be obtained thus proving the validity.

Starting with

$$u^2 v\cos\theta + \frac{1}{2}\Delta S\left(v^2 - v_{(0)}^2\right) = \Gamma$$

differentiate with respect to $\zeta$.

$$\begin{aligned}
\frac{\mathrm{d}}{\mathrm{d}\zeta}\left(u^2 v\cos\theta\right) + \frac{1}{2}\Delta S\frac{\mathrm{d}}{\mathrm{d}\zeta}\left(v^2 - v_{(0)}^2\right) &= \frac{\mathrm{d}}{\mathrm{d}\zeta}(\Gamma) \\
\frac{\mathrm{d}}{\mathrm{d}\zeta}\left(u^2 v\cos\theta\right) + \frac{1}{2}\Delta S\frac{\mathrm{d}}{\mathrm{d}\zeta}\left(v^2 - v_{(0)}^2\right) &= 0 \\
\left(2uv\cos\theta\frac{\mathrm{d}u}{\mathrm{d}\zeta} + u^2\cos\theta\frac{\mathrm{d}v}{\mathrm{d}\zeta} - u^2 v\sin\theta\frac{\mathrm{d}\theta}{\mathrm{d}\zeta}\right) + \frac{1}{2}\Delta S\frac{\mathrm{d}}{\mathrm{d}\zeta}v^2 &= 0 \\
\left(2uv\cos\theta\frac{\mathrm{d}u}{\mathrm{d}\zeta} + u^2\cos\theta\frac{\mathrm{d}v}{\mathrm{d}\zeta} - u^2 v\sin\theta\frac{\mathrm{d}\theta}{\mathrm{d}\zeta}\right) + \Delta S v\frac{\mathrm{d}v}{\mathrm{d}\zeta} &= 0
\end{aligned}$$

note from Eq. A.18 that

$$v\frac{\mathrm{d}v}{\mathrm{d}\zeta} = u^2 v\sin\theta$$

giving

$$2uv\cos\theta\frac{\mathrm{d}u}{\mathrm{d}\zeta} + u^2\cos\theta\frac{\mathrm{d}v}{\mathrm{d}\zeta} + u^2 v\sin\theta\left(\Delta S - \frac{\mathrm{d}\theta}{\mathrm{d}\zeta}\right) = 0$$

Further, substitute in for Eq. A.17 and Eq. A.18 and divide through by $\sin\theta$

$$-2u^2v^2\cos\theta + u^4\cos\theta + u^2 v\left(\Delta S - \frac{\mathrm{d}\theta}{\mathrm{d}\zeta}\right) = 0$$

re-arranging gives

$$\begin{aligned}
u^2 v\frac{\mathrm{d}\theta}{\mathrm{d}\zeta} &= u^4\cos\theta + u^2 v\Delta S - 2u^2v^2\cos\theta \\
\frac{\mathrm{d}\theta}{\mathrm{d}\zeta} &= \frac{u^2\cos\theta}{v} + \Delta S - 2v\cos\theta \\
&= \Delta S + \cos\theta\left(\frac{u^2}{v} - 2v\right)
\end{aligned}$$

Now compare this result with the following,

$$\begin{aligned}
\frac{\mathrm{d}}{\mathrm{d}\zeta}\ln\left(u^2 v\right) &= \frac{1}{u^2 v}\left(2uv\frac{\mathrm{d}u}{\mathrm{d}\zeta} + u^2\frac{\mathrm{d}v}{\mathrm{d}\zeta}\right) \\
&= \frac{1}{uv}\left(2v\frac{\mathrm{d}u}{\mathrm{d}\zeta} + u\frac{\mathrm{d}v}{\mathrm{d}\zeta}\right) \\
&= \frac{-2v^2\sin\theta + u^2\sin\theta}{v}
\end{aligned}$$

Therefore,

$$\frac{u^2 - 2v^2}{v} = \frac{\mathrm{d}}{\mathrm{d}\zeta} \ln\left(u^2 v\right) \frac{1}{\sin\theta}$$

Substituting this result the original definition of Eq. A.19 is obtained, thus proving that

$$u^2 v \cos\theta + \frac{1}{2}\Delta S\left(v^2 - v_{(0)}^2\right) = \Gamma$$

is indeed a more general solution for the integration constant.

# Appendix B

# Publications

## Published Journal Papers

[1] H. E. Major, C. B. E. Gawith, and P. G. R. Smith. Gouy phase compensation in quase-phase matching. *Opt. Commun.*, 281(19):5036–5040, October 2008.

[2] H. E. Major, A. C. Peacock, J. C. Gates, C. B. E. Gawith, and P. G. R. Smith. Deleted domains and $\pi$ phase shift scheme for flat-top temperature tuning response in periodically poled nonlinear crystals for second-harmonic generation. *Opt. Commun.*, 2009.

## International meetings

[1] H. E. Major, A. C. Peacock, J. C. Gates, C. B. E. Gawith, and P. G. R. Smith. Flat-top temperature tuning response in periodically-poled nonlinear crystals. In *SPIE Europe Optics and Optoelectronics Conference Prague*, 2007.

[2] H. E. Major, A. C. Peacock, C. B. E. Gawith, and P. G. R. Smith. Design considerations for the manufacture of temperature stable periodically-poled nonlinear crystals. In *CLEO Europe/IQEC Munich*, 2007.

[3] H. E. Major, C. B. E. Gawith, and P. G. R. Smith. Gouy phase compensated quase-phase matching (GQPM). In *CLEO/QELS 2008 San Jose*, May 2008.

# Other publications stemming from the work detailed in this thesis

[1] C. Holmes, H. E. Major, J. C. Gates, C. B. E. Gawith, and P. G. R. Smith. Period adapted Bragg mirror multimode interference device. In *CLEO/IQEC 2009 Baltimore*, May 2009.

# Appendix C

# Patents

**Improved Electric Field Poling Of Ferroelectric Materials**
International PCT Application No. PCT/GB2008/001993
International Publication No. WO2008/152377 A1

**Gouy phase compensation for improved second harmonic efficiency**
UK Patent Application No. GB0801322.9

**A process for poling a ferroelectric material doped with a metal**
UK Patent Application No. GB0802852.4

(12) INTERNATIONAL APPLICATION PUBLISHED UNDER THE PATENT COOPERATION TREATY (PCT)

(19) World Intellectual Property Organization
International Bureau

(43) International Publication Date
18 December 2008 (18.12.2008)

PCT

(10) International Publication Number
WO 2008/152377 A1

(51) International Patent Classification:
*G02F 1/355* (2006.01)

(21) International Application Number:
PCT/GB2008/001993

(22) International Filing Date: 11 June 2008 (11.06.2008)

(25) Filing Language: English

(26) Publication Language: English

(30) Priority Data:
0711275.8 11 June 2007 (11.06.2007) GB

(71) Applicant *(for all designated States except US)*: **UNIVERSITY OF SOUTHAMPTON** [GB/GB]; Highfield, Southampton SO17 1BJ (GB).

(72) Inventors; and

(75) Inventors/Applicants *(for US only)*: **GAWITH, Corin, Barry, Edmund** [GB/GB]; Centre for Enterprise & Innovation, Universty of Southampton, Highfield, Southampton SO15 1BJ (GB). **MAJOR, Huw, Edward** [GB/GB]; Centre for Enterprise & Innovation, Universty of Southampton, Highfield, Southampton SO15 1BJ (GB). **MING, Lu** [CN/CN]; Centre for Enterprise & Innovation, Universty of Southampton, Highfield, Southampton SO15 1BJ (GB). **SMITH, Peter, George, Robin** [GB/GB]; Centre for Enterprise & Innovation, Universty of Southampton, Highfield, Southampton SO15 1BJ (GB).

(74) Agent: **McGOWAN, Catherine**; D Young & Co, 120 Holborn, London EC1N 2DY (GB).

(81) Designated States *(unless otherwise indicated, for every kind of national protection available)*: AE, AG, AL, AM, AO, AT, AU, AZ, BA, BB, BG, BH, BR, BW, BY, BZ, CA, CH, CN, CO, CR, CU, CZ, DE, DK, DM, DO, DZ, EC, EE, EG, ES, FI, GB, GD, GE, GH, GM, GT, HN, HR, HU, ID, IL, IN, IS, JP, KE, KG, KM, KN, KP, KR, KZ, LA, LC, LK, LR, LS, LT, LU, LY, MA, MD, ME, MG, MK, MN, MW, MX, MY, MZ, NA, NG, NI, NO, NZ, OM, PG, PH, PL, PT, RO, RS, RU, SC, SD, SE, SG, SK, SL, SM, SV, SY, TJ, TM, TN, TR, TT, TZ, UA, UG, US, UZ, VC, VN, ZA, ZM, ZW.

(84) Designated States *(unless otherwise indicated, for every kind of regional protection available)*: ARIPO (BW, GH, GM, KE, LS, MW, MZ, NA, SD, SL, SZ, TZ, UG, ZM, ZW), Eurasian (AM, AZ, BY, KG, KZ, MD, RU, TJ, TM), European (AT, BE, BG, CH, CY, CZ, DE, DK, EE, ES, FI, FR, GB, GR, HR, HU, IE, IS, IT, LT, LU, LV, MC, MT, NL, NO, PL, PT, RO, SE, SI, SK, TR), OAPI (BF, BJ, CF, CG, CI, CM, GA, GN, GQ, GW, ML, MR, NE, SN, TD, TG).

**Published:**
— *with international search report*

(54) Title: IMPROVED ELECTRIC FIELD POLING OF FERROELECTRIC MATERIALS

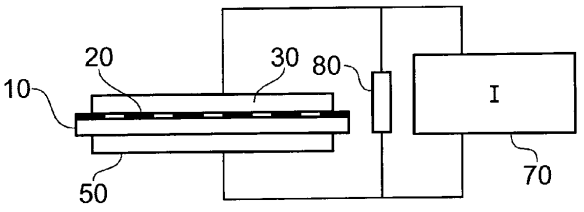


FIG. 5

(57) Abstract: A method of inducing a periodic variation of nonlinearity value in a sample of ferroelectric material comprises arranging a pair of electrodes on opposite faces of the sample, one electrode defining a desired pattern of nonlinearity variation, applying a pre-bias voltage across the sample for a predetermined time using the electrodes, the pre-bias voltage being less than the coercive field of the ferroelectric material; and after the predetermined time, applying a current-controlled poling voltage across the sample using the electrodes, to produce domain inversion in the sample according to the desired pattern of nonlinearity variation. The pre-bias voltage may be 75% of the coercive field or more, and applied for a pre-determined time between 1 and 100 seconds.

WO 2008/152377 A1